

Imperial College London  
Department of Chemical Engineering

**Emergence of Colour by Tunable Surface  
Wrinkling in One and Multi-Dimensions**

Soon Nee Annabelle Tan

Submitted in part fulfilment of the requirements for the degree of  
Doctor of Philosophy in Chemical Engineering of Imperial College London, 13 March 2023



## **Declaration**

I hereby declare that this thesis and the work reported herein was composed by and originate entirely from me. Information derived from the published and unpublished work of others has been acknowledged in the text and references are given in the list of sources.

The copyright of this thesis rests with the author. Unless otherwise indicated, its contents are licensed under a Creative Commons Attribution-Non Commercial 4.0 International Licence (CC BY-NC). Under this licence, you may copy and redistribute the material in any medium or format. You may also create and distribute modified versions of the work. This is on the condition that: you credit the author and do not use it, or any derivative works, for a commercial purpose. When reusing or sharing this work, ensure you make the licence terms clear to others by naming the licence and linking to the licence text. Where a work has been adapted, you should indicate that the work has been changed and describe those changes. Please seek permission from the copyright holder for uses of this work that are not included in this licence or permitted under UK Copyright Law.

## Abstract

Naturally occurring surface patterns often exhibit micro and nano-scale topography with various functionalities, including displaying optical and photonic effects. One such natural topography that contributes to structural colour is the presence of wrinkles. This thesis explores the controlled wrinkling of bi-layered materials as a powerful patterning method to create bioinspired topographies, and examines their optical properties. The primary method employed in this work involves the use of plasma oxidation of polydimethylsiloxane, combined with mechanical strain, to create wrinkles with varying topographies, ranging from nano to micronscales, by controlling the plasma and strain conditions, as well as the superposition of various generations of wrinkles with prescribed relative angle of orientation. This work firstly investigates the formation of one-dimensional uniaxial wrinkles acting as tunable sinusoidal phase gratings, and quantitatively models the diffractive behaviour of the wrinkled surfaces as a function of strain. Under white light, these wrinkles exhibit iridescent, structural colour on the surfaces that depends on the observation angles and incident light spectrum, and we explored the concept of optical and colour directionality by creating gradient and isotropic wrinkles. In addition to surface diffraction in reflection, we found that the wrinkled materials could act as transmission gratings, leading to multi-faceted structural colour through diffraction combined by total internal reflection. Finally, we investigated the potential and limitations of sequential two-dimensional wrinkling and its structural colour properties. The results of this study provide promising directions for using structural coloured wrinkles in applications such as sensors, displays, and packaging.



## Acknowledgements

I would like to thank João for the support and guidance these past few years. He has been an inspiration in my work with his passion in the research field, and with his endless stream of ideas. I have enjoyed the many conversations we have shared, and I never fail to learn something new in these conversations with him.

I am grateful to everyone I have met in the Polymers and Microfluidics group, for all the memories we have had together, and forming an integral part of my PhD experience. I am especially thankful for Will, Roisin and Liva, who have been there since the start of my journey in the group. I treasure all the chats we have shared, and that they are people I can always go to for any advice and help. I am grateful to Gunjan, who constantly reminds us to look at life positively and that nothing is too hard to overcome.

I am extremely lucky to have had Luca as my supervisor (and then became more of a mentor) since I started the group. He has played an immensely huge role in guiding me to be the researcher I have become. He showed me the building blocks to grow to be a good, independent researcher and I have been inspired by his resilience in tackling any problems. Most of all I am grateful for the times he pushed me to my potential, and for the friendship we have developed.

I thank the Plastic Electronics CDT, for the opportunities it has provided and for giving me a platform to have a cohort of people I could share this experience with. I am grateful to Cohort 10, for the experiences we have shared together and for helping to make this journey much more enjoyable. I would also like to thank the EPSRC-funded Plastic Electronics CDT, in collaboration with Procter & Gamble for funding my PhD (Grant Number EP/L016702/1).

## Publications

Some of the original work of the author herein has been previously published in the following publications:

1. Tan, Annabelle, Zain Ahmad, Pete Vukusic, and João T. Cabral. 2023. "Multifaceted Structurally Coloured Materials: Diffraction and Total Internal Reflection (TIR) from Nanoscale Surface Wrinkling" *Molecules* 28, no. 4 (2023): 1710.

Author Contributions: Conceptualization, A.T. and J.T.C.; methodology, A.T., Z.A. and P.V.; formal analysis; A.T.; validation, A.T., Z.A.; investigation, A.T; writing—original draft preparation, A.T., Z.A., P.V., J.T.C.; writing—review and editing, A.T., Z.A., P.V., J.T.C.; supervision, J.T.C.; project administration, J.T.C.; funding acquisition, J.T.C. All authors have read and agreed to the published version of the manuscript.

2. Tan, Annabelle, Luca Pellegrino, Zain Ahmad, and João T. Cabral. "Tunable Structural Color with Gradient and Multiaxial Polydimethylsiloxane Wrinkling." *Advanced Optical Materials* (2022): 2200964.

Author contributions: A.T. and L.P. performed all experiments, Z.A. assisted with the fabrication of gradient wrinkles. J.T.C. conceived and directed the project. All authors analysed the data, wrote, and revised the manuscript.

3. Pellegrino, Luca, Annabelle Tan, and João T. Cabral. "Ripple Patterns Spontaneously Emerge through Sequential Wrinkling Interference in Polymer Bilayers." *Physical Review Letters* 128, no. 5 (2022): 058001.

Author contributions: L.P. performed all main paper experiments, A.T. assisted with fabrication of variable angle and film floating experiments. J.T.C. conceived and directed the project. All authors analysed the data, wrote and revised the manuscript.

4. Tan, Annabelle, Luca Pellegrino, and João T. Cabral. "Tunable Phase Gratings by Wrinkling of Plasma-Oxidized PDMS: Gradient Skins and Multiaxial Patterns." *ACS Applied Polymer Materials* 3, no. 10 (2021): 5162-5170.

Author Contributions: A.T. and L.P. performed all experiments: sample preparation, light diffraction, optical and atomic force microscopy, and mechanical measurements. J.T.C.

conceived and directed the project. All authors analysed the data, wrote, and revised the manuscript.



# Contents

<b>Abstract</b>	<b>ii</b>
<b>Acknowledgements</b>	<b>iii</b>
<b>Publications</b>	<b>iii</b>
<b>List of Figures</b>	<b>xvi</b>
<b>1 Introduction</b>	<b>1</b>
1.1 Surface topography and optical properties . . . . .	1
1.1.1 Role and importance of surface topography . . . . .	1
1.1.2 Structural colour mechanisms in nature . . . . .	3
1.1.3 Optical effects of natural occurring structures . . . . .	5
1.1.4 Theory of Diffraction Grating . . . . .	9
1.2 Influence of natural surfaces in photonic application . . . . .	11
1.2.1 Wrinkle structures . . . . .	12
1.2.2 Sinusoidal Phase Grating . . . . .	15

---

1.3	The Project . . . . .	18
<b>2</b>	<b>Mechanisms and methods of wrinkling</b>	<b>20</b>
2.1	Introduction . . . . .	20
2.1.1	Bilayer model . . . . .	22
2.1.2	Approaches to bilayer formation . . . . .	25
2.2	Methods to induce wrinkles . . . . .	27
2.2.1	2D wrinkling . . . . .	29
<b>3</b>	<b>Experimental Methodologies</b>	<b>33</b>
3.1	Samples preparation and fabrication . . . . .	33
3.1.1	PDMS Substrate fabrication . . . . .	33
3.1.2	Strain application . . . . .	34
3.1.3	Surface Oxidation . . . . .	35
3.1.4	Replica moulding . . . . .	37
3.2	Surface Characterisation . . . . .	38
3.2.1	Optical Microscopy . . . . .	38
3.2.2	Atomic Force Microscopy . . . . .	39
3.2.3	Static Light Scattering . . . . .	40
3.3	Material characterisation . . . . .	42
3.3.1	UV Vis Spectrometry . . . . .	42
3.3.2	Tensile Strain Measurements . . . . .	43

---

3.3.3	Thin film Analyser . . . . .	44
<b>4</b>	<b>Plasma-oxidised Wrinkles for Tunable Phase Gratings</b>	<b>45</b>
4.1	Introduction . . . . .	45
4.2	Methodology . . . . .	46
4.2.1	Sample preparation . . . . .	46
4.2.2	Replication of wrinkle topography using Norland Optical Adhesive (NOA)	47
4.2.3	Tensile strain measurement . . . . .	47
4.2.4	Pattern characterisation . . . . .	48
4.3	Wrinkled bilayer characterisation . . . . .	50
4.3.1	Diffraction intensity modulation in wrinkled tuneable gratings . . . . .	53
4.3.2	Modelling of plasma-oxidised tuneable grating: Effect of gradient in- terface on diffraction . . . . .	56
4.3.3	Effect of PDMS mechanical properties on diffraction of tuneable gratings	61
4.3.4	Additional diffraction orders at high deformations: period doubling in- stability . . . . .	63
4.3.5	Real-space reconstruction from diffraction pattern (1D) . . . . .	65
4.4	Conclusion . . . . .	66
<b>5</b>	<b>Tunable structural colour and mechanochromic response of wrinkles: 1D and mul- tiaxial</b>	<b>68</b>
5.1	Introduction . . . . .	68
5.2	Methodologies . . . . .	71

5.2.1	Sample preparation . . . . .	71
5.2.2	Material characterisation . . . . .	72
5.2.3	Surface characterisation . . . . .	72
5.3	Structural color from nano- to microscale wrinkles . . . . .	73
5.3.1	Mechanochromic response: tuning colors with strain . . . . .	78
5.3.2	Effect of relative illumination and viewing angles on colour perception . . . . .	83
5.3.3	Azimuthal viewing angle and color of 1D and isotropic wrinkles . . . . .	85
5.3.4	Homogeneity and directional color . . . . .	86
5.4	Conclusion . . . . .	92
<b>6</b>	<b>Structural colour through TIR</b>	<b>94</b>
6.1	Introduction . . . . .	94
6.2	Methodologies . . . . .	96
6.2.1	Sample preparation . . . . .	96
6.2.2	Surface Characterisation . . . . .	97
6.2.3	Light source and spectrum calibration . . . . .	97
6.3	Structural colour of wrinkled surfaces through surface diffraction . . . . .	98
6.3.1	Total Internal Reflection (TIR) and selection of facet colour . . . . .	100
6.3.2	A minimal model for facet colour: TIR and incident light dispersion . . . . .	101
6.3.3	Colour changes induced by environmental conditions . . . . .	108
6.3.4	Specimen geometry in producing structural colour . . . . .	110



6.3.5	Structural colour TIR in GRISM . . . . .	111
6.4	Conclusion . . . . .	114
<b>7</b>	<b>2D Diffraction Interference and Structural Colour</b>	<b>115</b>
7.1	Introduction . . . . .	116
7.2	Methodologies . . . . .	117
7.2.1	Simultaneous and sequential 2D wrinkling . . . . .	117
7.2.2	2D floating and lamination . . . . .	118
7.2.3	Thin film measurement . . . . .	118
7.2.4	Pattern Characterisation . . . . .	119
7.3	Wrinkling Superposition at various $\theta$ . . . . .	120
7.4	Real space reconstruction from 2D Diffraction Pattern . . . . .	123
7.5	Structural Colour of 2D samples . . . . .	126
7.5.1	Varying $\theta$ angle 2D samples . . . . .	126
7.5.2	Comparing 90° simultaneous vs sequential 2D samples . . . . .	130
7.6	Conclusion . . . . .	131
<b>8</b>	<b>Conclusions</b>	<b>133</b>
	<b>Bibliography</b>	<b>137</b>
	<b>Appendices</b>	<b>155</b>

# List of Figures

1.1	Summary of nature’s topography and functionalities . . . . .	2
1.2	Five fundamental physical optical processes . . . . .	4
1.3	Examples of structural colours in nature involving diffraction effects . . . . .	6
1.4	Principles of observed blue colour in the Morpho butterfly . . . . .	7
1.5	Schematic of diffraction grating accounting for incident and diffracted angle . .	10
1.6	Smart window through tunable surface wrinkles . . . . .	14
1.7	Optical signal changes due to surface wrinkles in a wearable optical sensor . .	15
1.8	Bessel function of the first kind . . . . .	16
2.1	Examples of wrinkles caused by buckling of instabilities . . . . .	21
2.2	General formation of wrinkles in bilayered system . . . . .	23
2.3	Wrinkle instabilities phase diagram . . . . .	24
2.4	Frontal photopolymerisation profile of surface conversation of plasma-oxidised PDMS with dose . . . . .	27
2.5	Methods to measure uniaxial and isotropic buckling . . . . .	29
2.6	Buckling modes on films on PDMS substrates and their normalised energies . .	30

2.7	Schematic of fabrication of sequential 2D wrinkles . . . . .	31
3.1	Strain stages employed in experiments . . . . .	35
3.2	Plasma chambers employed . . . . .	36
3.3	Schematic of Static Light Scattering (SLS) setup . . . . .	40
3.4	Correlation of pixels to wavenumber in SLS image for SLS system . . . . .	41
3.5	Dimensions of tensile test specimen according to ASTM D412 . . . . .	43
4.1	Stress-strain plot obtained from Lloyd EZ 50 Tensile Machine . . . . .	48
4.2	Schematic of SLS intensity measurements . . . . .	49
4.3	Schematic of the formation of 1D wrinkled surfaces and AFM measurements . . . . .	51
4.4	Aspect ratio of wrinkles with exposure time . . . . .	52
4.5	Diffraction pattern with compressive strain . . . . .	53
4.6	Dependence of normalised diffraction intensities with strain . . . . .	55
4.7	Modelling of plasma-oxidised tuneable grating using an exponential distribution . . . . .	57
4.8	Exponential vs Gaussian distribution in modelling of plasma-oxidised tuneable grating . . . . .	60
4.9	Diffraction efficiency of tunable grating . . . . .	61
4.10	Non-hookean behaviour in PDMS at high strain . . . . .	62
4.11	First order diffraction intensities in the non-hookean behaviour regime . . . . .	62
4.12	Formation of period doubling . . . . .	64
4.13	Reconstruction of a real-space image using a SLS diffraction patterns. . . . .	65

5.1	Formation of 1D and isotropic wrinkling samples . . . . .	70
5.2	Structural colour of nano-wrinkled samples formed using 10.5 W, MHz plasma	74
5.3	Effect of carbon black on PDMS . . . . .	75
5.4	Comparison of observed diffracted structural colour between clear PDMS and coloured backgrounds . . . . .	76
5.5	Structural colour of micro-wrinkled samples . . . . .	77
5.6	Intensity of the first diffraction order with increasing plasma exposure time . . .	79
5.7	Sensitivity of mechanochromic response . . . . .	80
5.8	Mechanochromic response of wrinkled sample . . . . .	81
5.9	Parameters to account in model: Light spectrum, UV-Vis absorbance, Intensity vs $\lambda$ . . . . .	82
5.10	Effect of relative illumination and viewing angles on colour perception . . . . .	84
5.11	Comparison of directional structural colour in 1D and isotropic wrinkles . . . . .	86
5.12	Direction of periodicity variation affect on structural colour . . . . .	88
5.13	Structural colour behaviours for 1D samples with gradient periodicity . . . . .	89
5.14	Schematic of fabrication of step-wise plasma-oxidised PDMS in fabricating gradient periodicity structure . . . . .	90
5.15	Schematic of fabrication of gradient periodicity structure through using a geo- metric shape . . . . .	91
6.1	Schematic of structural colour of a 1D wrinkled surface through diffraction and Total Internal Reflection (TIR) . . . . .	95
6.2	Spectrometer calibration with PDMS thickness . . . . .	98

6.3	Schematic of fabrication of 1D samples and AFM measurements . . . . .	99
6.4	Structural colour images of 1D wrinkled surfaces ( $d = 700$ nm) and spectrometer measurements . . . . .	101
6.5	Modelling of structural colour TIR spectrometer measurements . . . . .	103
6.6	Effect of sample's geometry on structural colour due to TIR ray exit . . . . .	104
6.7	Effect of sample's length on structural colour intensity . . . . .	106
6.8	Effect of surface periodicity $d$ on top (reflective diffraction) and facet (TIR) structural colour . . . . .	107
6.9	Limits in wrinkle periodicities in exhibiting facet (TIR) colour . . . . .	108
6.10	Top and facet structural colour change upon solvent-induced swelling. . . . .	109
6.11	Effect of polyhedrop shape on top and facet structural colour . . . . .	110
6.12	'GRISM' fabrication and its structural colour optical images . . . . .	112
7.1	Schematic of 2D wrinkling fabrication . . . . .	117
7.2	Characterisation and modeling of non-orthogonal wrinkling superposition . . .	120
7.3	Calibration of PS film thickness with mass fraction of polystyrene-toluene solution	122
7.4	AFM structures of polystyrene film onto a pre patterned PDMS surface at $20^\circ$ and $70^\circ$ . . . . .	122
7.5	Wavelength and amplitude models for plasma-oxidised PDMS at $P = 20$ W, 120 s	123
7.6	2D AFM reconstruction via SLS intensities . . . . .	124
7.7	Ratio of 1st to 2nd generation diffraction intensities with angular dependency .	125
7.8	2D structural colour with varying strain at $\theta = 30^\circ$ . . . . .	126

7.9	2D Structural colour at varying $\theta$ . . . . .	128
7.10	2D structural colour parameters for $\theta = 70^\circ$ . . . . .	129
7.11	Structural color in $90^\circ$ 2D wrinkled surfaces . . . . .	131
8.1	Fabrication of crack-free wrinkles with $CHF_3$ . . . . .	137

# Chapter 1

## Introduction

### 1.1 Surface topography and optical properties

#### 1.1.1 Role and importance of surface topography

The surfaces of materials often consist of undulations, slopes, and pores, which collectively form the surface topography. Describing this topography can be challenging, as it requires more than just a few parameters. However, the surface topography is a vital factor that significantly affects the performance of various applications. These properties closely resemble the functionalities that are naturally present in the environment, such as adherence [1], optical properties [2], and wettability [3]. The surface topography found in nature is responsible for many of its biological functions, inspiring the field of biomimetics or biologically inspired technology. Over 515 million years of evolution, biological species have developed highly intricate and multifunctional natural surfaces that allow them to interact with the environment in various ways [4]. With the advancements in technology, scientists can now better understand the natural surfaces by using spectroscopy techniques. This allows for further research into the relationship between the structure and performance of natural biomaterials, which serves as the basis for the development of biomimetic structures and materials.

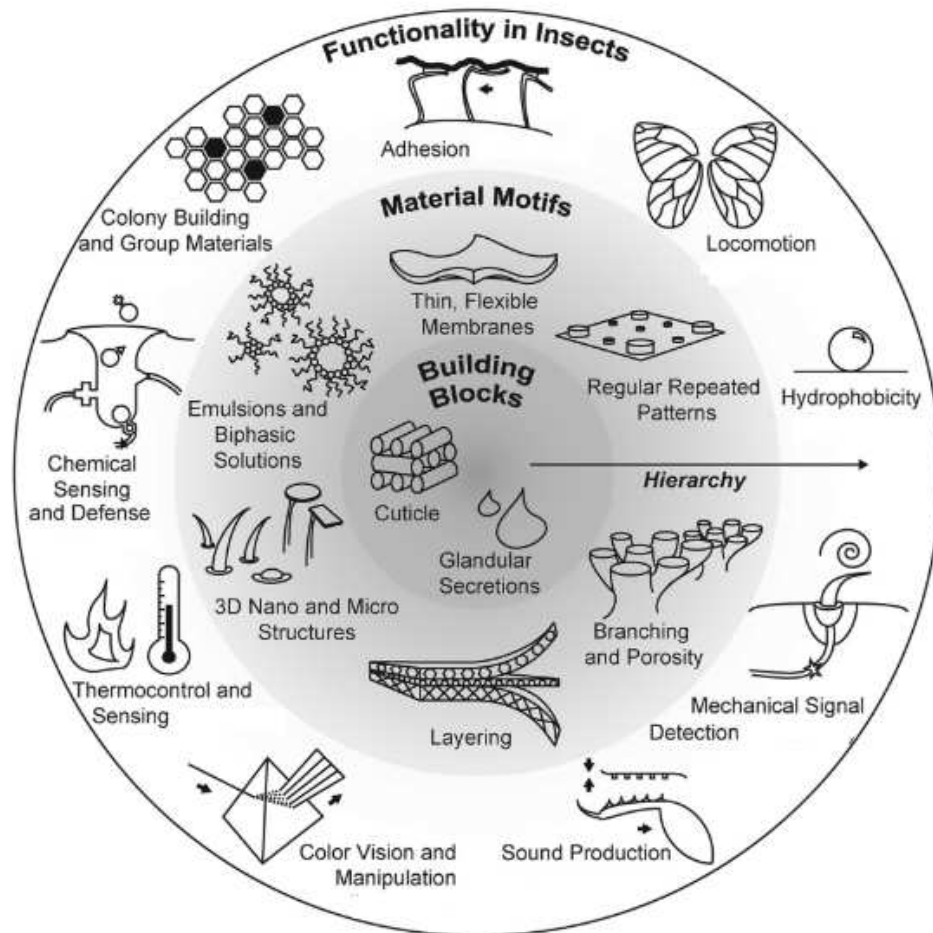


Figure 1.1: Summary of the functionality that can be found in insects and the structures responsible for them. Reproduced from [5] under the Creative Commons Attribution-Non Commercial 4.0 International Licence (CC BY-NC).

The structures of natural surfaces exhibit many functionalities. For example, some leaves have tiny bumps that cause water to bead up and roll off the surface, helping to keep the leaf clean and dry [6]. Gecko feet have millions of tiny hairs that allow them to climb smooth surfaces, increasing the van der Waals forces between the foot and the surface [7]. Many animals, such as chameleons [8] and octopuses [9], use surface topography to blend in with their surroundings, while the surface topography of the human tongue allows us to sense the texture of food [10]. Finally, the surface topography of some butterfly wings and shark skin is characterised by microscopic ridges and grooves that prevent dirt and bacteria from adhering to the surface, helping to reduce the risk of infection and disease.



In this thesis, we center on the investigation of the optical characteristics associated with surface topography, specifically on the role of diffraction properties surface topography may exhibit in producing structural colour.

### **1.1.2 Structural colour mechanisms in nature**

The origins of colour can be attributed to a variety of physical mechanisms, which can be categorised into five groups, with four chemical and one physical [11]. The physical mechanisms are classified as interference, scattering, or diffraction, based on how they interact with light. While chemical pigments produce observable colours that are not affected by the angle of observation, iridescence can result from micro- or nano-structures, with the observed colour changing depending on the angle of observation. The colours produced by structural colouration are often more vivid and intense than those produced by pigments or dyes. This is because the physical structure of the material can interact with light waves in a more complex and precise way than a simple chemical pigment. In addition, structural colours can be more durable and resistant to fading or discolouration over time.

In nature, the mechanisms responsible for structural colouration can be divided into two main categories: "surface" mechanisms, which include diffraction gratings and scattering, and "bulk" mechanisms, which consist of multilayer interference and photonic crystals. When electromagnetic radiation, such as visible light or ultraviolet light, interacts with spatial variations in a material's dielectric properties that are similar in size to the incident light, it can result in the production of structural colour. The interactions of surfaces with light causing structural colours can be described as either interference, scattering or diffraction of the structures. Iridescence can be produced from micro or nano-structures [12], where the observed colour is dependent on the angle from which is viewed while chemical pigments on the hand, produces colour that is independent of angle. As in feathers and butterfly wing scales, structures can be a single layer acting as a thin film. While in outer shell of beetles and opals, they act as multilayers and a complex photonic crystal respectively.

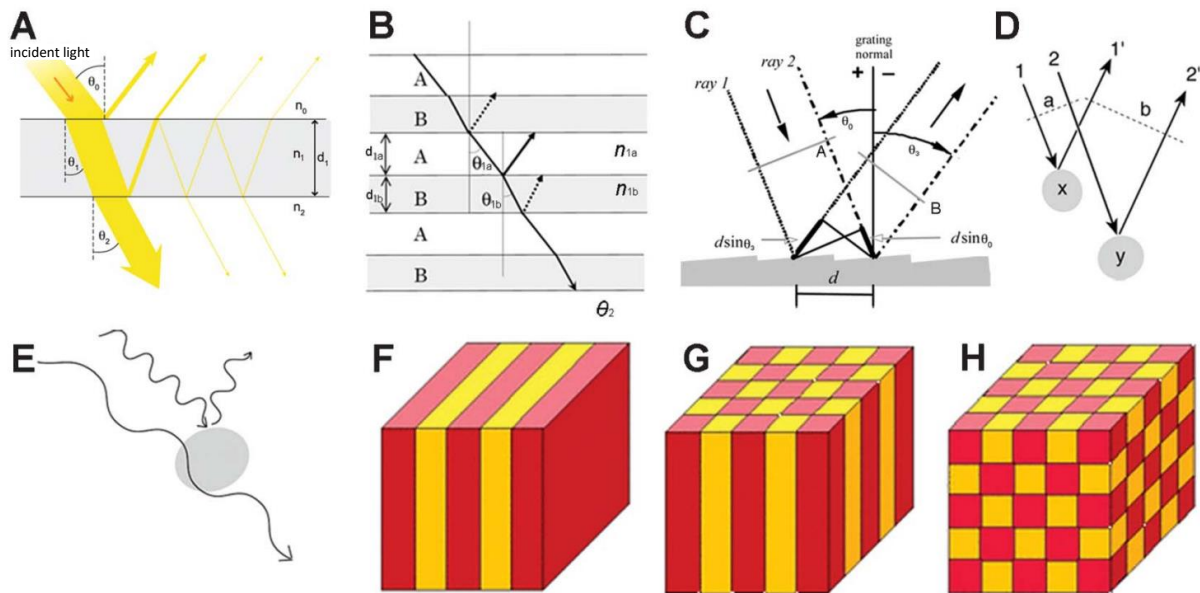


Figure 1.2: Five fundamental physical optical processes: A) thin-film interference, B) multi-layer interference, C) diffraction grating, D, E) scattering (coherent and non-coherent) F, G, H) photonic crystals (1-D, 2-D, 3-D). Adapted from [2] with permission from Royal Society of Chemistry.

In optics, a thin film refers to a layer of material with thickness ranging from sub-nanometer to micron levels. When light strikes the surface of the film, it can either be reflected or transmitted at the surface. If the light undergoes transmission through the film, it can be reflected or transmitted once again at the bottom surface. These two processes result in reflected light interfering with each other. The extent of constructive or destructive interference on the light waves depend on the difference in phase between them, which can be influenced by the film thickness, its refractive index, and the angle at which the original wave is incident on the film. Thin film interference are commonly see in the case of soap bubble, an oil slick on water and on the surface of a CD, producing iridescent colours [2].

Multilayer interference, on the other hand, occurs when light interacts with multiple layers of materials. Each layer of the structure have a different refractive index and thickness, allowing it to produce its own thin-film interference pattern. The resultant interference pattern generated by the layers can cause certain colours to be enhanced or suppressed, and it can be modified by

changing the thickness and refractive index of the layers in the multilayer structure. Multilayer interference is the most commonly observed form of structural colour in nature, whereas thin-film interference is less frequently observed [13].

Photonic crystals, or PCs have garnered significant attention within the field of materials science. These materials exhibit a periodic variation in refractive index, resulting in a photonic band gap (PBG) which prohibits certain wavelengths of light within the PBG from transmitting through the material. Depending on the spatial period and refractive index variations, PCs can be categorised into one-dimensional (1D), two-dimensional (2D), and three-dimensional (3D) structures [14]. The vibrant visual characteristics of photonic crystal materials can be explained by the concepts of interference and reflection, and can be commonly seen in nature, such as in the structure of opals [15], feathers [16] and beetles [17].

Although diffraction grating-type structural colouration is not commonly found in nature, it is a powerful mechanism due to the periodic nature of the grating that enhances its effect. This is likely due to the variation of colours it produces rather than a specific colour, which may not adapt to the purposes of animals [13]. However, diffraction grating structures can be found in a variety of natural structures, such as on the petals of flowers [18], butterfly scales [19], mollusc shells [20], beetles [21, 22], and meat surfaces [23, 24]. These diffraction structures often work together with one or more of the previous mechanisms described. These structures use diffraction gratings to separate white light into its component parts and produce a rainbow effect.

### **1.1.3 Optical effects of natural occurring structures**

So far, we have detailed the different type of mechanisms that can occur to produce structural colour in nature. Colour is at the heart of most optical effects found in natural structures. They play a vital role in nature by attracting mates, warning predators, or camouflaging animals. Although multilayer interference and photonic crystals are fascinating mechanisms occurring in nature, in this thesis we focus on the phenomenon of diffraction grating structures in producing

structural colours. Here, we detail a couple of examples of some well known optical effects observed in nature involving diffraction.

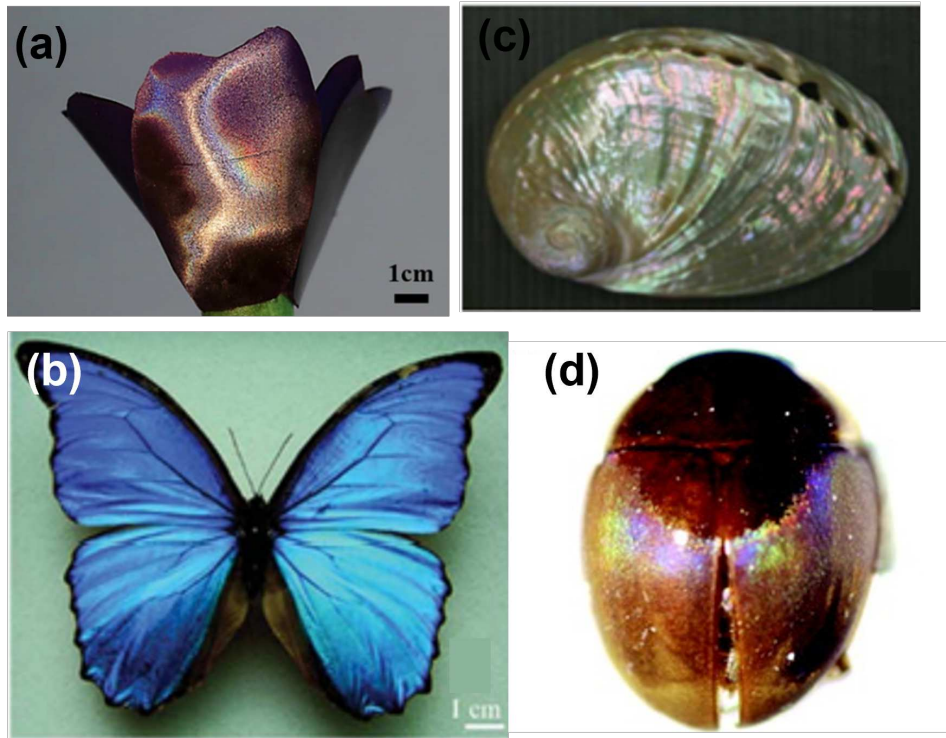


Figure 1.3: (a) Queen of the Night tulip petals exhibit an iridescent and glossy colour due to the diffraction and scattering of light [25]. (b) Morpho butterfly's distinctive blue colouration is due to a combination of mechanisms involving multilayer interference, diffraction and scattering [26]. (c) Mollusc *Haliotis Glabra* mollusc has fine-scale diffraction grating structure, together with interference they are responsible for its iridescence [27] (d) Male *Aglyptinus tumerus* beetles have the presence parallel grating structures giving iridescence effects, which are absent in females [28, 29]

The intricate nanostructures on the surface of butterfly wings create an optical phenomenon known as structural colour, which results in a wide range of iridescent hues and tones. The Morpho butterfly which is famous for its brilliant blue colouration, has physical composition and colouration that creates a unique interplay of optical phenomena, resulting in specific effects. These includes: 1) quasi-multilayer interference, which enhances reflectivity in the blue region, 2) diffusive reflection caused by the narrow width and irregular height of the ridge, 3) pigmentation that amplifies the contrast of blue colouration through the absorption of green to

red light, and 4) transparent scales that act as an optical diffuser, covering the butterfly's structure [13]. For over a century, scientists have attributed the colour and reflective properties of the Morpho butterfly's wings to merely interference of light caused by the layered structure of its cuticle and air. However, it has since been established that the combined action of interference and diffraction is crucial in explaining the structural colour exhibited by the butterfly, where the diffraction grating model in the wings allow for the explanation their uniform blue reflection in a broad angular range of their wings [30]. The diffraction effect on the Morpho butterfly's wings serves to increase the range of angles at which incident light is reflected - as if the wings were to reflect light purely spectrally, the range of observable angles would be severely limited [31].

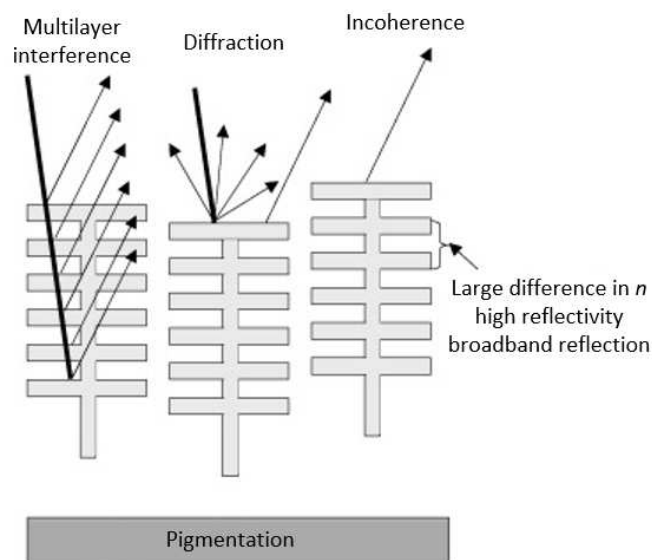


Figure 1.4: Principles of observed blue colour in the Morpho butterfly. Adapted from [13] with permission from John Wiley and Sons.

Feathers are among the most striking examples of structural colouration found in the natural world. Birds use their feathers not only for flight and insulation, but also for communication, camouflage, and social signaling [32]. Structural colouration in feathers is produced by the interaction of light with the microscopic structures within the feather, which can produce a wide range of vivid and iridescent colours. The most common type of structural colouration in feathers is produced by the scattering of light by microstructures such as barbs, barbules,

and melanosomes [33]. The microscopic structure of the feather surface can create grooves or ridges that act as a diffraction grating, splitting incoming light into its component colours and producing iridescence. The arrangement and spacing of these structures can determine the specific colours and patterns that are observed [34].

Molluscs, such as abalone and pearl oysters, are also capable of producing structural colouration through their shells [35]. An example is the mollusc *Haliotis Glabra*, or more commonly known as abalone, exhibits striking iridescence hues on its polished shell. Upon closer inspection, the shell's surface reveals a fine-scale diffraction grating structure, while below the surface are stacks of thin crystalline layers or platelets known as nacre [36]. These features indicate that the shell's iridescence is created by a combination of diffraction and interference. Specifically, the high density of grooves on the shell's surface leads to diffraction, resulting in intense colours. Meanwhile, the uniform stacking of nacre layers beneath the surface produces interference effects that also contribute to the iridescence of the shell [27].

In some natural occurring plants and insects such as petals of *Queen of the Night* tulip [25], *Hibiscus trionum* [37, 38] and daisies [39], as well as in the hindwings of the *Rhyothemis resplendens* dragonfly [40], they have wrinkle-like structures contributing to their optical properties. In particular, the petals possess hierarchical structures which imparts structural colour and also allows for broadened diffraction signals and specular reflection. In the case of flowers, a petal cuticle is composed of the cuticular layer and the cuticle proper, and a layer of epicuticular wax covers the surface of the cuticle, serving as a barrier against moisture and protecting the underlying tissues. As a result of the different rates in the growth of the epidermal cells and the epicuticular wax layer, they undergo different levels of strain. When the compressive strain in the wax layer exceeds a certain threshold, the surface of the petal becomes wrinkled, creating tiny creases. As a result, the wax layer of the petal remains smooth during the initial stages of blooming, but becomes wrinkled as the petal continues to grow [39, 41, 42]. In the wing membrane of the dragonfly, a multilayer structure is present and the wrinkling increases the angle over which incident light is backscattered. This causes the wings to be more visible over a broader angle range than the wings of other dragonflies with smooth multilayers, allowing the

wings to be more noticeable [40].

### 1.1.4 Theory of Diffraction Grating

Diffraction gratings, which are essential components in optics, were first discovered through the study of bird feathers. James Gregory studied feathers and discovered the principles of the diffraction grating, leading to the development of modern diffraction gratings that are now used in various applications, such as lasers and spectrometers. Diffraction gratings can be reflective or transmissive and are composed of a set of slits with a spacing of  $d$ . The interaction of light with the slits in the grating is the basis of diffraction gratings. The diffracted waves can interfere with each other to form constructive or destructive interference patterns.

Bragg's Law states that for constructive interference to occur between waves diffracted by adjacent crystal planes, the path difference between the waves must be an integer multiple of the wavelength. Mathematically, this can be expressed as:

$$2d \sin \theta = n\lambda \quad (1.1)$$

where  $d$  is the spacing between crystal planes,  $\theta$  is the angle of incidence of the incoming beam with respect to the crystal planes,  $n$  is an integer representing the order of the diffraction, and  $\lambda$  is the wavelength of the incident light.

For a diffraction grating, the crystal planes are replaced by a series of equally spaced slits, so the spacing  $d$  between the slits is used instead. Using Huygens' principle, which states that every point on a wavefront can be considered as a source of secondary spherical waves. We consider that each slit acts as a source of secondary wavelets, which interfere constructively and destructively to produce a diffraction pattern on a screen. Assuming that the screen is far enough away from the grating that the rays can be treated as parallel, we can use the geometry of the diffraction pattern to relate the angle of diffraction  $\theta$  to the spacing between the slits and the wavelength of light. The path difference between the waves from adjacent lines is given

by  $d \sin \theta$ , where  $d$  is the spacing between the lines and  $\theta$  is the angle of diffraction. If the path difference is equal to an integer multiple of the wavelength  $\lambda$ , the waves will interfere constructively and a bright spot will be observed in the diffraction pattern.

For constructive interference, the path difference must be an integer multiple of the wavelength, so we can write:

$$d \sin \theta = n\lambda \quad (1.2)$$

where  $n$  is an integer representing the order of the diffraction. This is the diffraction equation, which relates the angle of diffraction to the wavelength and the spacing between the slits.

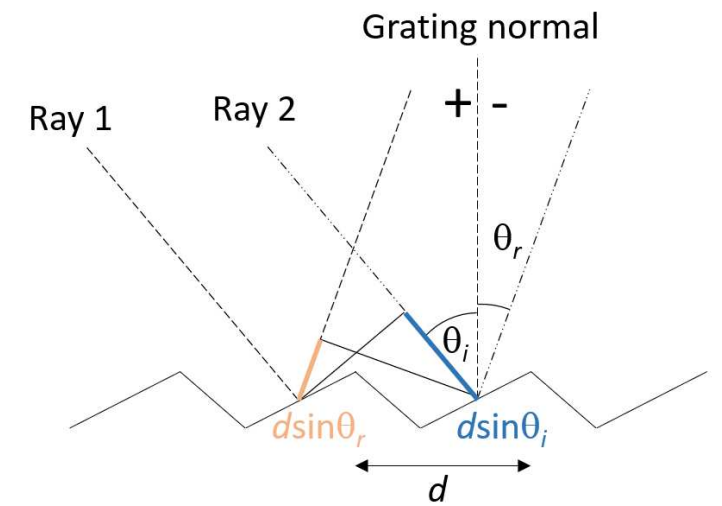


Figure 1.5: Schematic of a diffraction grating, accounting for incident beam  $\neq$  normal. Two parallel rays of beam, labelled Ray 1 and Ray 2, are incident on the grating at an angle of  $\theta_i$  and the diffracted beams are at an angle of  $\theta_r$ , measured from the normal. Upon diffraction, the geometrical path difference between light from adjacent grooves is seen to be  $d \sin \theta_i + d \sin \theta_r$ . Conventionally, the angle is denoted as negative when the diffracted beam is on the opposite side of the normal compared to the incident beam.

When light is incident at an angle  $\theta_i$  to the grating normal, we can then express the path difference between adjacent grooves in terms of both  $\theta_i$  and  $\theta_r$ . The total difference in path length is  $d \sin \theta_i + d \sin \theta_r$ , as shown in Figure 1.5. To obtain the condition for constructive interference, we set this path difference equal to an integer multiple  $n$  of the wavelength  $\lambda$ :



$$d(\sin \theta_i + \sin \theta_r) = n\lambda \quad (1.3)$$

This formula gives the condition for constructive interference of the diffracted beams for a diffraction grating, taking into account both the angle of incidence and the angle of diffraction. Conventionally, the angles of incidence and diffraction are gauged in relation to the grating normal to the beam. In the case of reflection or transmission gratings, if the two angles are measured from opposite sides of the grating normal, their algebraic signs will differ where one angle would be denoted with a + and the other a −.

## 1.2 Influence of natural surfaces in photonic application

The influence of natural surfaces in photonic applications is vast and diverse, having a significant influence on photonic applications, both as a source of inspiration for new materials and structures, and as a substrate or interface for photonic devices. Optics and photonics are essential fields in modern technology with vast applications such as communication, data storage, medicine, cosmetics, manufacturing, and security. The optical properties of periodic or rough interfacial microstructures are crucial components in optical engineering as they influence the modulation of the optical state through refraction and reflection [43]. Scientists have been inspired by optical features found in nature, leading to investigations, applications, and adaptations of similar structures in various fields, including sensors, anti-counterfeiting devices, and organic photovoltaics. These applications can be achieved by either precisely replicating the structures found in nature or by extracting new principles from the structures and implementing them to produce similar effects [44]. Famously, the structural colouration of the morpho butterfly's wings has inspired the development of new materials with similar structures and properties, with a wide range of potential applications including displays, sensing and optical communications [45, 46, 47, 48, 49, 50].

### 1.2.1 Wrinkle structures

We have previously mentioned how the occurrence of wrinkle structures found in nature can contribute to optical effects observed. Wrinkle structures are advantageous due to their tunability and flexibility - they are able to be stretched, compressed and deformed [51], dynamically tuned through various methods such as stretching [52], light [53] and moisture response [54]. This makes them attractive to be implemented into electronics such as photovoltaics, sensors and displays.

A study from Kim *et al.* have investigated the role of wrinkles and deep folds structures in the context of photovoltaics [55]. In this research, they find that polymer solar cells benefit from folds as they cause light to be trapped and guided within the photo-active layer, leading to a significant increase in light harvesting efficiency. The folds are particularly useful because they can extend light absorption beyond the range that is normally useful for energy conversion by the organic semiconductor constituents of the layer. This simple, non-chemical method enhances and extends the absorption range of these devices, including those that use low-bandgap materials. In addition, these structures are easy to implement and have been shown to be mechanically robust. Consequently, they hold great potential for creating low-cost opto-electronics on a large scale.

The use of wrinkles in smart windows have been reported in several studies. The development of smart windows is a response to the need to reduce energy consumption in buildings. These windows can save on air conditioning costs by becoming opaque on hot days to block or reflect sunlight, and they can improve light harvesting and capture free heat from the sun by returning to a transparent state when lighting conditions are low [56, 57]. Smart windows are frequently created using polymer-dispersed liquid crystals (PDLC) and electrochromic windows, but they are often expensive, require complicated manufacturing processes and have limited tuning capabilities in the case of PDLC or are prone to deterioration [58]. Therefore, low-cost tunable window devices have been developed using elastomeric tunable optical diffusers consisting of deformable transparent elastomer substrates. The optical properties of window or coating materials are altered by an external stimulus-triggered switch in chemistry and/or morphology to

generate a change in optical properties [59]. These smart windows use reversible wrinkle patterns to modulate the optical transmittance. The surface roughness of these substrates can be altered with mechanical compression, resulting in a change in their transparency. They are transparent when flat, but they scatter light by refraction or diffraction when the surfaces are roughened. Studies have shown the design of smart windows using different materials such as  $TiO_2$  nanometric films [60],  $Fe_3O_4$  nanochains array in an elastic polyacrylamide matrix [61], carbon nanotube-containing PDMS [53] as well as various skin layer materials on PDMS [52, 62]. Smart windows incorporating these materials exhibit impressive control over optical diffusion, and their switchable characteristics can be completely restored after undergoing 1000 cycles of stretching and releasing [52, 59, 60]. One of the simplest fabrication methods to produce such materials have been reported by Li *et al.* [52], where they developed a straightforward, inexpensive, and highly efficient one-step manufacturing process for producing durable elastomeric films with an extremely broad range of optical transmittance tuning. They fabricate these through ultraviolet/ozone (UVO) etching of the surface of a freestanding PDMS film to create a thin layer of  $SiO_x$  on the PDMS film. When the PDMS film is mechanically stretched and released, it produces wrinkling-cracking patterns on the surface, resulting in a significant change in optical transmittance from transparent to opaque states. A similar study was also done by Wu *et al.* [63], however instead of mechanical stretching they controlled the reversibility and stability of the surface through solvents, creating solvent-responsive wrinkling.

Engineered wrinkle formation have been investigated in the use of ultrasensitive flexible sensors, such as in the development of strain [64, 65, 66], pressure [67, 68], temperature [69] and chemical sensors [70]. In many cases, the sensors use optical signalling in their applications, such as a change in colour or light transmittance. Lee *et al.* [69] developed an user-interactive electronic skin that is stretchable, thermochromic and thermotherapeutic by using nanocomposites of silver nanowires (AgNWs) and thermochromic dyes in stretchable PDMS elastomers. They demonstrated that the AgNWs could be spontaneously patterned on PDMS surfaces with surface wrinkles which allows for control and adjustment of the electrical performance of the stretchable devices. Furthermore, they found that a thermochromic film on a stretchable strain sensor could undergo variation of colour under different external strains. Some strain sensors

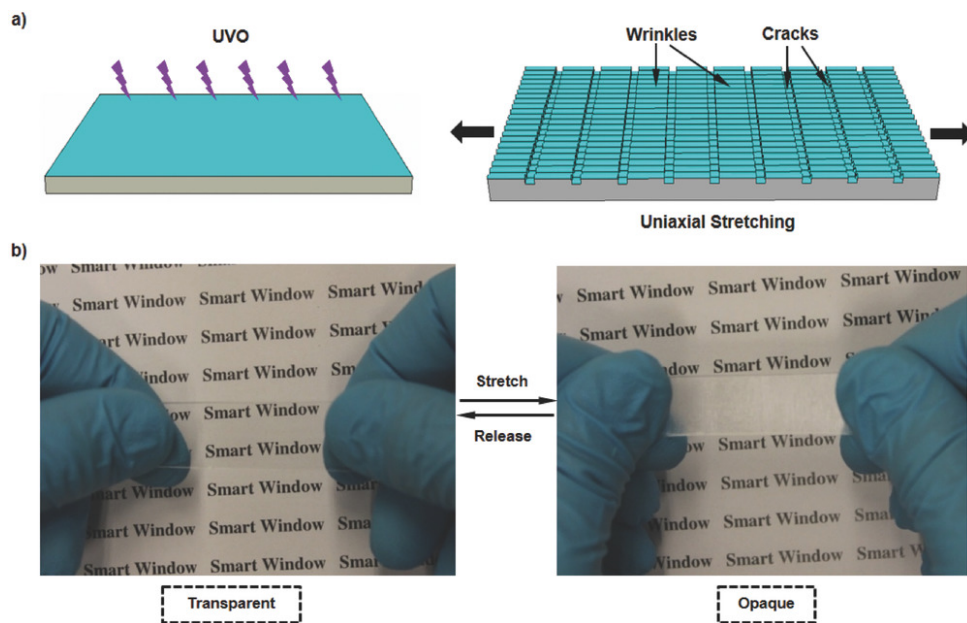


Figure 1.6: (a) Fabrication process of surface wrinkling-cracking patterns through straining of UVO treated PDMS b) Optical images of a PDMS film that demonstrate reversible light transmittance from a state of high transparency (left, not stretched) to a state of opacity (right, stretched). Reproduced from [52] with permission from John Wiley and Sons.

fabricated on the foundations of wrinkle structures can produce optical signals due to diffraction. In a study by Ma *et al.* [71], they fabricate wearable optical sensor based on surface wrinkles made with spin coated anthracene-containing copolymer (PAN-BA) on PDMS. During the initial formation of the film, random wrinkles were formed due to a mismatch in elastic moduli and thermal expansion coefficients between the film and substrate. These wrinkles were generated through thermal treatment and subsequent cooling to room temperature. The initial state of the wrinkles resulted in diffraction observed as concentric rings. When strain was applied to the random wrinkles, they became ordered, resulting in a transformation of the diffraction pattern from concentric rings to a line. The visual response to this transformation could be seen through the interference colour of the film. The initial state of the wrinkles caused strong light scattering, while the specular reflection only allowed for viewing from a specific single direction. This led to a clear observation of colour switching, which was sensitive to strain. The diffraction of wrinkles has also been applied in other studies, such as the development of mechanochromic responsive substrates. These wrinkles structures are capable of exhibiting structural colour sensitive to strain [72, 73].

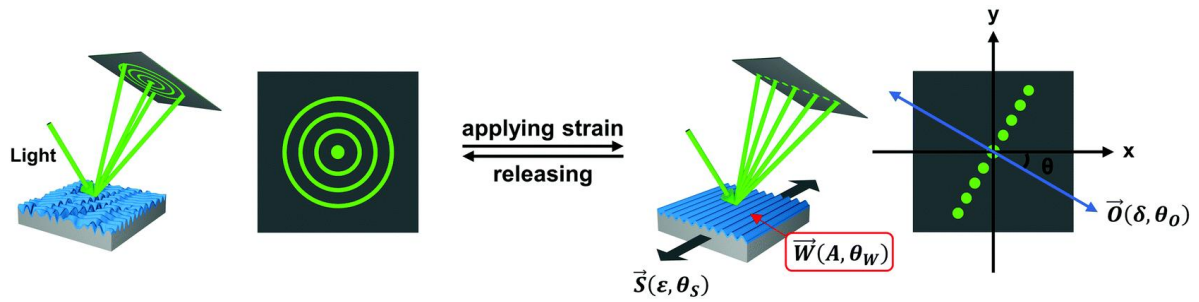


Figure 1.7: Schematic illustration of optical signal change in a wearable optical sensor: initial random wrinkles show concentric ring diffraction pattern, while upon strain wrinkles become ordered and show diffraction pattern in a line. Adapted from [71] with permission from Royal Society of Chemistry.

### 1.2.2 Sinusoidal Phase Grating

Through the examples in nature and bioinspired device, we observe that when a surface is wrinkled, the wrinkles can act as a diffraction grating that scatters light and is able to produce a pattern of bright and dark fringes. The wrinkles act as a type of sinusoidal phase grating because they produce a sinusoidal variation in the surface height or refractive index, that consists of a periodic pattern of alternating regions of different optical path lengths. The grating is typically composed of a transparent substrate with a thin film of material that produces a phase shift in the transmitted light. The grating period  $d$  and the modulation depth of the phase shift determine the angular and spatial distribution of the diffracted light. The intensity of the diffracted light varies with the diffraction angle and can be calculated using the Fraunhofer diffraction formula, which relates the intensity distribution of the diffracted light to the Fourier transform of the grating structure. Sinusoidal phase gratings are commonly used in a variety of optical applications, including spectroscopy, interferometry, and optical communications. They can be designed to operate at specific wavelengths and angles of incidence, and can be optimised for high efficiency and low scattering.

Here, we proceed to derive the diffraction intensity of a sinusoidal phase grating. The theory of the sinusoidal phase grating has been described by Goodman [74]. For a grating, bounded by an aperture of half-width  $w$ , illuminated by a unit-amplitude normally incident plane wave has its amplitude transmittance function defined as:

$$t_A(\xi, \eta) = \exp\left[j\frac{m}{2}\sin(2\pi f_0\xi)\right] \text{rect}\left(\frac{\xi}{2w}\right) \text{rect}\left(\frac{\eta}{2w}\right) \quad (1.4)$$

The average phase delay through the grating has been ignored through this derivation. The parameter  $m$  represents the peak-to-peak excursion of the sinusoidal phase variation.

By making use of the Bessel function identity:

$$\exp\left[j\frac{m}{2}\sin(2\pi f_0\xi)\right] = \sum_{p=-\infty}^{\infty} J_p\left(\frac{m}{2}\right) \exp(i2\pi p f_0\xi) \quad (1.5)$$

where  $J_p$  is a Bessel function of the first kind, with order  $p$ .

$$\mathcal{F}\left\{\exp\left[j\frac{m}{2}\sin(2\pi f_0\xi)\right]\right\} = \sum_{p=-\infty}^{\infty} J_p\left(\frac{m}{2}\right) \delta(f_\chi - p f_0, f_r) \quad (1.6)$$

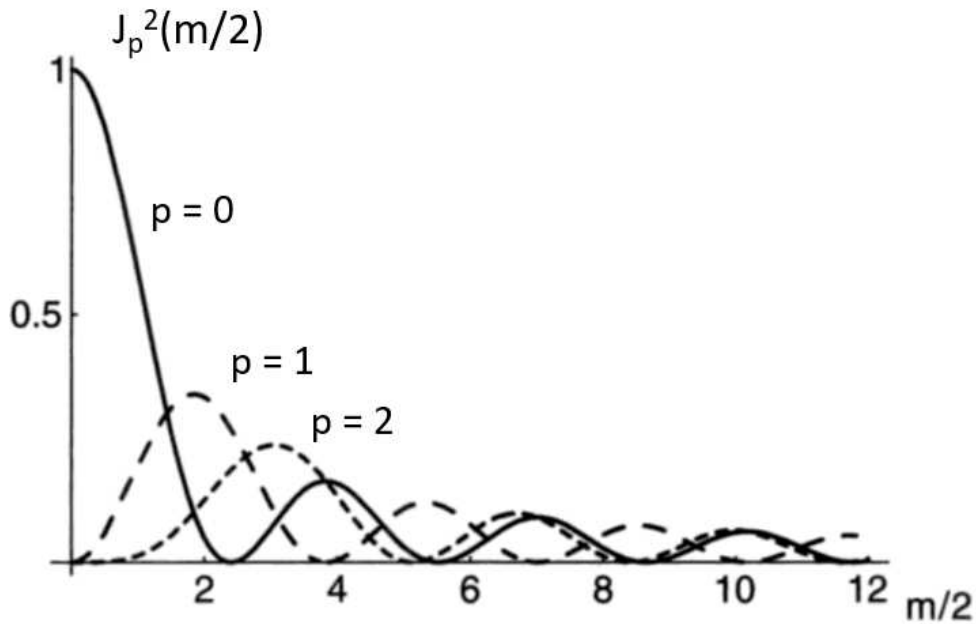


Figure 1.8: Visual representation of the Bessel function of the first kind as a function of  $m/2$ .

Adapted from [74].

The Fourier transform of the field strength can thus be expressed as:

$$\begin{aligned}
\mathcal{F}\{U(\xi, \eta)\} &= \mathcal{F}\{t_A(\xi, \eta)\} \\
&= [A \operatorname{sinc}(2wf_\chi) \operatorname{sinc}(2wf_\Upsilon)] \otimes \sum_{p=-\infty}^{\infty} J_p\left(\frac{m}{2}\right) \delta(f_\chi - pf_0, f_\Upsilon) \\
&= \sum_{p=-\infty}^{\infty} AJ_p\left(\frac{m}{2}\right) \operatorname{sinc}(f_\chi - pf_0) \operatorname{sinc}(2wf_\Upsilon)
\end{aligned} \tag{1.7}$$

Therefore, the field strength of the Fraunhofer diffraction pattern can be written:

$$U(x, y) = \frac{A}{i\lambda z} \exp^{ikz} \exp^{i\frac{k}{2z}(x^2+y^2)} \times \sum_{p=-\infty}^{\infty} J_p\left(\frac{m}{2}\right) \operatorname{sinc}\left[\frac{2w}{\lambda z}(x - pf_0\lambda z)\right] \operatorname{sinc}\left(\frac{2wy}{\lambda z}\right) \tag{1.8}$$

With the assumption that there are many grating periods within the bounding aperture, the various diffracted terms have negligible overlap within them. The intensity pattern becomes:

$$I(x, y) \approx \left(\frac{A}{\lambda z}\right)^2 \sum_{p=-\infty}^{\infty} J_p^2\left(\frac{m}{2}\right) \operatorname{sinc}^2\left[\frac{2w}{\lambda z}(x - pf_0\lambda z)\right] \operatorname{sinc}^2\left(\frac{2wy}{\lambda z}\right) \tag{1.9}$$

Following this derivation, we can use the following relations to relate the size of the aperture or diffractive element ( $W$ ) to the size of the diffraction pattern ( $w$ ) at a given distance from the element ( $z$ ) and the wavelength of the light ( $\lambda$ ). The  $\pi$  in the equation  $\frac{2w}{\lambda z} = \frac{W}{\pi}$  comes from the definition of the period of a sinusoidal function:

$$\frac{2w}{\lambda z} = \frac{W}{\pi}, \quad pf_0\lambda z = \frac{2p\pi}{d}$$

which result in:

$$\operatorname{sinc}^2\left[\frac{2w}{\lambda z}(x - pf_0\lambda z)\right] = \operatorname{sinc}^2\left[\frac{W}{\pi}\left(x - \frac{2p\pi}{d}\right)\right] \tag{1.10}$$

Substituting this relation into the expression for  $I(x, y)$  and rearranging, we get:

$$I(x,y) \approx \left(\frac{A}{\lambda z}\right)^2 \sum_{p=-\infty}^{\infty} J_p^2\left(\frac{m}{2}\right) \text{sinc}^2\left[\frac{W}{\pi}\left(x - \frac{2p\pi}{d}\right)\right] \text{sinc}^2\left(\frac{2wy}{\lambda z}\right) \quad (1.11)$$

The sinc function is said to be orthogonal if the integral of the product of two sinc functions over a given interval is zero, except when the two functions are equal. Using the orthogonality of the sinc function, we can simplify this expression. In addition, we change notation of position  $x$  into  $q$  (wavenumber), and now transform the intensity argument as a function of  $q$  to give the final equation that we will reference subsequently as [75]:

$$I(q) \approx \sum_{p=-\infty}^{\infty} J_p^2\left(\frac{m}{2}\right) \text{sinc}^2\left[\frac{W}{\pi}\left(q - \frac{2p\pi}{d}\right)\right] \quad (1.12)$$

### 1.3 The Project

The study of natural occurring wrinkled surface patterns and their role in optics, specifically through diffraction is the inspiration of this research. This research work seeks to understand how the mechanical instabilities of soft matter enables a fabrication framework to obtain uniaxial and complex patterns to explore their optical effects, including the fabrication of structural colour. This work is structured as follows: in Chapter 2, the controlled wrinkling pattern formation is described starting from the fundamentals of wrinkling instabilities and formation of uniaxial and non-uniaxial patterns. In Chapter 3, the experimental techniques employed in this research work are detailed. Chapter 4 describes the development and modelling of plasma-oxidised wrinkles for tunable gratings. These wrinkles, acting as sinusoidal phase grating can modulate their diffraction intensities through the application of strain. In Chapter 5, we explore the application in the diffraction of these wrinkles in terms of their structural colours and mechanochromic responses, exploring wrinkles ranging from the nano to micro meter range. In Chapter 6, the combination of diffraction in reflection as well as transmission mode was investigated to result in the observation of multi-faceted structural colour due to the occurrence of total internal reflection (TIR) within the medium. In Chapter 7, we extend the study of structural



---

colour of wrinkling patterns beyond the one dimension, fabricating 2D patterns through both simultaneous and sequential methods. Finally in Chapter 8, a brief summary of the finding of this work and future perspectives are presented.

# Chapter 2

## Mechanisms and methods of wrinkling

### 2.1 Introduction

Numerous methods attempting to replicate the exceptional properties of natural surfaces have either proven unsuccessful or requires the use of complex and expensive techniques. Polymer surface development has mostly been associated with technological advancements, but alternative methods have recently emerged. These approaches utilize surface instabilities rather than refined fabrication techniques to generate surface patterns. Surface instabilities can arise intrinsically in thin films or induced through external factors such as heating, electric fields, or exposure to solutions with varying pH levels. Depending on the stimuli and external conditions, various surface patterns can manifest. Surface wrinkles are one of the most extensively studied patterns produced through surface instabilities. Surface wrinkles can be obtained through different materials (hydrogels, elastomers, or thermoplastics), external stimuli (heating, swelling, mechanical stretching, etc.), and film structures (bilayer, gradient, and homogeneous films).

In this chapter, we seek to explore the mechanisms and methods of wrinkling formation, which occurs through mechanical instabilities in soft matter. As we have seen from Chapter 1, wrinkling occurs in nature to contribute to the appearance of optical effects. However, this is a common phenomenon that can be observed in a much wider scope, occurring with length scales

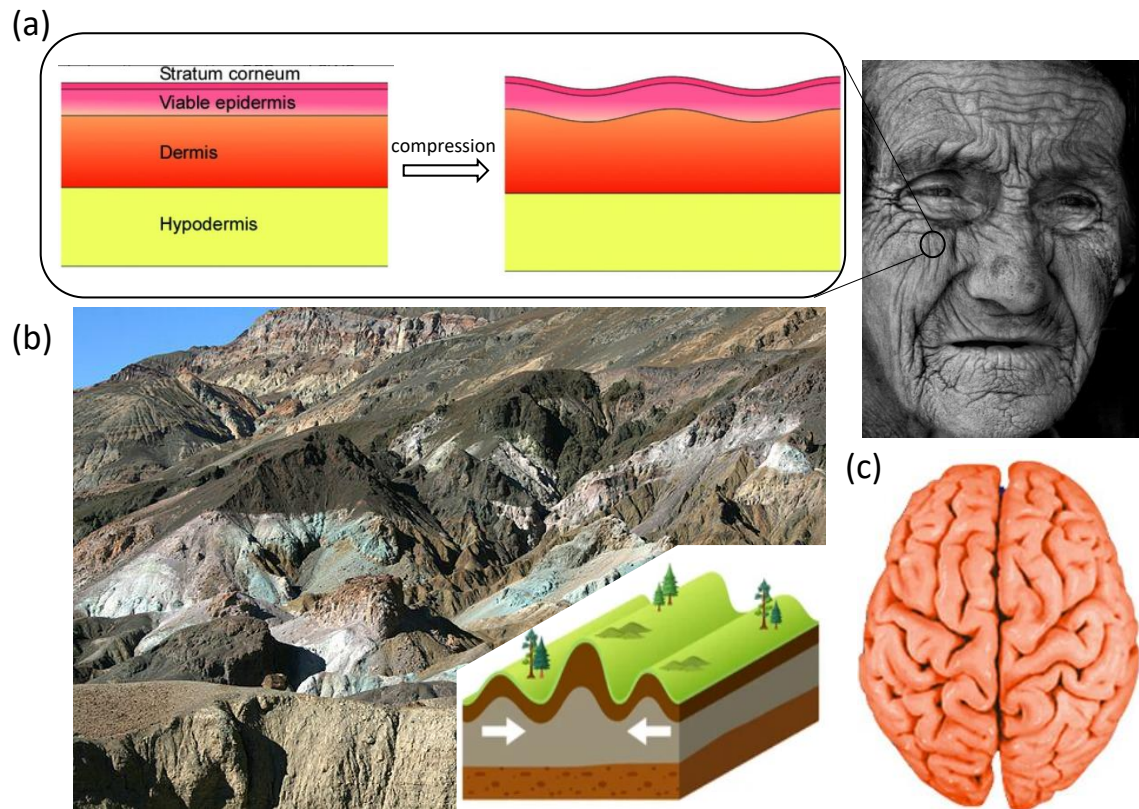


Figure 2.1: (a) Wrinkles found in skin can be caused due to compression of the layers, resulting in buckling of the surface and thus the formation of wrinkles. Schematic adapted from [76]. (b) Geological formations such as mountains can be formed through compression when continental plates collide, resulting in folded mountains. (c) Process of buckling and creasing in the brain's evolution has a function of expanding the surface area of the cortex, resulting in a greater quantity of neural connections.

spanning many orders of magnitude, from microscopic to macroscopic scales. It is a result of the interplay between mechanical forces and material properties, and can be observed in a wide range of systems, including biological tissues and geological formations.

One of the most well-known examples of wrinkling in nature is seen in skins of human. Our skin is made up of three layers: the epidermis, dermis, and hypodermis. The outer layer, the epidermis which consists of the stratum corneum and visible epidermis, is stiff and is followed by a thick dermis layer and then the underlying hypodermis [77]. As the body ages, various biological changes occur in the different layers of the skin, such as changes in moisture and collagen fiber density levels. These changes alter the morphology and mechanical strength of the skin, leading to the formation of wrinkles. When compressive stresses of sufficient magnitude

are applied to the epidermis layer, it can lead to skin wrinkling [76].

On a larger scale, wrinkling can also be observed in the geological formations on the surface of Earth and other planets [78, 79, 80]. For example, the formation of mountain ranges is often accompanied by wrinkling of the Earth's crust. This is caused by the tectonic forces acting on the Earth's surface, which create stresses that deform the crust and cause it to wrinkle and fold [81]. At the microscopic scale, wrinkling can be observed in biological tissues such as the human brain [82]. The brain is composed of a highly folded structure that allows for efficient processing and communication of neural signals. The wrinkling of the brain is caused by a combination of mechanical forces and the growth and development of the brain tissue [83]. In all of these examples, wrinkling is a result of the interplay between mechanical forces and material properties. The specific form of the wrinkles depends on the type of material, the nature of the forces acting on it, and the length scale of the system.

### 2.1.1 Bilayer model

Sinusoidal surface undulations can occur spontaneously due to a mechanical instability that is common in sandwiched structures or bilayers that are formed through techniques such as film sputtering, deposition, lamination, or chemical modification of an elastomeric substrate. This phenomenon has been well-documented in the literature, with several studies reporting on it [84, 85, 86, 87]. The instability arises when a thin sheet of material, which is stiffer than the substrate, is bonded to an elastomeric substrate, causing a mismatch in mechanical properties within the bilayer. When a compressive strain is applied to the bilayer, a buckling instability is induced, leading to sinusoidal surface undulations. The undulations result from the minimization of energy of bulk deformation and skin bending.

At low deformations where the strain is  $< 10\%$ , the wavelength and amplitude of the sinusoidal surface profile are well described by [89]:

$$\lambda = 2\pi h \left( \frac{\bar{E}_f}{3\bar{E}_s} \right)^{\frac{1}{3}} \quad (2.1)$$

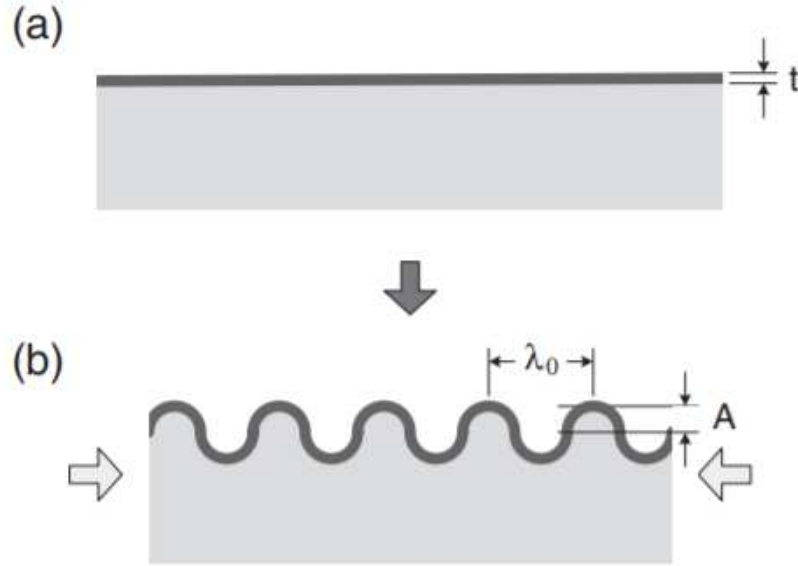


Figure 2.2: Illustration depicting the general formation of wrinkles in a bilayer comprising of a thin stiff film on an elastic substrate. Upon compression exceeding critical strain, buckling that occurs can lead to a sinusoidal pattern with characteristic wavelength  $\lambda$  and amplitude  $A$ . Reproduced from [88] with permission from John Wiley and Sons.

$$A = h \left( \frac{\varepsilon}{\varepsilon_c} - 1 \right)^{\frac{1}{2}} \quad (2.2)$$

where  $h$  is the film thickness,  $\bar{E}_f$  and  $\bar{E}_s$  are the in-plane strain moduli of the film and substrate respectively, given by  $\bar{E} = E/(1 - \nu^2)$ , where  $E$  is the Young's modulus and  $\nu$  is the Poisson ratio ( $\simeq 0.5$  for PDMS). A critical strain must be exceeded to trigger the buckling instability:

$$\varepsilon_c = \frac{1}{4} \left( \frac{3\bar{E}_s}{\bar{E}_f} \right)^{\frac{2}{3}} \quad (2.3)$$

In this limit, the amplitude alone depends on strain, thus allowing for  $\lambda$  and  $A$  to be decoupled in surface patterning. Generally, at 'high-deformation' (HD)[90], the wrinkling wavelength too becomes strain dependent and

$$\lambda_{HD} = \frac{\lambda}{(1 + \varepsilon)(1 + \xi)^{\frac{1}{3}}} \quad (2.4)$$

$$A_{HD} = \frac{A}{(1 + \varepsilon)^{\frac{1}{2}}(1 + \xi)^{\frac{1}{3}}} \quad (2.5)$$

where  $\xi = 5\varepsilon(1 + \varepsilon)/32$ , accounting for the non-linearity of the stress-strain relationship of the substrate in the finite deformation regime (i.e., non-Hookean response), with  $\lambda$  and  $A$  given by Eqn. 2.1,2.2. Under high deformation conditions, uniaxial strain leads to a transition from the low deformation sinusoidal patterns into further modes, such as the formation of folds, period-doubling and ridges or to failure modes such as delamination [91].

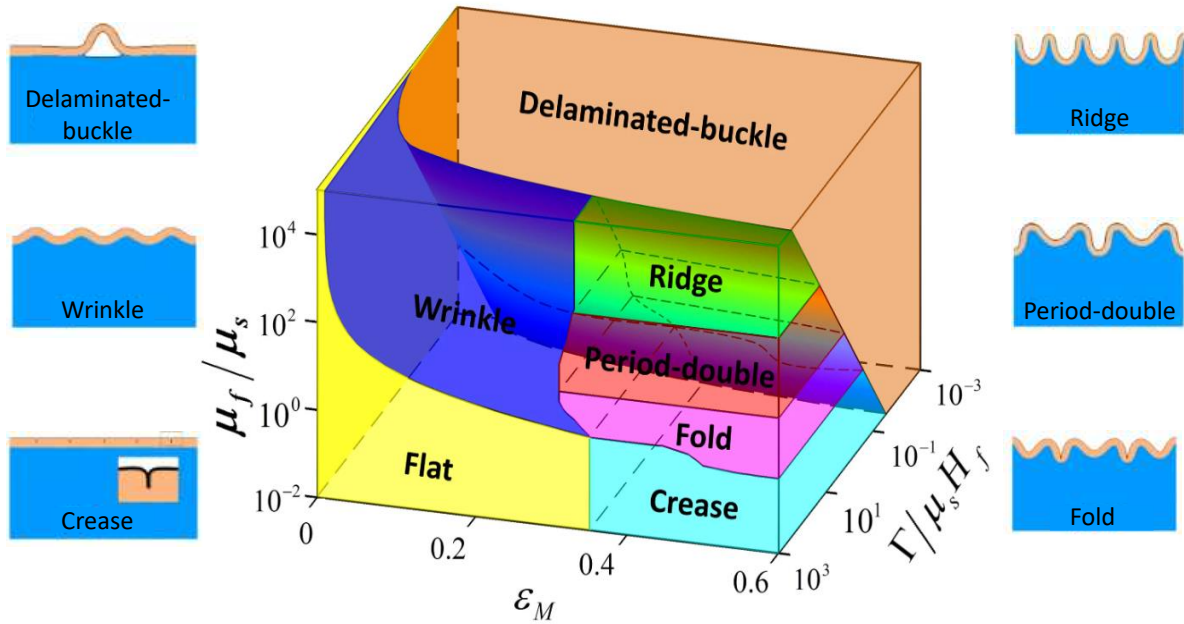


Figure 2.3: Three-dimensional phase diagram computed to illustrate different surface instability patterns caused by mismatch strains and the associated schematic representation of the bilayer surface instabilities. The instability pattern is determined by three non-dimensional parameters: mismatch strain  $\varepsilon_M$ , modulus ratio  $\mu_f/\mu_s$  and normalized adhesion energy  $\Gamma/\mu_s H_f$ . Adapted from [91] under the Creative Commons Attribution-Non Commercial 4.0 International License (CC BY-NC).

Fig 2.3 represents a phase diagram that tracks the development of mechanical instabilities in bilayered sandwiches. The diagram illustrates the ratio of shear modulus between the film and substrate ( $\mu_f/\mu_s$ ) in relation to applied strain, indicating the degree of mismatch in mechanical properties. When the shear moduli are similar, no instabilities or patterns arise. However, a significant mismatch in the bilayer's mechanical properties triggers sinusoidal wrinkling within a specific strain range ( $0\% < \varepsilon < 20\%$ ). Higher deformations can induce a range of instabilities and failures, including the upward delamination of the top film. As the strain increases, a frequency doubling effect occurs, leading to structures with higher aspect ratios and deviation from the sinusoidal regime, such as outward ridges and inward folds.

### 2.1.2 Approaches to bilayer formation

There are various methodologies to induce wrinkles on a surface, but one commonly used technique involves inducing a strain mismatch between a bilayer of a thin film and a soft substrate, which causes instability and wrinkling of the film. To create the bilayer, one of the simplest methods is thin film deposition, which is usually done through floating or vapour film deposition. In this process, the substrate and thin film are selected independently to achieve the required modulus mismatch, resulting in a perfect bilayer system.

To float thin polymer films, a dilute solution of the material is spin-coated onto a silicon wafer or glass slide. As the solvent evaporates, a film is formed which can then be transferred to the substrate to create the bilayer. The thickness of the film can be controlled by adjusting the solution concentration and spin rate. One way to transfer the film to the substrate is by peeling it off using water-based methods [92]. The force required to transfer a thin elastic film is dependent on the interfacial surface energy, peeling angle, and the thickness and elasticity of the film. To ensure minimal residual stress in the transferred film, it's crucial to use a hydrophobic material coated on a hydrophilic slide, transfer slowly to avoid energy dissipation, and then transfer the film to a prestrained substrate, such as PDMS, which can be compressed to create the wrinkles.

An attractive route to PDMS patterning is via surface oxidation using an oxygen (or air) plasma source, generating a gradient glassy skin that can induce sinusoidal features [93, 94, 95, 96, 97]. Plasma oxidation involves the use of a low-pressure gas discharge plasma to expose a material to highly reactive species, which can cause surface modifications. In the case of PDMS, oxygen plasma is commonly used due to its ability to introduce hydrophilic functional groups onto the surface. The plasma can be generated in various ways, including radiofrequency (RF) discharge or corona discharge, with the latter being preferred for its lower cost and simpler setup. During plasma oxidation, the highly reactive oxygen species react with the surface of the PDMS, breaking its Si-C bonds and generating reactive sites. These sites can then react with the oxygen species to form polar functional groups, such as hydroxyl (-OH) and carbonyl (C=O) groups. The density and type of functional groups introduced depend on the duration and intensity of the

plasma treatment, as well as the initial properties of the PDMS. This methodology is suited for fabrication of patterns ranging from nanometre scales to several hundreds microns by several by tuning the oxidation and strain conditions. PDMS can either undergo UV ozonolysis (UVO) or plasma oxidation resulting in a thin glassy layer to form upon conversion from the bulk material, providing a mismatch in elastic modulus compared to the softer substrate underneath. Although both UVO and plasma oxidation are fundamentally similar, the surface wavelength in which is accessible differs – plasma oxidation is able to achieve periodicity of 100s nm to 10  $\mu\text{m}$  while UVO, typically 1-100  $\mu\text{m}$ . The wrinkling instability can be mechanically induced through a predetermined extensional or compressive strain, with  $\sim \mu\text{m}$  resolution, allowing for a precise pattern control, as compared to drying and thermal alternatives to skin deposition and strain.

A model, comparable to one of frontal photopolymerisation can be used describe the skin growth of the glassy layer on top of PDMS [95, 96]. This model describes the rate of change of conversion fraction of the film with respect to depth from the surface and plasma oxidation exposure time. The skin formation via oxidation proceeds where an increase in skin thickness is accompanied by surface densification by cleaving of  $\text{Si} - \text{CH}_3$  groups. The rate of change is expected to depend on the fraction of sites available for conversion, the local intensity of ionised or radical oxygen species at any point in the material and a coefficient that represents the overall reaction rate constant from unconverted to converted species. The rate of conversion fraction of the glassy skin thin film follows a sigmoidal profile with respect to depth from the surface, leading to a gradient bilayer system in a three-step process: “induction”, where no evidence of wrinkling is found, “formation”, where the build-up of the glassy layer develops and “film propagation”, during which the fully-propagated glassy layer propagates normal to the surface, increasing the skin thickness.

The conversion profiles for skin formation can be seen in Figure 2.4 where it shows the conversion  $\phi$  with thickness of the PDMS. The surface conversion quickly rises as dose increases, where a thin film of completely converted PDMS is first formed. After the initial layers of conversion, sigmoidal profiles depicting the conversion of the bulk of PDMS with time can be



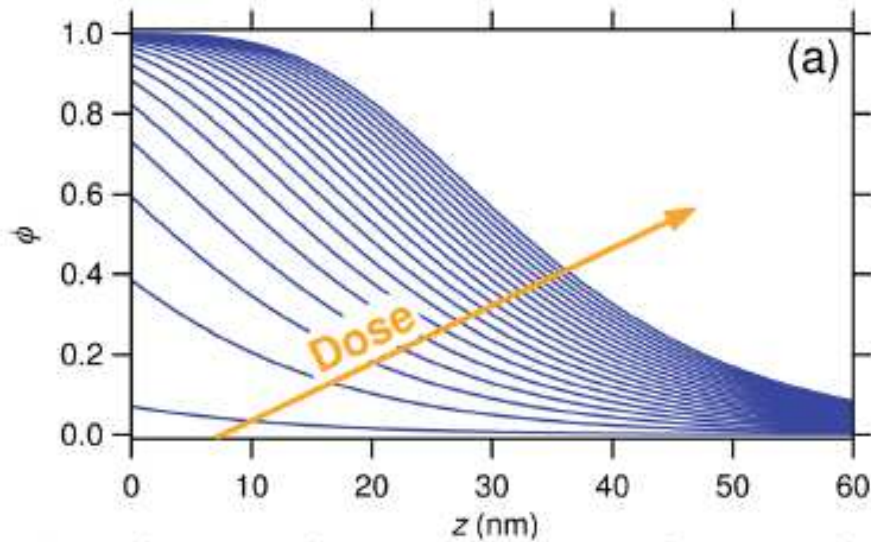


Figure 2.4: Frontal photopolymerisation profile of surface conversion of plasma-oxidised PDMS with dose, showing a gradient bilayer. Reproduced from [95] with permission from Royal Society of Chemistry.

seen. This results in a gradient bilayer with varying levels of conversion of PDMS to the glassy silicon layer with respect to thickness.

## 2.2 Methods to induce wrinkles

The formation of wrinkles of various sizes (ranging from nano- to micrometers) and orientations (random, parallel, or following pre-patterned substrate morphologies), are caused by factors such as swelling, temperature changes, and mechanical stretching which ultimately are ways to apply strain to a bilayer. One of the most common ways to apply strain is by utilizing the elastic mechanical properties of a polymer substrate. This technique usually involves applying uniaxial strain to the substrate, followed by depositing a film onto it. When the stress is released, wrinkles form on the surface of the elastic foundation. The application of uniaxial stretching causes the surface of the PDMS to buckle and form wrinkles perpendicular to the direction of the strain. By controlling the pre-strain and the rate of strain, the wavelength and amplitude of the wrinkles can be tuned. The creation of these surface wrinkles occurs due to the difference in Young's modulus between the rigid top layer (with a modulus of  $E \approx \text{GPa}$ ) and the polymeric

substrate (with a modulus of  $E \approx \text{MPa}$ ), which causes out-of-plane deformation. By altering the sequence of application of strain, for example when a strain is applied after the deposition of a film, this can lead to ‘OFF’ samples, which only forms wrinkles when a strain is being applied. Conventionally, ‘ON’ samples are fabricated, where a wrinkling pattern is apparent at rest [73].

Wrinkle patterns can also be achieved by inducing swelling using a monomer solution or solvents [98, 99, 100]. Regular wrinkles are formed when the layered film is immersed in a solvent vapor or a monomer mixture. In this case, the final wrinkle characteristics and morphology can be precisely controlled by considering solvent diffusion kinetics and film characteristics, such as the geometry of the diffusion front or the cross-linking density [101]. Typically, swelling-induced surface patterns originate from the selective swelling of the top of the film because the bottom of the polymer films is constrained due to the rigid interface [102].

Finally, the formation of wrinkles can result from thermal variations based on the different expansion coefficients between the top layer and the foundation. Wrinkles are formed spontaneously when the applied stress (caused by either heating or cooling) exceeds a critical value, specific to each system, due to the mismatch in thermal expansion coefficients between the substrate and the capping layer. When the substrate is heated, expansion occurs, and either a physical process is used to treat the substrate [103] or polymer/metal is deposited onto it [87, 104]. Upon cooling the bilayered system, a compressive stress is created in the stiff surface layer, causing surface buckling and ultimately forming wrinkles that remain intact when the sample is cooled down [105]. Thermal wrinkling usually results in random wrinkles on the surface due to the compressive stress generated during thermal annealing. For example, Bowden *et al.* [87] presented an instance of the fabrication of isotropic wrinkles by depositing thin layers of gold on thick PDMS at high temperatures, which induced compressive stresses in the samples. When the substrate was cooled, these stresses were alleviated, resulting in the formation of periodic buckles with wavelengths ranging from 20 to 50  $\mu\text{m}$ . The buckling pattern can be ascertained using laser light diffraction, where isotropic buckling results in a concentric circular pattern [106].

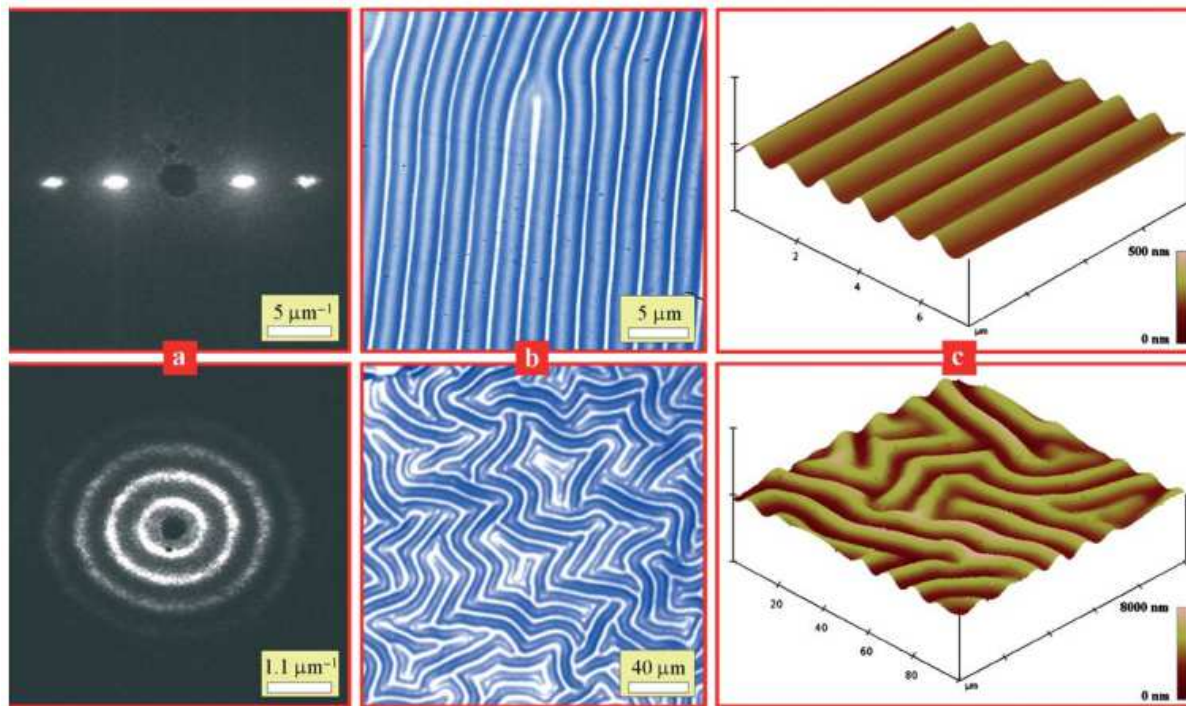


Figure 2.5: (a) laser light diffraction, (b) optical microscopy, and (c) AFM. The top row of images corresponds to oriented buckling whereas the bottom row corresponds to isotropic buckling. Reproduced from [106] with permission from Elsevier.

### 2.2.1 2D wrinkling

In general, one-dimensional wrinkles have been formed through either stretching or compression in a single direction. However, some other groups have investigated the option of stretching in different directions. For example, Lin and Yang [107] demonstrated this alternative by creating various submicron wrinkle patterns on polydimethylsiloxane films. The authors were able to transition these patterns from one-dimensional ripples to two-dimensional herringbone structures by applying mechanical forces that allowed them to control the amount and timing of the strain on both planar directions separately, either at simultaneously or sequentially. The use of bi- or multi-axial strains produces more intricate wrinkle patterns, such as dimples, herringbone (chevron), square (checkerboard), or labyrinthine features. These patterns are selected based on the minimization of overall elastic and bending energy [94, 108, 109, 110, 111].

Simultaneous 2D wrinkling is a phenomenon where a thin film undergoes multiple simultaneous deformations in two dimensions. This can occur when the film is subject to biaxial compression, such as when it is stretched in two perpendicular direction. When subjected to simultaneous bi-

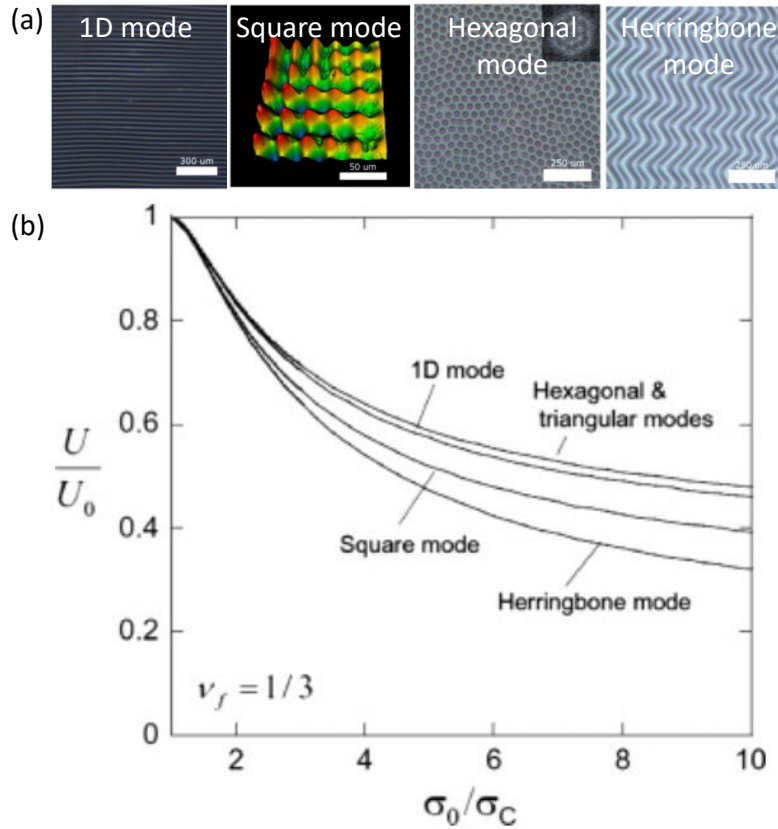


Figure 2.6: (a) Experimental observations of 1D mode, square checkerboard mode, hexagonal mode and herringbone mode. (b) Associated normalised elastic energy/area diagram as a function of buckling overstress. Adapted from [108] with permission from Elsevier.

dimensional strain, the herringbone or chevron pattern is typically preferred due to its lower surface energy [110], although other patterns, including checkerboards, may appear as defects [111].

Although herringbone patterns are predicted to be equilibrium equi-biaxial structures, they are often difficult to achieve experimentally due to the imprecise control of biaxial stress or its rapid release. An alternative method for creating and adjusting 2D or hierarchical wrinkled structures is through sequential application of strain or sequential 2D wrinkling. By using this method, a variety of unique patterns can be generated, and their characteristic features can be adjusted independently [94]. Davis *et al.* [109] reported that 2D wrinkled morphologies were produced by a two-step film floating process shifted by  $90^\circ$ . The curing ratio and time of the PDMS substrate were adjusted to control the pattern features. Various bilayer formation processes can be used to create the sequential 2D patterns. For instance, Watanabe [112] utilized UV

ozonolysis to generate the first 1D wrinkling along the x-axis, and wrinkles parallel to the y-axis were formed by swelling the sample with acetonitrile. Chiche *et al.*[94] demonstrated that the production of well-defined checkerboard structures can be performed through a multi-step approach involving multiple strain-oxidation cycles and a replication step. The process begins with the creation of a 1D pattern by applying uniaxial stress and plasma exposure. After octadecylchlorosilane (ODS) adsorption/grafting onto the wrinkled PDMS surface, replication is performed. Finally, the 2D structure is obtained by a second exposure step, which orients the replica along the orthogonal direction to the first 1D direction. This process enables the fabrication of structures with a sequence of peaks and saddles. Similarly, Pellegrino *et al.* has also recently done a study on the formation of checkerboards [111] and sand ripples [113] (where the angle  $\theta$  between generations range from  $0 < \theta < 90^\circ$ ) through a sequential wrinkling step with the plasma oxidation of PDMS, and establishing a superposition model to describe 2D wrinkled surfaces which can be readily calculated from 1D wrinkling behaviour.

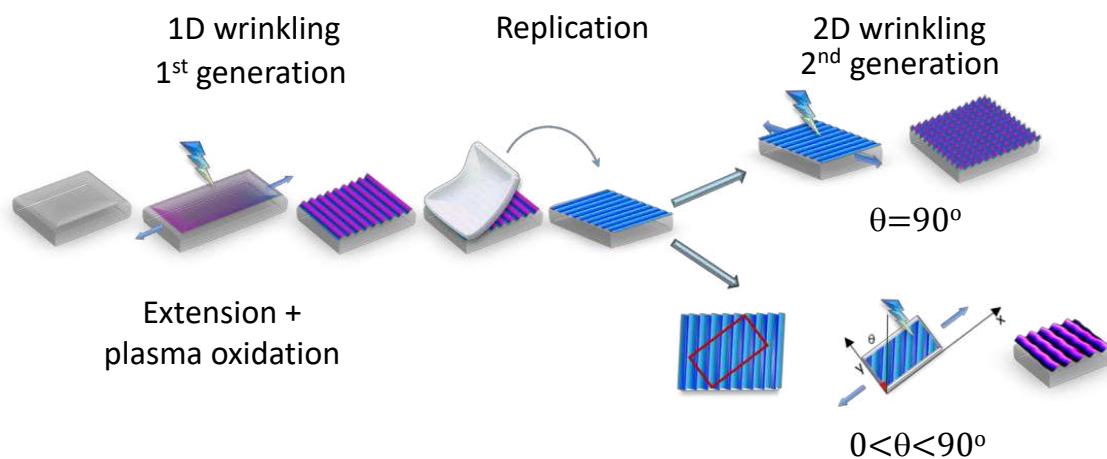


Figure 2.7: Schematic of sequential 2D wrinkling fabrication: the 1st generation of wrinkles ('1D master') is generated through strain and plasma oxidation which undergo replication. A sequential wrinkling step is then performed on the 1D master to generate 2D wrinkling through a second wrinkling step at  $\theta$  angle. Orthogonal wrinkling performed at  $90^\circ$  can form checkerboards while sand ripples can be fabricated when  $0 < \theta < 90^\circ$ . Adapted from [111] with permission from Royal Society of Chemistry.

In order to account for the resultant wrinkles fabricated in 2D wrinkling, the second pattern cannot simply be added onto the first, but must be superimposed on. A simple and effective mathematical description of these 2D wrinkling waves involves modelling the pattern forma-

tion as sequence of interfering buckling events [114]. In this framework, we approximate each generation to a single sinusoidal wave, which are superposed at a prescribed  $\theta$ , and with standard wrinkling equations for a bilayer model [64, 87, 115, 116]. Considering the surface as defined by the sum of two cosine waves

$$w(x, y) = A_1 \cos(k_1 x_1) + A_2 \cos(k_2 x_2), \quad (2.6)$$

we select the  $x_2$  axis, corresponding to the second generation, to coincide with the  $x$  axis (thus  $x_2 \equiv x$ ), and where the  $x_1$  axis is oriented with respect to the  $x$  axis with (compression) angle  $\theta$ ; consequently  $x_1 = x \cos(\theta) + y \sin(\theta)$ .

The surface topography Eqn. (2.6) can be expressed in terms of the principal co-ordinates  $x$  and  $y$  as

$$\begin{aligned} w(x, y) = & A_1 \cos(k_1 \cos(\theta)x) \cos(k_1 \sin(\theta)y) - \\ & - A_1 \sin(k_1 \cos(\theta)x) \sin(k_1 \sin(\theta)y) + A_2 \cos(k_2 x) \end{aligned} \quad (2.7)$$

describing a surface where a  $xy$  interference is generated by the diagonal superposition of the two wrinkling waves. When both wrinkling generations are fabricated using the same plasma and strain conditions, Eqn. 2.7 can be simplified since  $A_1 = A_2 \equiv A$  and  $k_1 = k_2 \equiv k$ . This model despite being simple, has been reported to describe experimental results well [113].

# Chapter 3

## Experimental Methodologies

### 3.1 Samples preparation and fabrication

#### 3.1.1 PDMS Substrate fabrication

Polydimethylsiloxane (PDMS) was used as the substrate material in the experiments - chosen for its favorable properties such as optical transparency, chemical inertness and good thermal stability. PDMS is a two-component system consisting of a polymer (PDMS), and a curing agent, which is a cross-linker. The mixing ratio between these two components determines the amount of curing agent added to the PDMS polymer. The mixing ratio can significantly affect the properties of PDMS. As the mixing ratio of PDMS to curing agent increases, the resulting PDMS material becomes harder, less elastic and less tacky. This is due to the excess curing agent creating more cross-links, which increases the degree of cross-linking in the material resulting in a stiffer and less flexible material [117]. Conversely, as the mixing ratio decreases, the PDMS becomes softer, more elastic, and more tacky. This is because there are fewer cross-links in the material, resulting in a more flexible and less stiff material. In addition, the mixing ratio can also affect PDMS's adhesion to different surfaces and its optical properties, amongst others [118].

Typically, PDMS is prepared with a mass ratio of 10:1 of prepolymer to curing agent, which we employ in the majority of the following experiments. In addition to this, we also utilise PDMS prepared with a 20:1 mixing ratio to increase its tackiness for the adhesion of polystyrene to its surface by floating (Chapter 7). The PDMS utilised in this work is obtained from Dow Corning - Sylgard 184. The PDMS is first thoroughly mixed with the required cross-linker ratio (either 10:1 or 20:1) through vigorous stirring and subsequently degassed for 30 minutes in a vacuum dessicator to eliminate bubbles that were formed during mixing due to the introduction of air. A glass surface was used to cast the mixture to achieve substrate thickness of  $\approx 2.5$  mm (or other thicknesses as required). The thermal curing process was performed at 75 °C for an hour. The curing temperature is a crucial factor in determining the stiffness of the PDMS elastomer. Longer curing times at lower temperatures or quicker curing at higher temperatures can influence the final stiffness. However, curing processes carried out at very high temperatures and for short durations can lead to increased stiffness and reduced mechanical homogeneity of the material.

### 3.1.2 Strain application

Amongst the different methods to induce wrinkling on bilayers, mechanical strain was the primary method employed through the use of a strain stage. In the following experiments, three different types of strain stages were used - a 1D ‘small’ strain stage, a motorised strain stage equipped with a 25 mm travel linear actuator, and a biaxial strain stage to fabricate 2D herring-bone surfaces.

The principles of the strain stages are the same - the sample is clamped on the strain stage, and is elongated using by adjusting the screws. The length in between the clamps is first measured ( $L_0$ ), and the final length ( $L_1$ ) can be calculated by stipulating the desired strain ( $\epsilon$ ) through the following equation:

$$\epsilon\% = \left(1 - \frac{L_1}{L_0}\right) \times 100 \quad (3.1)$$



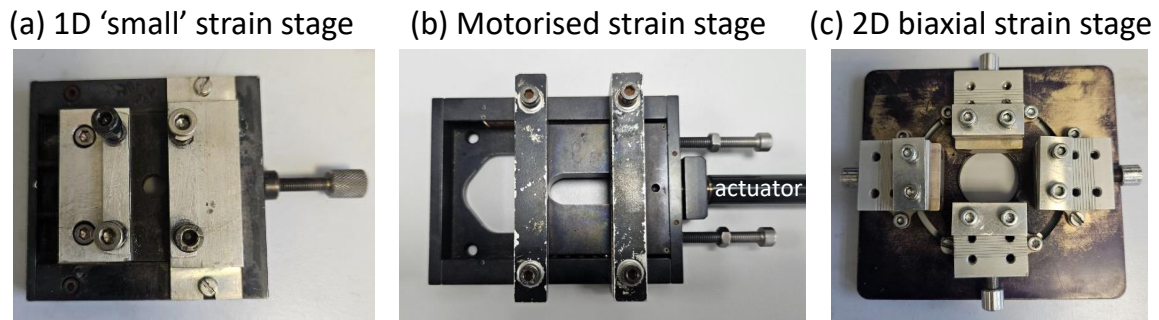


Figure 3.1: Custom built strain stages used to stretch PDMS substrates prior to oxidation. (a) 1D 'small' strain stage, employed for use in 1D samples and in sequential 2D samples. (b) Motorised strain stage attached to a linear actuator, controlled by an external stepper motor. (c) 2D strain stage employed in the fabrication of simultaneous 2D samples (herringbones) with 4 movable clamps using built-in screws.

where the lengths are measured with a precision of  $\pm 0.01$  mm.

The strain application could be performed before or after the plasma oxidation of the PDMS sample, where it would result in 'ON' or 'OFF' samples respectively. 'ON' samples refer to those showing wrinkles in their relaxed state, while 'OFF' samples only show wrinkles upon the application of strain after the initial plasma oxidation of a non-strained coupon. The wrinkling experiments performed in this work are 'ON' samples.

### 3.1.3 Surface Oxidation

The surface oxidation of the PDMS surface was employed throughout experiments to create a thin glassy layer on top of the PDMS bulk. Two plasma chambers were employed for the oxidation of PDMS - a Harrick Plasma Cleaner (PDC-002) and a Diener Plasma Oven (Femto). The Harrick Plasma cleaner generates an oscillating electric field with a frequency of 8-14 MHz and is usually referred to as MHz plasma chamber. The system comprises an RF coil and a three power settings (7, 10, 30 W) and equipped with a pressure sensor with gas inputs with flow rate controls. The Diener plasma oven has a frequency of 40 kHz and referred to as kHz plasma where it has a single gas input and power setting ranging from 10 to 99 W. In a plasma chamber, gas molecules are ionized and become plasma when accelerated ions in the

gas collide with them under sufficiently low pressure and caused by high frequency oscillations of the electromagnetic field. When PDMS is exposed to the plasma, the ionized gas particles in the plasma interact with the solid surface placed in the same environment by modifying or enhancing the physical and chemical characteristics of the surface. The type of interaction between the plasma and the surface depends on parameters such as the intensity and frequency of the radio frequency (RF) power used to excite the plasma, the type of gas that are ionized, the pressure and flow rate of the gas, the type of sample and the amount of time the surface is exposed to the plasma.

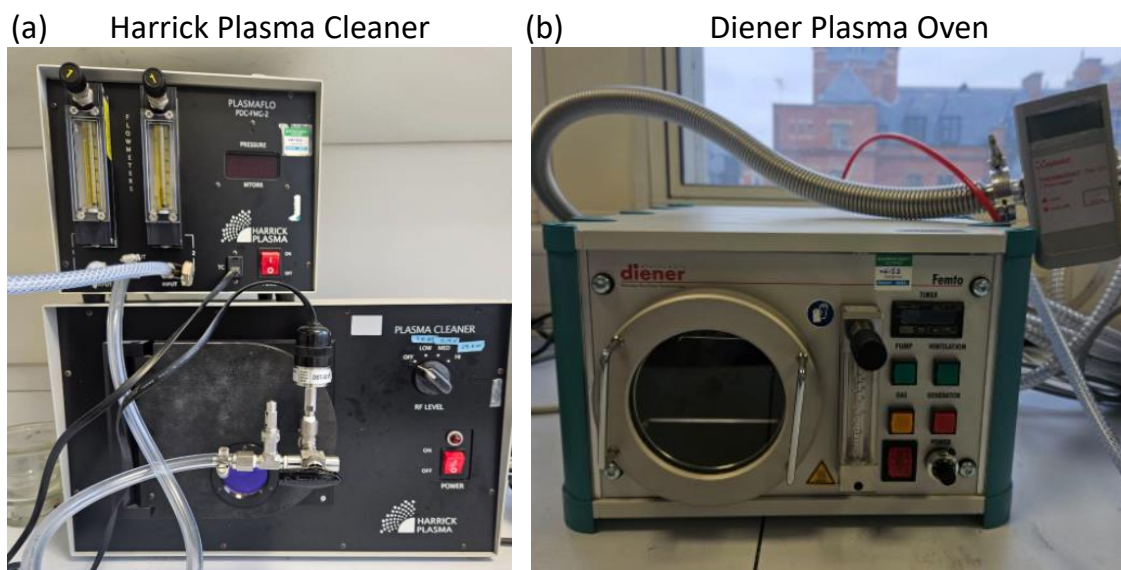


Figure 3.2: (a) Harrick Plasma Cleaner (PDC-002), referred as MHz plasma. (b) Diener Plasma Oven (FEMTO), referred as kHz plasma.

With the 40 kHz plasma chamber, there is higher ion density compared to that of the MHz plasma. This increases the efficiency and improve the uniformity of the particles. As a result, the two plasma chambers have different effects on the skin formation on the exposed PDMS surfaces. The Diener Plasma forms stiffer and thicker skins, which can result in wrinkle periodicities ranging from  $\approx 1 \mu\text{m}$  up to  $10 \mu\text{m}$ . Conversely, the Harrick chamber produces thinner and softer skins, allowing it to fabricate wrinkles in the nanometres to couple of  $\mu\text{m}$ . In the experimental conditions reported through the thesis, PDMS samples are initially loaded onto the strain stage having undergone application of strain, and placed in the plasma chamber. The pressure in the chamber is evacuated down to 0.2 mbar, before allowing oxygen to flow in for 5

minutes to allow for the stabilisation at the desired pressure. Subsequently, the plasma is ignited at the desired power for the chosen exposure time.

### 3.1.4 Replica moulding

To create a higher elastic modulus required for bilayer formation and generate wrinkling patterns, the surface of PDMS can be oxidized through plasma or UV methods, resulting in a glassy skin layer with silanol groups Si-OH. However, if the surface is further subjected to mechanical deformations after strain application, extensive cracking can occur, which partially destroys the original topography. Therefore, if additional strain applications are necessary to increase pattern complexity, the surface must be replicated into an un-oxidized sample to reset residual stresses and avoid cracking. The replication process allows for the creation of a new PDMS sample with the same surface pattern without residual stresses, enabling further strain applications to generate more complex patterns.

The replication of PDMS samples using octadecyltrichlorosilane,  $CH_3(CH_2)_{17}SiCl_3$  (OTS) is a common technique used to create surface patterns on PDMS. The process involves first creating a master mold on a substrate, typically using a lithographic technique such as photolithography or electron beam lithography. The master mold is then coated with a self-assembled monolayer (SAM) of OTS, which serves as a release agent for the replication process. OTS has several properties that make it useful as a release agent for PDMS replication. First, it has a high surface energy, which allows it to strongly bond to the substrate and form a stable SAM layer. OTS has a high surface energy when it is bonded to the substrate because the silanol groups (-Si-OH) on the OTS molecules can interact strongly with the surface, forming a covalent bond. This strong bond leads to a high surface energy, which means that the surface of the substrate coated with OTS is highly wettable by polar solvents and can easily attract other molecules to adhere to its surface. On the other hand, when the PDMS is poured onto the OTS-coated substrate, the PDMS molecules interact more strongly with the OTS layer than with the substrate underneath. This interaction leads to a low surface energy because the PDMS does not strongly bond with the substrate, making it difficult for other molecules to adhere to its surface. This low surface

energy allows the PDMS to be easily peeled off from the OTS layer, leaving behind a replica of the surface pattern.

In the experiments, to prepare the PDMS masters for replication, a dessicator is used with 5 ml of OTS ( $\geq 90\%$  solution, CAS 112-04-9, Sigma-Aldrich) placed in a small petri dish to facilitate the evaporation process. The dessicator is then connected to a vacuum pump and evacuated for 5 minutes, creating a low-pressure environment that enhances the OTS evaporation rate and generates a saturated atmosphere. The system is allowed to sit for 30 minutes to ensure the silanes are properly adsorbed onto the surface of the master. Following the silanisation process, PDMS frames were created and placed on to the silanised masters. Fresh PDMS at a 10: 1 ratio was then cast into the molds and baked at 75 °C for one hour. After the curing process, the replica was carefully peeled off from the master.

Another method of fabricating replicas of the topography is through using UV curable photoresist, Norlad Optical Adhesive (NOA 81). NOA is a type of adhesive that is specifically designed for use in optical and optoelectronic applications. It is a clear liquid that cures when exposed to ultraviolet (UV) light. The adhesive is transparent and has excellent optical properties, making it ideal for use in applications where high optical clarity is required. With this method, we only require a replica of the surface and not the entire sample. In order to achieve this, drops of NOA can be casted onto the wrinkle sample before covering it with a glass slide, ensuring that the photoresist is spread evenly beneath it. The sample is cured under UV light for 5 minutes, before gently peeling off the glass slide resulting in a replica.

## **3.2 Surface Characterisation**

### **3.2.1 Optical Microscopy**

An optical reflection microscope, Olympus BX41M was used in the characterisation of the wrinkling patterns. As a result of the optical transparency of the PDMS, a reflection mode set up is preferable in the acquisition of the microscopic images of the patterns, where its homogeneity

and the characteristic wavelengths can be estimated. Images were obtained utilising lenses of different magnification, 5x, 10x, and 50x and an initial calibration through imaging a micro-graded ruler was used. One limitation of optical microscopy is its resolution, which is limited by the diffraction of light. The smallest structures that can be resolved by traditional optical microscopy are on the order of a few hundred nanometers.

### 3.2.2 Atomic Force Microscopy

In comparison to the optical microscope with a micron-resolution, Atomic Force Microscopy (AFM), with a nanoscale resolution, is more accurate and suitable for smaller scale features. The AFM is a surface analysis technique for topographic and spatial surface chemistry characterisation. The topographical analysis was performed in tapping mode, where the sample is mounted and its surface scanned by a probe supported by a cantilever. The cantilever vibrates at its resonance frequency using a piezoelectric element, with vibration amplitudes typically on the order of a few nanometers. As the cantilever tip scans over the surface of the sample, the interaction between the tip and the sample causes a deflection in the cantilever. The deflection is measured using a laser beam that reflects off the back of the cantilever and is detected by piezoelectric detector sensitive to the position. Through the use of a four quadrant photo piezoelectric detector, the position deflected transforms the electrical signal into 3D micrograph images.

The tip-sample interaction can also be used to measure other properties of the sample such as its mechanical properties or electrical conductivity. For example, the cantilever can be used to apply a small force to the sample and measure the resulting displacement, which can be used to calculate the sample's stiffness or elasticity. The resolution of the AFM image is determined by the size and shape of the tip, as well as the interaction between the tip and the sample. AFM images can be optimised by adjusting the scanning frequency and proportional-integral-derivative (PID) parameters in the AFM. The optimisation of these parameters are verified by recording the forward and backward height profiles of the sample of interest.

A Bruker Innova microscope, in tapping mode, equipped with Al-coated Si tips (MPP-11100-

W, Bruker) was employed in the characterisation of surface topographies in this work. The measurements were performed at scanning frequencies ranging from 0.1 to 1.0 Hz, adjusted accordingly to the desired spatial resolution. The resultant graphs obtained from the AFM allows for the wavelengths  $\lambda$  and amplitudes  $A$  of the samples to be extracted with NanoScope 9.3 Software or a freeware analysis software, Gwyddion.

### 3.2.3 Static Light Scattering

Another method of characterisation of wrinkled samples is the use of Static Light Scattering (SLS). When the laser shines through a PDMS wrinkled sample, the sample acts as a sinusoidal diffraction grating and creates a diffraction pattern. Since a diffraction pattern is the two-dimensional Fourier transform of the function of the aperture, information about the grating apertures can be extracted from the images captured.

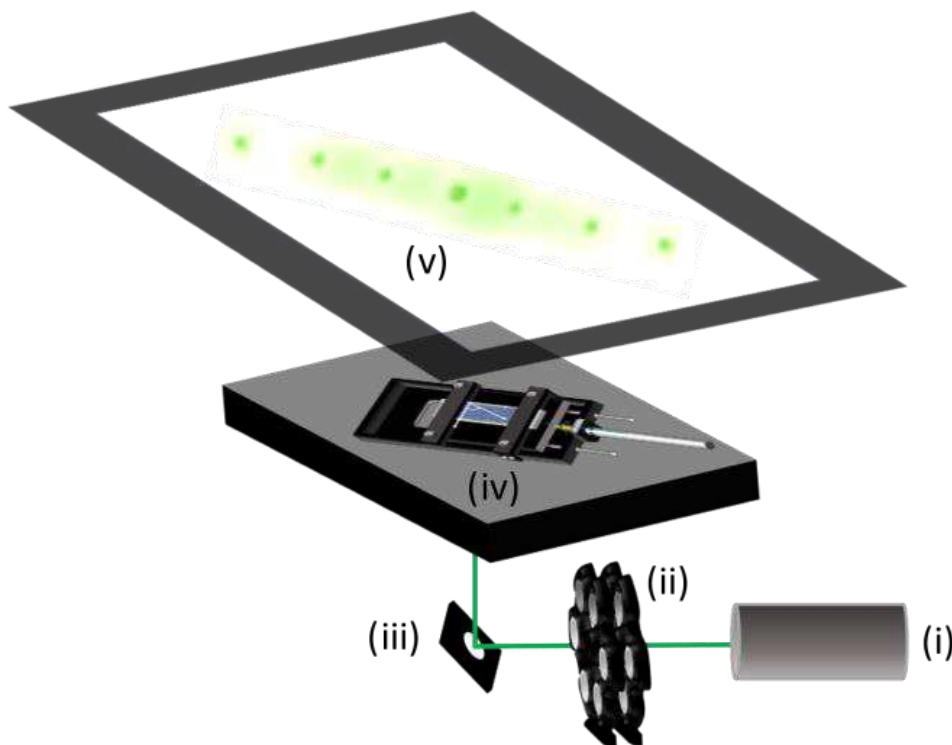


Figure 3.3: SLS setup depicting the (i) 533 nm diode laser, (ii) ND filter wheel, (iii) 45° mirror, (iv) motorised linear strain stage, (v) diffraction pattern imaged on a screen, and recorded by a cooled CCD detector.

The SLS set up consist of a 100 mW 532 nm diode pumped laser (Crystalaser), Prior stage,

Neutral Density filters (Thor Labs) on a double rotating filter wheel, consisting of two sets of filters - 0.2-0.6 and 1.0-4.0, an imaging screen, and a 16-bit Hamamatsu Orca camera cooled to  $-40\text{ }^{\circ}\text{C}$  to improve signal to noise ratio of the captured image. The laser light is reflected by a mirror (iii) at  $45^{\circ}$  and passes perpendicular through the sample. The distance from the sample to the screen is 10 cm.

The correlation between pixel distance in the images and the wavenumber  $q$  was obtained using a standard 200 lines/mm diffraction grating, using:

$$q = \frac{4\pi n_0 \sin\left(\frac{\theta}{2}\right)}{\lambda} \quad (3.2)$$

where  $\theta$  is the angle of diffraction,  $\lambda$ , the wavelength of the laser light;  $n$  is the order of diffraction, to obtain the resultant relationship of:

$$q = -0.000153(\text{pixels})^2 + 0.084469(\text{pixels}) \quad (3.3)$$

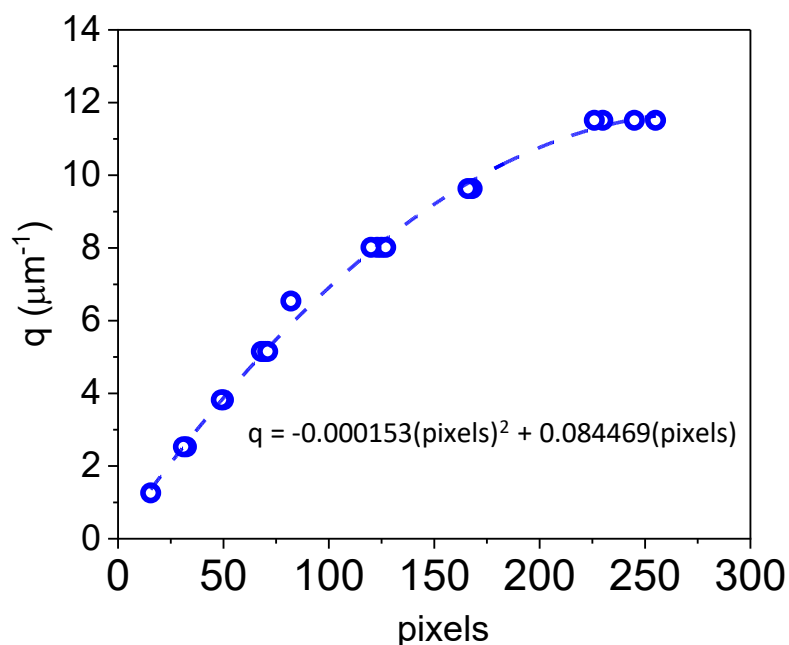


Figure 3.4: Correlation of pixels to wavenumber in SLS image for SLS system

Neutral density (ND) filters, which reduce the transmission of light were required in taking the measurements due to the saturation limit of the camera sensor. Various ND filters were used in experiments due to the tunability of intensities between and within each order – selected to obtain the highest non-saturated readings possible. This allows for the optimisation of signal to noise ratio. The ND filters are placed on two adjacent filter wheels, one with filters ranging from 0.2-0.6 and the other with filters from 1.0 to 4.0. The optical density (OD) values of ND filters are additive when combined in series. For a wavelength of 532 nm, the transmission value, T can be obtained from the optical densities of as follows:

ND Filters OD	0.2	0.3	0.4	0.5	0.6	1.0	2.0	3.0	4.0
% T at 532 nm	$6.55 \times 10^1$	$5.09 \times 10^1$	$3.90 \times 10^1$	$3.63 \times 10^1$	$2.51 \times 10^1$	$1.01 \times 10^1$	$9.62 \times 10^{-1}$	$7.65 \times 10^{-2}$	$7.25 \times 10^{-3}$

Table 3.1: Transmission attenuation values of neutral density filters

## 3.3 Material characterisation

### 3.3.1 UV Vis Spectrometry

UV-Vis spectrometry is a technique that involves measuring the absorption or transmission of light by a sample in the ultraviolet (UV) and visible (Vis) regions of the electromagnetic spectrum. There are various ways in which matter can react when exposed to radiation such as scattering, reflection, absorbance, fluorescence or phosphorescence, and photochemical reactions. In most cases, the absorbance of the sample is measured when determining its UV-visible spectrum. The absorption of light by matter results in the increase of energy content in the molecules or atoms of the matter since light is a form of energy. The overall potential energy of a molecule can be determined by adding up its electronic, vibrational, and rotational energies.

When light passes through or is reflected from a sample, the amount of light absorbed is the difference between the incident radiation ( $I_0$ ) and the transmitted radiation ( $I$ ). The amount of light absorbed is expressed as absorbance. According to the Beer-Lambert law, there is a linear relationship between the absorbance and path length, given by



$$I = I_0 \exp^{-\mu(x)} \quad (3.4)$$

where  $I$  is the intensity,  $I_0$  the initial intensity,  $\mu$  is the absorption coefficient and  $x$  is the thickness of the sample.

The transmittance, or light that passes through a sample can be obtained by  $T = I/I_0$  while absorbance is defined as  $A = -\log(T)$ .

### 3.3.2 Tensile Strain Measurements

Tensile strain measurements can be performed to measure the elastic modulus of materials. In this thesis, these measurements of PDMS were performed employing Lloyd EZ50 Tensile Strain Machine - a testing instrument designed for measuring the mechanical properties of materials under tension. The EZ50 Tensile Strain Machine is designed to apply a constant rate of deformation to the material being tested, typically between 0.1 and 500 mm/min. The machine consists of two arms that are fixed to the ends of the material at a fixed distance apart, as the material is subjected to tensile force, the arms move apart with the deformation and applying tension to the material. The load cell measures the force being applied, and the machine records the force and displacement data.

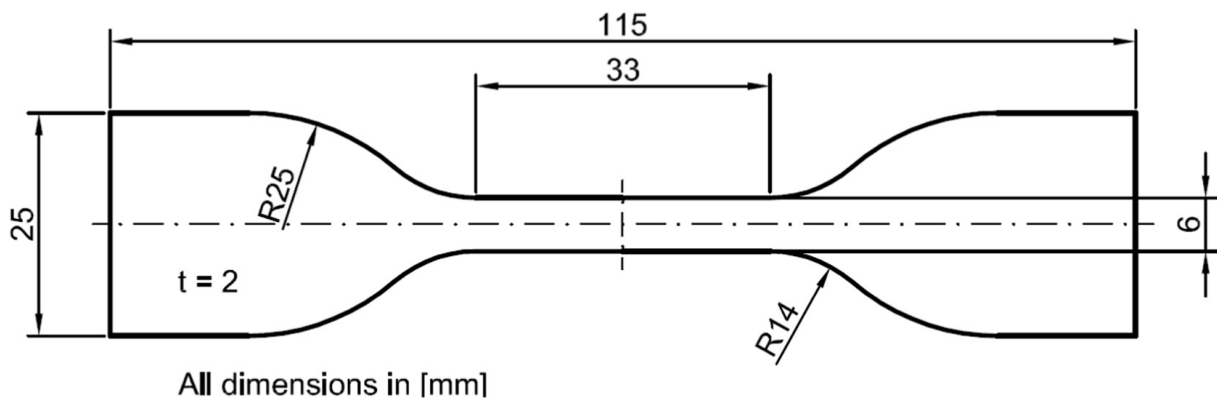


Figure 3.5: Dimensions of tensile test specimen according to ASTM D412. Adapted from [119]

These measurements are typically performed on samples of a specific shape and size to ensure accurate and repeatable results. The most commonly used shape for tensile testing is a straight

cylindrical or rectangular bar, also known as a dog-bone or dumb bell specimen, with a uniform cross-section along its length. From the displacement results, the elastic modulus can be calculated.

### **3.3.3 Thin film Analyser**

Film thicknesses can be measured using optical interferometry. Filmetrics F20-UV is a thin-film measurement tool that is commonly used to analyse the thickness and optical properties on thin films. The properties of a thin film, including its thickness, optical constants, and roughness, determine how light is reflected off it. To determine these characteristics, the F20 measures the amount of light reflected from the thin film across various wavelengths, known as the reflectance spectrum. Then, it analyzes this data by comparing it to a set of calculated reflectance spectra. This method allows for the determination of thin-film properties using the F20. It is equipped with a UV spectrometer that operates in the wavelength of 200 to 1100 nm, and the device is capable of measuring films with thicknesses ranging from a few nanometers up to several micrometers.

# Chapter 4

## Plasma-oxidised Wrinkles for Tunable Phase Gratings

Part of the work presented in this chapter has been published in ACS Applied Polymeric Materials 2021, 3, 10, 5162–5170 [120]. Dr. Luca Pellegrino (co-author) assisted with the optimisation of the static light scattering set up, and guided in the replication of topography with NOA.

### 4.1 Introduction

Wrinkling instabilities in polymeric bilayers have been exploited as optical phase gratings with tuneable performance. While this approach can be implemented via polymer [75] and metal [121] thin film deposition, surface oxidation of PDMS provides an attractive, facile route to PDMS patterning that has recently been explored to control opacity of otherwise transparent films [122]. Through the use of sinusoidal phase gratings, efficiency of gratings can be adjusted, allowing for different distributions of energy in the diffraction orders, which has practical applications in optics like projection systems [123], optical switches [124] and lasers [125]. Transmission phase gratings are transparent optical elements that can have periodic refractive

index variations or surface reliefs, which can be created by exciting sinusoidal wrinkles on a surface.

This chapter focuses on exploring the fabrication and use of sinusoidal phase gratings created by plasma-oxidised PDMS, specifically investigating the effect of compressive strain and the mechanical response of the samples on grating efficiency. Significantly, the surface oxidation of PDMS using an oxygen (or air) plasma source, generates a gradient glassy skin [93, 94, 95, 96, 97] whose density, and thus refractive index, varies in the direction normal to the surface. In order to explore the fabrication of tuneable phase gratings by wrinkling of oxidised PDMS, we consider quantitatively the impact of such gradients, intrinsic to this ubiquitous approach in soft matter patterning. The intensity modulation of diffraction patterns using static light scattering (SLS) was tracked and quantitatively examined, and the role of the gradient oxide layer in the light diffraction response was modelled. The reconstruction of real-space patterns from a combination of a simple optical model and diffraction images obtained by SLS was successfully shown.

## 4.2 Methodology

### 4.2.1 Sample preparation

PDMS elastomer samples were obtained by mixing the prepolymer and crosslinker (Sylgard 184, Dow Corning) at a 10:1 ratio by mass and stirred vigorously with a spatula. The resulting mixture was degassed under vacuum, deposited on a glass slab, and cured at 75°C in a convection oven for 1 hour to create an elastomer. The PDMS slab was then cut into coupons with dimensions of 2.5 cm  $\times$  3 cm and a thickness of 2.5 mm. The samples were clamped onto a strain stage attached to a motor actuator and strained at a speed of 0.02 mm/s to the desired  $\epsilon_{prestrain}$  with a precision of  $\pm 0.001$  mm.

Surface plasma oxidation was performed using a 40 kHz Diener Plasma (Femto), fitted with a pressure sensor (TM 101, Thermovac) and an oxygen gas cylinder (BOC, 99.5% purity). The

chambers were evacuated to a pressure of 0.2 mbar, before flowing the gas for 5 min until the desired pressure was reached and stabilised. The plasma was then ignited, at the required power, and exposure, controlled with a timer. Power setting of  $p = 70 \text{ W}$  and oxygen pressure of  $P = 1 \text{ mbar}$  was used, with exposure time  $\tau = 420 \text{ s}$ .

### 4.2.2 Replication of wrinkle topography using Norland Optical Adhesive (NOA)

In order to obtain scans of wrinkle topography while it undergo compressive strains, a drop of NOA was casted onto the wrinkle sample before covering it with a square glass slide, ensuring that the NOA is spread evenly beneath it. The sample was then placed under UV exposure for 5 minutes, allowing it to cure. The glass slide was subsequently removed resulting in a replica produced at a specific intermediary strain.

### 4.2.3 Tensile strain measurement

Tensile strain measurements of PDMS were performed employing Lloyd EZ50 Tensile Strain Machine. The PDMS samples tested were cut according to the required specimen shape (Chapter 3.3) before being loaded on the strain machine. The resultant force and displacement data can be computed within the system to produce a stress-strain plot, with an example of a PDMS sample with 2.5 cm thickness in Figure 4.1.

The resultant stress-strain graph can be used to obtain the elastic modulus of the material, by calculating the slope of the linear portion of the graph by dividing the change in stress ( $\Delta\sigma$ ) by the corresponding change in strain ( $\Delta\epsilon$ ). The equation for this calculation is Elastic modulus =  $\Delta\sigma/\Delta\epsilon$ .

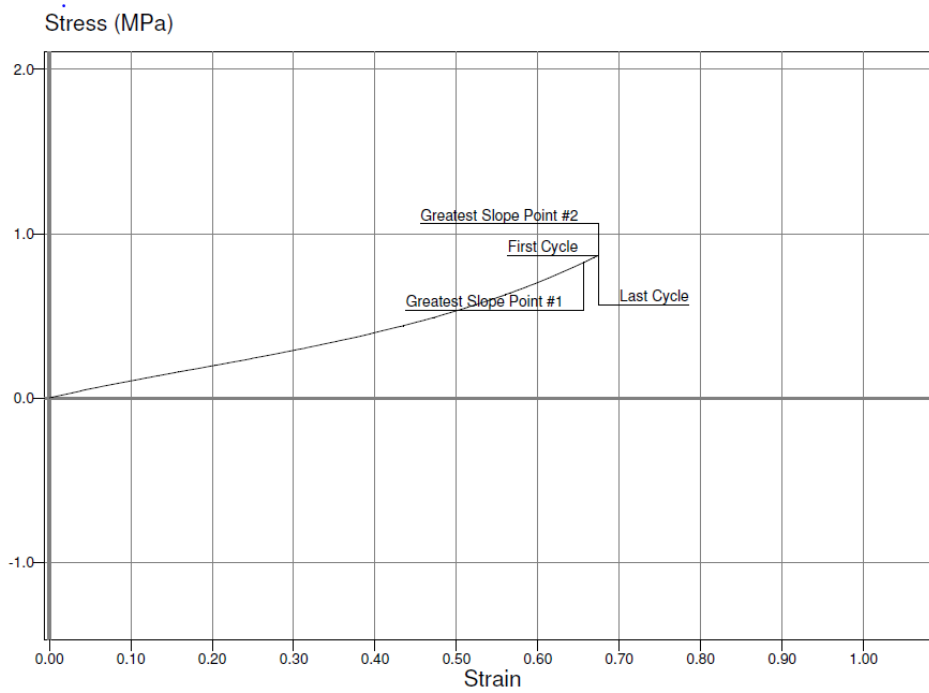


Figure 4.1: Example of a stress-strain plot obtained from Lloyd EZ 50 Tensile Machine for a PDMS sample of thickness 2.5 cm

#### 4.2.4 Pattern characterisation

##### Atomic Force Microscopy

Wrinkling morphology of samples were evaluated by means of atomic force microscopy (AFM) employing a Bruker Innova microscope in tapping mode, equipped with with Si tips (MPP-11100-W, Bruker), at 0.2 Hz , and analysed with the in-built Nanoscope software. Wavelengths and amplitudes were averaged over a series of three measurements recorded over areas of  $50 \mu\text{m} \times 50 \mu\text{m}$  scanning windows.

##### Static Light Scattering

Characterisation of the surfaces were performed using Static light scattering, with its setup consisting of a Diode Pumped CrystaLaser (532 nm, 500 mW), Neutral density filter wheel consisting of 2 sets of filters - 0.2-0.6 and 1.0-4.0 (Thor Labs). The laser light is reflected by a mirror at  $45^\circ$  and passes perpendicular through the sample. The distance from the sample

to the screen is 10 cm. The diffraction patterns formed on the screen are monitored when the sample undergo light scattering as it undergoes motorised compression through an automated strain stage to form sinusoidal wrinkles. SLS images are collected by means of a 16-bit CCD cooled camera (Hamamatsu Orca), controlled by the in-built software Wasabi.

The SLS images were then analysed using ImageJ software. Wavelengths of the wrinkled surfaces can be obtained by first measuring the distance (in pixels) between the first order diffraction and the central beam. This can then be converted to the corresponding wavenumber and hence wavelength as per SLS calibration (Chapter 3.2).

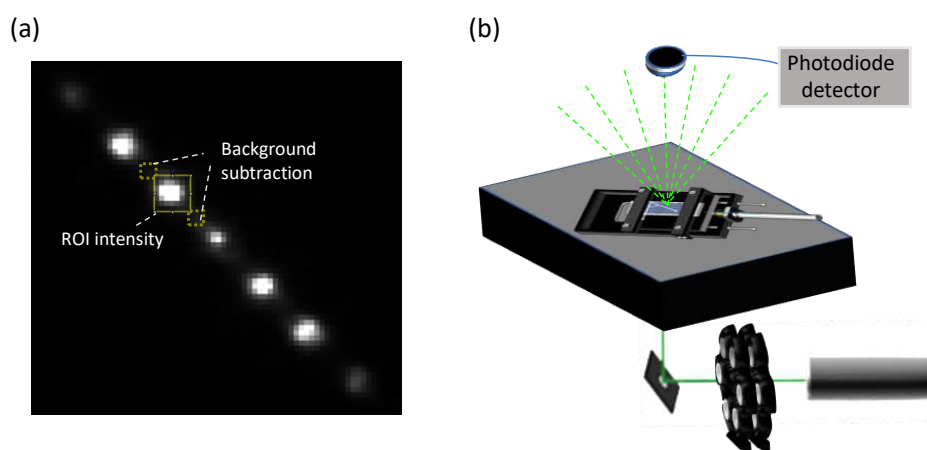


Figure 4.2: (a) SLS image for diffraction pattern observed when a plasma oxidised sample of PDMS undergo compressive strain. The intensity of a diffraction order is taken by subtracting adjacent ROI along the line of diffraction from the cumulative intensity in the diffraction order ROI. (b) SLS set-up using photodiode detector attached to a digital console. The use of the sensor removes the need for a screen, reducing the diffusion of the diffraction orders.

Due to scattering effects of the screen, the finalised intensities for the diffraction orders were obtained through a background correction. A square region of interest (ROI) was taken around each order with the cumulative intensity measured. A background intensity summative of two neighbouring ROI (each half of the original) along the line of diffraction was then subtracted from the original, to obtain the intensity. The obtained intensity from ImageJ is corrected by the appropriate attenuation depending on the ND filter used. A photodiode attached to a digital

console (Thorlabs, PM121D Digital Power and Energy Console with Si Sensor) was used to check the individual diffraction orders without the screen. The photodiode can be used to check for the zeroth and first order accurately. However for subsequent orders, the diffraction was too diffused to allow the photodiode sensor to pick up its intensity accurately.

### 4.3 Wrinkled bilayer characterisation

When an uniaxial strain ( $\epsilon_{prestrain}$ ) is applied to a flat PDMS coupon from  $L_0$  (initial length) to  $L_1$  (final length), which undergoes plasma-oxidisation, a stiff skin gradient bilayer is created. The gradient interface is generated, conversely to lamination and floating methodologies [86, 126, 127], through a temporal conversion of the bulk material into a mixed silicon oxide layer, where thickness and modulus increase with applied plasma exposure time. [94, 89, 128] Wrinkles are generated in the glassy skin upon compression of the bilayer due to a strain release, creating a buckled surface when a strain exceeding the critical strain  $\epsilon_c$  is applied. The application of oxygen plasma conditions at 70W for 7 minutes on a range of PDMS samples with different prestrains produces various wavelengths and amplitudes. The surface of the PDMS samples were examined using AFM to measure wavelength and amplitude, and SLS to measure wavelength only (Figure 4.3). Good agreement was shown between the results obtained from both techniques. The data obtained from the experiments are represented by the black and red dashed lines, respectively, until  $\epsilon_{prestrain} = 0.1$ . This corresponds to the low deformation model for wavelength  $\lambda$  and amplitude  $A$ , which is given by Eqn. 2.1 and 2.2. We can estimate that the elastic modulus of the PDMS samples increases from 1.02 MPa (for pure PDMS) to 40 GPa for the glassy skin layer formed due to wrinkling. This estimate is based on the aspect ratio of the wrinkles and a film thickness of about 30 nm, as determined by X-ray reflectivity measurements [95].

The elastic modulus of the glassy thin film from plasma oxidation can be directly estimated



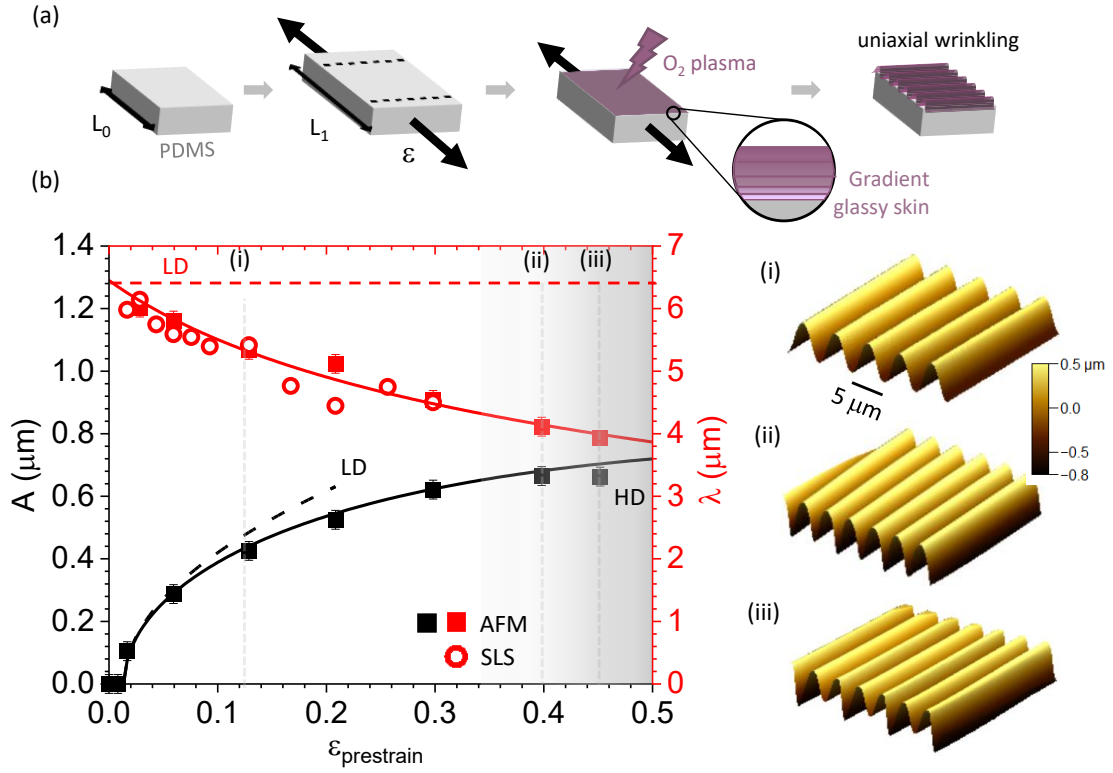


Figure 4.3: (a) Schematic of the formation of a 1D wrinkled surface on PDMS by pre-straining ( $\epsilon_{prestrain}$ ) an elastomer coupon, followed by plasma oxidation and relaxation of strain; the resulting glassy skin layer exhibits a conversion gradient normal to the surface. (b) Wrinkling wavelength ( $\lambda$ , red) and amplitude ( $A$ , black) measured by AFM (■) and SLS (○) as a function of prestrain  $\epsilon_{prestrain}$  for plasma-treated (40 kHz) PDMS coupons at power  $P = 70$  W for a duration  $\tau = 7$  min. The dashed and solid lines correspond to the low and high-deformation models, respectively (see text). The vertical dashed lines correspond to the AFM scans on the right, representative of (i) low-deformation, (ii) high-deformation, and (iii) period-doubling.

through the aspect ratio ( $A/\lambda$ ) of the wrinkles, derived from Eqn. 2.1 and 2.2 to obtain:

$$A/\lambda = \frac{1}{\pi} \sqrt{\epsilon - \epsilon_c} = \frac{1}{\pi} \sqrt{\epsilon - \frac{1}{4} \left( \frac{3\bar{E}_s}{\bar{E}_f} \right)^{\frac{2}{3}}} \quad (4.1)$$

A series of samples are fabricated at  $\epsilon = 0.20$  at 70 W with varying exposure time. The wrinkling behaviour shows a plateau in aspect ratio beyond exposure time,  $\tau$  of 90 s showing no significant change of the elastic modulus of the glassy film where film propagation occurs. At the plateau region where the aspect ratio can be approximated to 0.142, we can estimate  $\bar{E}_f$  to 40 GPa.

While this skin thickness is in line with previous literature [95, 96, 97, 129], this modulus is higher than those estimated by nanoindentation for UVO [130], or MHz plasma exposure [129]

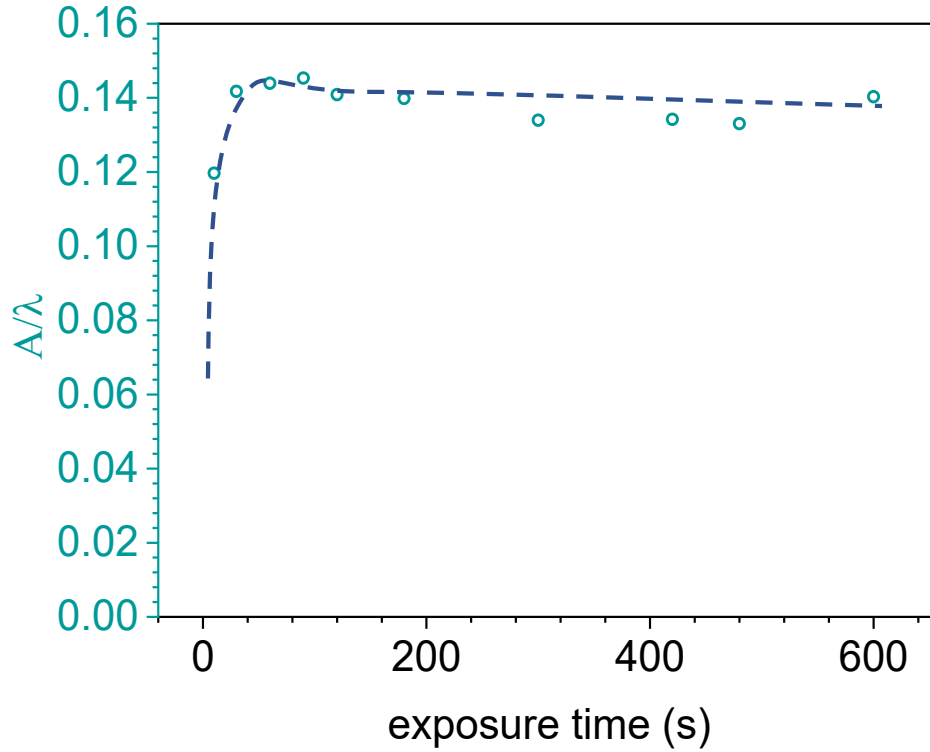


Figure 4.4: Aspect ratio of wrinkles with exposure time, showing a plateau as exposure time  $> 90$  s, indicating film propagation without a change in film elastic modulus.

(up to  $\sim 7$  GPa), which we associate with the more aggressive and faster 40 kHz process conditions [96]. The amplitude model predicts a square root dependency directly proportional to the thickness of the glassy layer and the critical strain  $\epsilon_c$  while  $\lambda$  is described by a straight line with dependence on  $h$  and the mismatch in the elastic modulus of the bilayer, expressed as a constant elastic moduli ratio  $\bar{E}_f/\bar{E}_s$ . However, this representation is not sufficient to describe the experimental data in this PDMS/ $SiO_x$  system due to the progressive build up in the glassy skin thickness and ultimately elastic modulus in “induction” and “formation” stages [95]. In order to take into account the evolution of  $\lambda$  and  $A$  beyond prestrain of 0.1 two solid lines are represented solid, corresponding to a implemented “high deformation model” for wrinkling instabilities developed employing prestrains above 0.2, described by Eqn. 2.4 and 2.5 respectively, where a bellow mechanics model is introduced to take into account deviations from linearity of the elastic modulus of PDMS with strain [90]. The evolution of initially sinusoidal wrinkled bilayers with strain can be visualised in the 3D AFM micrographs reported in Figure 4.3 (i), (ii), (iii),

showing a  $25\ \mu\text{m}$  by  $25\ \mu\text{m}$  region of the surface structures in samples having a prestrains  $\epsilon$  of 0.115 and in the higher deformation region where  $\epsilon = 0.4$  and  $0.45$ , respectively. As prestrain increases, the surface deviates from the original sinusoidal regime towards more complex buckling instabilities, such as period-doubling, characterised by a splitting in the original periodicity, induced by lateral compression due to the increase in the applied prestrain.

### 4.3.1 Diffracted intensity modulation in wrinkled tuneable gratings

Upon analyzing the preliminary results, we seek to gain a deeper understanding of the processes that contribute to the formation of gradient tuneable phase gratings. In addition, we aim to establish a connection between the diffraction patterns observed and the operational conditions utilized during the plasma oxidation stage. As a result, we investigate a series of fabrication conditions that permit access to various pattern wavelengths and amplitudes, which will be characterized using the SLS setup described in Chapter 3. This will enable us to observe, modulate, and track the evolution of these gratings up to the third diffraction order.

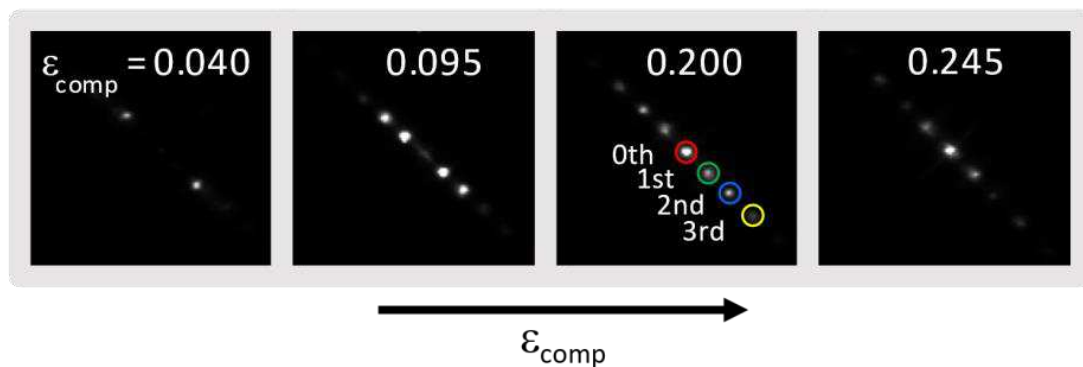


Figure 4.5: Series of diffraction patterns obtained at varying  $\epsilon_{comp}$  and constant ND attenuation, for a PDMS sample pre-strained at  $\epsilon_{prestrain} = 0.3$  and plasma treated at  $P = 70\ \text{W}$  for 7 min. The intensity of diffraction orders  $0^{th}$  (red),  $1^{st}$  (green),  $2^{nd}$  (blue),  $3^{rd}$  (yellow) is tuneable with  $\epsilon_{comp}$ .

To investigate the diffraction characteristics present in wrinkled skins, we employed SLS to monitor the motorized release of a plasma-oxidized sample with an initial prestrain of  $\epsilon = 0.3$ , at a rate of  $0.005\ \text{mm/s}$  in increments of  $0.5\%$ . Prior to being released under extensional strain

conditions ( $\epsilon_{comp} = 0$ ), the sample did not exhibit any diffraction pattern and only the direct beam was observed. The buckling instability can only be stimulated, as the bilayer model reports, once a particular critical strain is surpassed. This results in the laser light only beginning to diffract after the critical strain is exceeded while a compressive strain is being applied, indicating the formation of sinusoidal undulations on the sample surface and allowing for the presence of a diffraction pattern in the form of a phase grating. The use of Neutral Density (ND) filters allowed for the control of the amount of transmitted light, allowing the maximum amount of light to pass through without saturating the CCD camera sensor, and adjusting for each order as required. Wrinkles that resemble phase gratings can be created using the same set of ND filters (0.2 and 2.0) when a strained sample is slowly released and buckles as a result of the applied compressive strain. Figure 4.5 visually captures the modulation of intensities of the different orders as the sample undergoes compressive strain ( $\epsilon_{comp}$ ) using a single set of ND filters. The compressive strain ( $\epsilon_{comp}$ ) can be calculated by subtracting  $\epsilon$  from the prestrain,  $\epsilon_{prestrain}$ . For example, if a sample starting at a prestrain of 0.30 is released to 0.20, the resulting  $\epsilon_{comp}$  would be 0.10. The intensities of the orders can be adjusted by the amount of applied compressive strain. At  $\epsilon = 0.20$ , the zero-th, first, second, and third orders (red, green, blue, and yellow circles, respectively) can be observed using the same set of ND filters, indicating that their intensities are of the same order of magnitude. To observe other orders, the ND filters must be adjusted to increase or decrease the attenuation factor based on the compressive strain.

The individual orders' intensities are normalized based on the zero-th order's intensity at  $\epsilon_{comp} = 0.0$  ( $I/I(q=0, \epsilon=0)$ ), and their mapping is presented as a function of wavenumber  $q$  ( $\mu\text{m}^{-1}$ ) and compressive strain. The ability to exhibit strain-dependent phase grating behavior is demonstrated by a sample prestrained at  $\epsilon_{prestrain} = 0.3$  and plasma treated at 70 W for 7 min upon compression, as shown in Figure 4.6a. Harrison previously reported similar behavior in wrinkled bilayers fabricated via polystyrene film floating [75]. Within the explored strain range, the light intensity of the four observable orders modulates quantitatively with strain. The zero-th order can be seen to modulate through a minimum and maximum, while the other orders have intensities reaching a maximum before decreasing with strain. The  $q$  range in Figure 4.6b reflects the transition from the low deformation (LD) regime to the high deformation regime for

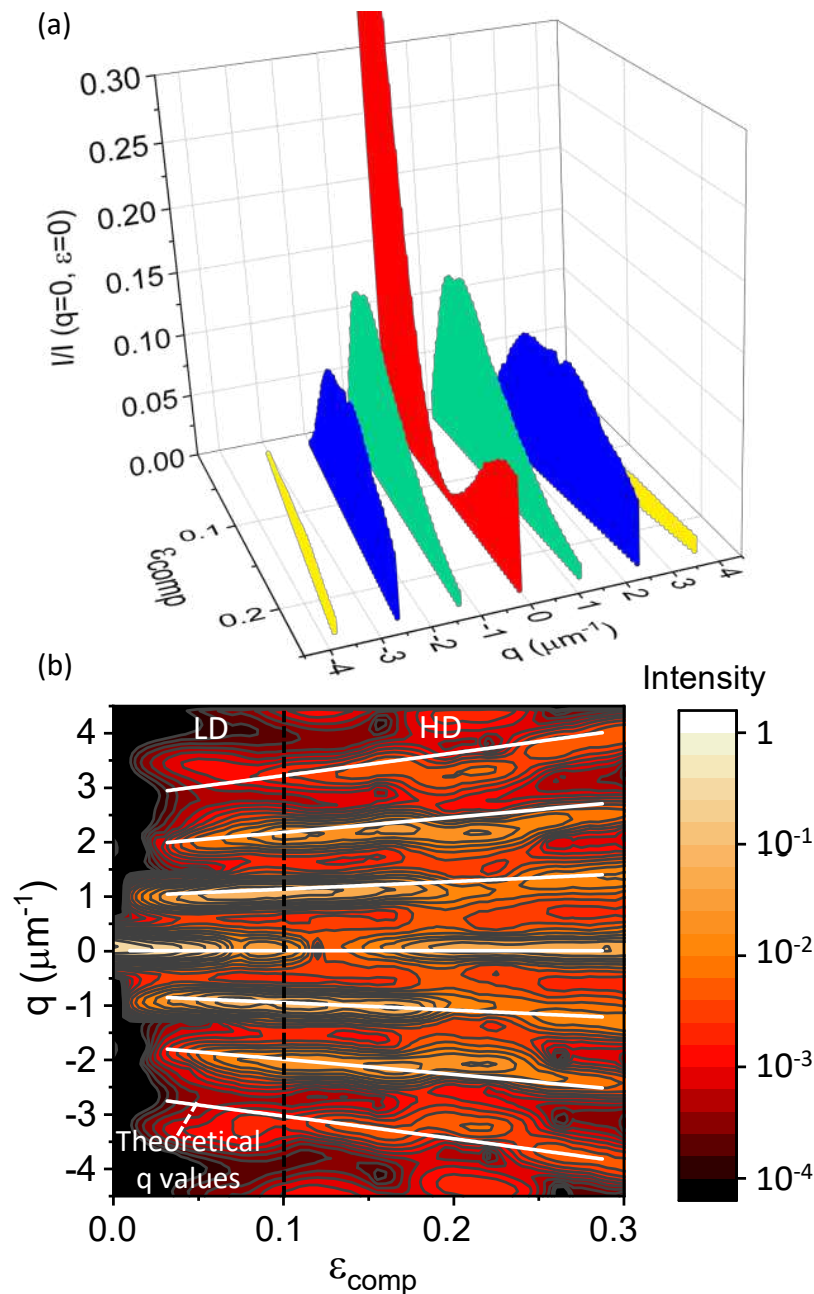


Figure 4.6: (a) Dependence of (normalised) diffraction intensities with  $\epsilon_{comp}$  and  $q$  for a PDMS sample at  $\epsilon_{prestrain} = 0.3$  and plasma treated at  $P = 70$  W for 7 min (shown in Fig 2b). Note the modulation of intensity and presence of well-defined maxima and minima with  $\epsilon_{comp}$  ( $\equiv \epsilon_{prestrain} - \epsilon$ , see text). (b) Contour plot of the diffraction data, showing the variation of wavenumber  $q_n$  with strain  $\epsilon_{comp}$ . The white lines represent the theoretical wavenumber calculated from  $\lambda_{HD}$ , and vertical black line indicates the approximate boundary for applicability of the LD model.

the wavelength. The wavenumber  $q$  has an inverse relationship with the wavelength  $\lambda$ . In the LD regime, the orders' positioning is independent of strain; therefore, the  $q$  range of the contour plots is independent of strain below  $\epsilon = 0.1$ , which is the LD limit. However, past this

threshold, the  $q$  dependence in the experimental data "fans out," following the high deformation approximation, where the pattern wavelength is strain-dependent due to non-linearities in the stress-strain response of the sample [90]. To compute this strain dependence, we need to employ the high deformation wavelength Eqn. 2.4. Following this behaviour, we are able to quantitatively characterise the angular variation of each diffraction order and its intensity in our phase grating.

### 4.3.2 Modelling of plasma-oxidised tuneable grating: Effect of gradient interface on diffraction

As previously discussed in Chapter 1.2, the diffraction pattern of a sinusoidal phase grating can be modelled for all diffraction orders  $p$  according to [74, 75]:

$$I \approx \sum_{p=-\infty}^{\infty} J_p^2\left(\frac{m}{2}\right) \text{sinc}^2\left[\frac{W}{\pi}\left(q - \frac{2p\pi}{d}\right)\right] \quad (4.2)$$

where  $J_p$  is a Bessel function of the first kind,  $W$  is the half-width of the aperture,  $d$  is the wrinkling wavelength (referred to as  $\lambda$  in the experimental data),  $m/2$  is the maximum phase shift impart to the light and  $p$  is an index accounting for the  $p^{\text{th}}$  diffraction order. Often  $W \simeq 0.5$  mm, determined by the typical profile of laser beam (in the Fraunhofer limit conditions). The maximum intensity of the  $p^{\text{th}}$  order can be approximated to be proportional to the Bessel function  $J_p^2(m/2)$  as the *sinc* function is narrowly distributed in  $q$  about each order without significant overlap between adjacent orders. The phase shift,  $m(\Delta)$  can be rationalised in terms of the wrinkling bilayer model of amplitude,  $A(\Delta)$  by

$$\frac{m(\Delta)}{2} = 2\pi \frac{A(\Delta)}{\lambda} [n - 1] \quad (4.3)$$

where  $A(\Delta)$  is taken from the high deformation model as described in Eqn. 2.5, with  $n$  is the refractive index, and here  $\lambda$  is the laser wavelength (532 nm in our work).

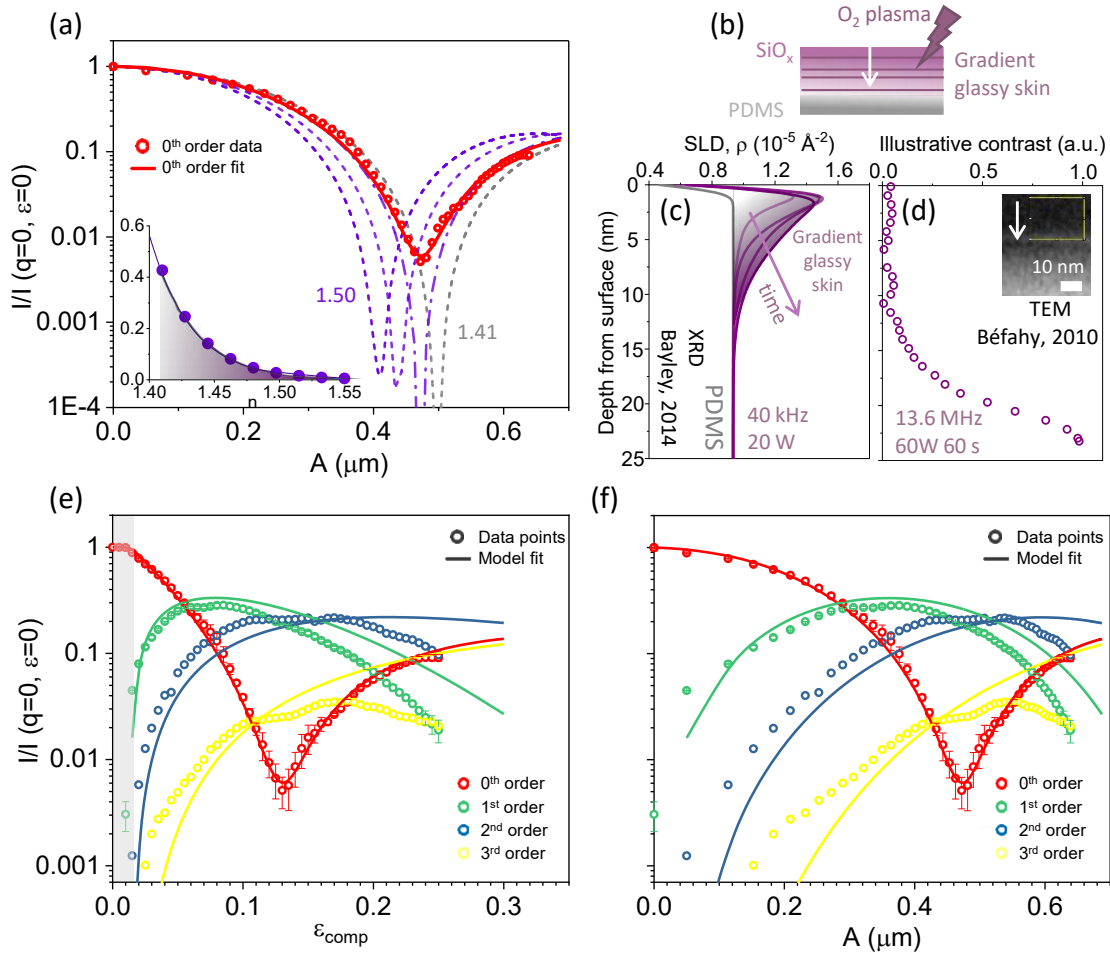


Figure 4.7: (a) Zero-th diffraction order intensity as function of pattern amplitude (red data points), modelled by Eqn. 4.4 by assuming an exponential distribution of refractive index (from  $n = 1.41$ , pure PDMS to 1.55, silica; shown in inset and described in the text), shown by the solid red line. The dashed lines correspond to model predictions from single  $n$  values. (b) Schematic of the conversion in a gradient bilayer towards silicon oxide when PDMS is exposed to oxygen plasma. (c) X-ray reflectivity data [95] supports the refractive index distribution in graded bilayers fabricated by means of oxygen plasma through an increase in the scattering length density in the formation of thicker glassy skin layer, reported by several authors (e.g., [131]). (d) Representative TEM data [129] illustrating the skin conversion with thickness, progressing from a darker region, corresponding to the denser silicon oxide gradient to a lighter background value, corresponding to untreated PDMS. (e) The distribution described in (a) and (b) is then applied in modelling the modulation of experimental diffraction patterns from zero-th to third order (red, green, blue and yellow solid lines respectively) ( $\circ$ ), as function of (e) strain,  $\epsilon_{\text{comp}}$ , and (f) amplitude,  $A$ .

The diffraction pattern and individual diffraction intensities of each order in a sinusoidal phase grating with a single refractive index  $n$  can be described using the model by Eqn. 4.2 and 4.3. When thin polymer film is deposited onto PDMS, a sharp interface is created to the bulk, and a single refractive index (that of bulk PDMS) is sufficient to model the diffraction pattern [75].

The value of  $n$  shifts the positions of the minima and the depth of the individual orders, describing the specific strain and intensity modulation for the diffraction pattern. When  $n$  increases, there is a 'left' shift in a graph of intensity vs amplitude (or strain), as depicted by the dashed lines of Figure 4.7, calculated with the model. However in this case, a single refractive index phase grating model is not enough to fully explain the experimental data. This is believed to be due to the different nature of plasma oxidised bilayers, which creates a gradient interface. The plasma oxidation process induces a heterogeneous, frontal conversion that results in a different refractive index distribution of the skin, generating a leading to a "gradient skin phase grating".

Evidence for gradient bilayer (illustrated in Figure 4.7) formation in plasma oxidised PDMS abounds, as previously reported by X-ray reflectivity (XRR) [95] (data reproduced in Figure 4.7c) and transmission electron microscopy (TEM) [129] (data reproduced in Figure 4.7d). XRR can be employed to determine the scattering length density profile for surface-oxidised PDMS and, in Figure 4.7c, such profile indicates that the densification of the top layer increases with plasma exposure time at a given power, with a gradual surface to bulk interface with thickness showing the plasma conversion in the PDMS. A frontal model has been used to describe the skin growth of the glassy layer, where the hydrogen and methyl groups are substituted with hydroxyl groups and oxide links, creating a thin, silica-like skin layer [132]. This conversion is dependent on the plasma dose applied, and creates a logarithmic dependence conversion profile with thickness, where the surface of the layer is fully reacted into a denser silica-like layer with decreasing conversion in the subsequent intermediate layers [95]. A representative TEM data by Behafy also supports the gradient nature through width contrast. The chemical modification and surface densification due to plasma treatment is responsible for the contrast observed in a TEM image [129]. By tracing a line through the image, spanning from a plasma-oxidised PDMS surface to the bulk, a qualitative graph can be extrapolated, showing contrast variation from fully converted plasma surface - where illustrative contrast = 0, to pure PDMS - where contrast approaches 1. The contrast width, reflecting the gradient skin thickness, can be approximated to 20 nm.

Due to the nature of the wavefront kinetics of film growth in the plasma oxidation of PDMS, this



system is unlike to behave as a perfect bilayer phase grating, where a single, sharp interface is usually defined. Therefore, to account for the graded silicon-oxide interface, instead of using a single refractive index for the skin as in Eqn. 4.3, we define a refractive index distribution, which is able to better represent the densification from the bulk PDMS ( $n \simeq 1.41$ ) to glass ( $n \simeq 1.46-1.55$ ) as reported from XRR and TEM experiments. Hence, we consider the signal to arise from a distribution of  $n$  values with an exponential decay function, such that

$$I(\bar{x}, y) \approx \sum_{i=0}^8 A_0 e^{-kn_i} I_{ni}(x, y) \quad (4.4)$$

where  $n_i$  ranges 1.41 to 1.55. The choice of 9 (or more) terms to implement the normalised exponential curve is supported by the subsequent TEM and XRR data, where  $A_0 = 8.0 \times 10^{18}$  and  $k = 31.5$ . In Figure 4.7a, this resultant model using a distribution (red solid line) quantitatively captures the representation the data (red circles) for zero-th order intensities. We find that a Gaussian distribution (among others) can also adequately model the data. For simplicity we can also consider the signal to arise from a distribution of  $n$  values with a Gaussian profile, such that:

$$I(\bar{x}, y) \approx \sum_{i=0}^8 \frac{1}{\sqrt{2\pi\sigma^2}} e^{-\frac{(n_i - \langle n \rangle)^2}{2\sigma^2}} I_{ni}(x, y) \quad (4.5)$$

where  $n_i$  ranges from  $\langle n \rangle \pm 2\sigma$ . The use of the distribution effectively replaces a well defined  $n$  by  $\langle n \rangle$ , and includes one additional parameter to the model, namely the width of the distribution  $\sigma$ . The choice of 9 (or more) terms to implement the normalised Gaussian ensures that the profile is smooth (Figure 4.8b), but the model parameters are largely insensitive to the number of terms employed. When  $\langle n \rangle = 1.41$  with  $\sigma = 0.045$ , the Gaussian distribution can also effectively describe the model with little variation from the exponential distribution (Figure 4.8c, d), supporting the need for a gradient use of refractive indices in the data.

The results of the model with the gradient distribution of refractive index for the zero-th and the other orders (first to third) are presented in Figure 4.7e, where solid lines indicate good agreement with experimental data. Based on the correlation between strain and amplitude established in the bilayer model Eqn. 2.2, we can obtain a relationship between the intensity of

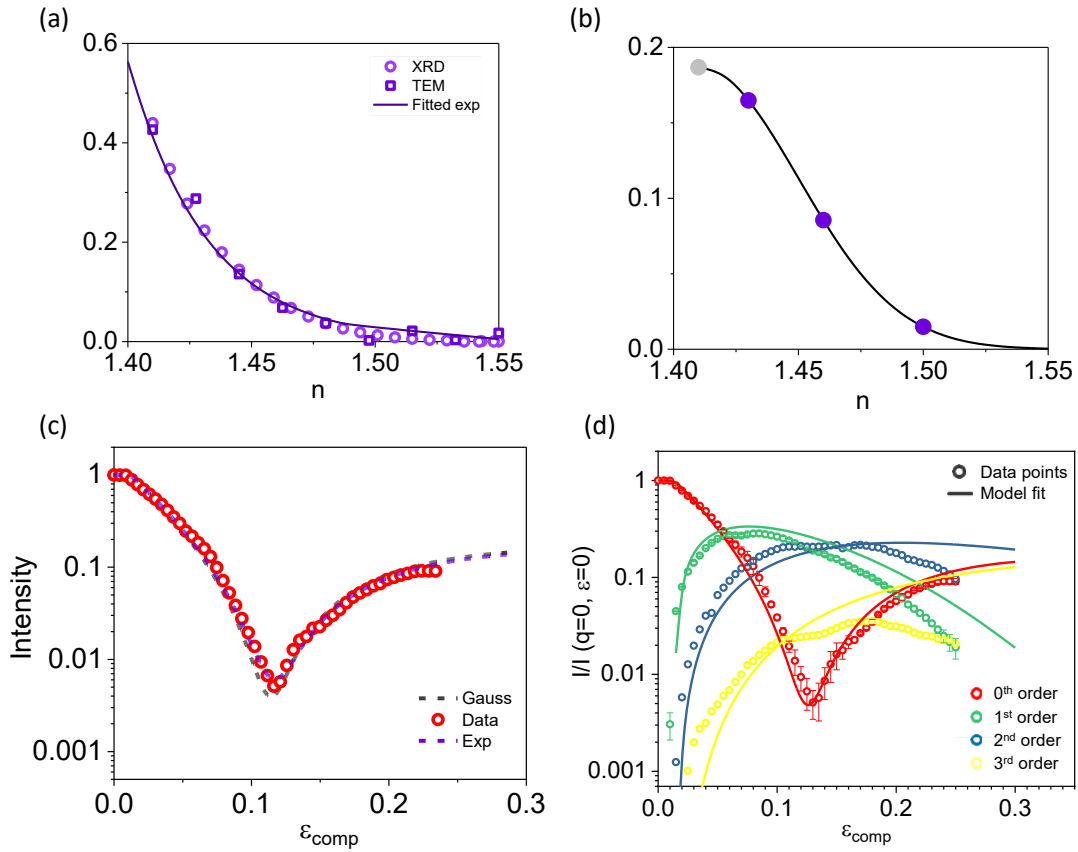


Figure 4.8: (a) Exponential distribution ( $A_0 = 8.0 \times 10^{18}$ ,  $k = 31.5$ ) supported by XRD and TEM (b) Gaussian distribution ( $\langle n \rangle = 1.41$ ,  $\sigma = 0.045$ ) (c) Resultant zeroth order model using the different distribution functions both accurately describe the data with little variation between them (d) Gaussian distribution model implemented for all the orders in the low deformation tunable grating

orders and amplitude in Figure 4.7f. This intensity modulation of orders describes the dependence of diffraction efficiency on the profile of the grating as a function of strain or amplitude. The diffraction efficiencies of the first to third orders can be represented linearly as a function of strain. The maximum efficiency of the grating is estimated when the zero-th order goes through the main minimum around  $\epsilon_{comp} \approx 0.11$  or  $A \approx 0.45$ , with an efficiency of 48% (Figure 4.9a). However, there is a deviation between the experimental and theoretical efficiencies, which may be attributed to the development of cracks in the sample with increasing strain, leading to the scattering of light (Figure 4.9b). The diffused nature of the higher orders can also account for the disparity between the model and data in the 2nd and 3rd order.

Here the other three orders modulate towards a maximum, progressively increasing the amount of diffracted light. This can be calculated as a percentage with respect to the total diffracted

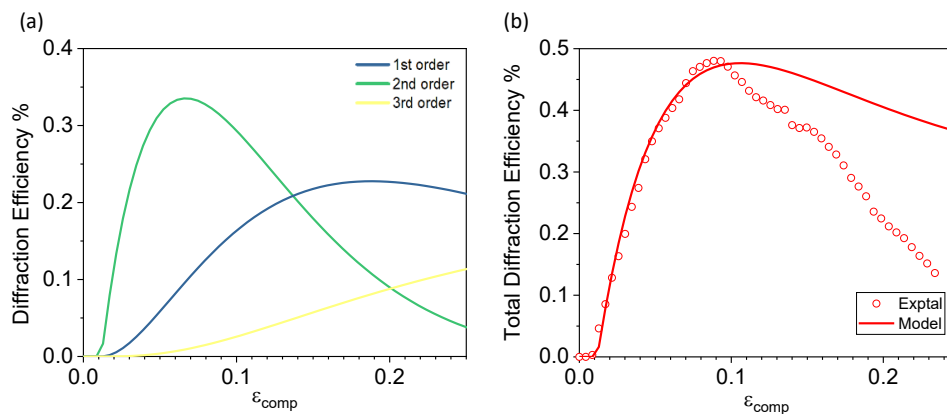


Figure 4.9: (a) Theoretical diffraction efficiency of 1st (green), 2nd (blue) and 3rd order (yellow) linearly as a function of strain. (b) Total diffraction efficiency as a function of strain, experimental and theoretical

intensity (zero-th order at 0 strain or Amplitude), reaching  $\approx 30\%$  of the total light for the first and second order, and 5% for the third order. The residual loss might be ascribed to adsorption/diffusion phenomena due to the PDMS thickness, and additional light coming from the zero-th order.

### 4.3.3 Effect of PDMS mechanical properties on diffraction of tuneable gratings

When samples with various initial prestrains are subjected to the same plasma treatment with identical power and exposure time, the modulation of intensities is found to be dependent on the amplitude versus strain evolution of the wrinkles. In particular, we observed that when we compared the intensity of the zero-th order in samples with prestrains of 19%, 29%, 36%, and 51%, we observed initial discrepancies in intensity against  $\epsilon_{comp}$ . By plotting the intensities with respect to  $\epsilon_{comp}$ , we found that the position of the minimum for the highest  $\epsilon_{prestrain}$  differed from the lower three (as shown in Figure 4.10b). This can be attributed to the non-linear behavior of the mechanical properties of PDMS with strain, which leads to two different values for the elastic modulus (i) and (ii) (as shown in the inset in Figure 4.10a) when a PDMS coupon is stretched beyond  $\epsilon = 0.4$ . Since the elastic modulus of PDMS directly affects  $\epsilon_c$  and hence  $A$ , we were able to remodel the  $A$  vs  $\epsilon_{comp}$  curve by accounting for the different mechanical

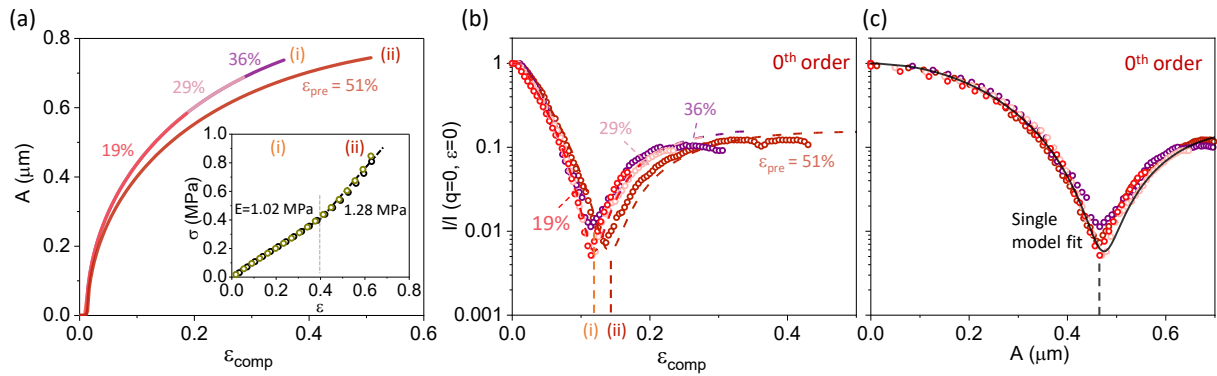


Figure 4.10: (a) Dependence of pattern amplitude on compressive strain  $\epsilon_{comp}$ , employing different prestrains. The disparity between the two lines (from  $\epsilon_{prestrain} = 19\%$ - $36\%$  and  $51\%$ ) is ascribed to the onset of non-Hookean behaviour in PDMS in high-deformation conditions, and non-linearity in the stress-strain relationship shown in inset. (b) Normalised zero-th order intensities comparing experimental data ( $\circ$ ) and modelled profile ( $- -$ ) at different prestrains. The slight variation in the minimum position, at the highest prestrain ( $0.51$ ), is due to the non-Hookean behaviour of  $E$ , resulting in a higher critical strain. (c) Near collapse of all zero-th order normalised intensity data when plotted as function of pattern amplitude (demonstrating that apparent offsets in (b) arise from the mechanical history of the material).

responses at a given prestrain. After converting the Intensity vs  $\epsilon$  graphs to Intensity vs  $A$  using the relationship between  $\epsilon$  and  $A$ , we found that the results for the different prestrains collapsed onto a single curve, implying that the intensities are solely dependent on the amplitude evolution of the samples for a given condition.

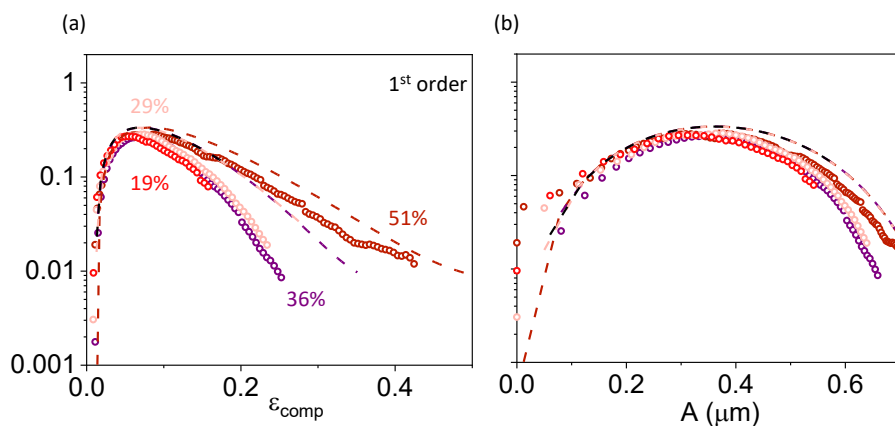


Figure 4.11: (a) Normalised intensities comparing experimental ( $\circ$ ) and modelled ( $- -$ ) first order at different prestrains. The slight variation in the breadth of maximum, at the highest prestrain ( $0.51$ ), is due to the non-Hookean behaviour of  $E$ , previously discussed (c) Collapsed first order normalised intensities when plotted as function of the amplitude

Similarly to the zeroth order, the intensity vs amplitude curves for the first order collapsed into a single curve (4.11). This observation suggests that the modulation of intensities is dependent on the amplitude evolution of the samples and not on the initial prestrain or the plasma treatment. Therefore, the modulation of intensities in our experimental setup can be explained by the amplitude evolution of the wrinkles alone, and this phenomenon is not unique to a particular prestrain or plasma treatment.

#### 4.3.4 Additional diffraction orders at high deformations: period doubling instability

We next seek to investigate the effect of high deformations, specifically for prestrain above 50% on the sample. An initial  $\epsilon_{prestrain}$  of 0.6 was applied to the PDMS coupon undergoing plasma treatment and the observation of the buckling development as the sample relaxes was assessed using a photopolymer. As the sample is partially released, a drop of Norland Optical Adhesive (NOA) is placed on the surface and covered with a glass slide. The NOA is UV cured and the glass slide is removed to produce a replica at a specific intermediate strain. This is repeated to produce a series at varying compressive strains and the wavelengths of the replicas are characterised via AFM and SLS. As expected, the primary wavelength  $\lambda_1$  decreases with increasing strain, as per Eqn. 2.4. However as  $\epsilon_{comp}$  increases, the initially sinusoidal-like buckling (Figure 4.12c(iii)) deviates into a period doubling regime (Figure 4.12c(i)), resulting in the arise of a secondary wavelength,  $\lambda_2$  when  $\epsilon_{comp} \geq 0.36$ .

This transition to frequency doubling can be observed and quantified with SLS. The occurrence of an additional order can be clearly seen between the zero-th and first order, giving rise to wavelengths corresponding to  $\lambda_2$ . The order has a smaller wavenumber due to the formation of a larger wavelength in a period doubling. By monitoring the intensity of the new order as the sample is continually released, we are able to observe more accurately the point of transition from sinusoidal to period doubling. In Figure 4.12e, the grey circles indicate the formation of a new order, where its intensity increases as the period doubling formation becomes more

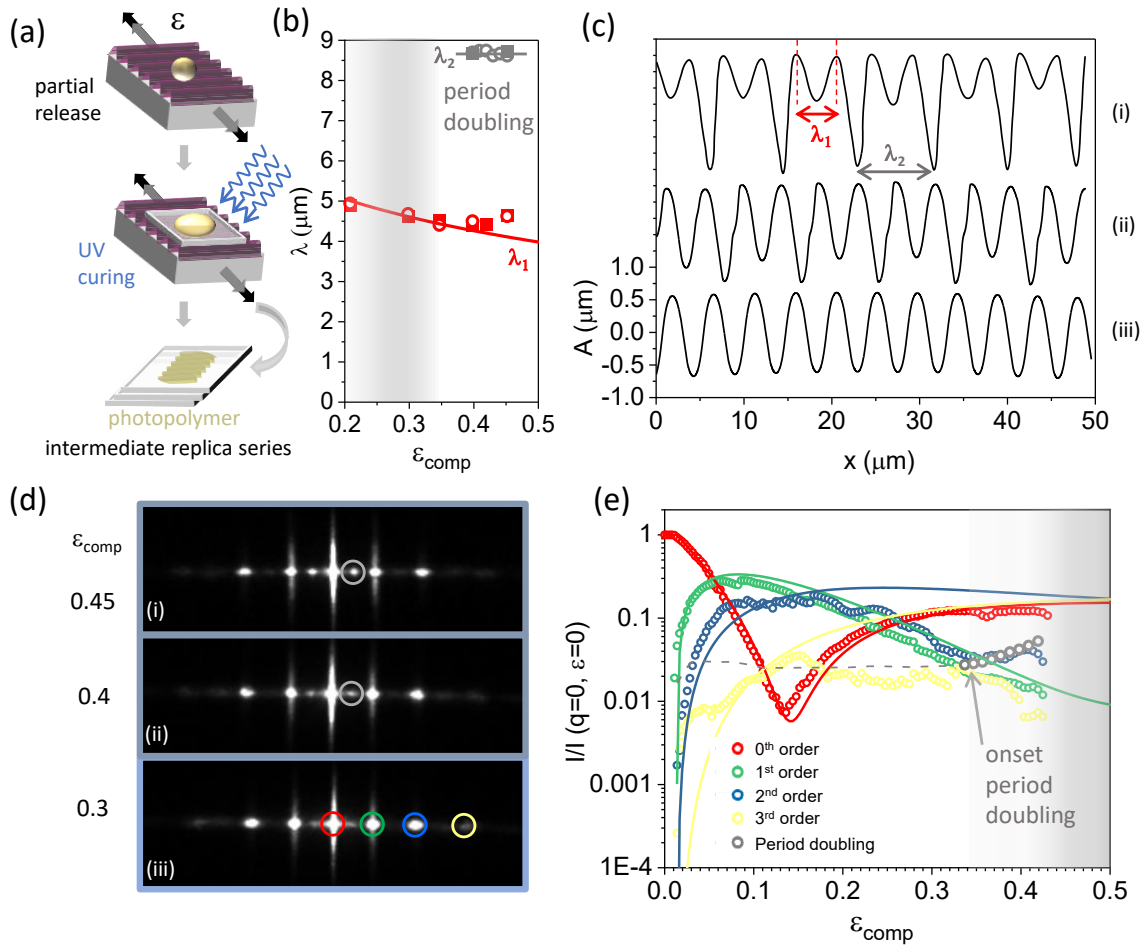


Figure 4.12: (a) Schematic describing the process of characterisation of wrinkled samples in partial release, using a photopolymer (NOA) replica. (b) Pattern wavelength  $\lambda$  and secondary period-doubling  $\lambda_2$  obtained by AFM (■) and SLS (○) measurements of the replicas. (c) AFM cross-sectional line profiles of conditions in the (iii) sinusoidal-like regime, (ii) transition, and (i) period doubling regime. (d) SLS images showing the onset of period doubling as an additional observable order (light grey) between the original zero-th and first orders, whose intensity becomes increasingly pronounced with  $\epsilon_{comp}$ . (e) Dependence of the normalised diffraction intensities of the  $0^{th}$ - $3^{rd}$  order with strain into high deformation regime, depicting the emergence of period doubling at  $\epsilon_{comp} \gtrsim 0.3$ .

prominent. For the other orders, the experimental (○) and model (—) were plotted accordingly with strain, and there shows good agreement for the zero-th and first order. The discrepancies for the second and third order, where the experimental data show lower intensities compared to the model curves could be attributed to the light being redirected towards the formation of the new additional order, causing therefore a different phase shift in the phase grating.

### 4.3.5 Real-space reconstruction from diffraction pattern (1D)

Up till now, we have established the relationships between the wavenumber  $q$ , the wavelength  $\lambda$ , and the intensity and amplitude  $A$  of the graded wrinkled gratings. With this knowledge, we devise a method to reconstruct the pattern of the real space structure from an SLS image. For example, in Figure 4.13a, we observe three diffraction orders in the SLS image, and we can readily obtain the wrinkling wavelengths from the spatially calibrated SLS data, as shown under Methodologies in this chapter. To compare the intensity ratios between adjacent orders, we further develop the model that we reported in Figure 4.7. By comparing the intensity ratios between adjacent orders, we eliminate the need for a reference intensity (at zero strain for the zero-th order), leaving the dependency to the intensities of the orders solely within the image. We only require two sets of adjacent orders ( $I_0/I_1$ ,  $I_1/I_2$ ) to extrapolate the corresponding amplitude of the sample. We choose the first three orders (0th to 2nd) because they have the smallest standard error between the experimental results and the model.

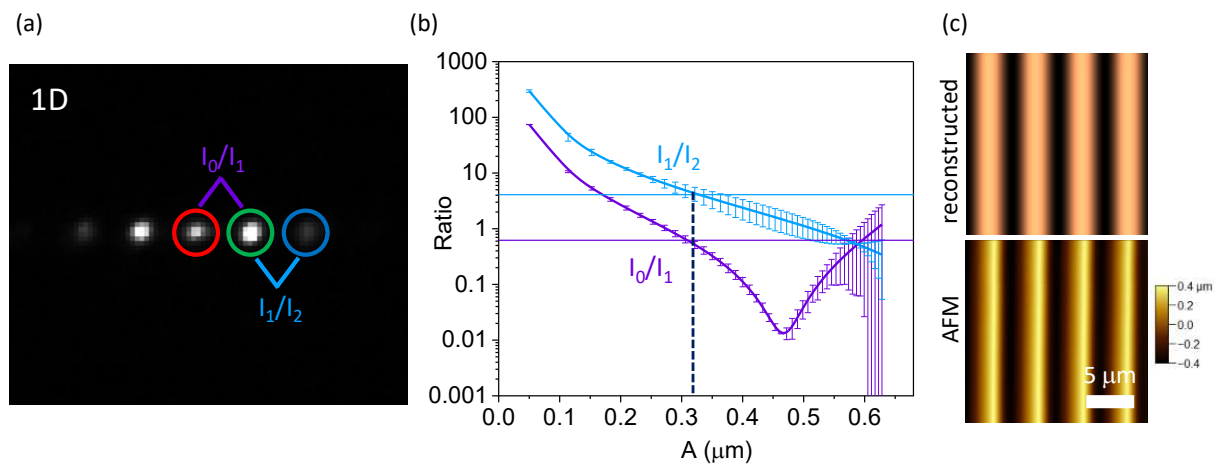


Figure 4.13: Reconstruction of a real-space image using a SLS diffraction patterns. (a) A standard 1D SLS image with its zero-th, first and second order intensities identified. (b) The purple and blue line represent model  $I_0/I_1$  and  $I_1/I_2$  with amplitude of the pattern, reported in Figure 4.7. Intersecting the equivalent intensity ratios from the experimental SLS image with the model curve ratios, the surface amplitude can be extrapolated. (c) Reconstructed AFM image obtained plotting a sinusoidal profile with Amplitude and wavelength extracted using the previous analysis, compared with the relative experimental AFM profile.

For a given SLS image, we can calculate the ratio of intensities for the two sets of orders, which allows us to determine the corresponding amplitude of the wrinkles. With both the wavelength

and amplitude, we are able to create the real space image by inputting  $A$  and  $\lambda$  in a sine wave equation describing the wrinkled surface where  $f(x) = A\sin(2\pi x/\lambda)$ . This produces Figure 4.13c, which agrees well with the experimentally measured AFM profile.

## 4.4 Conclusion

- We have explored the fabrication of 1D and 2D strain-tuneable phase gratings by means of the mechanical wrinkling of plasma oxidised PDMS. While 1D phase gratings have been previously demonstrated by the wrinkling of bilayers comprising a polymer thin-film supported onto PDMS[75, 84], the fabrication method employed here is considerably simpler, removing the need to float and deposit the glassy film, as well as more robust, by ensuring covalent bonding of the skin layer and preventing delamination or crumpling.
- We resolve and quantify up to 4 diffraction orders resulting from plasma-oxidised PDMS samples, which are strain-controlled and thus tuneable, or fixed (or static) by the release of a selected pre-strain condition. The intensity of the various diffraction orders is modulated by strain, as the sample undergoes relaxation ( $\epsilon_{comp}$ ), providing a maximum total diffraction efficiency of 48%.
- Phase gratings fabricated via this method cannot be described by conventional sinusoidal phase grating equations. We attribute this fact to the gradient nature of the glassy skin layer, originating from the directional conversion process that emanates from the top surface during plasma oxidation. By incorporating a distribution of refractive index in the skin formed, we succeed in quantitatively modelling the diffraction data. Further, the precise data modelling of the strain dependence of the diffraction data requires the consideration of non-Hookean properties of PDMS, due to the change in elastic modulus at sufficiently high strain affecting primarily the buckling amplitude.
- We then also examine the optical behaviour of these phase grating at higher deformation, when buckling deviates from the sinusoidal regime towards period doubling. This leads to the emergence of an additional diffraction order, as a result of a secondary wavelength



formed upon 'doubling' events. The precise strain of period doubling formation can be monitored through light scattering, where the increase in intensity of the new order is an indication of its development.

- Diffraction patterns can be used to fully resolve the surface structure in simple manner. The real-space image of a wrinkled sample can be effectively reconstructed by obtaining the wavelength and amplitude through a diffraction image

# Chapter 5

## Tunable structural colour and mechanochromic response of wrinkles: 1D and multiaxial

Part of the work presented in this chapter has been published in *Advanced Optical Materials* 2022, 10(17), 2200964 [133]. Co-author Zain Ahmad assisted with the fabrication and characterisation of gradient wrinkle structures.

### 5.1 Introduction

So far, we have demonstrate that wrinkling of plasma oxidised PDMS is an effective method to produce a phase grating that can be tuned in the context of a monochromatic light source. However, to broaden the range of applications of this technique, it is necessary to investigate how these wrinkles behave under white light. Inspired by the abundance of structural color in nature [8, 31, 134, 135, 136, 137, 138], a range of material synthesis and processing approaches have been developed to design nano- and microstructures, including multilayer films [139, 140], photonic crystals [141, 142], and metasurfaces [143, 144], exhibiting static and variable structural

colors, tailored to various practical applications [145, 146, 147, 148].

Wrinkled surface structures, found in flowers and insects [39, 38, 40] have been shown to act as surface diffraction gratings, imparting structural color to flower petals such as in the Queen of the Night tulip [25] and the *Hibiscus trionum* [37], as well as enhancing the diffuse reflection in dragonflies *Rhyothemis resplendens* [40]. Randomly oriented wrinkles were demonstrated to produce uniform bright structural colors with broad viewable angles, which can further be tunable using light sensitive polymers skins [149]. Mechanochromic response, i.e. the change of color under stress, of wrinkled structures has been recently reported, employing various bilayer film structures [37, 61, 150]. The use of soft matter substrates, including elastomers, is advantageous as it readily allows optical properties to be tuned by the applied strain, by adjusting surface periodicity and amplitude, in addition to film thickness and mechanical modulus. Further, a wide range of surface patterns, including uni- and multiaxial and hierarchical wrinkles, can be readily fabricated. Similar to the work in the previous chapter, we can take advantage of the wide range of wavelengths and amplitudes that can be achieved through different plasma conditions. In this chapter, we present a study that demonstrates how colour tunability and mechanochromic response can be easily achieved by adjusting plasma and strain parameters, and by dynamically varying strain (with a maximum of  $\varepsilon \lesssim 50\%$ ). To further explore the capabilities of this technique, we use different parameters such as strain directionality, employing uniaxial, isotropic and gradient strain, as well as skin thickness (and thus  $d$ ) and amplitude gradients. These facile and scalable fabrication approaches lead to striking spatial colour variation, homogeneity and directionality, expanding the possibilities of this method for a wide range of applications.

In this study, we build upon the phenomenon of structural color and mechanochromic response exhibited by 1D plasma oxidized wrinkled PDMS topographies, ranging from nano to the micronscale. Our goal is to not only qualitatively examine these phenomena, but to also quantitatively investigate the emergence of color mixing by the superposition of diffraction orders of distinct colors at similar observation angles. This involves a comprehensive analysis of the joint roles of amplitude and periodicity in determining color brightness, which is an important

aspect of this technique. Additionally, we investigate the potential for colour modulation and directionality using gradient wrinkles, where the surfaces have spatially varying periodicity, as well as isotropic patterns that can be easily fabricated. The results of this study demonstrate that these methods can produce both uniform and spatially varying colors, depending on the observation angle.

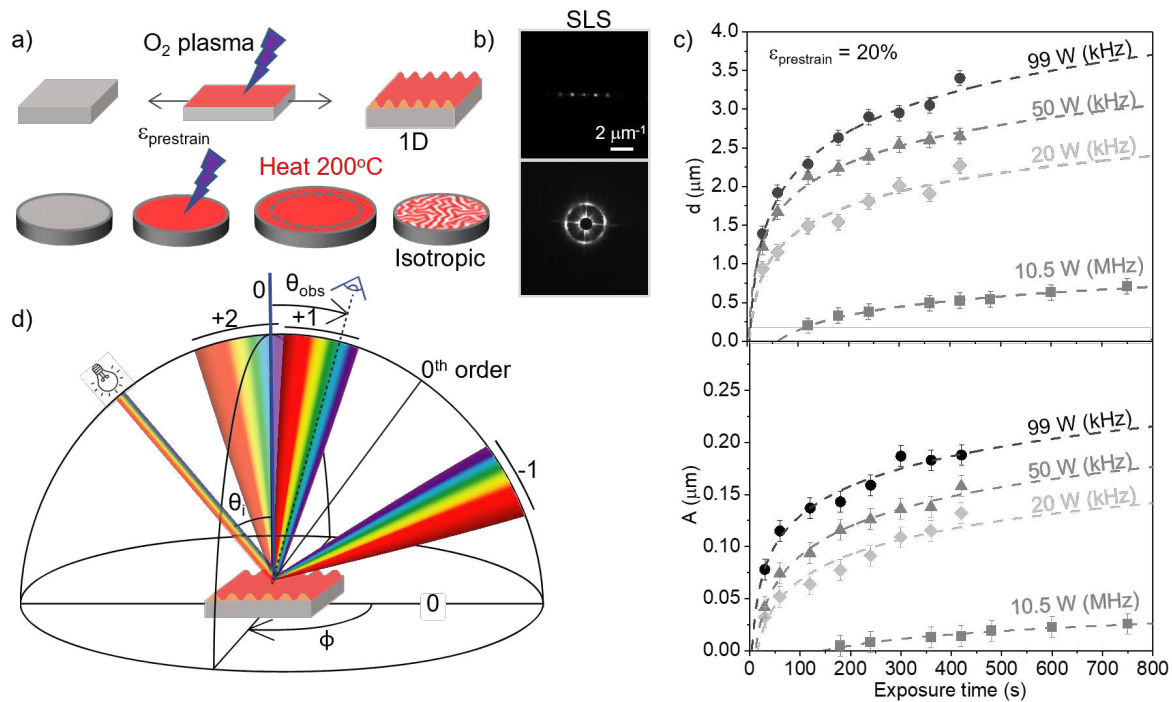


Figure 5.1: (a) Schematic of the formation of 1D and isotropic wrinkling samples. 1D wrinkles: plasma oxidation on a prestrained PDMS elastomer coupon and relaxation of strain. Isotropic wrinkles: plasma oxidation on a flat, round PDMS elastomer coupon, heated to 200° for 30 min to induce strain through thermal expansion, and cooled to induce the wrinkles. (b) Diffraction pattern for the 1D (99 W, 120 s) shows orders 0<sup>th</sup> to 2<sup>nd</sup> and a ring diffraction of 1<sup>st</sup> order for the isotropic (20 W, 120 s). (c) Wrinkling periodicity ( $d$ ) and amplitude ( $A$ ) measured as a function of plasma exposure time (s) for treated PDMS coupons with different power and plasma frequency (13.6 MHz: 10.5 W, 40 kHz: 20 W, 50 W, 99 W). (d) Schematic of light diffraction of wrinkled samples showing up to three orders (-1, +1, +2): a white LED light at  $\theta_i$ , observer/camera at  $\theta_{\text{obs}}$ .

Specifically, in this work we fabricate 1D structures by uniaxial mechanical strain, and isotropic structures by a thermal cycling treatment, expanding and contracting the bilayer as illustrated in Figure 5.1a. By diffracting a laser light, we have been able to observe that the periodic 1D surfaces respond as planar (tunable) 1D phase gratings [75, 120], displaying a series of point symmetric with respect to the direct beam (center), and their spacing in the reciprocal space reflects pattern periodicity in the real space. On the other hand, isotropic wrinkles yield

single-frequency centro-symmetric diffraction patterns, with a circular annulus reflecting the average pattern periodicity, as shown in Figure 5.1b. The experimentally measured logarithmic dependence of  $d$  and  $A$  on plasma exposure time [95, 96] for both a 13.6 MHz and 40 kHz plasma chambers employed in this work, is shown in Figure 5.1c.

In a 1D wrinkled sample, light diffraction occurs perpendicular to the direction of the wrinkles (Figure 5.1d). As the periodicity of the wrinkles increase, multiple orders of diffracted light can be seen. Positive orders are defined as those located between the incident light and the reflected  $0^{th}$  order, while negative orders are those located on the opposite side. The observation angle, denoted as  $\theta_{obs}$ , refers to the position of the observer or camera. By varying  $\theta_{obs}$ , we have been able to observe different structural colors. This allows us to examine the behavior of the wrinkled structures under different conditions.

## 5.2 Methodologies

### 5.2.1 Sample preparation

A carbon-black PDMS (CB-PDMS) (Sylgard 184, Dow Corning) substrate was prepared by casting a mixture of prepolymer, curing, and carbon black acetylene powder (50% compressed, 99.9+%, VWR) at a 10:1:0.03 mass ratio for 1D and 2D samples, and a mass ratio of 20:1:0.03 for isotropic samples. The mixture was stirred vigorously, degassed under vacuum, deposited onto a glass plate and cured at 75°C in a convection oven for 1 h to crosslink into an elastomer with the resultant CB-PDMS with a thickness of 2.5 mm.

Surface plasma oxidation of the samples were performed using two different plasma chambers: a 13.6 MHz Harrick Plasma PDC-002 at  $P = 10.5$  W for sub-micron wrinkle periodicity samples, and a 40kHz Diener Plasma (Femto), fitted with a pressure sensor (TM 101, Thermovac) at  $P = 20, 50, 99$  W and variable exposure times for samples with a larger wrinkle periodicity. Oxygen (BOC, 99.5%) supplied both plasma chambers. The chambers were evacuated to a pressure of

0.2 mbar, before flowing the gas for 5 min until the desired pressure was reached and stabilized. The plasma was then ignited, at the required power and exposure time.

1D, regular periodic sinusoidal patterns were fabricated through uniaxial strain of a PDMS coupon (2.5 cm × 2.5 cm) using a strain stage. The applied prestrain is calculated with respect to the initial ( $L_0$ ) and final distance ( $L_1$ ) between the clamps,  $\epsilon_{prestrain} = \frac{L_1 - L_0}{L_0}$ . The sample is stretched with a prestrain of 0.2, before it undergoes plasma oxidation and subsequently released to form sinusoidal wrinkles. Samples with a varying periodic structure were fabricated either a step-wise plasma oxidation or by changing the geometry of the sample to a trapezoidal shape. Isotropic samples were fabricated through the plasma treatment of an unstretched circular CB-PDMS coupon (2.5 cm radius) which then undergoes thermal heating to 200°C for 30 min and cooled to room temperature to form the isotropic wrinkles.

## 5.2.2 Material characterisation

The use of UV-Vis was employed to study the absorption of light in various concentrations of carbon-doped PDMS (0 - 5%/wt). UV-Vis spectrophotometer (Shimadzu UV-2600) was employed to measure the material's absorbances which was recorded using UVProbe software.

The carbon-doped PDMS of various concentrations was also measured for its elastic modulus using Lloyd EZ50 Tensile Strain Machine. These samples were prepared in the required specimen shape as discussed in Chapter 3.3 for testing.

## 5.2.3 Surface characterisation

Surface topographies were characterized by atomic force microscopy (AFM) using a Bruker In-nova microscope, in tapping mode at 0.2 Hz, equipped with Al-coated Si tips (MPP-11100-W, Bruker) and analysed with the in-built Nanoscope software. The diffraction patterns were obtained through static light scattering (SLS), using a 532 nm diode pumped laser (CrystaLaser). The mechanochromic phenomena were observed and recorded on an optical camera with a

white light source (Advanced Illumination) in a dark environment, which were then analysed with ImageJ software.

In this work, the intensity of the structural colour produced in the samples were measured indirectly through the optical images captured. The optical images were analysed using the software ImageJ. The desired area of structural colour was selected within ImageJ, and the intensity was obtained through measuring the integrated density of RGB/3.

### 5.3 Structural color from nano- to microscale wrinkles

Diffraction of white light from wrinkled surfaces, acting as phase gratings, can yield brilliant structural colors which depend on pattern periodicity  $d$  as well as observation angle  $\theta_{obs}$ . Depending on the plasma oxidation conditions and strain, the wrinkling periodicity and amplitude can be precisely tuned to select the color observed from the surface. The relation between pattern topography and observation diffraction angle, given by Eqn. 1.2 enables the prediction of the color wavelength  $\lambda$  at all angles,  $0^\circ \geq \theta_{obs} \geq 90^\circ$ , for instance when the incident white light is normal to the sample surface ( $\theta_i = 0^\circ$ ). Practically, beyond  $\theta_{obs} = 70^\circ$ , the observer's field of the surface becomes restricted. Figure 5.2a shows the first diffraction order for wrinkled surfaces with periodicities up to  $d = 800$  nm. When wrinkles display periodicities shorter than the wavelength of visible light, no color will be seen to be diffracted from the surface. In these regions, UV and X-ray diffraction could be accessed. MHz plasma oxidation allows for the fabrication of sub-micron structures, yielding single structural color diffraction at accessible observation angles. By varying the plasma exposure time,  $d$  ranging from 490 nm to 710 nm were achieved as shown in AFM micrographs in Figure 5.2b. The resulting diffracted colors were captured at different  $\theta_{obs}$ . For  $d = 490$  nm, diffracted wavelengths are limited to larger  $\theta_{obs}$ , where color is only accessible beyond  $60^\circ$  (Figure 5.2c(i)). As plasma exposure time increases, resulting in larger  $d$ , a red-shift is observed with  $\theta_{obs}$  with colors detected at lower observation angles. When  $d = 710$  nm, a red color can be observed for  $\theta_{obs} = 70^\circ$  (Figure 5.2c(iv)).

The structural colors are optimally observed by minimising light reflection and scattering from

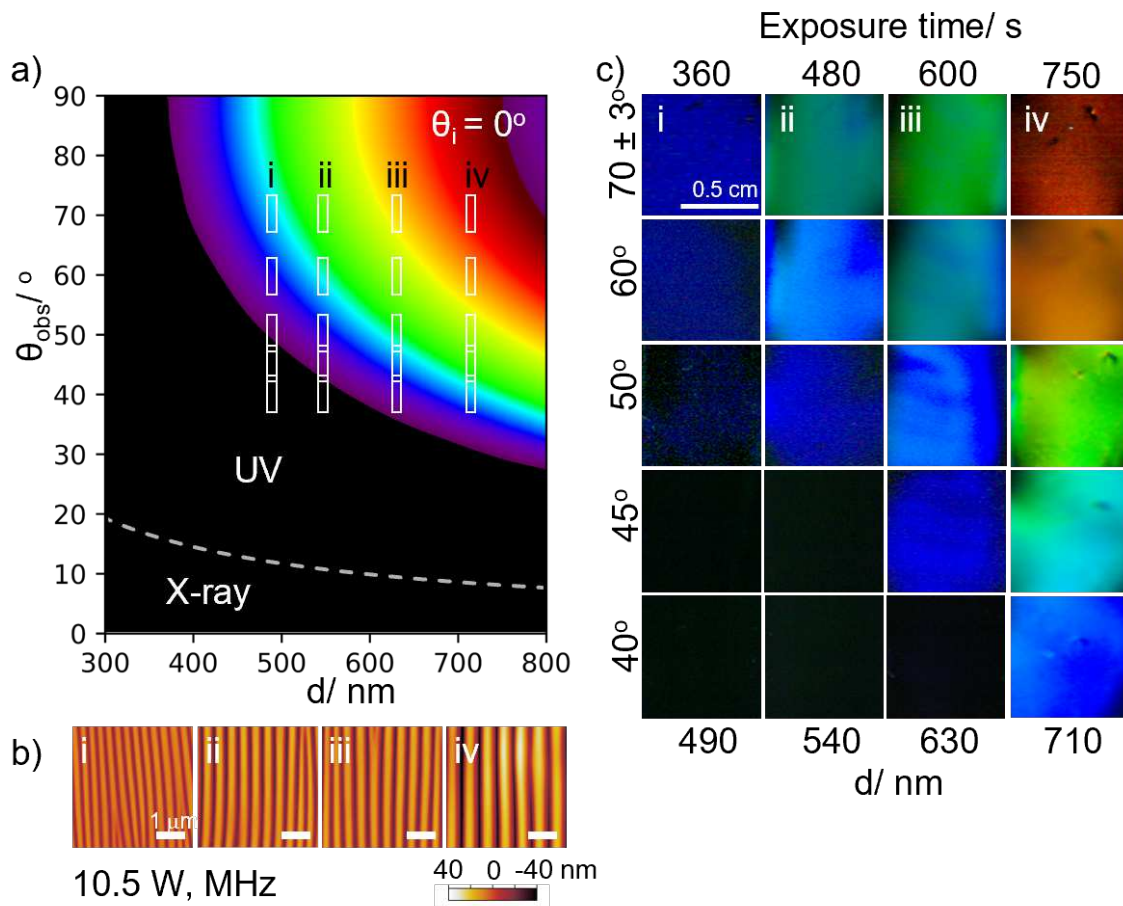


Figure 5.2: (a) Nano-wrinkled samples displaying discrete angular dependency of colors when white light is shone normal to the sample,  $\theta_i = 0^\circ$ . color observed in the first order with observation angle  $\theta_{obs}$  and wrinkling periodicity,  $d$  up to 800 nm. White boxes indicates the region of colors accessible ( $\pm 3^\circ$ ) for each sample (i-iv), at different  $\theta_{obs}$ , corresponding to Figure 5.2c. Below the threshold light wavelength of 380 nm, diffraction limits of UV and X-ray are reached. (b) AFM scans corresponding to the samples i-iv. (c) Single color diffraction observed in plasma-treated samples at exposure times of 360 s, 480 s, 600 s and 750 s yielding periodicities of 490, 540, 630 and 710 nm respectively.

the substrate. This can be achieved through doping the PDMS elastomer, for instance with carbon-black, resulting in uniform light absorbance in the visible range. The effect on optical and mechanical properties of PDMS doped with varying concentrations of carbon-black was investigated, by measuring the absorbance and elastic modulus of carbon-black PDMS (CB-PDMS). Carbon black is a convenient dopant as it absorbs uniformly across the visible range, and can be uniformly dispersed within PDMS, thus with high absorption and low scattering, allowing for excellent visualisation of structural colour. With increasing carbon-black concentration, the absorbance increases (Figure 5.3a) as a result of the increasing attenuation



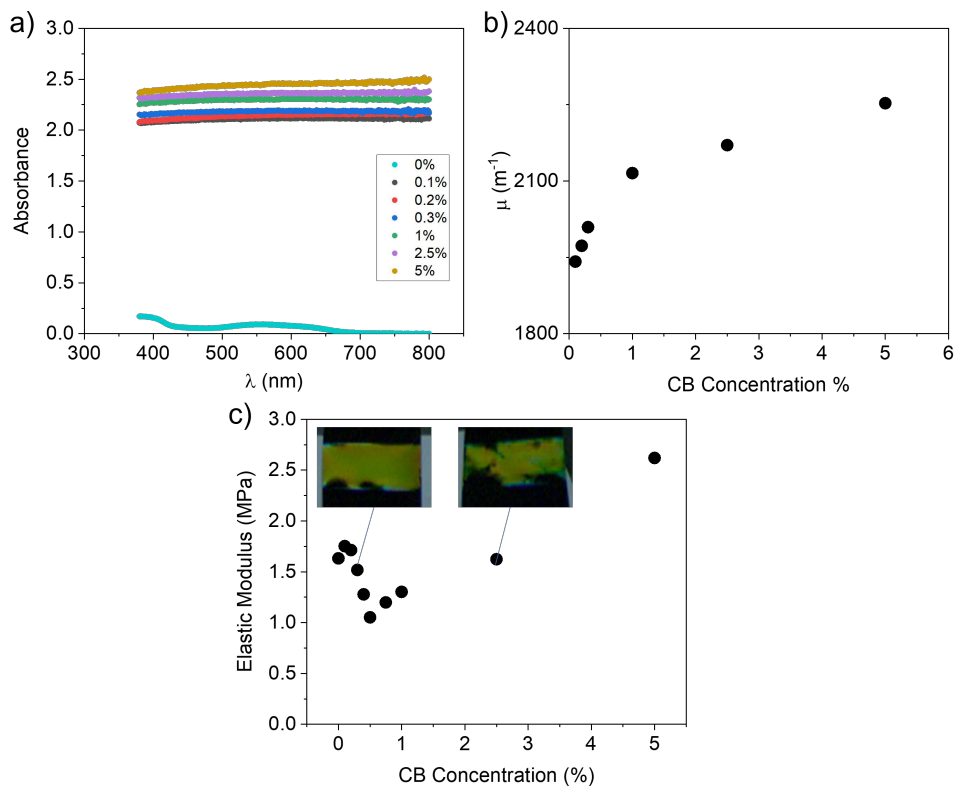


Figure 5.3: Effect of carbon black on PDMS: Absorbance (a) and attenuation constants (b) of PDMS with concentrations of carbon-black 0-5% measured with 2.5 mm thick coupons. (c) Elastic modulus of CB-PDMS with varying carbon-black concentration, measured with a Lloyd EZ50 Tensile Testing Machine. Comparison between 0.3% and 2.5% CB concentration showed insignificant color difference and similar modulus (1.6 MPa).

constant of the resulting material (Figure 5.3b). The addition of small amounts of carbon-black (0.1%) decreases the transmission of light by  $< 99.9\%$ . A carbon-black loading of 0.3% w/w is selected, as it yields a comparable elastic modulus to neat (clear) PDMS. When structural color is formed with CB-PDMS of different concentration, an indistinguishable difference in the diffracted colors can be observed. Measured intensity (RGB/3) of the color from 0.3 and 2.5% CB-PDMS measures to be 61 and 60 respectively. However, with increasing CB concentration, agglomeration and high viscosity prevents PDMS samples from forming uniform smooth surfaces.

In order to examine the impact of CB, wrinkled clear PDMS and CB-PDMS were subjected to white light illumination and compared, as shown in Figure 5.4. Due to the optical transparency of neat PDMS, the observed color is also dependent on its background, as shown in Figure 5.4 (top row). Clear PDMS placed on colored background results in observed colors that are

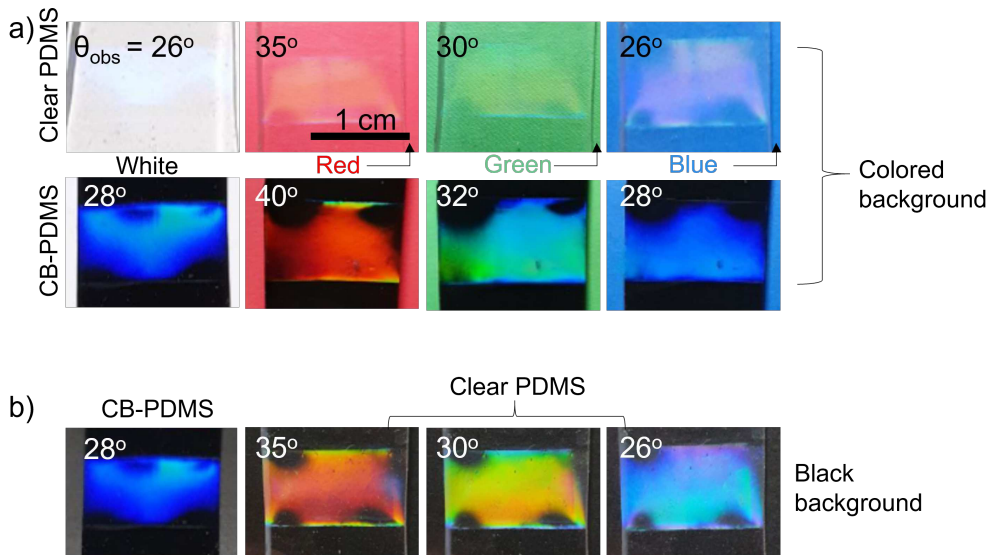


Figure 5.4: (a) Comparison of observed diffracted structural colour between clear PDMS (wrinkle periodicity  $\sim 1.1 \mu\text{m}$ ) and CB-PDMS (periodicity  $1 \mu\text{m}$ ) with different coloured backgrounds, and (b) black background. In all cases,  $\theta_i = 0^\circ$  and  $\theta_{obs}$  is indicated.

largely dominated by the background and the contribution from the additional, diffracted color is minimal. By contrast CB-PDMS is insensitive to the background color. In Figure 5.4b, PDMS and CB-PDMS are compared using a black background. Here, the reflected light is considerably suppressed allowing for the diffracted light (and thus ‘structural color’) in clear PDMS to be observed with high contrast. Again here, CB-PDMS is insensitive, exhibiting the same color regardless of colored or black background underlayer. As a result, the incorporation of carbon-black in PDMS yields more vibrant colors, regardless of background. In simple terms, CB effectively incorporates an absorbing, intrinsic ‘black background’ within the system.

In the case of micron-scale surface wrinkles, additional diffraction orders can be observed. The diffraction orders, initially discrete and well separated at low surface periodicities, start to overlap resulting in color mixing when  $d \gtrsim 1.1 \mu\text{m}$ . The color mixing arises from the contribution of different diffraction orders at the same  $\theta_{obs}$  at fixed periodicity. Figure 5.5a shows the expected resulting colors by taking into consideration diffraction order mixing (computed by expressing and combined each diffracted color in RGB format). Plasma oxidation at KHz, performed at 99 W at different exposure times, allows the development of  $d$  ranging from  $1.3 \mu\text{m}$  to  $3.4 \mu\text{m}$  (Figure 5.5b). The observed colors at varying  $\theta_{obs}$  are shown in Figure 5.5c, with the contributing orders labelled within each image. When  $d = 1.3 \mu\text{m}$ , single color diffraction

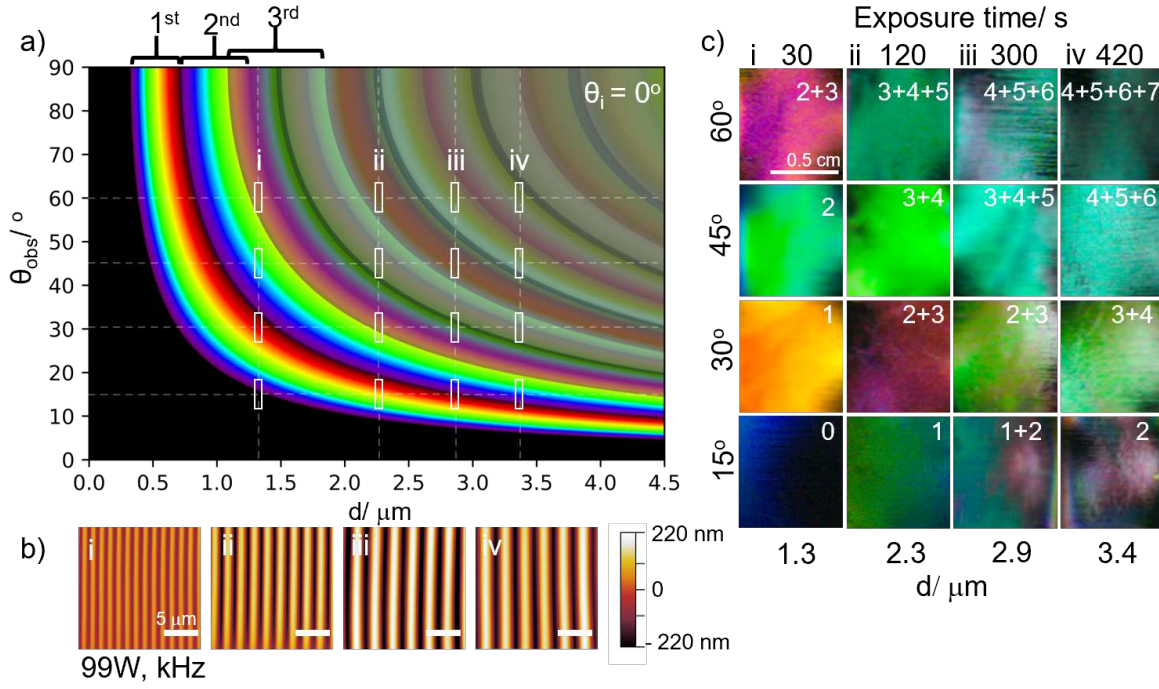


Figure 5.5: (a) Micro-wrinkled samples formed using 99 W, kHz plasma exhibiting colors contributed from up to 7 diffraction orders. From the 2nd diffraction order, overlap of different orders becomes prominent, resulting in mixed colors with increasing angles. (b) AFM scans corresponding to the samples i-iv. (c) color diffraction for plasma-treated samples at  $P = 99$  W and exposure time of 30, 120, 300 and 420 s yielding wavelengths of 1.3, 2.3, 2.9 and 3.4  $\mu\text{m}$  respectively. The diffraction orders contributing to the final color are reported at the top right corners of each condition.

is observed until  $\theta_{obs} \geq 60^\circ$  where the resulting “magenta” color is a contribution from the 2nd and 3rd order. As the wrinkle wavelengths increase, the overlap of two or more orders results in non-discrete colors.

From the previous chapter, it has been theoretically established that the diffraction intensities for colored wrinkled structures can be quantified for each order modifying Eqn. 4.2 to account for the gradient glassy skin [120]:

$$I(\bar{x}, y) \approx \sum_{i=0}^8 A_0 e^{-kn_i} I_{ni}(x, y) \quad (5.1)$$

where  $n_i$  ranges 1.41 to 1.55,  $A_0 = 8.0 \times 10^{18}$  and  $k = 31.5$ . From this, we use the relationship between exposure time with  $d$  and  $A$  to get an intensity plot, which is also dependent on the wavelength of light  $\lambda$ . We would expect that for a given condition and diffraction order, the in-

tensity of a longer wavelength of light like red light (760 nm) would have a lower intensity than a violet light (380 nm). In Figure 5.6, the theoretical dependence of diffraction intensities with exposure time for different wavelengths of light - from violet of 380 nm to red of 760 nm are plotted for the first order. Assuming that the incident white light has uniform intensity across the visible range, the intensity of the color for the first order can be modelled according to Eqn. 5.1. Increasing exposure time, increases the surface wrinkle periodicity and amplitude accordingly. By using the equation with corresponding  $d$  and  $A$  at each exposure time  $\tau$ , it follows that shorter wavelengths of light (violet,  $\lambda = 380$  nm) exhibit considerably higher intensities than those of longer wavelengths (red,  $\lambda = 760$  nm), as shown in Figure 5.6. The intensity for larger wavelength of light are lower and the intensities can be seen to modulate with exposure time, as a result of the evolution of wrinkling periodicity and amplitudes.

In the event that color mixing occurs due to the contributions from multiple orders, the intensity of colors arising from the different orders can be computed in a similar manner. In Figure 5.6b we plot the intensities of green light (533 nm) up to the 6th order. For a single wavelength of light, one expects higher orders to have lower intensities than a lower order. However, due to the spread of intensities with one order from red to violet, higher orders exhibit an overlap of intensities, which would mean that a violet from a 6th order would have higher intensity than a red in the 5th order, for example.

### 5.3.1 Mechanochromic response: tuning colors with strain

The mechanochromic response of wrinkled surfaces can be tuned modulating the compressive strain release after the plasma oxidation step. The sensitivity in color variation can be adjusted by considering the relationship between pattern periodicity  $d$  and strain, ensuring that only the first diffraction order ( $n = 1$ ) contributes at the accessible  $\theta_{obs}$ . For a range of applications, including strain sensing, avoidance of color mixing is desirable. This requires a selection of a  $d$ -range appropriated for the intended  $\theta_{obs}$ . The dependence of diffracted color on  $\theta_{obs}$  and  $d$ , depicted in Figure 5.7, can be used to select adequate surface periodicity and the window of strain (or  $d$ ) of interest. Figure 5.7 illustrates that for a system that experiences small  $d$

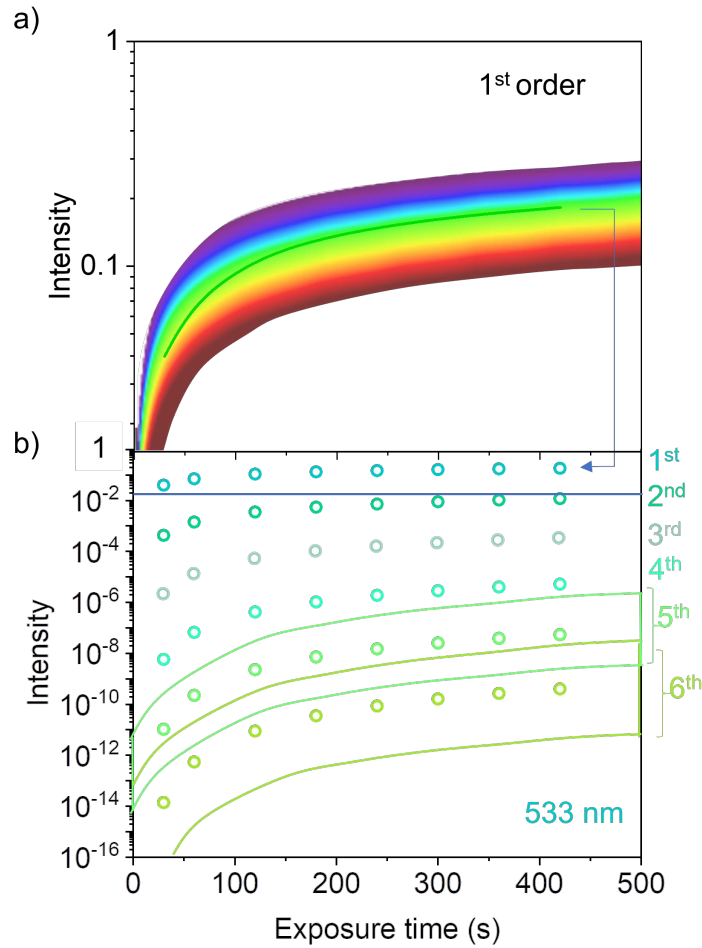


Figure 5.6: (a) Intensity of the first diffraction order with increasing plasma (99 W, 40 kHz, O<sub>2</sub>) exposure time, exhibiting higher intensity for shorter wavelengths of light, and lower for longer wavelengths (i.e. from purple to red). (b) Intensity of up to 6 orders of diffraction computed for green light ( $\lambda = 533$  nm).

changes, a low  $d$  value and high  $\theta_{obs}$  would give optimal strain response. Conversely with larger periodicity changes, sensing would be optimal with surfaces of larger  $d$  at lower  $\theta_{obs}$ . with larger  $d$  changes, a large  $d$  and small  $\theta_{obs}$  should be used. The design of such responses can be tuned by changing the plasma conditions, where the bilayer film parameters can be designed to achieve the appropriate periodicity range through altering  $h$  and  $E_f$ .

The observed color at a given  $\theta_{obs}$  can be readily calculated as a function of strain  $\epsilon$ , by combining Eqn. 1.2 and 2.4 to yield:

$$\lambda = \frac{2\pi h (\bar{E}_f / (3\bar{E}_s))^{1/3}}{(1 + \epsilon)(1 + \xi)^{1/3}} \sin\theta_{obs} \quad (5.2)$$

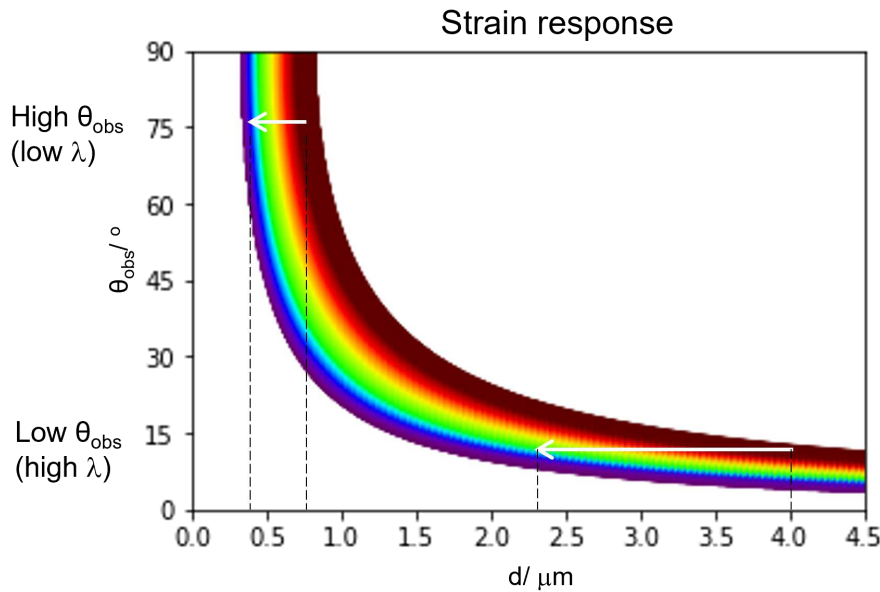


Figure 5.7: Color map depicting the dependence of diffracted color with  $d$  and  $\theta_{obs}$ . Small changes in  $d$  can optimally be monitored at high  $\theta_{obs}$  while large changes in  $d$  at low  $\theta_{obs}$ .

Specifically, Figure 5.8a reports the color shifting from red (buckling onset) to blue (full release) as function of compressive strain  $\varepsilon$  for a sample treated at  $P=50$  W and  $\tau=30$  s and prestrained to 0.5. At a fixed  $\theta_{obs}$ , the diffracted color observed can be manipulated by a change in the wrinkling periodicity,  $d$ . When  $\theta_{obs} = 31^\circ$ , the spectrum of the rainbow can be observed when  $d$  is tuned between 0.9 to 1.5  $\mu\text{m}$  as described in Figure 5.8b. Due to the intrinsic nature of the buckling relaxation process and as described by Eqn. 2.4, we are able to exploit this relationship to create tunable colors with strain. The decrease of the wrinkling periodicity with strain fulfills the required range to tune the sample to the color of the spectrum. As the sample experiences compressive strain the wrinkling amplitude increases with strain, therefore it is possible to determine the theoretical relationship with diffraction intensity through the previously established diffraction model in Eqn. 5.1.

Following the ability to tune the wrinkling periodicity and amplitude with strain, we would expect the sample to experience a continuous increase in intensity from red to blue (Figure 5.6). However, this model alone assumes an equal intensity of the white light at all wavelengths, and it is thus insufficient to explain the intensity exhibited by the samples at their respective colors. Unsurprisingly, there is an effect on the intensity of the light source with the resultant intensity of the color observed. Therefore, modelled color intensity was parametrized by the

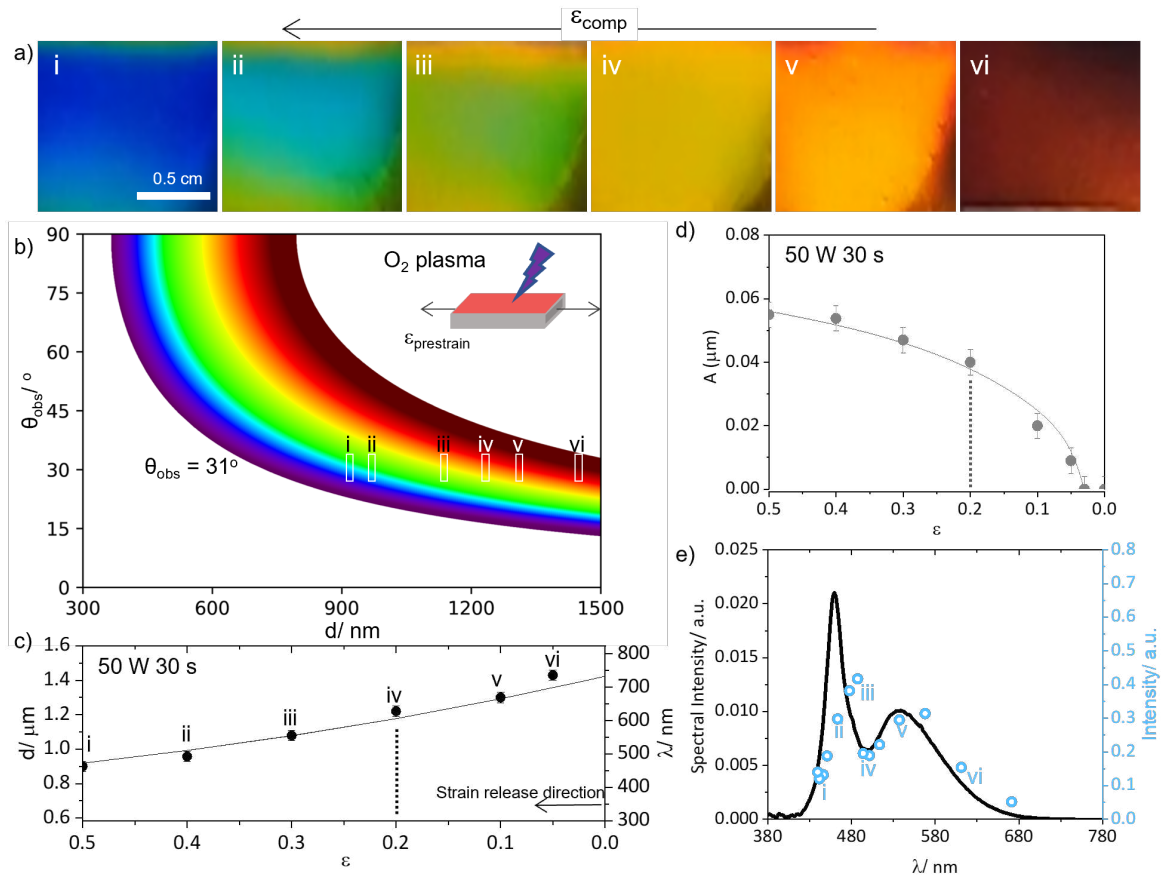


Figure 5.8: (a) Mechanochromic variation in CB-PDMS samples oxidized at 50W 30s undergoing compressive strains from i  $\epsilon = 0.5$  to vi  $\epsilon = 0.05$ , at  $\theta_{obs} = 31^\circ$ . (b) First order colors observed at wrinkling periodicity from 300-1500 nm. Series of colors in the first order observed from  $\lambda \approx 700$  nm (red), when  $d \approx 1.4 \mu\text{m}$ , to  $\lambda \approx 450$  nm (blue), when  $d \approx 900$  nm. White boxes i-vi corresponds to the color areal region reported in Figure 5.8a. (c) Wrinkling periodicity,  $d$  as a function of strain for samples i-vi. The solid line corresponds to Eqn.(6.1). Each  $d$  corresponds to an observed diffracted wavelength,  $\lambda$  on the right y-axis. (d) Amplitude of wrinkles as a function of strain with the solid line corresponding to Eqn.(6.2). (e) Calculated diffracted intensity (black line) as function of  $\lambda$ , parametrized by the white light and CB-PDMS absorbance across the spectrum. Measured intensities (blue points) were extracted via RGB decomposition (RGB/3) of i-vi.

light spectrum and the absorbance of the CB-PDMS in the required range.

Figure 5.9 shows the spectrum of the white light, which has a non-uniform intensity across the visible spectrum of light, with 2 peaks around  $\lambda = 460$  nm and 580 nm. The UV-Vis absorbance of CB-PDMS were performed at different thicknesses, from 1.0 - 3.0 mm. Initially as the thickness increase, the absorbance increases accordingly. However the absorbance value reaches a plateau with increasing thickness past 2.0 mm. Absorbance value for thickness of 2.5 mm is taken into consideration in the final modelling of intensities. From Figure 5.8c, the expected



wavelength of light can be calculated with each  $d$  and hence  $A$ . As a result, the corresponding  $d$  and  $A$  can be inserted into Eqn. 5.1, yielding the intensities for each wavelength.

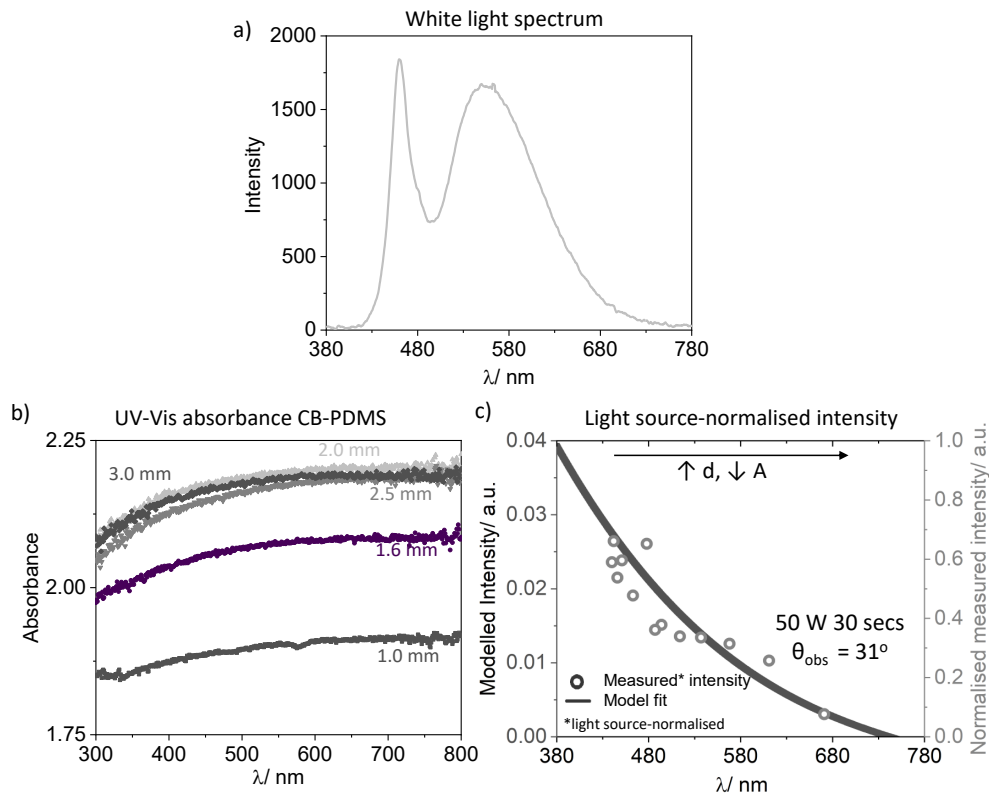


Figure 5.9: (a) Light spectrum of incident white light (b) UV-Vis absorbance of carbon-black doped PDMS (CB-PDMS) of different thickness, from 1.0 mm to 3.0 mm (c) Intensity expected for each wavelength of light, independent of light source spectrum, as the sample exhibits colour response with mechanical strain.

By normalising the light spectrum and absorbance, combining with the previous description, we attain the final model. The intensity of the samples were taken by normalizing the RGB values to 1 through ImageJ. From Figure 5.8e, we find that the experimental results agree well with the model, taking into account the spectrum of the light source. The experimental results can also be normalised with respect to the light source to obtain the data in Figure 5.9c, where the trend of intensities with wavelength agree with the model.



### 5.3.2 Effect of relative illumination and viewing angles on colour perception

So far, we have only considered cases for when incident light is normal to the sample. With this condition, the range of observed structural colour is limited. To explore a larger range of colours being exhibited in the nano-scale samples, the variation in incident angle of light with respect to the sample can be implemented.

When the angle between the incident light and camera is fixed at  $50^\circ$  with the sample being rotated along its axis, this allows for the simultaneous change in  $\theta_i$  and  $\theta_{obs}$  as reported in the schematic in Figure 5.10a(i-iii). By using Eqn. 1.3, we can predict the color wavelength while rotating the sample. Conventionally, when  $\theta_{obs}$  and  $\theta_i$  are on opposite sides with respect to the normal,  $\theta_{obs}$  would be denoted as a negative angle. When a plasma treated sample with wrinkling periodicity of 490 nm is observed at  $\theta_{obs}$  with a simultaneous change in  $\theta_i$ , color wavelengths up to  $\approx 650$  nm in the first order can be viewed between  $50^\circ \leq 70^\circ$ , while no color can be seen at other angles (Figure 5.10a). By changing the incident light angle, the sample can exhibit up to a yellow hue when  $\theta_i = 70^\circ$  (Figure 5.10b), compared to the limited accessibility in color when  $\theta_i$  is fixed at the normal, where only blue can be accessed at higher viewing angles (Figure 5.2c(i)). For  $d$  of 630 nm, 3 distinct orders (-1, +1, +2) can be observed while rotating the sample such that  $0^\circ \leq \theta_i \leq 70^\circ$ . Between  $8^\circ < \theta_i \leq 44^\circ$ , no color can be observed. At  $0^\circ \leq \theta_i \leq 8^\circ$ , the -1<sup>st</sup> order can be seen, the +1 order at  $44^\circ \leq \theta_i \leq 70^\circ$  and +2 order at  $68^\circ \leq \theta_i \leq 70^\circ$ . (Figure 5.10c). As a result, up to a red hue at  $\lambda = 760$  nm is observable when  $\theta_i = 70^\circ$  and  $\theta_{obs} = 20^\circ$ , as compared to a green visible when  $\theta_i$  is fixed at  $0^\circ$  (Figure 5.2c(iii)).

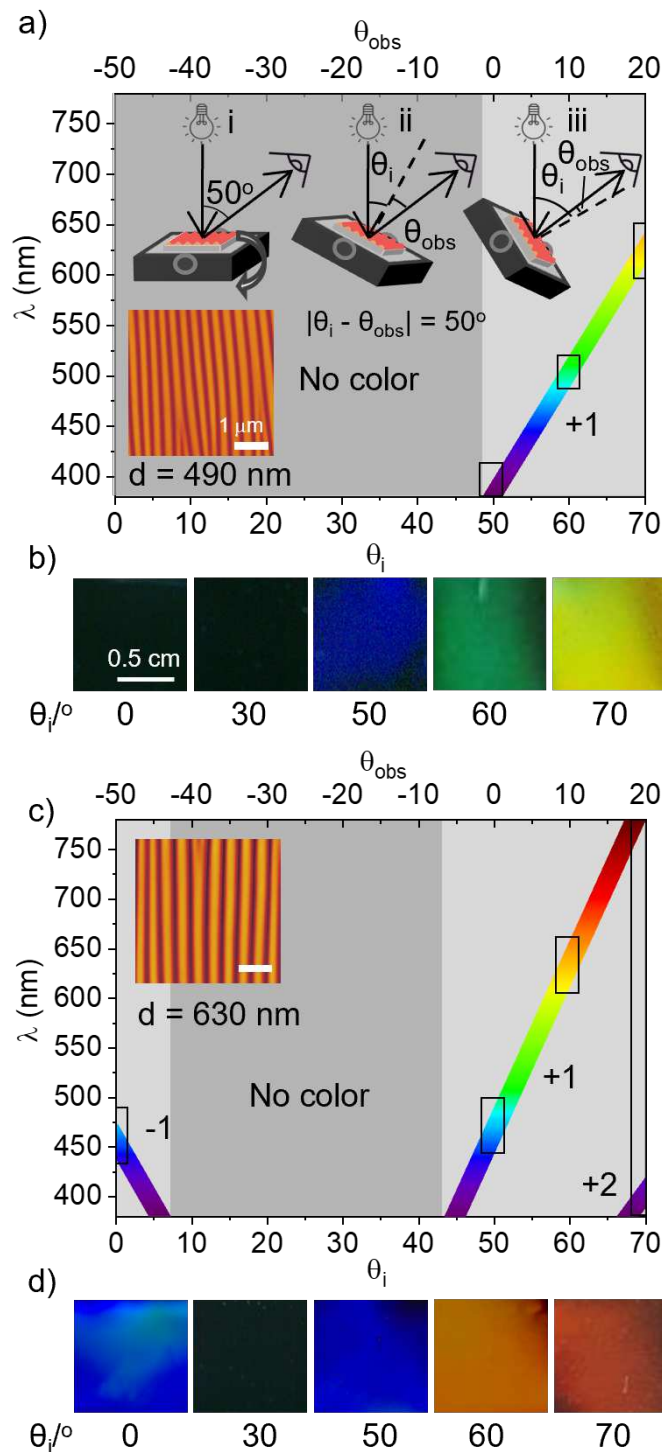


Figure 5.10: (a) Color variation observed changing simultaneously  $\theta_i$  and  $\theta_{obs}$ , for a MHz plasma-treated sample at 10.5 W, 360 s yielding  $d$  of 490 nm. (b) Images of sample showing increase range of accessible wavelength diffracted compared to in Fig. 5.2c(i) with blue color observed at 50° while yellow at 70°. (c) Color variation observed on a sample for MHz plasma-treated sample at 10.5 W, 600 s yielding  $d$  of 630 nm. Light can be observed to be diffracted in -1 order from 0° to 6°, +1 order from 45° to 68°, and +2 order from 68° to 70°. (d) Images of sample showing corresponding diffracted colors.

### 5.3.3 Azimuthal viewing angle and color of 1D and isotropic wrinkles

1D surfaces have structural colors limited to the direction of diffraction. When a 1D sample (kHz, 99 W, 60 s) is rotated about  $\phi$  ( $\theta_i = 0^\circ$ ,  $\theta_{obs} = 40^\circ$ ), the intensity of the colored sample can be monitored and observed as function of the angle as showed in Figure 5.11a. When  $\phi = 0$ , the intensity of the sample, measured by  $(R+G+B)/3$  can be seen at a maximum. As  $\phi$  increases, the intensity can be seen to decrease until it reaches a minimum at  $\phi \approx \pi/6$ . (Figure 5.11b) This occurs when the direction of diffraction of the sample becomes out of line with the observer. As the diffraction of sinusoidal wrinkles are perpendicular to the wrinkle direction, this only allows observance of the color in 1 axis with respect to the sample. (Figure 5.11c) The inset shows the 1<sup>st</sup> diffraction order pattern of a 1D structure.

In order to increase the viewing angle of structural colors, isotropic wrinkles can be employed. When an isotropic sample is fabricated under the same plasma conditions, it exhibits structural color as the sample rotates  $2\pi$  about  $\phi$ . The intensity (a.u.) of the color was measured to be comparatively lower between 40-60° while undergoing rotation, displaying color at every  $\phi$  ( $\theta_i = 0^\circ$ ,  $\theta_{obs} = 40^\circ$ ) as reported in Figure 5.11d. These isotropic structures have a ring diffraction pattern, diffracting light in all directions. Due to the light being diffracted in all directions, the line diffraction pattern is of a much lower intensity than the peaks in the 1D. An azimuthal average measurement can be used to clearly show the comparison between the two structures. In the 1D diffraction, 2 distinct intensity peaks are seen, reflecting the position of structural color observation. In the isotropic sample, the azimuthal average stays relatively constant, with structural color reflected about  $2\pi$  of  $\phi$ .

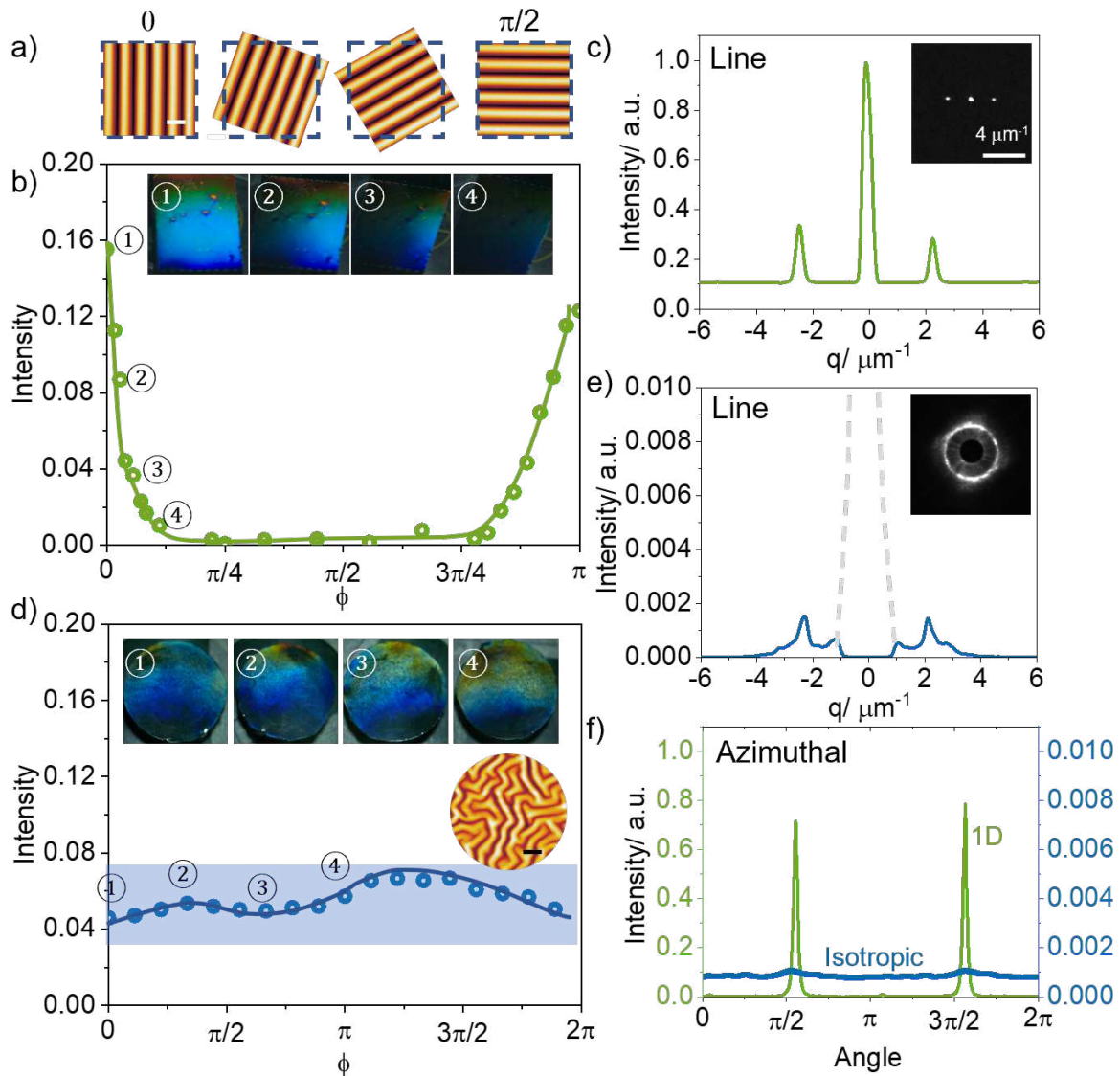


Figure 5.11: (a) Schematic of the rotation of wrinkled sample along  $\phi$  (b) Plot of normalized intensity for a 1D sample (kHz plasma, 99W, 60 s) with  $\phi$  shows a decreasing intensity from 0 to  $\pi/6$ . (c) The 1D diffraction pattern intensity where  $0^{\text{th}}$  and  $1^{\text{st}}$  diffraction orders are shown, with the light scattering image shown in the inset. (d) Plot of normalized intensity for an isotropic sample (kHz plasma, 99W, 60 s) when rotated along  $\phi$ . (e) The diffraction intensity of isotropic diffraction along a line. The grey dotted line reflects the middle beam where a beam stop was used. (f) Azimuthal averages for 1D and isotropic diffraction patterns. In the 1D diffraction, 2 intensity peaks are seen which reflects the positions of observed structural color. In the isotropic, the azimuthal average stays relatively constant range of 0.001, reflecting structural color  $2\pi$  about  $\phi$ .

### 5.3.4 Homogeneity and directional color

An implication arising from the fabrication of regular 1D wrinkling structures with homogenous wrinkling periodicity is a characteristic “rainbow” color perceived especially for large areas,

which is enhanced at a close observation distance. As the colors viewed are sensitive to  $\theta_{obs}$ , a small change can lead to different colors being seen at a single wrinkle periodicity. The spread of color occurs as the light reaching the observer has different viewing angles from the top and bottom of the sample ( $\theta_{obs1}$  and  $\theta_{obs2}$  respectively), thus yielding different wavelengths ( $\lambda_1$ ,  $\lambda_2$ ). (Figure 5.13a). The respective  $\theta_{obs}$  can be calculated with respect to the position of the observer:

$$\theta_{obs1} = 90 - \arctan \frac{L}{h} \quad (5.3)$$

$$\theta_{obs2} = 90 - \arctan \frac{(L-W)}{h} \quad (5.4)$$

where h and L describes the vertical and horizontal position of the observer, and W the distance between the observed reflected light.

Conversely, it is possible to create a variable structure to create local spatial periods required to only see a specific color, depending on the position of the observer. Previously, Voisiat *et al.* have demonstrated that the homogeneity of large samples can be improved through creating varying periodic spacing using Direct Laser Interference Patterning [151]. The resulting periodicity gradient can produce a distinct diffracted wavelength of light at a given angular range. The spatial period change required to produce a single color can be calculated, from the incidence angle of the light source and the position of the observer.

$$d = \frac{n\lambda}{\sin\theta_i - \sin\theta_{obs2}} \quad (5.5)$$

where  $\theta_i$  is the incident angle and  $\theta_{obs2}$  is the observer angle.

Using the color plots, the expected color for varying periodic structures can be predicted and designed, as illustrated in Figure 5.12. When variable periodic samples are viewed at  $45^\circ \leq \theta_{obs} \leq 55^\circ$  (corresponding to sample of 50 mm viewed at a distance of  $\sim 12$  cm) with a wavelength of 700-900 nm, either a homogeneous color or a "rainbow" effect can be obtained.

The arrow in Figure 5.12(a) shows the expected color path for decreasing  $d$  with increasing  $\theta_{obs}$  and conversely in Figure 5.12(b), for a gradient with increasing  $d$  and increasing  $\theta_{obs}$ .

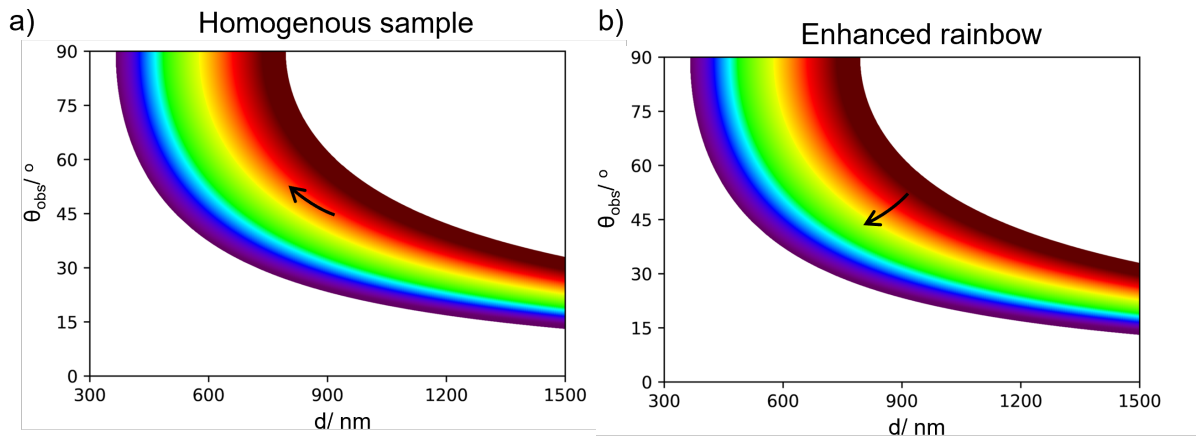


Figure 5.12: Plot of 1<sup>st</sup> order colors observed with wavelengths up to 1500 nm. Schematic arrows showing color along sample with periodicity ranging from 700-900 nm at 45-55°, with increasing  $\theta_{obs}$  a (a) homogeneous sample when viewing with decreasing  $d$  (b) enhanced rainbow when viewing with increasing  $d$ .

In the two methods employed, no significant variation of the wrinkling amplitude was observed, thus with a negligible impact on the color intensity. For the first approach, here referred to as step-wise plasma oxidation, different sections of the same area treated at different exposure times, yielding varying periodicities and amplitudes. Increasing the plasma exposure time increases the film thickness and accordingly the pattern periodicity and the amplitude. Lee et al. [152] reported the fabrication of stepwise gradient wrinkles by placing glass plates onto stretched PDMS. The glass plate partially blocks the oxygen plasma and by varying the plasma exposed region in each step the gradient in the film thickness is generated. However, a sharp discontinuity is induced between two adjacent regions of discrete periodicities. Based on the findings reported by Hiltl and co-authors [153], the discontinuity in periodicity and amplitude along the sample can be minimised by increasing the distance of the glass plates from the PDMS substrate.

Figure 5.14 describes the fabrication process to achieve variable wrinkle structure through sequential plasma exposure by the partial covering of PDMS using multiple glass slides. PDMS coupon of length 3.5 cm, 1 cm wide, and 0.25 cm thick was subjected to a strain of 20% and exposed to plasma by partially shielding with four glass slides and reducing the number of slides

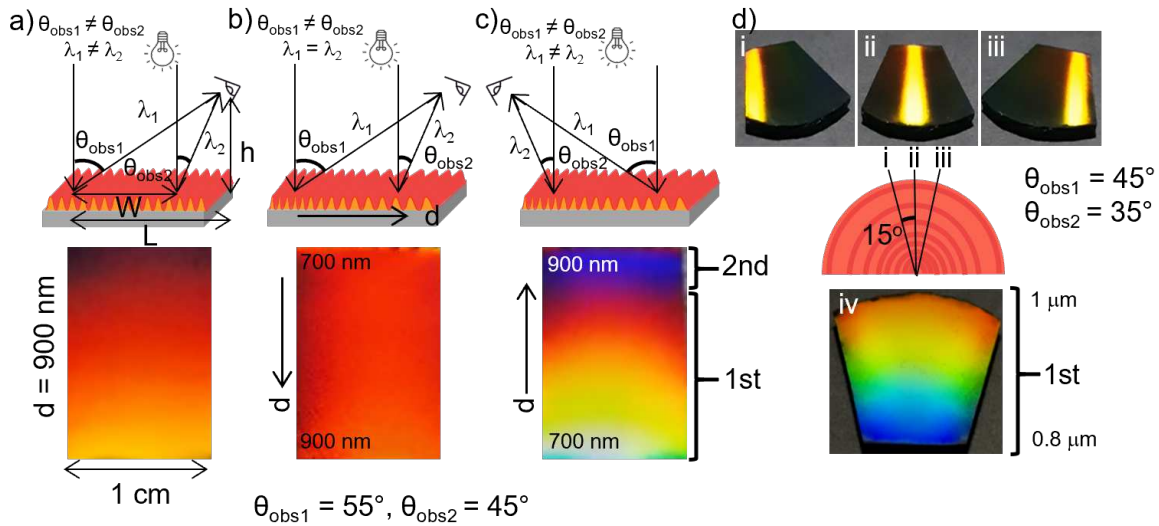


Figure 5.13: Structural color behaviour at various observation angles for (a) a 1D wrinkle surface, displaying a heterogeneous colored surface; (b) Step-wise gradient 1D wrinkles, observed from the longest periodicity ( $d=900$  nm), showing a homogeneous red color; (c) The same sample in (b), observed from the shortest periodicity ( $d=700$  nm), exhibiting an accentuated “rainbow” effect; (d) Samples prepared employing geometric graded coupons, exhibiting curved wrinkles directional color when rotated about  $\phi$ . (i), (ii), (iii) show homogeneous strips of yellow while (iv) showing a ‘rainbow’ effect.

after each step. The plasma exposure was carried out in 40 kHz Diener Plasma (Femto) at power 50 W and an oxygen pressure of 0.5 mbar. The first four steps of sequential plasma exposure are responsible for the gradient in film thickness, where the PDMS is exposed to plasma for a short duration of 15 s and after each exposure a glass slide is removed to increase the PDMS exposed area. Plasma exposure is performed for 100 s on unshielded PDMS slide to induce significant film thickness for wrinkle formation in the most shielded region. Subsequent removal of strain results in gradient wrinkles ranging from  $\approx 700$  nm to 900 nm in periodicity. When a stepwise sample (Figure 5.14) is viewed from a position with  $L = 10$  cm,  $W = 3$  cm and  $h = 7$  cm, this gives rise to  $\theta_{obs1} = 55^\circ$  and  $\theta_{obs2} = 45^\circ$ . The result wrinkle periodicities ranging 700 nm to 900 nm, viewed from the end of the sample with largest periodicity, exhibits a homogeneous red color spanning the sample can be observed as  $\lambda_1 = \lambda_2$ . Conversely, when the same gradient structured sample is viewed from the other end of the sample, the ‘rainbow’ effect of colors are accentuated, where the periodic change leads to an even greater variation in color observed.

The second approach allows for the fabrication of varying periodic structure by altering the geometry of the stretched sample, by using a trapezoidal shape for example (Figure 5.15). Gra-

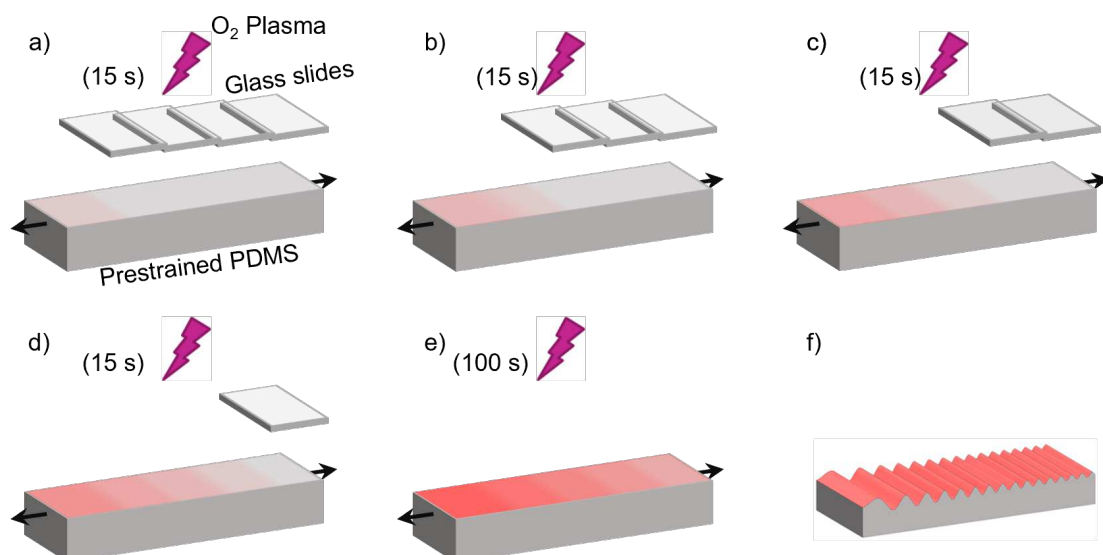


Figure 5.14: (a-d) Prestretched PDMS undergo short plasma exposures (15 s, 40 kHz, 50 W, 0.5 mbar) with increasing exposed area by removing a glass slide, (e) followed by a longer plasma exposure (100 s, 40 kHz, 50 W, 0.5 mbar). (f) Variable periodic structure with increasing periodicity and amplitude achieved upon relaxation of strain.

dient wrinkling topographies can be induced either tuning the thickness of the exposed glassy skin generated by plasma oxidation or by applying a gradient strain field, changing the geometry of the sample and therefore altering the strain components. Previously, Raayai-Ardakani et al. [154] demonstrated that the wrinkling of a polystyrene film on a graded PDMS coupon can achieve varying periodicity and amplitudes across a sample. Here, we employ the same principle for a plasma-oxidation of a pre-strained trapezoidal PDMS sample. Due to the strain distribution of the sample, there is a higher strain region close to the shorter side of trapezoid, and conversely a smaller strain region towards the larger side. From the bilayer model equations in the high deformation regime, a higher strain results in a larger amplitude but lower periodicity. This induces a torsional strain field that is reflected in a curvature of the wrinkling pattern. The sample experiences a higher strain at the narrow side, and lower strain on the wider side. The overall pattern can be rationalized as a damped sine wave evolving from the narrow side, or higher strain region. As a result, the amplitude decreases with the increase in the periodicity of wrinkles, yielding the wrinkle structure obtained in Figure 5.15a. PDMS coupon was obtained by cutting a trapezoid from an isosceles triangle having an apex angle of  $30^\circ$ . The distance between the parallel sides of the trapezoid was 3.5 cm and the length of the shorter side was 2 cm. This trapezoidal sample when stretched and exposed to plasma treatment for 50 W, 90



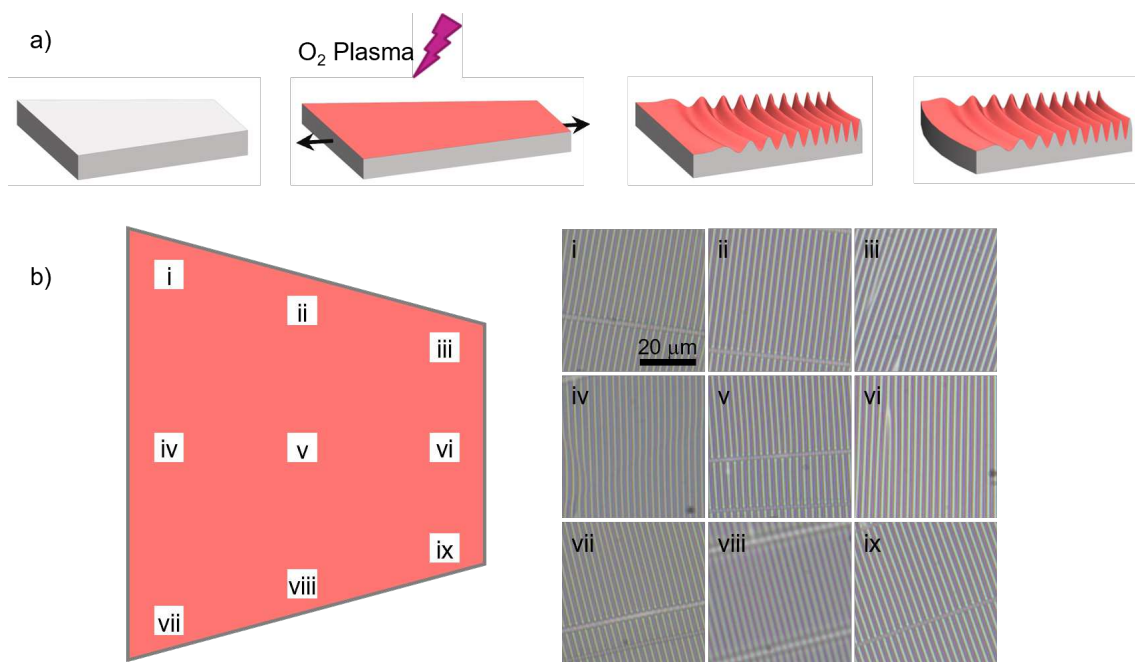


Figure 5.15: (a) Directional wrinkles with a gradient in periodicity and amplitude fabricated by plasma oxidation of a prestretched trapezoidal PDMS coupon. (b) Optical images acquired in different regions of the wrinkled trapezoidal PDMS, exhibiting induced curvature and directionality.

s at 0.5 mbar resulted in periodicity spanning from  $\approx 800$ -1000 nm and amplitudes of 60-40 nm, from the long to short side respectively. Additionally, the non-uniform direction of stress across the sample results in the curvature of wrinkles. The curvature of the wrinkles can be manipulated by changing the apex angle of the original isosceles triangle. The trapezoid coupons were further trimmed from the longer side to form a circular arc. In order to view the curvature optically under the microscope, larger periodicity of  $\approx 2.5 \mu\text{m}$  on the same geometric gradient sample were fabricated by undergoing plasma treatment for 50 W, 5 mins at 0.2 mbar (Figure 5.15b). From the microscope images, it is apparent that there is curvature at the edges of the sample (i-iii, vii-ix), while the middle of the sample has straight wrinkles.

The curve graded wrinkles display directional structural color, as the 1D wrinkles can only diffract perpendicular to the wrinkling direction (Figure 5.13d). When the wrinkles are convex with respect to the viewer, the sides of the sample are such that it diffracts color out of plane with respect to the centre of the sample. Strips of homogeneous color can be manipulated and seen dependent on the viewing angle  $\phi$ . When  $\phi = 0^\circ$ , a strip in the centre can be seen (Figure 5.13d(i)). Upon rotation of  $\pm 15^\circ$ , the strip of color can be seen to move towards the

edge of the sample (Figure 5.13d(ii, iii)). When the sample is positioned such that the wrinkles concave with respect to the viewer, the diffraction of the wrinkles converge onto the viewer and a ‘rainbow’ effect can be seen to be exhibited by the entire sample (Figure 5.13d(iv)).

## 5.4 Conclusion

In this chapter, we have demonstrated the generation of both simple and intricate tunable structural colour response in 1D and isotropic wrinkling patterns, fabricated by plasma oxidation of PDMS and mechanical or thermally-induced buckling. Our main findings are as follows:

- By using carbon-doped PDMS, the fabrication of wrinkles on this surface can produce brilliant structural colours on the surface, minimising the scattering of light. We benchmark and quantify the impact of surface periodicity of 1D wrinkling structures, in both nano and micron scales, on accessible colours. The effect of colour mixing induced by overlap of multiple diffraction orders were evaluated, showing that micro-wrinkles exhibit non-discrete structural colours.
- Quantitative relations between color intensity, the interplay between illumination and viewing angles were established, accounting for the wrinkling mechanics and diffraction phenomena.
- Owing to the nature of the gradient glassy skin, the model incorporates a gradient refractive indices to reflect this, alongside the established phase grating optics system, to quantitatively model the intensity of the various diffraction orders.
- The effect of complex topographies on the structural color response, inducing a gradient in pattern periodicity and amplitude by either tuning the glassy skin thickness (via stepwise exposure) or by inducing gradient strain field (via a non-rectangular sample geometry, e.g. trapezoidal) were investigated. The facile method of plasma-oxidised PDMS allows for the simplicity in surface patterns exhibiting either spatially uniform colour or enhanced ‘rainbow’ colour, depending on the observation angle.

- Structural colour of isotropic wrinkled surfaces exhibiting color at all  $\phi$  angles, i.e. ‘around’ the patterned surface were studied. Isotropic surfaces can overcome the limitations in directionality of 1D surfaces.

# Chapter 6

## Structural colour through TIR

The work presented in this chapter has been published in *Molecules* 2023, 28(4), 1710 under Special Issue Polymeric Photonic Materials [155]. Co-author Zain Ahmad assisted with the fabrication of GRISMs in this work. Fruitful discussions with Prof. Pete Vukusic helped in the direction of spectroscopy measurements and analysis of the work.

### 6.1 Introduction

Naturally occurring materials exhibiting structural colour generally often exhibit colour and colour modulations across multiple viewing angles. By contrast, colour generated from surface diffraction is directional, even in isotropic or multiaxial diffractive surfaces [133, 149], contrasting with the appearance of bulk photonic and anisotropic structures. We therefore explore the feasibility of designing multi-faceted and modulated structural colour through the combination of wrinkling and diffraction and TIR selection and propagation. We expect that such multi-faceted structurally coloured materials can approximate more closely ‘bulk’ structural colours found in nature [156].

Visible light diffraction through reflection can lead to the emergence of structural colour from patterned surfaces, of appropriate periodicity and amplitude, which varies with observation an-

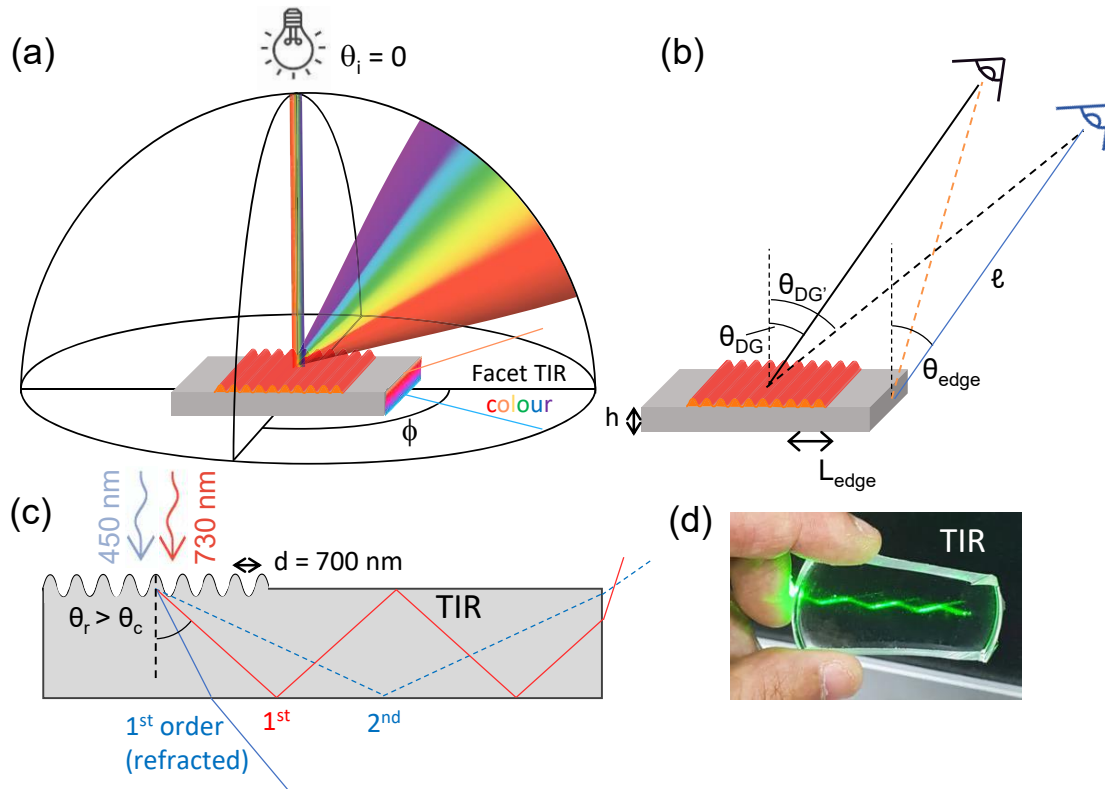


Figure 6.1: (a) Schematic of light diffraction from a 1D wrinkled surface, with normal incident light, and total internal reflection (TIR) leading to light propagation onto the sample facet. (b) Experimental geometry, defining different observation angles  $\theta_{DG}$ , defined from the normal of the diffraction grating;  $\theta_{edge}$ , defined from the normal of the sample edge, or facet;  $\theta_{DG'}$ , defined for the ‘edge observer’ from the normal of the diffraction grating when  $\theta_{edge} = \theta_{DG}$ . The lines from the facet (orange and blue) correspond to a (fixed) sample-observer distance of  $\ell$ . (c) Cross-sectional schematic of TIR propagation, illustrated for two incident wavelengths ( $\lambda = 450$  and  $730$  nm) and surface periodicity  $d = 700$  nm: for the shorter  $\lambda$ , the  $1^{st}$  diffraction order is below the critical angle on the sample’s bottom surface and is thus refracted out of the sample, while the  $2^{nd}$  order propagates by TIR and exits at the sample edge; the  $1^{st}$  diffraction order of the longer  $\lambda$  undergoes TIR thus also contributes to the edge colour. (d) Visualisation of TIR within a 5 mm thick PDMS coupon, with a monochromatic beam (laser  $\lambda = 533$  nm) at a high incident angle.

gle, as illustrated in Figure 6.1. Evidently, the surface can also act as a transmission grating where the light diffracts *into* the sample. If the material properties support TIR, we envisage that structural colour can be indirectly observed at the facet (or facets) of the material, which we term here ‘facet TIR colour’ (Figure 6.1a). However, light diffraction will generate a distribution of wavelengths at different angles, and several diffraction of varying intensities; therefore, such colour may differ from the original diffraction spectrum owing to TIR propagation rules. With structural colour observable from two (or more) different viewing perspectives for such a

material, we introduce the different nomenclatures for the observation angles with respect to the surface normal, one associated with the surface,  $\theta_{DG}$ , and the other with the facet,  $\theta_{edge}$ . The offset angle when viewing the surface with respect to  $\theta_{DG}$  is termed  $\theta_{DG'}$ , which depends on the length of unwrinkled material  $L_{edge}$  (Figure 6.1b). Figure 6.1c depicts the cross-sectional profile of light diffracting into the medium, and propagating through the medium, by total internal reflection, toward a facet (Figure 6.1c). Ray tracing for two wavelengths, 450 and 730 nm, is shown, to illustrate the colour and diffraction order selection, indicating that different colours to those diffracted by the surface pattern may be expected at the material facets. Figure 6.1d demonstrates the TIR of monochromatic light ( $\lambda = 532$  nm laser) within a slab of PDMS.

## 6.2 Methodologies

### 6.2.1 Sample preparation

PDMS (Sylgard 184, Dow Corning) coupons were prepared by casting a mixture of prepolymer and curing agent with a mass ratio of 10:1. The liquid mixture was stirred vigorously, degassed under vacuum, deposited onto a glass plate and cured at 75 °C in a convection oven for 1 h to crosslink into a PDMS elastomer slab with the required thickness (ranging from 2.0 to 3.0 mm). The coupons of 1.5 cm in width and varying lengths (4–8 cm) were then cut with a blade.

In order to create a bilayer with a glassy skin, surface plasma oxidation of the PDMS coupon samples was performed with a 40 kHz Diener Plasma (Femto), fitted with a pressure sensor (TM 101, Thermovac) and connected to oxygen (BOC, 99.5%). Samples were treated under plasma at 10 W intervals from  $P = 20$  to 60 W, with exposure time kept constant at  $\tau = 30$  s. The chambers were evacuated to a pressure of 0.1 mbar, before introducing oxygen for 5 min until the pressure reached 0.2 mbar and stabilised. The plasma was then ignited, at the required power and exposure time.

One-dimensional (1D), regular, sinusoidal patterns were fabricated by imposing uniaxial strain on a PDMS coupon (typically 2.5 cm long  $\times$  1.5 cm wide) using a strain stage. The strain

clamps were placed 1 cm apart onto the PDMS coupon, and the samples were stretched to a prestrain of 0.5, before undergoing plasma oxidation, and subsequently released from strain, yielding a sinusoidal diffraction grating (1 cm long) of prescribed wavelength and amplitude. The prestrain is calculated with respect to the initial ( $L_0$ ) and final distance ( $L_1$ ) between the clamps,  $\varepsilon = \frac{L_1 - L_0}{L_0}$ .

## 6.2.2 Surface Characterisation

The surface topographies were characterised by atomic force microscopy (AFM) using a Bruker Innova microscope, in tapping mode at 0.2 Hz, equipped with Al-coated Si tips (MPP-11100-W, Bruker) and analysed with the in-built Nanoscope software. Structural colour spectra were recorded using BLACK-Comet UV-VIS Spectrometer (StellarNet Inc) with F600-VIS-NIR fiber optic cable with a white light source (Advanced Illumination) in a dark environment. Optical photos were taken with a digital camera.

## 6.2.3 Light source and spectrum calibration

The spectrum of our light source is presented as ‘Ref’ in Figure 6.2a. The optical attenuation of PDMS was measured using a range of PDMS slabs with varying thicknesses, up to 12 cm. Optical transmission data are shown in Figure 6.2b. The transmission was then computed as  $T = \frac{(I_{sample} - I_{background})}{(I_{ref} - I_{background})}$ , where  $I_{ref}$  corresponds to the reference spectrum and  $I_{background}$  is the background spectrum accounted for by the spectrometer for the environmental background. The calibration of the spectrometer with the PDMS system yields  $T = e^{-0.021h}$ , where  $h$  is the PDMS thickness, as shown in Fig 6.2(c).

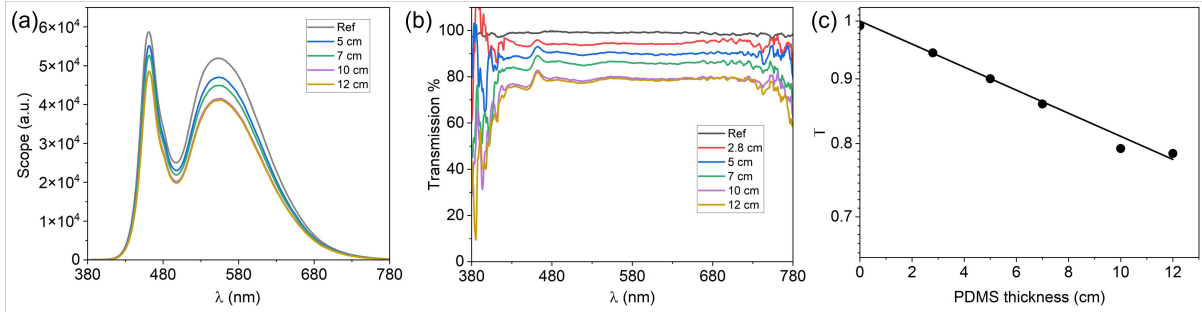


Figure 6.2: Spectrometer measurements with different thicknesses of PDMS: (a) Measurement intensity spectra; (b) Computed transmission data as a function of PDMS thickness; (c) Calibrated transmission dependence on thickness, yielding  $T = e^{-0.021h}$ , where  $h$  is PDMS thickness.

### 6.3 Structural colour of wrinkled surfaces through surface diffraction

We have fabricated a range of one-dimensional (1D) wrinkled structures by applying uni-axial mechanical strain ( $\varepsilon = 0.5$ ) on PDMS coupons, subsequently exposed to oxygen plasma at varying power (20-60 W). Upon relaxation of strain, the bilayer yields a sinusoidal profile, at sufficiently low deformations (Figure 6.3a). Wrinkles of different periodicities are readily obtained from the variation in plasma power (at constant exposure time), as shown by the atomic force microscopy (AFM) profiles in Figure 6.3b. The associated periodicity  $d$  and amplitude  $A$  can be expressed as [93, 90],

$$d = \frac{2\pi h (\bar{E}_f / (3\bar{E}_s))^{1/3}}{(1 + \varepsilon)(1 + \xi)^{1/3}} \quad (6.1)$$

$$A = \frac{h(\varepsilon/\varepsilon_c - 1)^{1/2}}{(1 + \varepsilon)^{1/2}(1 + \xi)^{1/3}} \quad (6.2)$$

where  $h$  is the converted film thickness,  $\bar{E}_f$  and  $\bar{E}_s$  are the in-plane strain moduli of the film and substrate respectively, given by  $\bar{E} = E/(1 - \nu^2)$ , where  $E$  is Young's modulus and  $\nu$  the Poisson ratio ( $\simeq 0.5$  for PDMS);  $\xi = 5\varepsilon(1 + \varepsilon)/32$ , accounting for the nonlinearity of the stress-strain relationship of the substrate in the finite deformation regime (i.e., non-Hookean response). Here, we refer to the surface periodicity as  $d$ , instead of the customary surface wavelength  $\lambda$ ,



to avoid confusion with the wavelength of light. In order to trigger the mechanical instability, a certain ‘critical’ strain  $\epsilon_c$  must be exceeded:

$$\epsilon_c = \frac{1}{4} \left( \frac{3\bar{E}_s}{\bar{E}_f} \right)^{\frac{2}{3}}. \quad (6.3)$$

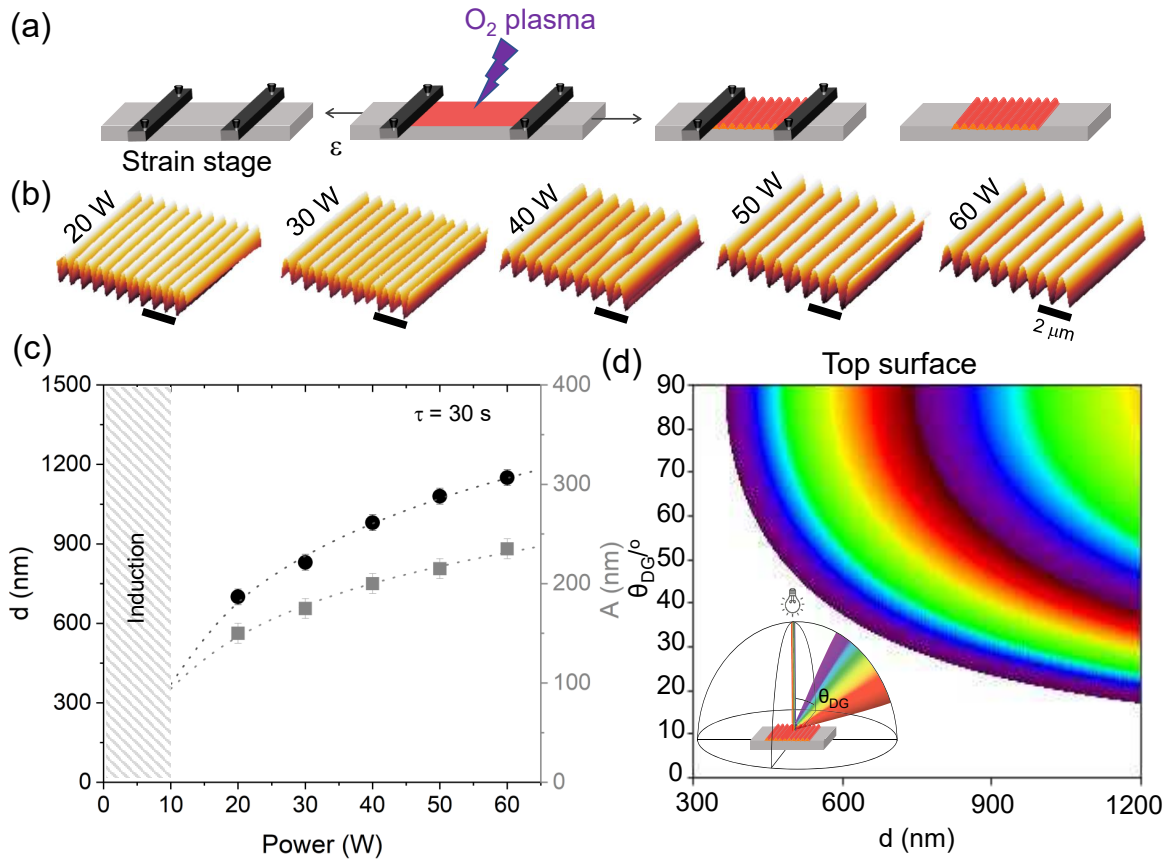


Figure 6.3: (a) Schematic of the fabrication of a 1D wrinkled sample: a PDMS elastomer coupon is mechanically strained and then exposed to oxygen plasma. Upon strain relaxation, a wrinkled surface remains (at rest conditions). (b) AFM scans of samples fabricated at different plasma powers ( $P = 20\text{ W}$  to  $60\text{ W}$ ) and fixed exposure time  $\tau = 30\text{ s}$ , and pre-strain  $\epsilon = 0.5$ ; the scale bar corresponds to  $2\ \mu\text{m}$ . (c) Wrinkling periodicity ( $d$ ) and amplitude ( $A$ ) measured for the samples above; the shaded area corresponds to an induction stage for glassy skin and wrinkling onset. (d) Structural colour map computed for incident white light at  $\theta_i=0$ , surface periodicity  $300 \leq d \leq 1200\text{ nm}$ , and observation angle  $0 \leq \theta_{DG} \leq 90^\circ$ , considering the first two diffraction orders. At lower  $d$  ( $\lesssim 380\text{ nm}$ ), UV can take place.

### 6.3.1 Total Internal Reflection (TIR) and selection of facet colour

Similarly to surface structural colour derived from the diffraction of light in reflection from a wrinkled surface, the observation of facet TIR colour is also expected to be angle-dependent. Light diffracted in transmission can be further propagated via TIR, under specific conditions, resulting in structural colour (indirectly) appearing on the facets of transparent materials. Figure 6.4a shows a series of optical images, taken at varying observation angles, of a sample with surface grating periodicity  $d = 700$  nm (fabricated with plasma conditions  $P = 20$  W,  $\tau = 30$  s,  $\varepsilon = 0.5$ ), that exhibits a range of structural colours. For clarity, the sample was placed on a mirror that acts as a reflective substrate and was observed at  $\theta_{edge}$  at  $10^\circ$  intervals of observation angle, from  $20$  to  $60^\circ$ . Concurrently, the surface structural colour can also be viewed, but with an offset angle of  $\theta_{DG'}$  ranging from  $30$  to  $65^\circ$  when  $l = 10$  cm and  $L_{edge} = 2$  cm. The white line on the optical images indicates the boundaries between facet colour, and the mirror reflection. Figure 6.4b shows a schematic of the sample set-up, including the role of the ‘TIR (mirror)’ where refracted rays from the facet impinging onto the mirror result in an additional colour perceived (which can be different from the facet colour).

As  $\theta_{edge}$  increases, the facet colour transitions from purple/red to dark blue while the surface colour is red-shifted from blue to orange. Transmission measurements were taken with respect to both facet and surface. The associated spectroscopy measurements at the facet are shown in Figure 6.4, indicating that the reflectance peak shifts from the red region ( $\approx 730$  nm) to the blue region ( $\approx 450$ - $480$  nm). For surface structural colour, 2 different sets of spectroscopy measurements are represented: Figure 6.4d shows the spectra when the measurements are taken with respect to  $\theta_{DG}$ , where  $\theta_{DG} = \theta_{edge}$  while Figure 6.4e show measurements taken at  $\theta_{DG'}$ , where the angle is offset with respect to  $\theta_{edge}$  (relationship shown in inset). The transmission spectra are recorded and then normalised for background and incident light intensities. Both spectra show that, as the observation angle increases, the measured spectra are red-shifted as the peak shifts from the blue region at  $\lambda \approx 450$  nm to  $\lambda \approx 650$  nm.

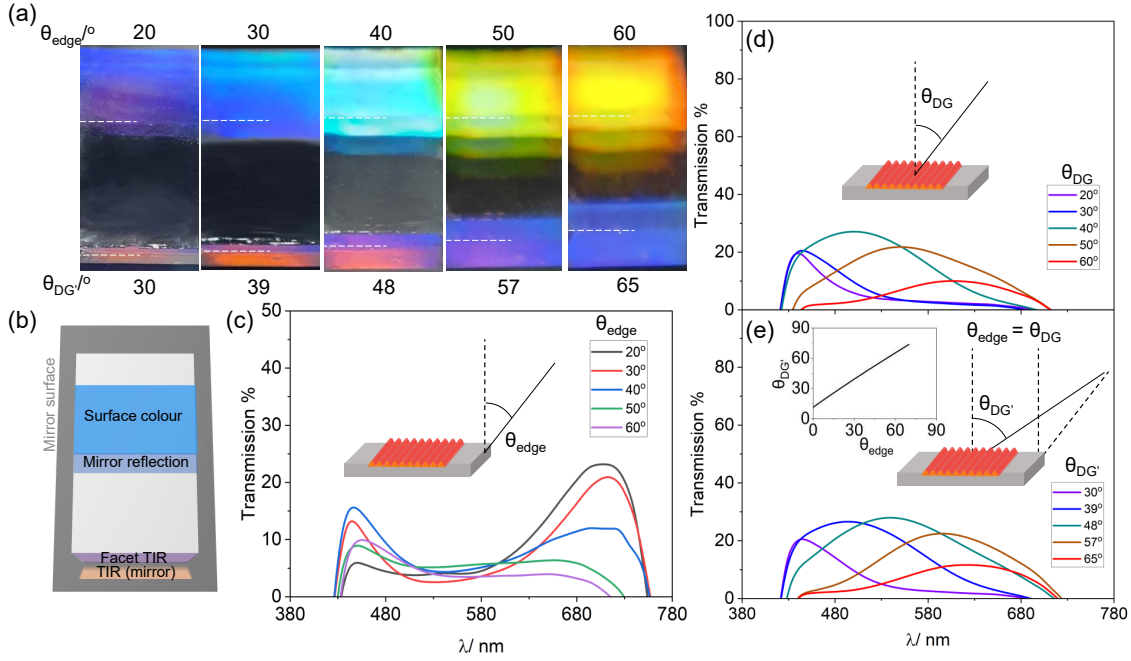


Figure 6.4: (a) Optical image of the structural colour of a 1D surface wrinkled sample with  $d = 700$  nm ( $P = 20$  W,  $\tau = 30$  s,  $\varepsilon = 0.5$ ): reflective diffraction (top) and TIR (facet) lead to distinct colours at fixed observation angles. (b) Experimental setup depicting the sample support on a mirror (reflecting also the downward refracted light) the dashed line in (a) demarcates the lower sample edge. (c) Spectroscopic measurements of (TIR) structural colour at the facet at varying  $\theta_{edge}$ . (d) Spectra of reflected diffracted light, measured as a function of  $\theta_{DG}$ , and (e)  $\theta_{DG'}$ , the offset in observation angle when  $\theta_{edge} = \theta_{DG}$ , defined in Figure 6.1, and related to  $\theta_{edge}$ , are shown in the inset.

### 6.3.2 A minimal model for facet colour: TIR and incident light dispersion

The resulting structural colour at the facet can be modelled using the principles of TIR within a medium. The angular dispersion of the incident white light from a flood-illuminating source is also included in the model, to reflect practically-relevant conditions. We first describe the behaviour of a sample with a surface diffraction grating of periodicity  $d = 700$  nm, depicted in Figure 6.4. Figure 6.5a is a schematic diagram showing three selected wavelengths,  $\lambda = 450$ , 480 and 730 nm, of light incident on the diffracting surface of the sample. These wavelengths were chosen due to their peak positions in the transmission measurements. We first consider that the rays are incident on the grating where  $\theta_i = 0^\circ$ . Within the medium, the general diffraction equation can be modified for a transmission diffraction grating to take into account the respective refractive index ( $n_0$  in air,  $n_1$  in PDMS):

$$m\lambda = d(n_0 \sin \theta_i + n_1 \sin \theta_r) \quad (6.4)$$

where  $\theta_r$  denotes the angle at which light is diffracted into the sample.  $\lambda = 450$  nm diffracts at  $27.1^\circ$  (1<sup>st</sup> order) and  $65.8^\circ$  (2<sup>nd</sup> order),  $\lambda = 480$  nm at  $29.1^\circ$  (1<sup>st</sup> order) and  $76.6^\circ$  (2<sup>nd</sup> order), and  $\lambda = 730$  nm at  $45.17^\circ$  (1<sup>st</sup> order). When the angle of light in the medium (with respect to the normal) exceeds the critical angle, the light undergoes total internal reflection. The critical angle within PDMS, taking into account the refractive index of air ( $n_0 = 1$ ) and of PDMS ( $n_1 \simeq 1.41$ ) is estimated to be

$$\theta_c = \arcsin\left(\frac{n_0}{n_1}\right) = 45.17^\circ \quad (6.5)$$

As the 1<sup>st</sup> order of 450 nm and 480 nm wavelengths does not exceed the critical angle, the ray of light refracts out of the sample without being reflected internally when reaching the boundary of the sample. On the other hand, as the angle of diffraction for the 2<sup>nd</sup> order of  $\lambda = 450$  nm and 480 nm and 1<sup>st</sup> order of 730 nm exceeds that of the critical angle for the system, these undergo TIR and propagate through the sample before exiting at the edge we term the ‘facet’ with an angle of  $\theta_{r'}$ , with respect to the (horizontal) facet normal, where  $\theta_{r'} = 90^\circ - \theta_r$ . From there, we can calculate  $\theta_{edge}$  from Equation 6.6, which is the complementary angle to that of the ray refracted at the facet:

$$\theta_{edge} = 90^\circ - \arcsin(n_1 \times \sin \theta_{r'}) \quad (6.6)$$

Refracted rays at the facet can either exit towards the mirror (below the sample) or the observer. Due to the size of the incident beam spot, light is incident across the entirety of the grating. As a result, it is insufficient to consider the pathway of only a singular ray incident on the grating, but it is also important to consider incidence at different points along the wrinkles (transparent lines). By considering this, it offers a better understanding of the colours emerging at the facet, thereby leaving the sample at an angle of  $\theta_{r'}$  with respect to the facet’s normal, and refracting towards the observer/ mirror with  $\theta_{edge}$ . This effect is also affected by the geometry of the

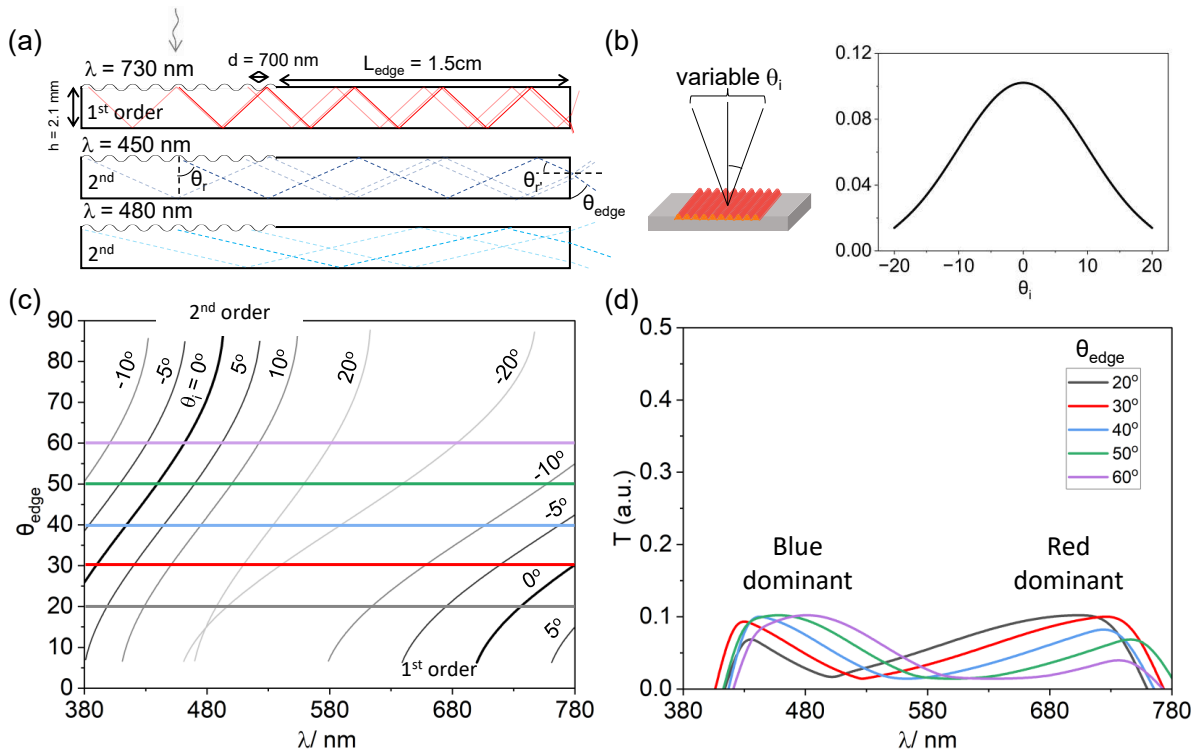


Figure 6.5: (a) Schematic diagram representing the modelling calculations, for a given coupon dimensions (height  $h$ , length  $L_{DG} + L_{edge}$ ) and periodicity  $d$ , each individual wavelength is ray-traced, diffraction orders that do not meet TIR conditions are excluded, and the refracted colours at the edge computed as a function of  $\theta_{edge}$ . (b) Schematic depicting the distribution of incident angles  $\theta_i$  onto a point in the sample and illustrative of angular dispersion, described by a Gaussian profile with a half-width at half-maximum (HWHM) of  $10^\circ$ . (c) Computed relation between ( $\theta_{edge}$ ) and  $\lambda$  at fixed  $\theta_i$  for the 1<sup>st</sup> and 2<sup>nd</sup> diffraction orders. Representative fixed  $\theta_{edge}$  angles are shown by the horizontal lines. (d) Predicted spectra for the edge colour, assuming the Gaussian distribution shown in (b), and accounting for the light source  $\lambda$  distribution (SI Fig x). At this  $d$ , the edge colour is expected to change from red-dominant to blue-dominant upon increasing  $\theta_{edge}$ , in agreement with Figures 6.4a and 3c.

sample, by changing the optical path of the rays travelling in the medium. When the TIR rays exit the PDMS at the facet, we can capture the signal where rays are refracted towards the mirror, by employing a reflective surface, for instance, a mirror. Radiation exiting towards the mirror can be observed in reflection, and its colour spectrum can be analysed. Employing reference conditions ( $P = 20$  W,  $\tau = 30$  s,  $\varepsilon = 0.5$ ), samples of two slightly different thicknesses ( $h = 2.75$  mm and 3 mm) were prepared, keeping the length constant where  $L_{edge} = 1.5$  cm. From Figure 6.6a, we observe that at  $\theta_{edge} = 30^\circ$  and  $40^\circ$ , there is a slight difference in the optical images between  $h = 2.75$  mm and 3 mm, where the facet colour appearing from the facet and the mirror ‘reflection’ is apparently switched between the two thicknesses. This is a geometric effect, that

can be readily explained by ray tracing, shown in Figure 6.6b. At these two  $\theta_{edge}$ , we find the spectra in Figure 6.6c have a maximum at  $\approx 750$  nm, which is responsible for the contribution in red colour. The single ray tracing diagram from the centre of the diffraction grating surface illustrates the observation: When  $h = 2.75$  mm, the ray exits downwards, towards the reflective surface, and a red-dominant component is observed through the mirror. Conversely when  $h = 3$  mm, the depicted ray exits upwards, towards the observer, and a dominant red colour is then observed at the facet. Figure 6.6c shows the associated spectra relating to the samples at the various  $\theta_{edge}$ . The shape of the spectra is similar to that of samples of the same condition, showing that the colours observed are dependent on the wrinkle periodicities. The intensity of the thicker sample is lower than that of the thinner ones, due to the longer pathlength and associated light attenuation.

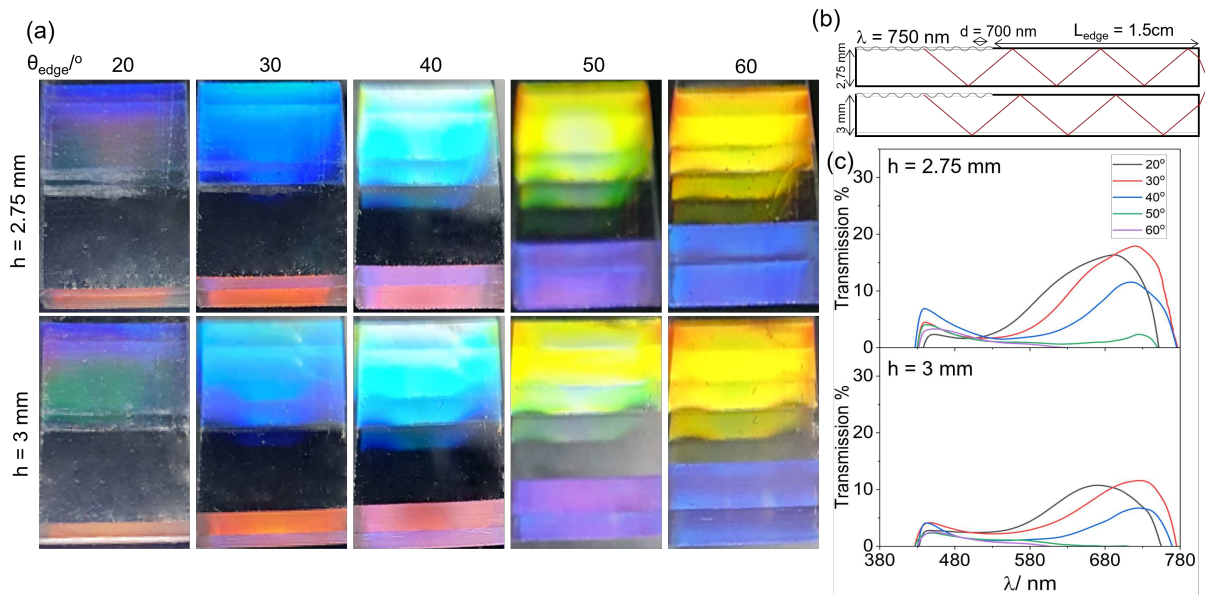


Figure 6.6: (a) Optical images of structural colour of a 1D surface wrinkled sample with  $d = 700$  nm ( $P = 20$  W,  $\tau = 30$  s,  $\epsilon=0.5$ ), with  $L_{edge} = 1.5$  cm and different thicknesses  $h = 2.75$  mm and  $3$  mm, observed with increasing  $\theta_{edge}$ . (b) Ray tracing diagram of a  $750$  nm ray for both sample thicknesses, depicting the different direction of ray exit at the facet. (c) Recorded transmission spectra for each sample at corresponding  $\theta_{edge}$ .

In order to describe the experimental observations, we also consider the intrinsic divergence of most incident light sources and account for the distribution of angles of incidence (variable  $\theta_i$ ) on the surface grating. We model our results using a Gaussian distribution of  $\theta_i$ , ranging from  $-20^\circ$  to  $20^\circ$  (Figure 6.5b). Combining equations 6.4 - 6.6, we compute the wavelength

of light  $\lambda$  observable at  $\theta_{edge}$  accounting for an incident angle  $\theta_i$  distribution (Figure 6.5c). When  $d = 700$  nm, light diffracts up to two diffraction orders within the medium, where the observation of higher wavelengths arises due to the contribution of the 1<sup>st</sup> order, while the lower wavelengths are due to the 2<sup>nd</sup> order. Graphically, for each fixed  $\theta_{edge}$ , the intersection with the  $\theta_i$  dispersion curves yields a series of  $\lambda$  values. In other words, imposing  $\theta_{edge}(\theta_i, \lambda) =$  fixed value (e.g.  $20^\circ$  leads to a  $\lambda(\theta_i)$  series. The intensity  $T(\lambda)$  of each  $(\lambda, \theta_i)$  pair (sampled every  $2.5^\circ$ ) is then assigned the corresponding Gaussian pre-factor attributed in Figure 6.5b, namely  $g(\theta_i) = \exp(\theta_i^2/(2\sigma^2))/(\sqrt{2\pi}\sigma)$  (with  $\sigma \simeq 10$ , to match experimental observation). This results in the spectra shown in panel (d); the expression is discretised with 17 terms and normalised to 1. Taking  $\theta_{edge} = 20^\circ$  for example,  $\lambda = 730$  nm is expected to be observed when  $\theta_i = 0^\circ$  (Figure 6.5c). As our model assumes this incident angle experiences a maximum, Figure 6.5d indicates this was associated with maximum intensity at 730 nm. Similarly, there is a minimum at  $\lambda \approx 480$  nm due to the smallest weighting when  $\theta_i = \pm 20^\circ$ . Below 480 nm, the contributions of wavelengths are due to the diffraction of the 2<sup>nd</sup> order, while above this, it is contributed by the 1<sup>st</sup> order. From this model, we observe that when  $\theta_{edge}$  is  $20^\circ$  and  $30^\circ$ , the measured spectrum shows that the colour observed is red in appearance while for  $40^\circ$ - $60^\circ$ , it is blue in appearance. This is in line with the experimental results, where we observe that there is a greater contribution in red at the facet at smaller  $\theta_{edge}$  while at  $40^\circ$ - $60^\circ$  the facet has a more discernible blue hue to it. The profile of the modelled spectrum agrees with the experimental results in Figure 6.4c. The spectral signature of the incident white light source does not emit below 400 nm, and therefore, the model does not yield results below 400 nm. The measured intensities are also dependent on the geometry of the sample which affects the distance over which each ray travels; accordingly, longer ray paths lead to lower intensities recorded for their observed wavelengths.

Additional specimens of different lengths were prepared under otherwise the same conditions as those of Figure 6.5, and Figure 6.6, namely with  $\varepsilon = 0.5$ ,  $P = 20$  W,  $\tau = 30$  s, where  $L_{edge} = 2.5$  cm and 4 cm. Upon clamping the PDMS coupons with different lengths, scotch tape was used to cover up the exposed areas, ensuring that the edge portion did not undergo plasma treatment. This experiment serves to show the feasibility of manipulating the geometry of PDMS coupons



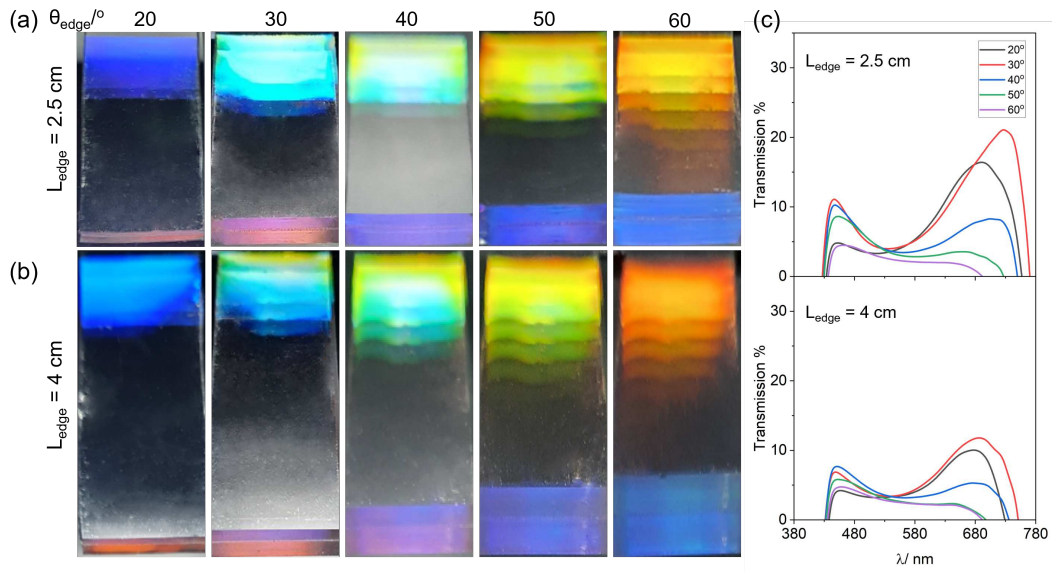


Figure 6.7: Optical images of the structural colour of wrinkled samples with  $d = 700$  nm and  $h = 2.1$  mm, with lengths (a)  $L_{edge} = 2.5$  cm, (b)  $L_{edge} = 4$  cm. (c) Measured spectra for samples with the different  $L_{edge}$  as a function of observation angle.

to accommodate longer samples. As in previous experiments, Figure 6.7 shows the structural colours of the sample, surface and facet when  $\theta_{edge}$  varies from 20 to 60°. For these geometries, the facet colours are similar, only decreasing in intensity with increasing length (and thus light attenuation along the pathlength, and losses at each surface reflection). The structural colour of the surface differs slightly due to the offset in angle  $\theta_{DG'}$ , affected by  $L_{edge}$ .

From the modelling of the structural colour, we establish that the colour observed is only dependent on the periodicity of the wrinkles and the observation angle (which themselves are affected by the incidence angle on the grating surface). We can take advantage of the tunability of plasma oxidation of PDMS to fabricate a range of structural colour designs that would achieve multifaceted structural colours. By increasing plasma oxidation power from 20 to 60 W in 10 W increments, we design wrinkles with periodicities ranging from 700 to 1150 nm. Viewing each sample at different  $\theta_{edge}$  angles, 20°, 40° and 60°, a gamut of colours is observed. The surface structural colour can be predicted based on previous work (Figure 6.3d) [120, 133]. A similar colour map can also be used to design and predict the observed facet colour at  $\theta_{edge}$  with  $d$ . This map was constructed from  $d = 300$  to 1200 nm, which includes up to three diffraction orders, with the assumption that  $\theta_i = 0^\circ$  and only taking into account the dominant colour with no colour mixing from contributions of different orders, and is shown in Figure 6.8b. Overall,



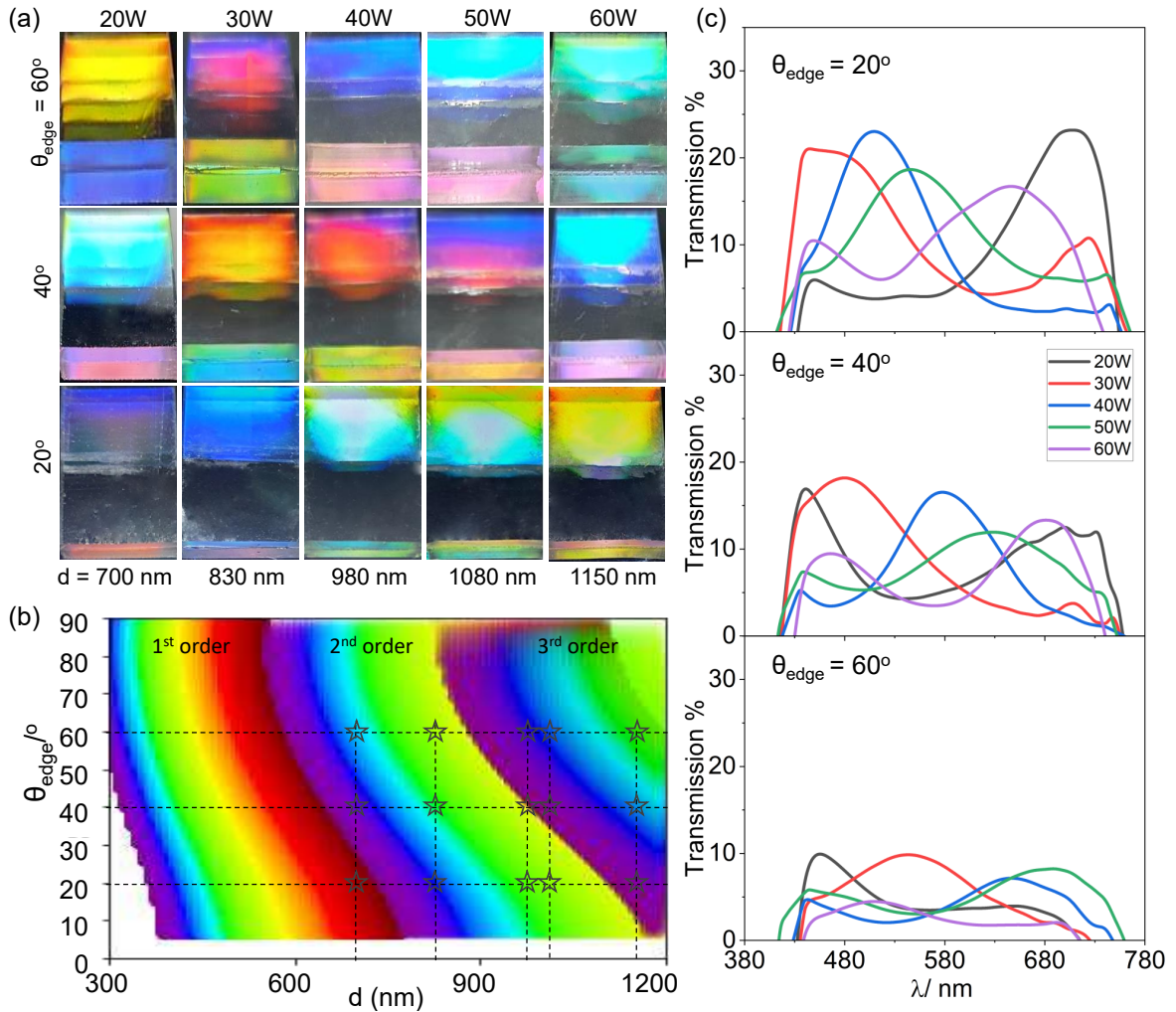


Figure 6.8: Effect of surface periodicity  $d$  on top (reflective diffraction) and facet (TIR) structural colour. (a) Optical images of illustrative samples of varying  $d$  (from 700-1150 nm) prepared through varying oxygen plasma power exposure ( $P=20-60$  W,  $\tau=30$  s,  $\varepsilon=0.5$ ), acquired at  $\theta_{edge}=20, 40$  and  $60^\circ$ . (b) Computed colour map for TIR facet colour, as a function of  $d$  and  $\theta_{edge}$ , for the first three diffraction orders. The star markers indicate conditions investigated experimentally in (a), showing qualitative agreement (see text). (c) Measured spectra of TIR facet colour, corresponding to the samples shown in (a) at the reference  $\theta_{edge} = 20^\circ, 40^\circ$  and  $60^\circ$ . As  $P$  increases, the observed colour is red-shifted and/or transitions into a higher diffraction order at a lower wavelength.

the model shows good agreement with the experimental results. Transmission spectra were also taken for each sample at the different angles, quantitatively showing that the structural colour is red-shifted, or shifted into higher orders, as the periodicity and  $\theta_{edge}$  increases.

Beyond  $1.2 \mu\text{m}$ , we reach the limits in the observation of the facet colour, as the sample generates increasing numbers of diffraction orders mixing additively together (Figure 6.9). A series of samples with higher periodicities were fabricated with plasma conditions  $P = 20$  W,  $\varepsilon =$

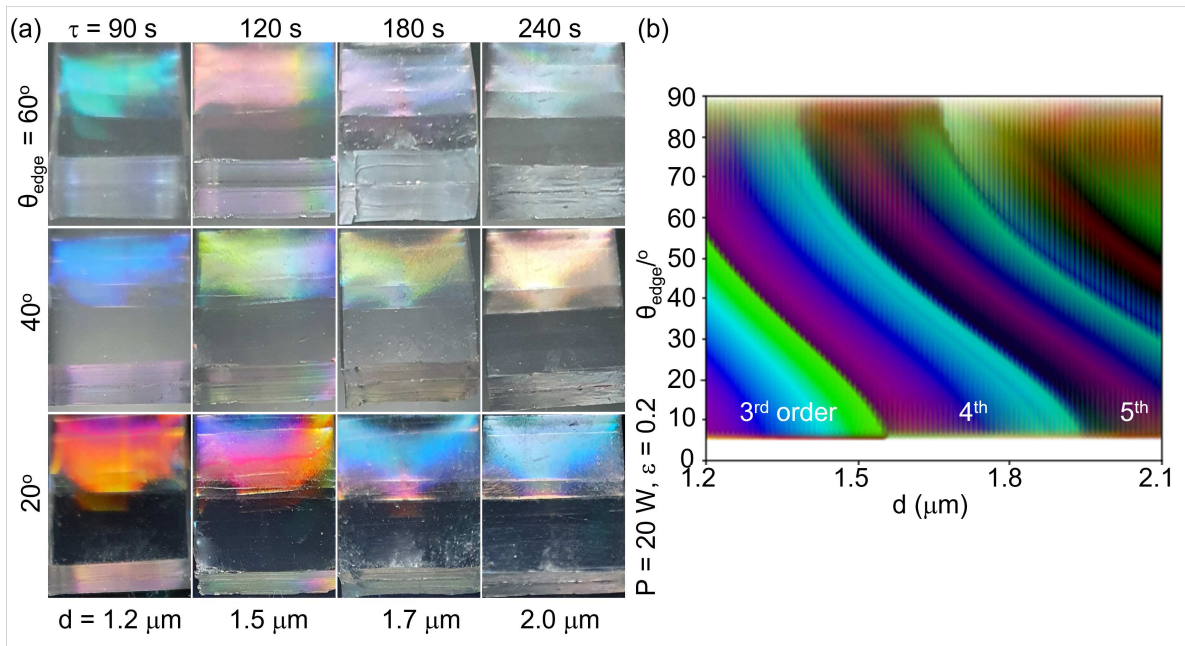


Figure 6.9: (a) Optical images of samples fabricated at  $P = 20$  W,  $\varepsilon = 0.2$ , and exposure times from  $\tau = 90$  to  $240$  s. These samples show the decreasing manifestation of facet TIR colours with increasing  $d$ . (b) Colour map of facet TIR for  $d = 1.2$  to  $2.1$   $\mu\text{m}$ , showing the mixing of up to 6 diffraction orders.

0.2, at increasing exposure times from 90 to 240 s. These conditions were selected as a lower prestrain allows higher periodicities to be achieved. With increasing periodicities, facet TIR colour becomes progressively less visible. At  $1.2$   $\mu\text{m}$ , a faded purple hue can be observed at  $\theta_{edge} = 20^\circ$ , while the other conditions, up to  $2$   $\mu\text{m}$ , display no observable facet colour. As  $d$  increases, additional orders diffract within the medium, causing wavelengths from different orders to undergo mixing. In addition, wavelengths from higher diffraction orders also exhibit lower intensities. As a result of the combination of both effects, we conclude that facet TIR can be prominently observed when wrinkle surfaces are fabricated at the nano-scale.

### 6.3.3 Colour changes induced by environmental conditions

Structural colour can reflect environmental conditions that affect the surface grating nanostructure. Environmental factors can include the presence of solvents in a liquid or gas atmosphere, or a medium with different refractive indices. When PDMS is exposed to a range of solvents, it can swell and deform significantly. Wrinkled samples ( $P = 30$  W,  $\tau = 30$  s) were soaked in

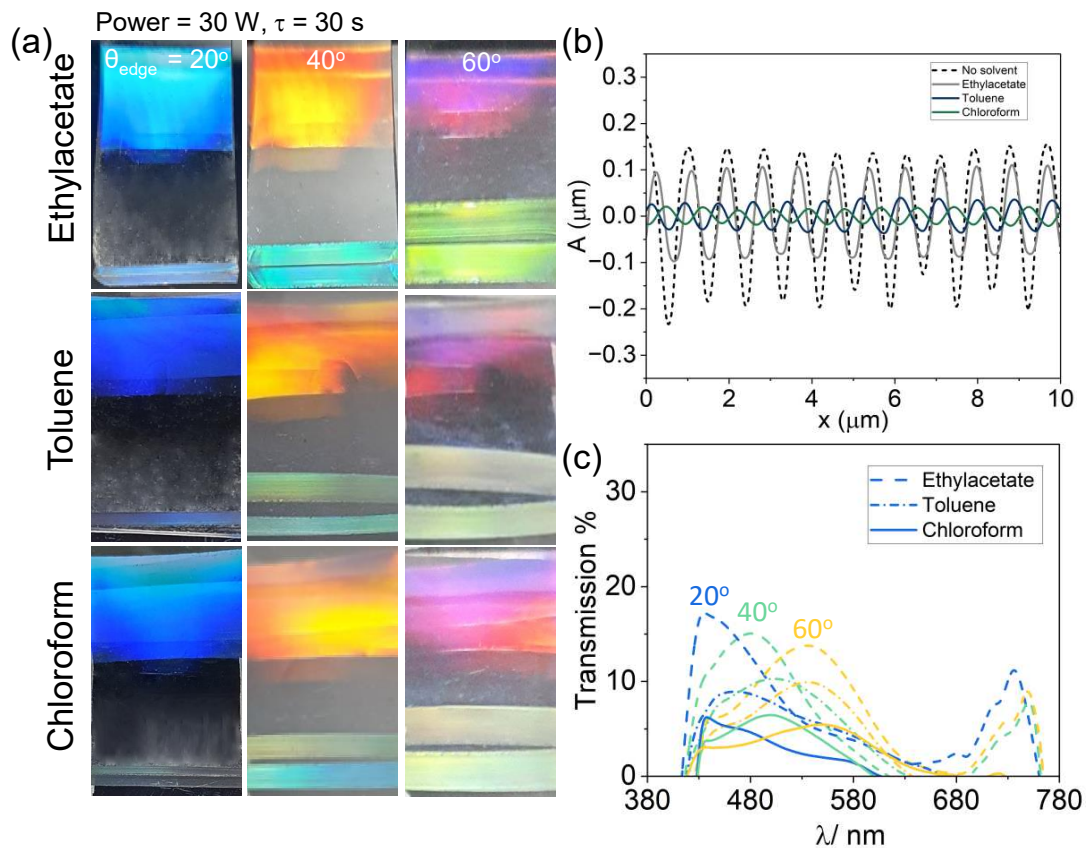


Figure 6.10: Top and facet structural colour change upon solvent-induced swelling. (a) Optical images of illuminated wrinkled samples with  $d = 830$  nm ( $P = 30$  W,  $\tau = 30$  s,  $\varepsilon = 0.5$ ) after immersion in ethyl acetate, toluene and chloroform (in increasing order of swelling) for 10 min, at  $\theta_{edge} = 20, 40$  and  $60^\circ$ . (b) AFM line scans showing the decrease in amplitude  $A$ , and marginal increase in  $d$  upon immersion, and air drying by excess solvent removal (see text). (c) Measured spectra of the TIR facet colour after soaking in ethyl acetate (dash), toluene (dash-dot), chloroform (solid), at observation angles  $\theta_{edge} = 20^\circ$  (blue),  $40^\circ$  (green),  $60^\circ$  (yellow). The reference dry images and spectra are shown in Fig 6.8a (second column) and c.

different solvents, ethyl acetate, toluene, and chloroform for 10 minutes each. These solvents were chosen for their different swelling ratios: 1.18, 1.31, and 1.39 respectively [157]. Prior to optical and AFM imaging, solvent-soaked PDMS coupons were carefully pad-dried with absorbent tissue paper to remove excess solvent, and allowed to air-dry for 2 min. Care was taken not to over-dry the sample and reverse swelling (as demonstrated with toluene and chloroform, for instance) [157, 158, 159]. The solvent-soaked samples can be seen in the optical images in Figure 6.10a, viewed at increasing  $\theta_{edge}$  at  $20, 40$  and  $60^\circ$ . When the samples are exposed to solvents with increasing swelling ratios, the facet colours appear to be disproportionately affected, decreasing in intensity. From the AFM scans of the solvent-exposed samples in Figure 6.10b, we observe that the wrinkling amplitude decreases from its original to a greater extent

with solvents of higher swelling ratios (from  $A \approx 175$  nm with no solvent to 12 nm with chloroform) while experiencing a marginal increase in periodicity ( $d = 830$  nm to  $\approx 900$  nm). The marginal increase in periodicity results in a negligible change in structural colour on the surface, however, the decrease in amplitude causes a decrease in measured transmission intensity, shown in Figure 6.10c. Due to the reversibility of the swelling process [160], such systems have potential uses in sensor technology.

### 6.3.4 Specimen geometry in producing structural colour

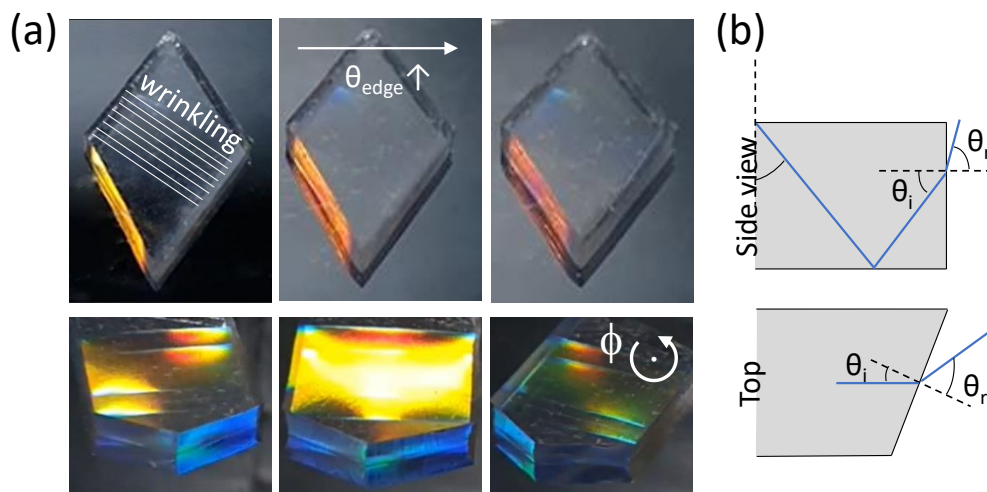


Figure 6.11: (a) Effect of polyhedron shape, illustrated with a diamond cut and relative orientation of the 1D wrinkled surface. The top row  $d = 620$  nm ( $P = 20$  W,  $\tau = 30$  s,  $\varepsilon = 0.7$ ) depicts increasing  $\theta_{edge}$ , and the row below ( $d = 700$  nm,  $P = 20$  W,  $\tau = 30$  s,  $\varepsilon = 0.5$ ) to varying rotation angle  $\phi$ . (b) Ray tracing diagrams schematically show the observations described from the side and top view

Specimen geometry can be exploited to further expand the variation of multifaceted structural colours. So far, results for 1D samples prepared using a rectangular slab were presented, resulting in facet colour to be observed in the same direction as that from the wrinkled surface. From such samples, the edges can be subsequently cut at different angles, to examine the impact of geometry. Cutting is done only after the fabrication of wrinkles to prevent any inhomogeneities in strain application. A schematic of the side and top view shows the expected direction travel of light rays while exiting a sample as shown in Figure 6.11a. In a rectangular sample, we only need to consider the side view to determine the pathway of ray travel. As previously shown,



we can determine the  $\theta_{edge}$  for observed wavelengths, and the facet colours are observed in the same direction as the surface. However, in a cut sample, we also have to consider another dimension for light refraction, where the direction of observation of facet colour is offset from that of the surface colour.

To demonstrate this effect, Figure 6.11a shows two samples with ‘diamond’ cuts at the edges, the top row sample prepared at  $P = 20$  W,  $\tau = 30$  s,  $\varepsilon = 0.7$  with periodicity  $d = 620$  nm, while the bottom at  $P = 20$  W,  $\tau = 30$  s,  $\varepsilon = 0.5$  with  $d = 700$  nm. The sample with periodicity  $d = 620$  nm was observed with increasing  $\theta_{edge}$  at an angle  $\phi = 40^\circ$  offset, where  $\phi$  is defined as the angle about the sample’s horizontal axis (Figure 6.1a), causing the wrinkling direction to be non-perpendicular to the observer. Since uniaxial wrinkled surfaces act as 1D phase gratings [75], these diffract light solely in the direction perpendicular to that of the orientation of the wrinkles. As a result, structural colour is only observable along that direction, and within a narrow off-specular range (of approximately  $\Delta\phi \pm 5-10^\circ$ , associated with wrinkling disorder and finite illuminated spot size). Structural colour is otherwise not observable away from this diffraction plane, as illustrated in Figure 6.11a where only edge colour, due to facet TIR, is visible.

As with the other samples, the colour of the facet can be seen to change with increasing  $\theta_{edge}$ , where it transitions from yellow to red. In the 2<sup>nd</sup> sample, where  $d = 700$  nm, the sample was observed at a fixed  $\theta_{edge} = 50^\circ$ , and rotated about  $\phi$ . We observe that the surface colour yellow can be effectively ‘switched on or off’ along with the facet colours. By exploiting different directions of cuts in the samples, we can manipulate different variations and combinations in the multi-faceted structural colours of these samples.

### 6.3.5 Structural colour TIR in GRISM

Incorporating a surface grating with a prism, we demonstrated the fabrication of GRISMs. In this context, a GRISM is a compound optical element that significantly reduces the influence of light dispersion from the individual elements. A prism deflects violet light more than red, while

a diffraction grating deflects red more than violet. By combining the two, light can be separated into its components while offsetting the beam deviations resulting from each element.

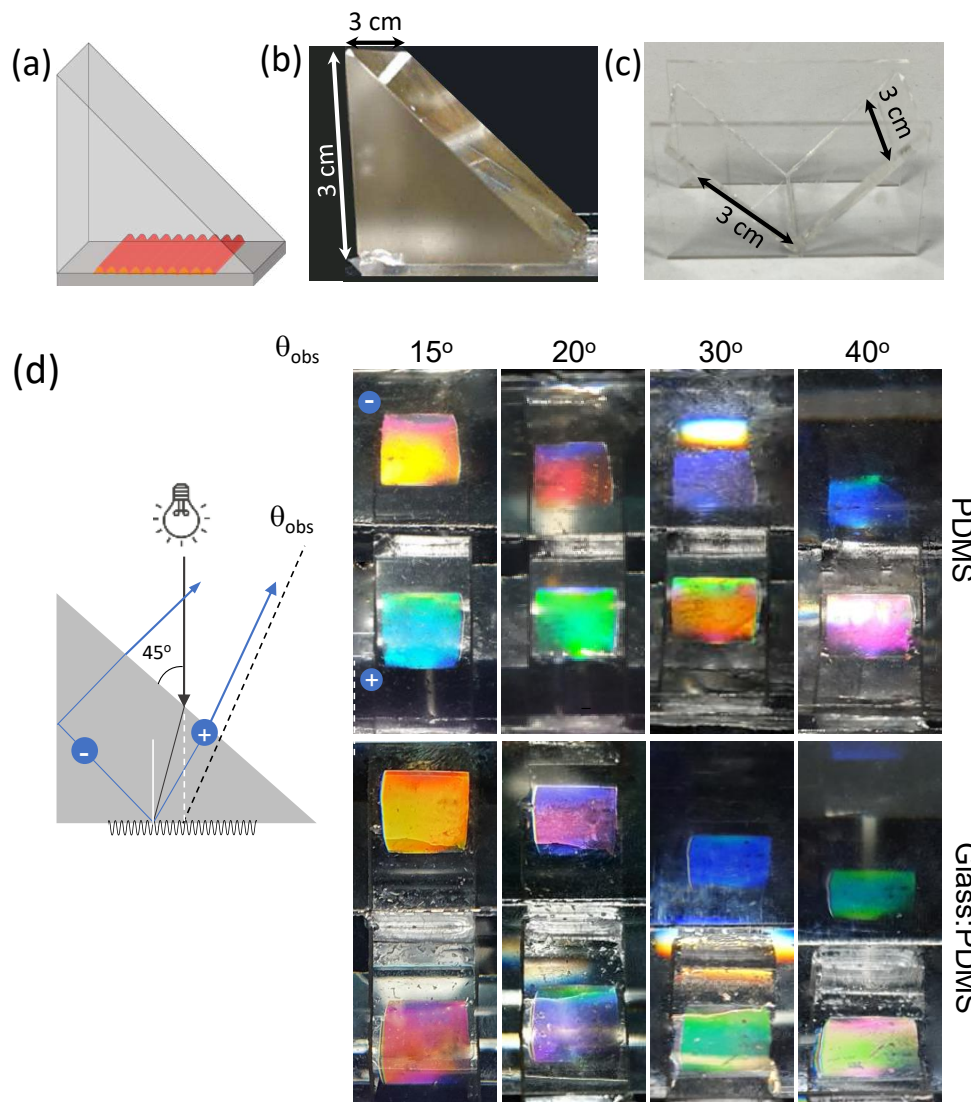


Figure 6.12: (a) Illustration of the fabrication of a 'GRISM' by combining a prism and a wrinkled PDMS layer onto its side surface. (b) Isosceles right-angled glass prism, with side length of 3 cm and width of 3 cm, coupled with a wrinkled surface, to demonstrate the dispersion of colours on the two surfaces of the prism. (c) A PMMA mould is utilised to create a PDMS prism. The mould is obtained by joining individual PMMA laser-cut pieces of thickness 3 mm. (d) Experimental realisation of the coupling of a grating (on a facet) and a prism, termed 'grism', whose setup is illustrated in the sketch. Optical images obtained for PDMS (top) and glass (bottom) prisms, obtained with  $d = 980$  nm ( $P = 40$  W,  $\tau = 30$  s,  $\varepsilon = 0.5$ ). Colour dispersion can be finely tuned by these two optical elements.

Here, we demonstrate the fabrication of a GRISM structure by placing an isosceles, right-angle prism, atop a wrinkled surface, with the wrinkles in contact with the prism, shown in Figure 6.12(a). We use two materials for the prisms: glass and PDMS. The setup with glass prism

(Edmund Optics) can be seen in Figure 6.12(b), with length and width of 3 cm each. The PDMS prism was fabricated using a PMMA mould, made by laser cutting and solvent bonding, as shown in Figure 6.12(c). Fresh PDMS was then poured into the mould and cured, and the PMMA mould was unmounted to yield a PDMS prism with identical dimensions as that made of glass. In a simple realisation of a GRISM, we placed model prisms made of either PDMS ( $n = 1.41$ ) or glass ( $n = 1.52$ ) on top of a wrinkled PDMS sample ( $P = 40$  W,  $d = 980$  nm) to create GRISMs (PDMS, and Glass:PDMS) as shown in the schematic in Figure 6.12b. The samples were placed such that the wrinkled surface was in contact with the prism. Employing white light, the GRISMs were viewed at increasing  $\theta_{obs}$ , from  $15^\circ$  to  $40^\circ$ .  $\theta_{obs}$  is taken from the normal of the base of the GRISM, directly under the centre of the incident light.

GRISMs show a ‘dual’ image of the wrinkled surface exhibiting different colours. When white light is shone vertically, it illuminates the prism surface at an angle of  $45^\circ$ , and then refracts into the medium, thus impinging on the grating at an angle, before diffracting back into the medium. The grating diffracts positive and negative diffraction orders, denoted in the schematic as + and -. The rays from the positive orders are then incident on the top face of the GRISM and are refracted out, while those from the negative orders will first hit the side face of the grism. If the angle of the rays incident on the side face exceeds the critical angle, it undergoes TIR before exiting from the top. The combination of the two diffraction orders produces dual-coloured appearances, shown in the optical images. From an observer’s perspective in an optical image, the top colour is produced by the negative diffraction order while the bottom is from the positive order. As  $\theta_{obs}$  increases, we observe a gamut of different colours, which can also be manipulated by changing the material composition of the prism. Figure 6.12d shows that by changing the refractive index of the medium (PDMS to glass), we are able to obtain distinct colours in the GRISMs.

## 6.4 Conclusion

In this chapter, a further exploration of structural colour of wrinkled surface was performed, where we successfully fabricate multi-faceted structural colour exploiting the combination of diffraction in reflection as well as transmission mode where total internal reflection can take place. The main findings in this work are as follows:

- The design and fabrication of multi-faceted structural colour on a transparent elastomeric material (PDMS) has been demonstrated in this work, through the patterning of a surface diffraction grating and exploiting TIR. The surface grating was generated by the facile method of mechanical wrinkling and oxygen plasma oxidation, enabling periodicities of wrinkles tunable for optical diffraction of visible light wavelengths to be achieved. Wrinkled surfaces can yield striking structural by colour acting as reflective diffraction gratings, whose response we model and validate experimentally.
- TIR process is selective - where only a certain sub-set of diffracted colours at distinct angles, and diffraction orders of each colour will be propagated by TIR. The combination of surface diffraction and transmission diffraction (combined with TIR) allows for different colours to be observed on the respective facets. The colours can be well defined with rules established and described in the chapter.
- As elastomeric materials can respond significantly to environmental changes, of gas or liquid medium, we demonstrate a simple concept for a colour sensor. The use of macroscopic shape of the 3D objects can impact light propagation and colour appearances, and we generate a 'GRISM' to illustrate the possible designs of using mediums of different refractive indices to exploit the TIR mechanism.
- This work shows that the design parameter space for inducing 'multifaceted' colour by combining diffraction and TIR, as well as coupling these with other optical elements, appears to be very large and promising. We therefore anticipate our findings will be relevant across a wide range of applications, including in displays, packaging, and sensors.



## **Chapter 7**

# **2D Diffraction Interference and Structural Colour**

This chapter is constructed through a collection of work that has been published in *Physical Review Letters* 2022, 128, 058001 [113], *ACS Applied Polymeric Materials* 2021, 3, 10, 5162–5170 [120], *Advanced Optical Materials* 2022, 10(17), 2200964 [133] and *Molecules* 2023, 28(4), 1710 under Special Issue Polymeric Photonic Materials [155], along with some unpublished material. In this work, experiments were collaboratively carried out by Annabelle Tan and Dr Luca Pellegrino. The initial experiments in laying down foundations for non/orthogonal wrinkling superposition were primarily carried out by Dr Pellegrino, supported by Annabelle. While the 2D film lamination, reconstruction of 2D diffraction pattern and the investigation in structural colour of 2D samples were primarily performed by Annabelle.

## 7.1 Introduction

Up till now, we have explored mainly the fabrication of 1D wrinkle surfaces with its optical effects and associated structural colour. These versatile surfaces although can be varied and tunable, lack directionality in diffraction - where it only diffracts light in one direction, perpendicular to that of the wrinkles. As previously discussed in Chapter 2.2, the application of bi- or multi-axial strains give rise to more complex patterns including dimples, herringbone (chevrons), square (checkerboard) or labyrinthine features [94, 108, 109, 110, 111]. The selection of a particular wrinkling mode is determined by the minimization of overall elastic and bending energy. Wave interference patterns can also be observed in layered rock formations where folded geological layers buckle in two or three dimensions [161, 162]. The superimposed buckling instabilities can lead to different modes such as domes and basin' or non-planar non-cylindrical folds with hinge replacement' depending on the interference angle [163, 164]. One way to create a large area checkerboard or 'spiky' topography is to first generate a one-dimensional wrinkled surface and then replicate it, allowing for a second, orthogonal generation to be superposed onto the first with individually set amplitudes and wavelengths [94, 109, 111].

Taking inspiration from the aforementioned concepts, in this chapter we investigate the possibilities and limitations of using wrinkling wave superposition as a tool for designing surface patterns for the application of structural colours with variation in directionality. Our approach involves exploring the sequential placement of two wrinkling generations induced by uniaxial strain of a bilayer, with the angle between them being allowed to vary. This methodology presents non-trivial aspects that need to be considered. For instance, the second wrinkling event no longer takes place on a planar bilayer, resulting in a coupling effect with the pre-existing wrinkled topography. Therefore, we must take into account the interactions between the two generations of wrinkles, and how they may influence the final pattern and colour observed on the surface. Finally, we also investigated how the different processes of sequential or simultaneous wrinkling in the fabrication of orthogonal wrinkles can affect the directionality of structural colour displayed.

## 7.2 Methodologies

### 7.2.1 Simultaneous and sequential 2D wrinkling

Simultaneous 90° samples can be created through a biaxial strain of a PDMS coupon using the 2D biaxial strain stage described in Chapter 3.1.2. In the experiment, the sample is clamped and stretched with a biaxial strain of 10% in the  $x$  and  $y$  direction, before undergoing plasma treatment ( $P = 20$  W,  $\tau = 60$  s). The simultaneous release of strain of the sample in a controlled manner results in a herringbone structure.

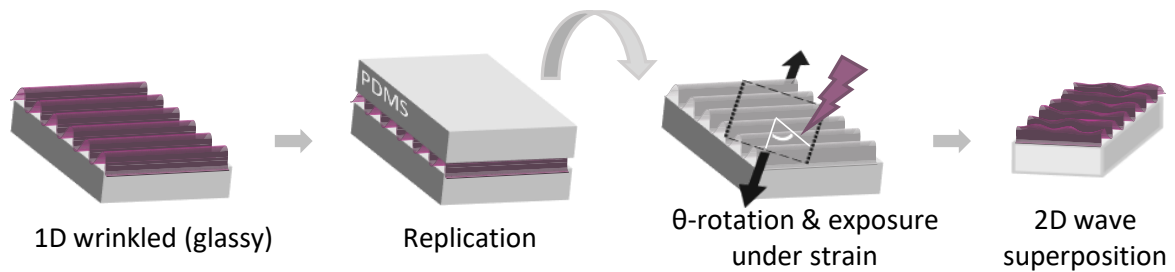


Figure 7.1: Schematic of 2D wrinkling pattern formation: An initial 1D wrinkled sample is replicated with fresh PDMS. The replica is then stretched uni-axially, rotated at an angle  $\theta$  and exposed to a second plasma oxidation. Upon release of the secondary strain, a secondary pattern is formed as result of a 2D Fourier wave superposition.

In the fabrication of 2D wrinkling through a sequential step, the first generation of wrinkles is referred to as “parallel”  $\parallel$  and the second generation referred to as “xz”. In the first instance, a standard 1D sample is fabricated through the plasma oxidation of a uniaxially stretched PDMS to produce a 1D pattern with periodicity  $\lambda_{\parallel}$  and amplitude  $A_{\parallel}$ , which are determined by the plasma and strain conditions. To achieve a 2D structure, the  $1D_{\parallel}$  master undergoes a replication step as described in Chapter 3.1.4. This replication steps involves the sample being coated with OTS by adsorption in the vapour phase in a dessicator for 30 minutes, before fresh PDMS is casted onto the the 1D master and cured at 75 °C for 1 h and carefully peeled off to produce the replica. The replicated sample is tilted to align the 1D pattern with the desired compression angle, and subsequently cropped into a rectangle to ensure uniformity during the secondary strain application and plasma oxidation step. After the strain is released, a  $2D_{\theta}$  pattern emerges

with a wavelength  $\theta_{xz}$  and amplitude  $A_{xz}$ , which determines the final topography through the interference of two superimposing wrinkling waves.

### 7.2.2 2D floating and lamination

The first generation specimen is then replicated by casting liquid PDMS made with 20:1 ratio of pre-polymer to curing agent onto the wrinkled ‘master’, previously coated with octadecyl trichlorosilane (OTS) (Acros Organics, 95%) from the vapour phase. The higher ratio is to induce higher tackiness for film adherence. The cast PDMS is then crosslinked at 75 °C for 1 hour and peeled off from the master. The replicated PDMS coupons were then stretched to the required prestrain, and polystyrene (PS) thin films were deposited on the surface using well-established floating procedures. Polystyrene ( $M_w = 100$  kg/mol) films were prepared by polymer dissolution into toluene to make up the appropriate concentrations for the film thickness required (0.01 mass fraction of polystyrene to toluene to make up a thickness of 30 nm). The solutions were then spun coated for 30 s at a speed of 2000 rpm to allow for the evaporation of solvent and the film formation, onto *Si* wafers which were cut into 1 cm<sup>2</sup> pieces and treated under UV ozonolysis (UVO) for 15 min to ensure hydrophilicity of its surface. The PS-coated wafer was then placed on the PDMS prestretched at a certain angle, with the PS side adhering to the surface. The sandwich was subsequently transferred to a petri dish filled with deionised water. Due to different surface energies, water preferentially adsorbs to the *Si* wafer, and detaches the film allowing it to be transferred to the PDMS surface. After 10 min, the *Si* wafer was carefully removed from the surface to prevent any delamination and the sample was dried under vacuum for 2 h under room temperature.

### 7.2.3 Thin film measurement

The thickness of polystyrene films were obtained with Filmetrics F20-UV. Prior to using the instrument, it must be first calibrated using a set of reference samples with known thickness and optical properties. The reference samples used for calibration have a similar structure

and composition to the samples being measured, and in this case we use  $SiO_2$  films on silicon substrate. After the calibration, the F20-UV can be used to accurately measure the thickness and optical properties of unknown thin films. The polystyrene samples were scanned within wavelengths of 200 - 1000 nm and checked with a goodness of at least 90%. Averages of the film at three different positions were taken to obtain the final film measurements.

#### 7.2.4 Pattern Characterisation

Wrinkle surfaces were obtained by atomic force microscopy (AFM) using a Bruker Innova microscope in tapping mode at 0.5 Hz with a Si tip (MPP-11100-W, Bruker). SLS experiments were carried out using the set up described in Chapter 3.2, comprising of a 532 nm, 100 mW diode pumped laser (CrystaLaser), spatial filter, double rotating filter wheel, imaging screen and 16-bit Hamamatsu Orca camera, cooled to  $-40\text{ }^\circ\text{C}$  to improve signal-to-noise ratio. To reduce the intensity of the direct beam, a circular beam stop that is opaque and black is used. Additionally, a neutral density filter wheel is used to attenuate the first and second generation orders selectively, in order to obtain more accurate measurements of distances and intensities. The camera is focused on the imaging screen, which captures pictures with  $512 \times 512$  pixels. These pictures are processed using ImageJ software. To measure the wavelength, the distance from the first diffraction order to the central direct beam is measured in both directions and then averaged. The compression angle is measured by determining the angle formed by two diffraction orders on either the right or left side and the direct beam. The images obtained from the SLS were analysed using ImageJ, to obtain the wavelengths and intensity. The optical microscopy analysis was carried out using an Olympus BX41M microscope in reflection mode using a 50X magnification, acquiring three images of  $500 \times 500\text{ }\mu\text{m}$  per sample, in different locations.

### 7.3 Wrinkling Superposition at various $\theta$

Non-orthogonal wrinkles were fabricated using the sequential method detailed in methodologies to examine individually the effect of  $\theta$  from  $0^\circ$  to  $90^\circ$ . In these initial experiments, the surfaces were fabricated employing symmetric couples of exposure times  $\tau_1 = \tau_2 = 120$  s, prestrain  $\varepsilon_1 = \varepsilon_2 = 10\%$  and plasma power  $P=20$  W. Upon release of the secondary strain application in the second wrinkling generation, a  $2D_\theta$  pattern is generated, which incorporates new features, denoted as  $\lambda_{xz}$  and  $A_{xz}$ , due to the superposition of the two 1D wrinkling waves. This approach produces a diverse range of patterns, as illustrated in Fig. 7.2, that are distinct from previously reported bi or multi-axial wrinkling patterns. For instance, when the angle between the generations is approximately  $\sim 30 - 60^\circ$ , patterns resembling sand ripples are formed, exhibiting a unique buckling instability in the  $xy$  plane. On the other hand, an orthogonal ( $90^\circ$ ) superposition results in checkerboard structures.

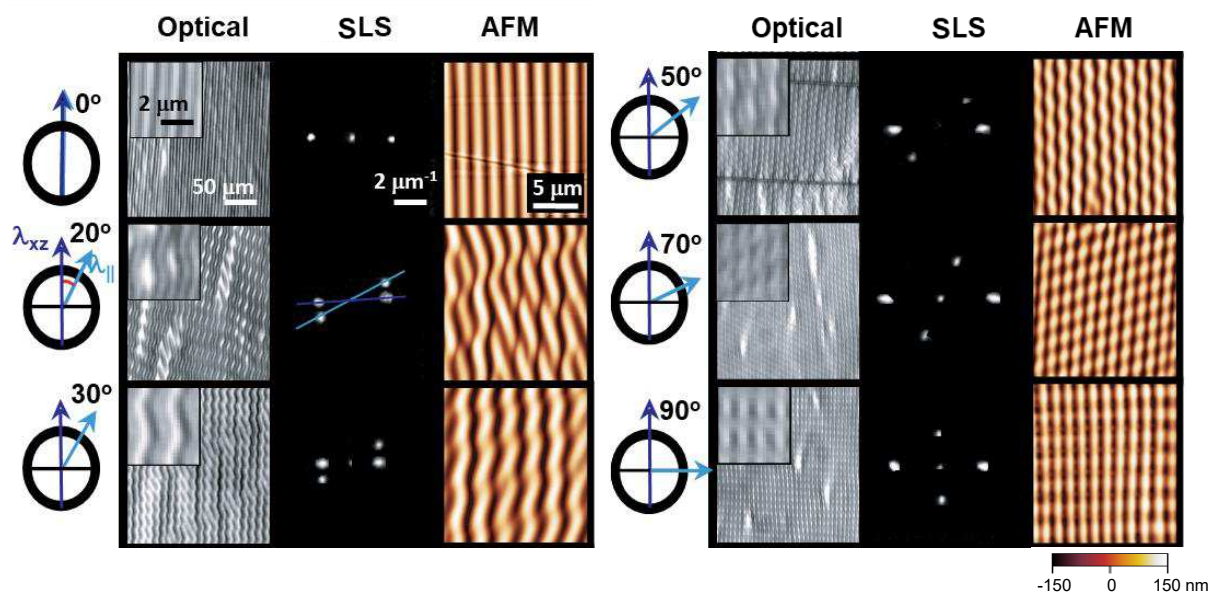


Figure 7.2: Schematic shows compression  $\theta$  angles, defined between first generation (cyan arrow) and second generation (blue, vertical arrow), with respective wavelength,  $\lambda_{\parallel}$  and  $\lambda_{xz}$ . Characterisation of sequential wrinkling topographies with  $\theta = 0$  to  $90^\circ$  performed by means of optical microscopy, static light scattering (SLS) and atomic force microscopy (AFM)

The topographical characterisation on 2D patterns at the various compression angles were obtained using different resolutions and magnifications, and presented in Fig. 7.2. Schematic representations of the two wrinkling generations are used to explain the specific orientations

that contribute to the final 2D pattern. The first generation is represented by a cyan arrow, oriented at the given angle  $\theta$ , while the second generation represented by a blue angle, which is always directed along the  $y$  axis. Each generation is characterised by a defined wavelength,  $\lambda_{||}$  for the first generation and  $\lambda_{xz}$ , formed by the superposition of the second generation in the  $xz$  plane. The pattern characterisation was carried out using optical and atomic force microscopy (AFM), as well as static light scattering (SLS). Optical images showed changes in the  $xy$  plane, from a vertical stripe arrangement for  $\theta = 0^\circ$  to a sinusoidal oscillation developed in the  $xy$  plane due to the interference of two superposed waves at two different orientations. Further increase in  $\theta$  led to a transition from 'sand ripple' to 'checkerboard' patterns, eventually reaching a "symmetric checkerboard" regime at  $90^\circ$ . The Fourier Transform images of the patterns were used to decouple the interference of the two wrinkling generations and to measure the compression angle  $\theta$  experimentally. When the samples were illuminated by a 532 nm laser diode, the diffraction pattern observed comprised of two series of spots representing the Fourier Transform of the two wrinkling generations in Fourier space, and symmetric with respect to the direct beam. From the spacing  $d$  between spots, the real space wave wrinkling wavelengths, and relative orientation of diffraction orders can be readily computed.

### **2D film lamination**

In order to establish the generality of our approach, an alternative bilayer formation procedure was explored, namely via polymer thin film deposition. To choose suitable conditions for the polystyrene film to match the wavelength required, a calibration of film thickness with mass fraction of polystyrene in toluene (PS-toluene) was first carried out.

In the 2D film lamination approach, we employ films made with a mass fraction of 0.01 to form the second generation. As per previous experiments, the formation of the first generation wrinkles was fabricated through the use of oxygen plasma exposure of PDMS, strain release and replicated. Subsequently, the polystyrene films were laminated on the prestrained 1D master at the desired  $\theta$  as described under the methodologies. In this case, the angles used were  $\theta = 20^\circ$  and  $70^\circ$ . Once the films were adhered, the strain was released to result in the 2D pattern.

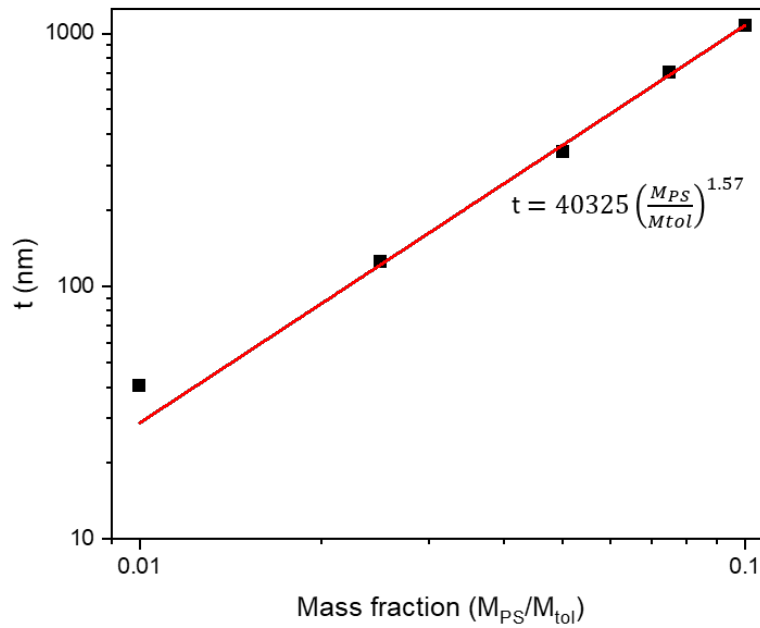


Figure 7.3: Calibration of PS film thickness with mass fraction of polystyrene-toluene solution

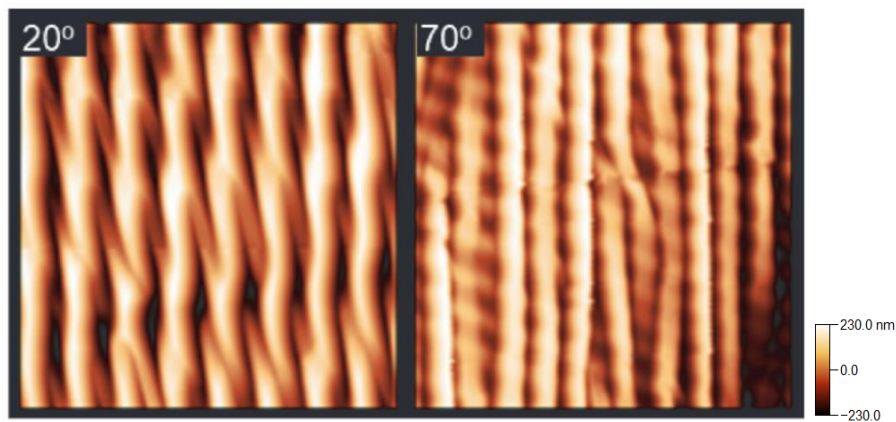


Figure 7.4: AFM structures of polystyrene film onto a pre patterned PDMS surface at 20° and 70°

AFM micrographs reported in Fig. 7.4 demonstrate the generality of the sand dunes interference pattern approach, whereby instead of glassy PDMS skins, the bilayer is now formed by conventional thin film lamination. Given the variation of mechanical moduli and film thicknesses accessible with different polymers and  $M_w$ , the accessible surface materials and topographies establish the versatility of the technique.



## 7.4 Real space reconstruction from 2D Diffraction Pattern

From Chapter 4, we have seen that 1D wrinkle surfaces can be ‘reconstructed’ from their diffraction patterns. Similarly, this concept can be applied to 2D surfaces as well with their diffraction properties. When 2D sample undergoes relaxation of its second generation strain, creating a ‘sand ripple’- like pattern which can be tuned with angle, 2 sets of first order intensities can be observed under SLS, each set corresponding to either the first or second generation.

In the reconstruction of the 2D real space image from the diffraction pattern, wavelengths and amplitudes from a 1D plasma-oxidised PDMS,  $P = 20\text{W}$ ,  $\tau = 120\text{s}$  were used in modelling the 1st order diffraction, shown in Fig. 7.5a. These values can be implemented to get intensity as a function of strain for this system, which can then be translated into amplitude.

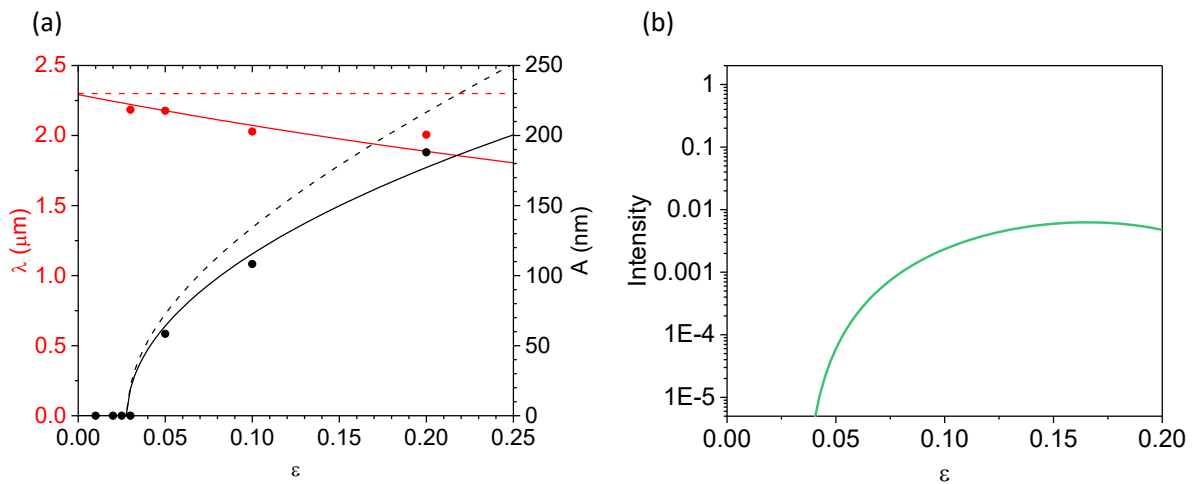


Figure 7.5: (a) Wavelength and amplitude models for plasma-oxidised PDMS at  $P = 20\text{ W}$ ,  $120\text{ s}$ . The values for  $\lambda$  and  $A$  are subsequently used in modelling the first diffraction order for the 2D samples (b) Modelled normalised intensity of first order for the sample as a function of strain,  $\varepsilon$

In a similar manner to the 1D case in Chapter 4, an intensity- $A$  model (Fig. 7.6b) can be established given wavelength and amplitude data (Fig. 8) with strain for the given conditions, according to Eqn. 5.1. From this relationship, by taking the ratio of intensities between the generations, the amplitudes of both the generations can be deduced from a model (Fig. 7.6a). For a 1D sample, the  $A$  for the maximum  $\varepsilon$  of 0.10 is  $0.115\ \mu\text{m}$ . When 2D samples with

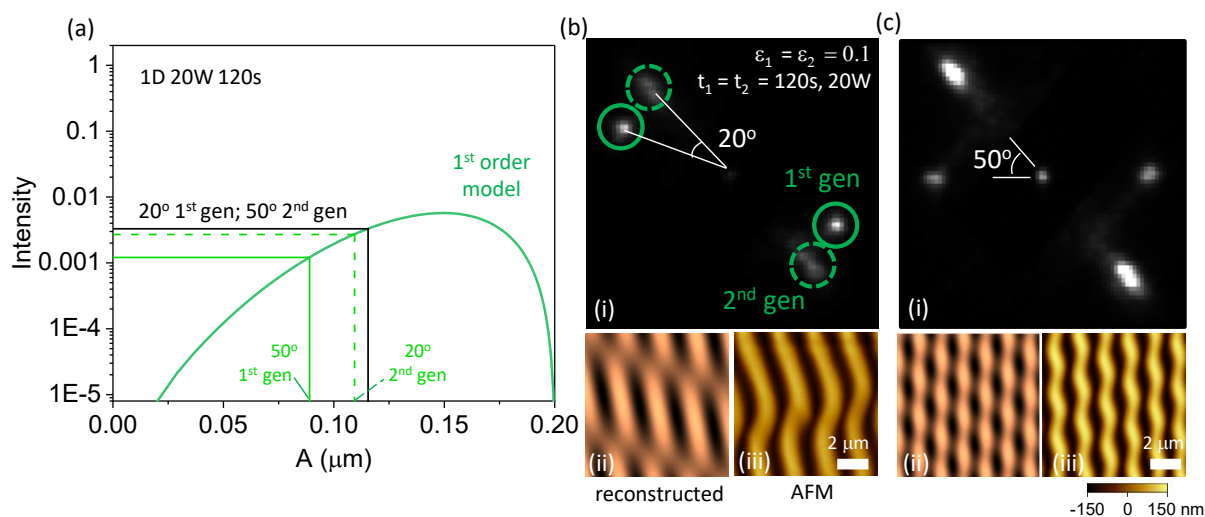


Figure 7.6: (a) Green solid line shows the first order intensity model at  $P = 20$  W,  $t = 120$  s. Black solid line shows the amplitude and intensity at  $\varepsilon = 0.1$  (experimental prestrain), with  $A = 0.11$  (maximum amplitude). At smaller angles, below the range of  $35$ - $45^\circ$ , the first generation component in the maximum amplitude is predominant, while at larger angles the 2nd generation component takes over. (c) Construction of a real space image of a 2D pattern. The SLS image of a 2D pattern with  $\theta = 20^\circ$  shows two sets of 1st order diffraction, belonging to the first and second generation, at an angle  $\theta$ . Wavelengths and amplitudes can be extracted and used to build a real-space image from the 2D SLS, shown in (ii). (d) For  $\theta = 50^\circ$ , the SLS image shows 2 sets of first order intensities separated by  $50^\circ$ , with intensity of the 2nd generation brighter than the 1st. The amplitude and wavelengths from the SLS allows for the reconstruction of real space image in (ii), agreeing with the experimental in (iii).

angles ranging from  $20^\circ$  to  $90^\circ$  are measured under light scattering, it is observed that there is a boundary between  $35$ - $45^\circ$ , where the intensity of the first generation exceeds that of the second below this range while the converse happens beyond. The evolution of 2D wrinkles with respect to the angular dependence can be observed via SLS. Due to the relationship between diffraction intensities and amplitude, the boundary where the 2nd generation of wrinkles dominates the 1st can be noted using the ratio of their respective 1st order diffraction intensities. We observe that this switch occurs within the boundary of  $35$ - $45^\circ$ , as a result we can ascertain that below this range, the first generation dominates the second while  $> 45^\circ$ , the converse occurs.

As a result, it can be observed that at  $20^\circ$ , the 1st generation is brighter than the 2nd (Fig. 7.6b), while at  $50^\circ$  the 2nd generation is more prominent (Fig. 7.6c). At lower angles where  $\theta < 35^\circ$ , the development of amplitude of the first generation takes precedence over the second, while when  $\theta > 45^\circ$ , the second generation formation dominates the first (Fig. 7.7). This

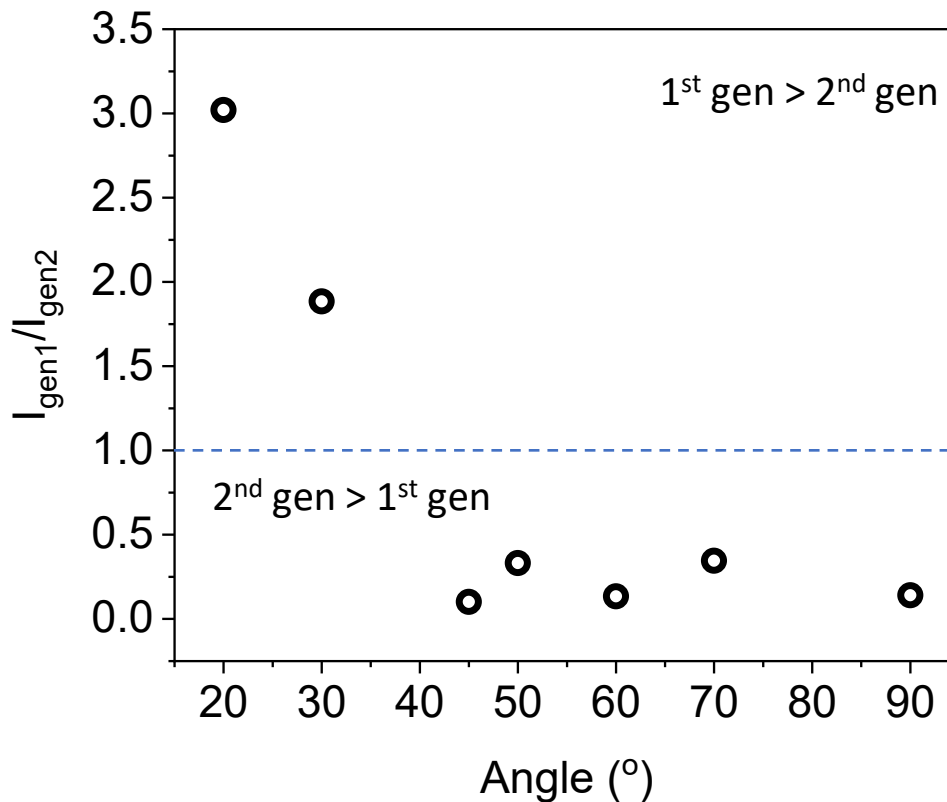


Figure 7.7: Ratio of diffraction intensities of the 1st generation to the 2nd generation are plotted against angular dependency. Below  $45^\circ$  where the ratio of intensities are more than 1.0, this indicates that the intensity of the 1st generation are greater than the 2nd, thus the domination of 1st generation compared to the 2nd. Where the ratio of intensities are less than 1.0 ( $\geq 45^\circ$ ), the 2nd generation can be shown to dominate.

is due to the relation of formation of the surface topography with respect to its principal coordinates  $x$  and  $y$ . When the second generation has a larger strain component in the  $y$  direction than  $x$ , it suppresses the amplitude in the first generation. As a result, when  $\theta = 20^\circ$  we can take the maximum amplitude to belong to the first generation while for  $\theta = 50^\circ$ , to the second generation. Subsequently, by taking the ratio of intensities of the two generations, the other generation can be deduced using the model. The wavelengths of the individual generations can be gathered as in the 1D case from the model in Fig. 7.5a. With both information of amplitude and wavelengths of the two cosine waves, a real space image can be reconstructed employing the model of superposition of waves as described in Eqn. 2.7, which is agreeable with the experimental AFM images.

## 7.5 Structural Colour of 2D samples

### 7.5.1 Varying $\theta$ angle 2D samples

Following from the 2D SLS images observed, we can expect these ‘sand ripples’ to exhibit colour about its  $\phi$  rotation (defined in Chapter 5 as the angle about the sample’s horizontal plane). This allows us to extend the idea of directionality first introduced in Chapter 5, where we aim to fabricate surfaces that can exhibit colours beyond a uniaxial direction. We thus investigate the effect of 2D structures in the context of structural colours, where we can further manipulate the colours exhibited depending on the observers’ perspective.

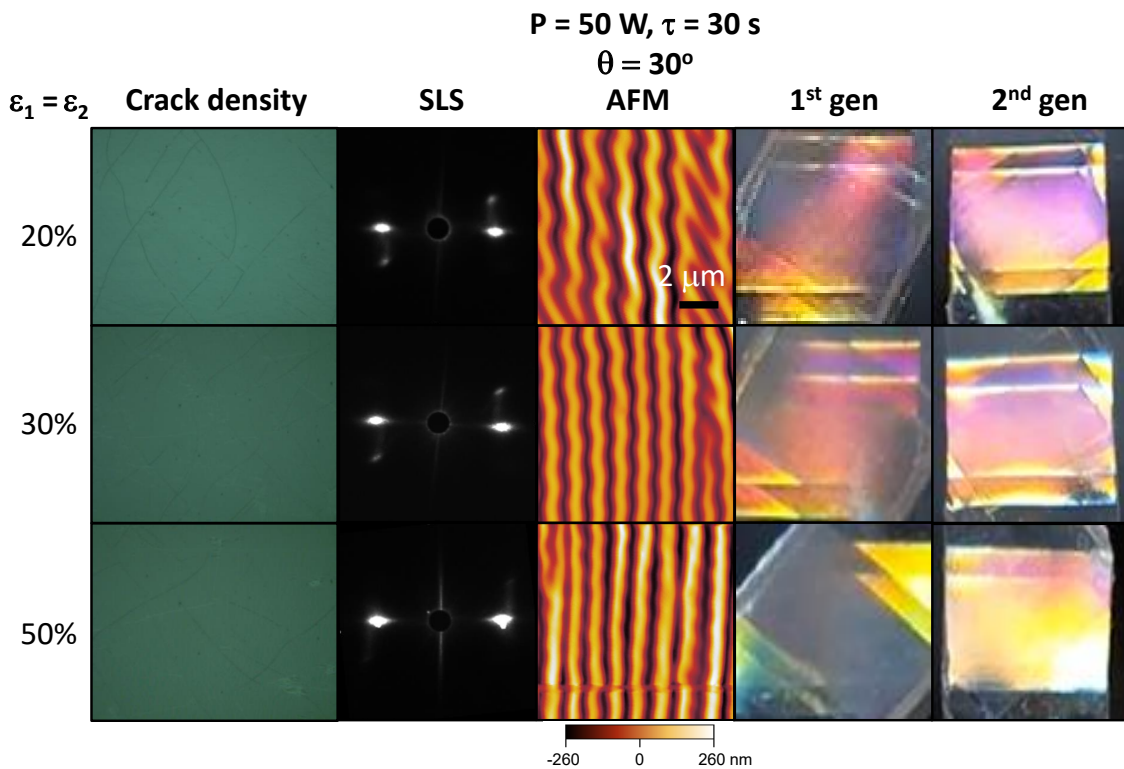


Figure 7.8: Characterisation of sequential wrinkling topographies with  $\theta = 30^\circ$  at varying strains where  $\varepsilon_1 = \varepsilon_2$  from 20 to 50%, performed by optical microscopy, static light scattering, and atomic microscopy. Structural colour images from the surfaces are observed with respect to their 1st and 2nd generation. Intensity of 1st generation decreases with increasing strain.

We first explore the effect of strain variation on these 2D samples at a fixed  $\theta = 30^\circ$ , varying  $\varepsilon_1 = \varepsilon_2$  from 20 to 50%. According to the bilayer equation, when strain is increased we can expect wrinkles to form with higher amplitudes, which could result in higher intensities. The

fabrication of 2D samples at a fixed angle between generation of  $\theta = 30^\circ$  was performed to explore the effect of strain in the structural colour observed. In both generations, the sample was exposed to plasma conditions of  $P = 50$  W,  $\tau = 30$  s, while both generations of strain  $\varepsilon_1$  and  $\varepsilon_2$  were changed simultaneously.

As  $\varepsilon$  increases, we find an increase in crack density in the surfaces when investigated under the optical microscope (Fig. 7.8). This is not surprising as, during plasma oxidation, reactive oxygen species are introduced to the surface of PDMS which can lead to the formation of cracks in the material. In general, higher strain during plasma oxidation of PDMS can result in more cracks in the sample as the increased strain causes the material to undergo more deformation. This in turn creates more opportunities for cracks to form. Additionally, the cracks that do form tend to be longer and more interconnected when the material is subjected to higher strain. As a result of the cracks, the first generation becomes less prominent as strain increases as shown in the SLS diffraction pattern. AFM images also start to deviate from a ‘sand ripple’ pattern towards a distorted 1D-like image with a less pronounced ripple-like topography. Converse to the initial hypothesis of a brighter structural colour resulting from a higher strain, we observe that the structural colour of the 1st generation significantly decreases in intensity, from a purple hue to white/colourless. This is likely owed to the formation of cracks in the first generation, leading to a scattering of light as  $\varepsilon$  approaches 50%.

Following from the investigation on the effect of strain, we proceed with the next set of experiments using  $\varepsilon = 20\%$  to minimise crack formation in the first generation, particularly through the replication step, to allow for structural colour to be better observed. We next investigate the effect of  $\theta$  on structural colour in the two generations, fabricating samples with the same plasma conditions as before ( $P = 50$  W,  $\tau = 30$  s) with  $\theta$  from  $20^\circ$  to  $70^\circ$  with  $\tau_1 = \tau_2 = 20\%$ . In Fig. 7.9, the surface characteristic of these surfaces were performed with SLS, AFM and optical imaging. In the SLS characterisation, the first generation of wrinkles are represented by the horizontal diffraction patterns, as seen in Fig. 7.2, and the second generation are at an angle of  $\theta$  with respect to the horizontal. The intensity of the second generation can be seen to decrease as  $\theta$  increases, where it becomes barely visible when  $\theta > 50^\circ$ . In the optical imag-

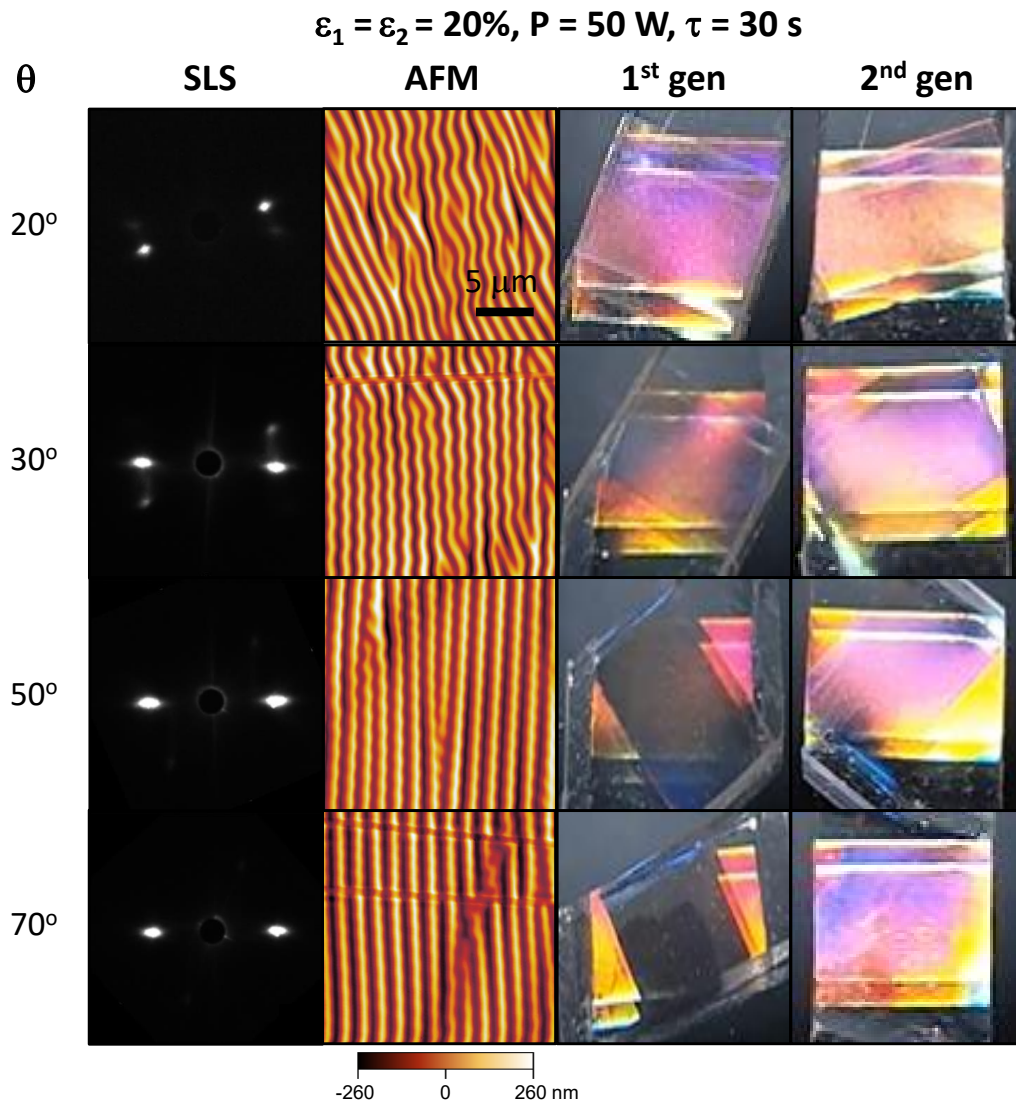


Figure 7.9: Characterisation of 2D surfaces at varying  $\theta$  from 20° to 70°, ( $P = 50 \text{ W}$ ,  $\tau = 30 \text{ s}$ ,  $\varepsilon_1 = \varepsilon_2 = 20\%$ ) using SLS, AFM and optical imaging of 1st and 2nd generation. Structural colour of 1st generation decreases with increasing  $\theta$ .

ing, the first generation and second generation images refer to the structural colour displayed when perpendicular to the direction of the wrinkles from that generation. As the samples were fabricated with the same plasma and strain conditions, we would expect the same colour to be observed for all samples. While the structural colour displayed with respect to the second generation appears to experience little deviation with  $\theta$ , it is apparent that this is not the case with the first generation. As  $\theta$  increases from 20° where the first generation clearly exhibits a strong purple, the intensity decreases when  $\theta$  approaches 70° where it appears to show no structural colour. This is the result of the relationship between the formation of the surface topography



and its principal coordinates  $x$  and  $y$ . When the second generation has a larger strain component in the  $y$  direction compared to the  $x$  direction, it suppresses the amplitude in the first generation to a greater extent. In this case, the first generation is dominated by the second and the resultant 2D topography acts similar to a 1D surface.

As a result of the observations in varying  $\theta$ , we seek to investigate the conditions in which structural colour could be observed in the first generation at high  $\theta$ , in particular when  $\theta = 70^\circ$ . In order to observe any structural colour in the first generation at high  $\phi$ , a large mismatch in strain and plasma conditions is required to compensate for the decrease in amplitude in the 1st generation. As a result, the 2D samples were fabricated at  $\theta = 70^\circ$  with the conditions of the first generation at  $P_1 = 50$  W,  $\tau_1 = 30$  s,  $\varepsilon_1 = 50\%$ , while decreasing the strain and plasma parameters of the second generations.

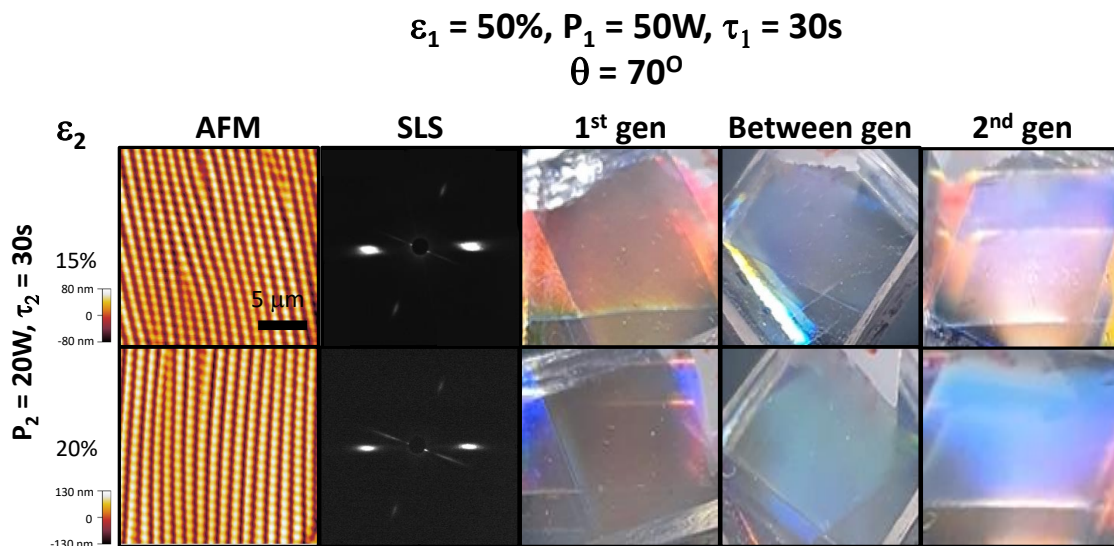


Figure 7.10: 2D structural colour parameters for  $\theta = 70^\circ$  to induce a mismatch in strain and plasma conditions: first generation conditions at  $P_1 = 50$  W,  $\tau_1 = 30$ s,  $\varepsilon_1 = 50\%$ , second generation conditions at  $P_2 = 20$  W,  $\tau_2 = 30$ s,  $\varepsilon_2 = 15\%$  (top row) or  $20\%$  (bottom row). Topography characterisation obtained by AFM, SLS and optical imaging. Optical imaging taken with respect to 1st generation, second generation and ‘between generation’ where  $\phi = \theta/2$  with respect to the first generation.

In Fig. 7.10, samples were fabricated with second generation plasma conditions of  $P_2 = 20$  W,  $\tau_2 = 30$ s, and strain of either  $\varepsilon_2 = 15\%$  (Fig. 7.10 top row) or  $20\%$  (bottom row). The lower plasma and strain conditions give rise to lower amplitudes in the secondary generation, which allows for

the first generation to be less ‘dominated’ by the second despite the larger strain component in the  $y$  direction. When  $\varepsilon_2 = 15\%$ , the resultant 2D surface give rise to three distinct colours that can be observed on the surface. When the observation angle  $\theta_{obs}$  is at  $35^\circ$ , the first generation gives a red hue while the second generation gives a blue-purple hue. A ‘between generation’ was also taken, which represents the perspective in the direction in between the two generations, where  $\phi = \theta/2$  at  $35^\circ$ , and this direction gives a blue hue. This is a result of the superposition of waves giving rise to a third intrinsic wavelength in the  $xy$  plane. When the strain is higher at  $\varepsilon_2 = 20\%$ , the first generation can be seen with a lower intensity, with a similar red hue due to the same first generation parameters. However the colour of the second variation changes slightly due to the higher strain, where the second generation shows a blue hue while ‘between generation’ shows a green-blue hue. This experiment shows not only that the conditions can be manipulated to overcome the domination of first generation wrinkles at higher  $\theta$  in 2D surfaces, but also we are able to fabricate surfaces to be multi-coloured with directionality.

### 7.5.2 Comparing $90^\circ$ simultaneous vs sequential 2D samples

Finally, we explore the structural colour of orthogonal 2D surfaces. As previously mentioned, these topographies can be fabricated either through a sequential or simultaneous step, where they will result in a checkerboard or herringbone pattern respectively.

A symmetrical checkerboard was achieved through a sequential step performed at  $90^\circ$  with the conditions stated in the experimental, achieving  $d = 680$  nm. When observed at  $\theta_{obs} = 40^\circ$ , a blue structural color can be observed at intervals of  $90^\circ$  along  $\phi$ , with no color exhibited at other angles, reflecting the orthogonal superimposed 1<sup>st</sup> and 2<sup>nd</sup> generation wrinkling waves, respectively at  $\phi = 0^\circ$  and  $\phi = 90^\circ$ . Therefore, the overall structural color is exhibited only alongside the specific generation orientation and not visible at other angles. On the other hand in a herringbone structure, arising from the simultaneous relaxation of a two-directional strain field, structural color can be observed for different  $\phi$ , however with varying intensities. Specifically, at  $\phi = 0^\circ$ , a lower intensity is observed progressively increasing at  $\phi = 45^\circ$  and  $\phi = 90^\circ$ . This can be ascribed to the more complex intrinsic morphology exhibited by the herringbone



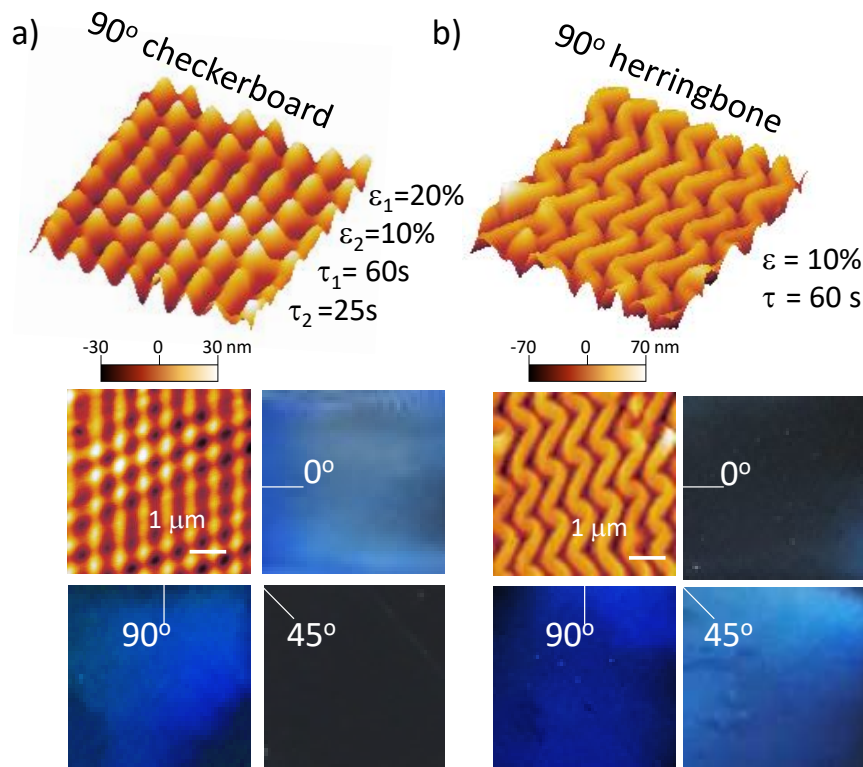


Figure 7.11: Structural color in  $90^\circ$  2D wrinkled surfaces. (a) Symmetrical checkerboard exhibiting colors in phases of  $90^\circ$ . At  $\theta_{obs}$  of  $40^\circ$ , a blue can be seen at  $\phi = 0^\circ$  and  $\phi = 90^\circ$  which “switches off” at  $\phi = 45^\circ$ . (b) In a herringbone structure, a rotation through  $\phi = 0$  to  $90^\circ$  shows a blue hue that varies in intensity.

pattern, where the color observed at  $\phi = 45^\circ$  is given by the overlap of two different periodicity, namely a “long”  $d$  ( $xy$  plane) along  $\phi = 90^\circ$ , giving a stronger blue reflectance, a “short”  $d$  ( $xz$  plane) showing a dimmer blue color.

## 7.6 Conclusion

This chapter investigates the use of non/orthogonal superposition of 1D wrinkling generations, with bilayer skins achieved through plasma oxidation and polymer film floating. Additionally, it examines the structural color displayed by different 2D structures. The main findings are as follows:

- By utilizing a variable compression angle in the sequential 2D wrinkling process, it becomes possible to create new 2D structures in a controlled manner. These structures, such as sand ripple patterns, resemble various natural formations such as geological metamorphic folds which occur due to the interference pattern of two superimposed wrinkling waves.
- It is possible to apply the same method to various bilayers by using a hard polymer thin film like polystyrene and laminating it onto a pre-patterned PDMS coupon. This leads to the creation of similar undulated structures.
- Structural colour observed through these fabricated 2D structures can be tuned through varying the angle of wave superposition  $\theta$  along with plasma and strain conditions. At higher  $\theta$ , strain mismatch can be induced to tailor the surface topography such that structural colour is visible from both generations fabricated.
- This method provides the possibility to explore and create large-scale patterns that would not normally be selected due to unfavourable energetic conditions, and allow for the design of multi-coloured surfaces with directionality.

# Chapter 8

## Conclusions

This thesis has explored the formation and fabrication of bioinspired topographies by means of wrinkling, specifically uniaxial, isotropic and sequential wave superpositions structures which can exhibit optical properties such as structural colour. These surfaces can act as diffraction gratings, allowing them to have optical properties which can be tuned by fabrication conditions. We take advantage of inducing pattern formation on elastomeric substrates by utilising mechanical buckling instability phenomena found in both natural and synthetic soft materials. This can be achieved through the plasma oxidation of PDMS and subsequent application of mechanical strain on the resulting bilayer structure. By carefully selecting and adjusting the experimental parameters, this approach is considerably simpler, removing the need to float and deposit the glassy film, as well as more robust, by ensuring covalent bonding of the skin layer and preventing delamination or crumpling.

We first started this project in Chapter 4 by employing the use of plasma oxidation of PDMS in the fabrication of a simple tunable, sinusoidal phase grating in uniaxial direction. We sought to understand and model the behaviour of this phase grating, which is able to modulate its diffraction intensity with strain. Due to the gradient nature of the glassy skin layer as a result of the plasma oxidation process, we were able to incorporate a distribution of refractive index in the skin formed in order to successfully model and quantify the diffraction data. We also considered the non-Hookean properties of PDMS due to the change in elastic modulus at sufficiently high

strain. Significantly, the process of monitoring this tunable phase grating under static light scattering (SLS) allows for the observation in the emergence of an additional diffraction order when the grating undergoes sufficiently high strain to form ‘period doubling’. We have also established the method of SLS to be a fast and efficient tool for determining the surface topology of such gratings through their diffraction patterns.

Having established how these tunable sinusoidal phase gratings behave under monochromatic light, we proceed to investigate its properties under white light where we begin to explore the structural colour of these surfaces in Chapter 4. The generation of 1D surfaces and isotropic wrinkling patterns were fabricated by plasma oxidation of carbon-doped PDMS and mechanical or thermally-induced buckling. With plasma oxidation of PDMS, the characteristic wavelength and amplitude of the resultant sinusoidal patterns are proportional to the thickness and elastic modulus of the film and decrease with substrate stiffness. With this, by employing the two plasma chambers available we were able to fabricate wrinkles ranging from hundreds of nanometres to a few microns. We could then benchmark and quantify the impact of surface periodicity in the accessible colours upon inspection of the mechanochromic responses of these surfaces. We evaluated the effect of colour mixing due to the overlap of diffraction orders and the interplay between illumination and viewing angles. Expanding on uniaxially strained surfaces, we fabricated more complex topographies through inducing a gradient in pattern periodicity and amplitude through stepwise exposure or a gradient strain field. These surface patterns are able to exhibit either spatially uniform colour or enhanced ‘rainbow’ colour depending on the observation angle. In this chapter, we also start to explore the idea of directionality of structural colour through the fabrication of isotropic wrinkled surfaces which can exhibit colour at all  $\phi$  angles around the patterned surface.

In Chapter 6, we built on the previous chapter’s foundations to explore the fabrication of multi-facet structural colours on wrinkled surfaces. Although the principles of diffraction grating produce typically only surface structural colour, this concept allows the wrinkled material to exhibit a ‘3D-like’ structural colour. When fabricating wrinkles on undoped PDMS, diffraction can occur in reflection mode (which we saw in Chapter 5), or in transmission mode. Light that

is diffracted in transmission mode can undergo total internal reflection, eventually exited on the edge of the sample which we term the facet to result in facet TIR colour. With this mechanism, we establish and validate design principles in which only a certain sub-set of diffracted colours at distinct angles, will be propagated by TIR, while the remainder is refracted out of the material resulting in a colour selection that is distinct from the diffracted surface colours. In this work, we also show that there is a limit in which this facet colour can manifest due to the interference of colours as the wrinkle periodicities increase. This phenomenon is only limited to wrinkle periodicities below  $\approx 1.2 \mu\text{m}$ . Additionally, we have also demonstrated that a change in external environment such as the shape of the sample, the presence of solvents, or integrating it with different materials can alter the appearance of structural colour of the facets of the wrinkled samples.

In the final section of this thesis, we further extended the patterning possibility to the fabrication of 2D structures through wave superposition and explored their structural colour properties. The initial focus of our study involved creating 2D wrinkling patterns that were not orthogonal. We accomplished this by utilizing varying compression angles between the two generations in the sequential 2D wrinkling process. As a result, we were able to produce novel 2D interference structures that resemble patterns found in sand ripples. This technique is both easy to implement and can be scaled up, allowing for the creation of a diverse array of undulated patterns. These patterns can be further modified by adjusting plasma and strain parameters, as well as controlling the superposition angle  $\theta$ . Furthermore, this method is not limited to the plasma oxidation of PDMS but can be extended to different bilayers. We show that these patterns can be fabricated by laminating a polystyrene thin film onto a pre-patterned PDMS sample, which results in similar topography. We next explore the optical properties of these 2D structures, which produce two sets of diffraction patterns under monochromatic light. Similar to Chapter 4, a reconstruction of their topography can be performed utilising their intensities of their diffraction image. The structural colour of these 2D surfaces were studied in terms of varying strain,  $\theta$ , where we found that structural colour in the first generation diminishes with increasing  $\theta$ . As a result, we sought to explore conditions that would allow structural colour to be visible with respect to both the first and second generation when  $\theta = 70^\circ$ . Finally, we fabricated orthogo-

nal 2D surfaces through sequential and simultaneous methods which resulted in checkerboard and herringbone patterns respectively, comparing the behaviour of structural colour between the two.

All the results presented highlight how wrinkling serves as an effective means to fabricate varying topographies to achieve a library of structural colours. Although the use of plasma oxidation have been a primary method to fabricate such surfaces in this work, there are many other means to achieve similar topographies which could also exhibit colour through the principles of diffraction grating.

Numerous possibilities remain open for future research on structural colour from wrinkling methods. Beyond simple uniaxial patterns, a wrinkling process that has not been covered within the scope of the thesis are hierarchical structures. Hierarchical structures can be fabricated where the topography consists of wrinkles of different periodicities and are commonly produced through sequential strain release [165] or via the use of wrinkled templates [166]. Although studies have shown that these structures contribute to broad-angle structural colour [38], a possible effect that could arise due to the different periodicities is colour mixing. When wrinkles of different periodicities interact with light, this could result in different wavelengths of light diffracted from the surface which could potentially show interesting structural colours. Additionally within the scope of this research, we find limitations with the method employed, such as the occurrence of cracking on the surface upon wrinkling generation where we have observed in Chapter 7 can become an issue in the generation of structural colour in 2D surfaces. Some studies have shown that by generating a soft skin on the PDMS surface such as the use of fluoropolymer skin, this enables the formation of crack-free wrinkles [167]. Future work could include the use of such skins in the design of structural coloured wrinkles, allowing for reversible mechanochromic responses that can be cycled repeatedly with minimal development of cracks.

Additionally, although wrinkling is found to occur naturally on soft matter due to buckling when strain is applied to a bi-layer of mismatched elastic modulus, wrinkles could be replicated onto a harder, more durable substrate. PDMS, despite having many advantageous such as its

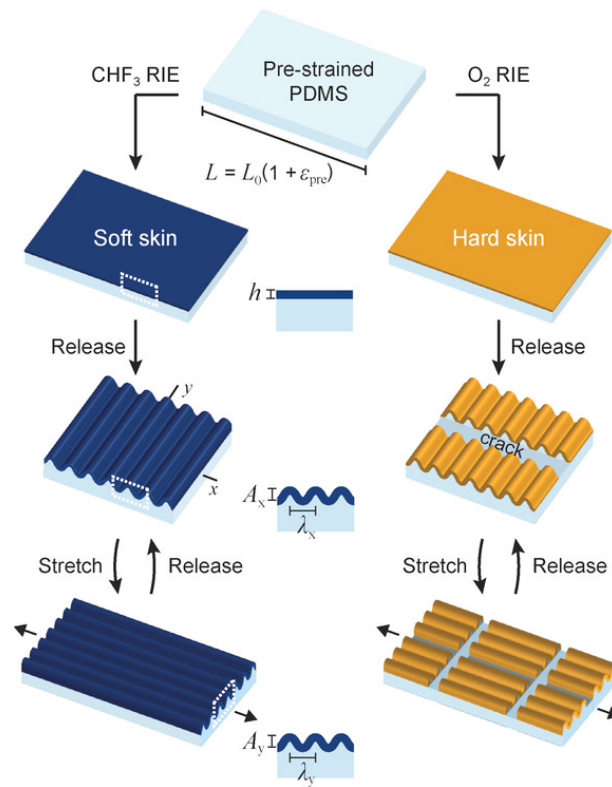


Figure 8.1: Treatment of PDMS skin with  $CHF_3$  yields softer skin yielding crack-free wrinkles upon strain, compared to that with  $O_2$  which results in a harder skin, prone to cracking with strain. Reproduced from [167] with permission from John Wiley and Sons.

optical transparency and its easily tunable properties, its tackiness can cause issues in the field of optics due to its ability to attract dirt and dust on its surface. This was found to affect the quality of colours displayed by the wrinkled PDMS surfaces in some instances due to the optical clarity. Further research could be carried out on different types of materials, to explore the ideal material for different applications as required. As with nature, wrinkled topographies can also be incorporated with other structural colour mechanisms such as photonic crystals in order to enhance their optical effects. For example, recent works by Lim *et al.* [168] report the fabrication of wrinkled photonic crystal papers to demonstrate the consistent reflection of colors regardless of viewing angles.

Overall, there is clearly plenty more to explore in this design space with wrinkling and structural colour observation, and we anticipate that the findings in this work to be relevant across a wide range of applications including in displays, packaging and sensors.

# Bibliography

- [1] D. E. Packham, “Surface energy, surface topography and adhesion,” *International journal of adhesion and adhesives*, vol. 23, no. 6, pp. 437–448, 2003.
- [2] J. Sun, B. Bhushan, and J. Tong, “Structural coloration in nature,” *RSC Advances*, vol. 3, pp. 14862–14889, 2013.
- [3] B. J. Papenburg, E. D. Rodrigues, M. Wessling, and D. Stamatialis, “Insights into the role of material surface topography and wettability on cell-material interactions,” *Soft Matter*, vol. 6, no. 18, pp. 4377–4388, 2010.
- [4] A. R. Parker, “515 million years of structural colour,” *Journal of Optics A: Pure and Applied Optics*, vol. 2, no. 6, p. R15, 2000.
- [5] T. B. H. Schroeder, J. Houghtaling, B. D. Wilts, and M. Mayer, “It ’ s Not a Bug , It ’ s a Feature : Functional Materials in Insects,” *Advanced Materials*, vol. 30, no. 1705322, pp. 1–48, 2018.
- [6] M. Kumar and R. Bhardwaj, “Wetting characteristics of colocasia esculenta (taro) leaf and a bioinspired surface thereof,” *Scientific reports*, vol. 10, no. 1, pp. 1–15, 2020.
- [7] K. Autumn, M. Sitti, Y. A. Liang, A. M. Peattie, W. R. Hansen, S. Sponberg, T. W. Kenny, R. Fearing, J. N. Israelachvili, and R. J. Full, “Evidence for van der waals adhesion in gecko setae,” *Proceedings of the National Academy of Sciences*, vol. 99, no. 19, pp. 12252–12256, 2002.



- [8] J. Teyssier, S. V. Saenko, D. Van Der Marel, and M. C. Milinkovitch, “Photonic crystals cause active colour change in chameleons,” *Nature communications*, vol. 6, no. 1, pp. 1–7, 2015.
- [9] L. M. Mäthger, E. J. Denton, N. J. Marshall, and R. T. Hanlon, “Mechanisms and behavioural functions of structural coloration in cephalopods,” *Journal of the Royal Society Interface*, vol. 6, no. suppl\_2, pp. S149–S163, 2009.
- [10] C. Spence, “The tongue map and the spatial modulation of taste perception,” *Current Research in Food Science*, 2022.
- [11] K. Nassau, *Color for science, art and technology*. Elsevier, 1997.
- [12] C. L. BOOTH, “Evolutionary significance of ontogenetic colour change in animals,” *Biological Journal of the Linnean Society*, vol. 40, no. 2, pp. 125–163, 1990.
- [13] S. Kinoshita and S. Yoshioka, “Structural Colors in Nature : The Role of Regularity and Irregularity in the Structure,” *ChemPhysChem*, vol. 6, pp. 1442–1459, 2005.
- [14] R. K. Cersonsky, J. Antonaglia, B. D. Dice, and S. C. Glotzer, “The diversity of three-dimensional photonic crystals,” *Nature Communications*, vol. 12, no. 1, p. 2543, 2021.
- [15] K. Hou, W. Ali, J. Lv, J. Guo, L. Shi, B. Han, X. Wang, and Z. Tang, “Optically active inverse opal photonic crystals,” *Journal of the American Chemical Society*, vol. 140, no. 48, pp. 16446–16449, 2018.
- [16] S.-W. Chen, J.-Y. Lu, P.-H. Tung, J.-H. Lin, M. Chiesa, B.-Y. Hung, and T. C.-K. Yang, “Study of laser actions by bird’s feathers with photonic crystals,” *Scientific Reports*, vol. 11, no. 1, p. 2430, 2021.
- [17] J. W. Galusha, L. R. Richey, M. R. Jorgensen, J. S. Gardner, and M. H. Bartl, “Study of natural photonic crystals in beetle scales and their conversion into inorganic structures via a sol–gel bio-templating route,” *Journal of Materials Chemistry*, vol. 20, no. 7, pp. 1277–1284, 2010.

- [18] H. M. Whitney, M. Kolle, P. Andrew, L. Chittka, U. Steiner, and B. J. Glover, “Floral iridescence, produced by diffractive optics, acts as a cue for animal pollinators,” *Science*, vol. 323, no. 5910, pp. 130–133, 2009.
- [19] A. L. Ingram, V. Lousse, A. R. Parker, and J. P. Vigneron, “Dual gratings interspersed on a single butterfly scale,” *Journal of the Royal Society Interface*, vol. 5, no. 28, pp. 1387–1390, 2008.
- [20] A. G. Dumanli and T. Savin, “Recent advances in the biomimicry of structural colours,” *Chemical Society Reviews*, vol. 45, no. 24, pp. 6698–6724, 2016.
- [21] H. Hinton and D. Gibbs, “Diffraction gratings in phalacrid beetles,” *Nature*, vol. 221, no. 5184, pp. 953–954, 1969.
- [22] L. Wei, K. E. Reiter, T. McElrath, M. Alleyne, and A. C. Dunn, “Diffraction gratings alter the surface friction of iridescent beetle cuticle against fibrous surfaces,” *Biotribology*, vol. 20, p. 100108, 2019.
- [23] C. Ruedt, M. Gibis, S. Barbut, and J. Weiss, “Colour change with longitudinal compression supports hypothesis of multilayer interference as cause for meat iridescence,” *International Journal of Food Science & Technology*, vol. 56, no. 1, pp. 250–258, 2021.
- [24] J. L. Martinez-Hurtado, M. S. Akram, and A. K. Yetisen, “Iridescence in meat caused by surface gratings,” *Foods*, vol. 2, no. 4, pp. 499–506, 2013.
- [25] J. H. Oh, J. Y. Woo, S. Jo, and C.-S. Han, “Iridescent and glossy effect on polymer surface using micro-/nanohierarchical structure: Artificial queen of the night tulip petals,” *ACS applied materials & interfaces*, vol. 11, no. 29, pp. 26442–26447, 2019.
- [26] A. Ingram and A. Parker, “A review of the diversity and evolution of photonic structures in butterflies, incorporating the work of John Huxley (the natural history museum, London from 1961 to 1990),” *Philosophical Transactions of the Royal Society B: Biological Sciences*, vol. 363, no. 1502, pp. 2465–2480, 2008.

- [27] T. Tan, D. Wong, and P. Lee, “Iridescence of a shell of mollusk *haliotis glabra*,” *Optics express*, vol. 12, no. 20, pp. 4847–4854, 2004.
- [28] A. E. Seago and Q. D. Wheeler, “Two new species of aglyptinus cockerell with unusual sexually dimorphic antennae and diffraction gratings (coleoptera: Leiodidae),” *The Coleopterists Bulletin*, vol. 58, no. 2, pp. 235–244, 2004.
- [29] A. E. Seago, P. Brady, J.-P. Vigneron, and T. D. Schultz, “Gold bugs and beyond: a review of iridescence and structural colour mechanisms in beetles (coleoptera),” *Journal of the Royal Society Interface*, vol. 6, no. suppl\_2, pp. S165–S184, 2009.
- [30] S. Kinoshita, S. Yoshioka, and K. Kawagoe, “Mechanisms of structural colour in the morphe butterfly: cooperation of regularity and irregularity in an iridescent scale,” *Proceedings of the Royal Society of London. Series B: Biological Sciences*, vol. 269, no. 1499, pp. 1417–1421, 2002.
- [31] P. Vukusic, J. Sambles, C. Lawrence, and R. Wootton, “Quantified interference and diffraction in single morphe butterfly scales,” *Proceedings of the Royal Society of London. Series B: Biological Sciences*, vol. 266, no. 1427, pp. 1403–1411, 1999.
- [32] T.-L. Gluckman and G. Cardoso, “The dual function of barred plumage in birds: camouflage and communication,” *Journal of Evolutionary Biology*, vol. 23, no. 11, pp. 2501–2506, 2010.
- [33] M. D. Shawkey and L. D’Alba, “Interactions between colour-producing mechanisms and their effects on the integumentary colour palette,” *Philosophical Transactions of the Royal Society B: Biological Sciences*, vol. 372, no. 1724, p. 20160536, 2017.
- [34] H. Gruson, M. Elias, C. Andraud, C. Djediat, S. Berthier, C. Doutrelant, and D. Gomez, “Hummingbird iridescence: an unsuspected structural diversity influences colouration at multiple scales,” *BioRxiv*, p. 699744, 2019.
- [35] K. M. Kocot, F. Aguilera, C. McDougall, D. J. Jackson, and B. M. Degnan, “Sea shell diversity and rapidly evolving secretomes: insights into the evolution of biomineralization,” *Frontiers in zoology*, vol. 13, pp. 1–10, 2016.

- [36] J. Wang, X. Peng, and C. W. Yuan, "Periodic structure of blaze grating in abalone shell," in *Key Engineering Materials*, vol. 288, pp. 669–672, Trans Tech Publ, 2005.
- [37] C. A. Airoidi, C. A. Lugo, R. Wightman, B. J. Glover, and S. Robinson, "Mechanical buckling can pattern the light-diffracting cuticle of hibiscus trionum," *Cell Reports*, vol. 36, no. 11, p. 109715, 2021.
- [38] C. Chen, C. A. Airoidi, C. A. Lugo, R. K. Bay, B. J. Glover, and A. J. Crosby, "Flower inspiration: Broad-angle structural color through tunable hierarchical wrinkles in thin film multilayers," *Advanced Functional Materials*, vol. 31, no. 5, p. 2006256, 2021.
- [39] X. Huang, Y. Hai, and W.-H. Xie, "Anisotropic cell growth-regulated surface micropatterns in flower petals," *Theoretical and Applied Mechanics Letters*, vol. 7, no. 3, pp. 169–174, 2017.
- [40] M. Nixon, A. Orr, and P. Vukusic, "Wrinkles enhance the diffuse reflection from the dragonfly rhythemis resplendens," *Journal of the Royal Society Interface*, vol. 12, no. 103, p. 20140749, 2015.
- [41] E. Moyroud, C. A. Airoidi, J. Ferria, C. Giorio, S. S. Steimer, P. J. Rudall, C. J. Prychid, S. Halliwell, J. F. Walker, S. Robinson, *et al.*, "Cuticle chemistry drives the development of diffraction gratings on the surface of hibiscus trionum petals," *Current Biology*, vol. 32, no. 24, pp. 5323–5334, 2022.
- [42] R. L. A. Kourounioti, L. R. Band, J. A. Fozard, A. Hampstead, A. Lovrics, E. Moyroud, S. Vignolini, J. R. King, O. E. Jensen, and B. J. Glover, "Buckling as an origin of ordered cuticular patterns in flower petals," *Journal of the Royal Society Interface*, vol. 10, no. 80, 2013.
- [43] T. Ohzono, K. Suzuki, T. Yamaguchi, and N. Fukuda, "Tunable Optical Diffuser Based on Deformable Wrinkles," *Advanced Optical Materials*, vol. 1, pp. 374–380, 2013.
- [44] L. P. Biro and J.-P. Vigneron, "Photonic nanoarchitectures in butterflies and beetles : valuable sources for bioinspiration," *Laser Photonics Rev.*, vol. 5, no. 1, pp. 27–51, 2011.

- [45] R. A. Potyrailo, H. Ghiradella, A. Vertiatchikh, K. Dovidenko, J. R. Cournoyer, and E. Olson, "Morpho butterfly wing scales demonstrate highly selective vapour response," *Nature Photonics*, vol. 1, no. 2, pp. 123–128, 2007.
- [46] A. D. Pris, Y. Utturkar, C. Surman, W. G. Morris, A. Vert, S. Zalyubovskiy, T. Deng, H. T. Ghiradella, and R. A. Potyrailo, "Towards high-speed imaging of infrared photons with bio-inspired nanoarchitectures," *Nature Photonics*, vol. 6, no. 3, pp. 195–200, 2012.
- [47] F. Zhang, Q. Shen, X. Shi, S. Li, W. Wang, Z. Luo, G. He, P. Zhang, P. Tao, C. Song, *et al.*, "Infrared detection based on localized modification of morpho butterfly wings," *Advanced materials*, vol. 27, no. 6, pp. 1077–1082, 2015.
- [48] Q. Li, Q. Zeng, L. Shi, X. Zhang, and K.-Q. Zhang, "Bio-inspired sensors based on photonic structures of morpho butterfly wings: a review," *Journal of Materials Chemistry C*, vol. 4, no. 9, pp. 1752–1763, 2016.
- [49] Z. Mu, X. Zhao, Z. Xie, Y. Zhao, Q. Zhong, L. Bo, and Z. Gu, "In situ synthesis of gold nanoparticles (aunps) in butterfly wings for surface enhanced raman spectroscopy (sers)," *Journal of Materials Chemistry B*, vol. 1, no. 11, pp. 1607–1613, 2013.
- [50] J. He, Q. Shen, S. Yang, G. He, P. Tao, C. Song, J. Wu, T. Deng, and W. Shang, "Coupling effects in 3d plasmonic structures templated by morpho butterfly wings," *Nanoscale*, vol. 10, no. 2, pp. 533–537, 2018.
- [51] J. A. Rogers, T. Someya, and Y. Huang, "Materials and mechanics for stretchable electronics," *science*, vol. 327, no. 5973, pp. 1603–1607, 2010.
- [52] Z. Li, Y. Zhai, Y. Wang, G. M. Wendland, X. Yin, and J. Xiao, "Harnessing surface wrinkling–cracking patterns for tunable optical transmittance," *Advanced Optical Materials*, vol. 5, no. 19, p. 1700425, 2017.
- [53] F. Li, H. Hou, J. Yin, and X. Jiang, "Near-infrared light–responsive dynamic wrinkle patterns," *Science Advances*, vol. 4, no. 4, p. eaar5762, 2018.

- [54] S. Zeng, R. Li, S. G. Freire, V. M. Garbellotto, E. Y. Huang, A. T. Smith, C. Hu, W. R. Tait, Z. Bian, G. Zheng, *et al.*, “Moisture-responsive wrinkling surfaces with tunable dynamics,” *Advanced Materials*, vol. 29, no. 24, p. 1700828, 2017.
- [55] J. B. Kim, P. Kim, N. C. Pégard, S. J. Oh, C. R. Kagan, J. W. Fleischer, H. A. Stone, and Y.-L. Loo, “Wrinkles and deep folds as photonic structures in photovoltaics,” *Nature Photonics*, vol. 6, no. 5, pp. 327–332, 2012.
- [56] M. G. Debiije, “Solar energy collectors with tunable transmission,” *Advanced Functional Materials*, vol. 20, no. 9, pp. 1498–1502, 2010.
- [57] C. Bechinger, S. Ferrere, A. Zaban, J. Sprague, and B. A. Gregg, “Photoelectrochromic windows and displays,” *Nature*, vol. 383, no. 6601, pp. 608–610, 1996.
- [58] C. M. Lampert, “Chromogenic smart materials,” *Materials today*, vol. 7, no. 3, pp. 28–35, 2004.
- [59] D. Ge, E. Lee, L. Yang, Y. Cho, M. Li, D. S. Gianola, and S. Yang, “A robust smart window: reversibly switching from high transparency to angle-independent structural color display,” *Advanced Materials*, vol. 27, no. 15, pp. 2489–2495, 2015.
- [60] M. Shrestha, A. Asundi, and G.-K. Lau, “Smart window based on electric unfolding of microwrinkled tio<sub>2</sub> nanometric films,” *Acs Photonics*, vol. 5, no. 8, pp. 3255–3262, 2018.
- [61] J. Li, X. Lu, Y. Zhang, X. Ke, X. Wen, F. Cheng, C. Wei, Y. Li, K. Yao, and S. Yang, “Highly sensitive mechanoresponsive smart windows driven by shear strain,” *Advanced Functional Materials*, vol. 31, no. 32, p. 2102350, 2021.
- [62] B. Jiang, L. Liu, Z. Gao, and W. Wang, “A general and robust strategy for fabricating mechanoresponsive surface wrinkles with dynamic switchable transmittance,” *Advanced Optical Materials*, vol. 6, no. 13, p. 1800195, 2018.
- [63] K. Wu, Y. Sun, H. Yuan, J. Zhang, G. Liu, and J. Sun, “Harnessing dynamic wrinkling surfaces for smart displays,” *Nano Letters*, vol. 20, no. 6, pp. 4129–4135, 2020.

- [64] R. Huang and Z. Suo, “Wrinkling of a compressed elastic film on a viscous layer,” *Journal of Applied Physics*, vol. 91, no. 3, pp. 1135–1142, 2002.
- [65] R. Nur, N. Matsuhisa, Z. Jiang, M. O. G. Nayeem, T. Yokota, and T. Someya, “A highly sensitive capacitive-type strain sensor using wrinkled ultrathin gold films,” *Nano letters*, vol. 18, no. 9, pp. 5610–5617, 2018.
- [66] Y. Zheng, Y. Li, Y. Zhou, K. Dai, G. Zheng, B. Zhang, C. Liu, and C. Shen, “High-performance wearable strain sensor based on graphene/cotton fabric with high durability and low detection limit,” *ACS applied materials & interfaces*, vol. 12, no. 1, pp. 1474–1485, 2019.
- [67] L. Miao, J. Wan, Y. Song, H. Guo, H. Chen, X. Cheng, and H. Zhang, “Skin-inspired humidity and pressure sensor with a wrinkle-on-sponge structure,” *ACS applied materials & interfaces*, vol. 11, no. 42, pp. 39219–39227, 2019.
- [68] J. Jia, G. Huang, J. Deng, and K. Pan, “Skin-inspired flexible and high-sensitivity pressure sensors based on rgo films with continuous-gradient wrinkles,” *Nanoscale*, vol. 11, no. 10, pp. 4258–4266, 2019.
- [69] G. Lee, G. Y. Bae, J. H. Son, S. Lee, S. W. Kim, D. Kim, S. G. Lee, and K. Cho, “User-interactive thermotherapeutic electronic skin based on stretchable thermochromic strain sensor,” *Advanced Science*, vol. 7, no. 17, p. 2001184, 2020.
- [70] W.-B. Jung, S.-Y. Cho, G.-T. Yun, J. Choi, Y. Kim, M. Kim, H. Kang, and H.-T. Jung, “Hierarchical metal oxide wrinkles as responsive chemical sensors,” *ACS Applied Nano Materials*, vol. 2, no. 9, pp. 5520–5526, 2019.
- [71] T. Ma, S. Chen, J. Li, J. Yin, and X. Jiang, “Strain-ultrasensitive surface wrinkles for visual optical sensors,” *Materials Horizons*, vol. 9, no. 8, pp. 2233–2242, 2022.
- [72] Y. Qi, C. Zhou, S. Zhang, Z. Zhang, W. Niu, S. Wu, W. Ma, and B. Tang, “Bar-coating programmable mechanochromic bilayer pdms film with angle-dependent and angle-independent structural colors,” *Dyes and Pigments*, vol. 189, p. 109264, 2021.

- [73] Z. Li, Y. Liu, M. Marin, and Y. Yin, “Thickness-dependent wrinkling of pdms films for programmable mechanochromic responses,” *Nano Research*, pp. 1–7, 2020.
- [74] J. W. Goodman, *Introduction to Fourier optics*. Roberts and Company Publishers, 2005.
- [75] C. Harrison, C. Stafford, W. Zhang, and A. Karim, “Sinusoidal phase grating created by a tunably buckled surface,” *Appl. Phys. Lett.*, vol. 85, no. 18, pp. 4016–4018, 2004.
- [76] O. Kuwazuru, K. Miyamoto, N. Yoshikawa, and S. Imayama, “Skin wrinkling morphology changes suddenly in the early 30s,” *Skin Research and Technology*, vol. 18, no. 4, pp. 495–503, 2012.
- [77] J. Genzer and J. Groenewold, “Soft matter with hard skin: From skin wrinkles to templating and material characterization,” *Soft Matter*, vol. 2, no. 4, p. 310, 2006.
- [78] J. Plescia and M. Golombek, “Origin of planetary wrinkle ridges based on the study of terrestrial analogs,” *Geological Society of America Bulletin*, vol. 97, no. 11, pp. 1289–1299, 1986.
- [79] T. R. Watters, “Wrinkle ridge assemblages on the terrestrial planets,” *Journal of Geophysical Research: Solid Earth*, vol. 93, no. B9, pp. 10236–10254, 1988.
- [80] T. R. Watters, “System of tectonic features common to earth, mars, and venus,” *Geology*, vol. 20, no. 7, pp. 609–612, 1992.
- [81] P. A. Allen, “From landscapes into geological history,” *Nature*, vol. 451, no. 7176, pp. 274–276, 2008.
- [82] L. A. Taber, “A new wrinkle on the brain,” *Nature Physics*, vol. 14, no. 5, pp. 435–436, 2018.
- [83] M. Ben Amar and A. Bordner, “Mimicking cortex convolutions through the wrinkling of growing soft bilayers,” *Journal of Elasticity*, vol. 129, pp. 213–238, 2017.
- [84] C. M. Stafford, C. Harrison, K. L. Beers, A. Karim, E. J. Amis, M. R. VanLandingham, H.-C. Kim, W. Volksen, R. D. Miller, and E. E. Simonyi, “A buckling-based metrology



- for measuring the elastic moduli of polymeric thin films,” *Nature materials*, vol. 3, no. 8, pp. 545–550, 2004.
- [85] N. Bowden, W. T. Huck, K. E. Paul, and G. M. Whitesides, “The controlled formation of ordered, sinusoidal structures by plasma oxidation of an elastomeric polymer,” *Applied Physics Letters*, vol. 75, no. 17, pp. 2557–2559, 1999.
- [86] E. P. Chan, E. J. Smith, R. C. Hayward, and A. J. Crosby, “Surface wrinkles for smart adhesion,” *Advanced Materials*, vol. 20, no. 4, pp. 711–716, 2008.
- [87] N. Bowden, S. Brittain, A. G. Evans, J. W. Hutchinson, and G. M. Whitesides, “Spontaneous formation of ordered structures in thin,” *Nature*, vol. 393, no. May, pp. 146–149, 1998.
- [88] S. Yang, K. Khare, and P.-C. Lin, “Harnessing surface wrinkle patterns in soft matter,” *Advanced Functional Materials*, vol. 20, no. 16, pp. 2550–2564, 2010.
- [89] H. Allen, *Analysis and Design of Structural Sandwich Panels*. The Commonwealth and International Library: Structures and Solid Body Mechanics Division, Pergamon, 1969.
- [90] H. Jiang, D.-Y. Khang, J. Song, Y. Sun, Y. Huang, and J. A. Rogers, “Finite deformation mechanics in buckled thin films on compliant supports,” *Proc. Natl. Acad. Sci.*, vol. 104, no. 40, pp. 15607–15612, 2007.
- [91] Q. Wang and X. Zhao, “A three-dimensional phase diagram of growth-induced surface instabilities,” *Scientific Reports*, vol. 5, no. iv, pp. 1–10, 2015.
- [92] S. Khodaparast, C. Poulard, and H. A. Stone, “Water-Based Peeling of Thin Hydrophobic Films,” *Physical Review Letters*, vol. 154502, no. October, pp. 1–5, 2017.
- [93] M. J. Owen and P. J. Smith, “Plasma treatment of polydimethylsiloxane,” *J. Adhes. Sci. Technol.*, vol. 8, no. 10, pp. 1063–1075, 1994.
- [94] A. Chiche, C. M. Stafford, and J. T. Cabral, “Complex micropatterning of periodic structures on elastomeric surfaces,” *Soft Matter*, vol. 4, no. 12, p. 2360, 2008.

- [95] F. A. Bayley, J. L. Liao, P. N. Stavrinou, A. Chiche, and J. T. Cabral, “Wavefront kinetics of plasma oxidation of polydimethylsiloxane: limits for sub- $\mu\text{m}$  wrinkling,” *Soft Matter*, vol. 10, pp. 1155–1166, 2014.
- [96] M. Nania, O. K. Matar, and J. T. Cabral, “Frontal vitrification of PDMS using air plasma and consequences for surface wrinkling,” *Soft Matter*, vol. 11, no. 15, pp. 3067–3075, 2015.
- [97] M. Nania, F. Foglia, O. K. Matar, and J. T. Cabral, “Sub-100 nm wrinkling of polydimethylsiloxane by double frontal oxidation,” *Nanoscale*, vol. 9, no. 5, pp. 2030–2037, 2017.
- [98] P. J. Yoo and H. H. Lee, “Evolution of a stress-driven pattern in thin bilayer films: Spindal wrinkling,” *Physical Review Letters*, vol. 91, no. 15, p. 154502, 2003.
- [99] H. S. Kim and A. J. Crosby, “Solvent-responsive surface via wrinkling instability,” *Advanced materials*, vol. 23, no. 36, pp. 4188–4192, 2011.
- [100] S. K. Basu, A. V. McCormick, and L. Scriven, “Stress generation by solvent absorption and wrinkling of a cross-linked coating atop a viscous or elastic base,” *Langmuir*, vol. 22, no. 13, pp. 5916–5924, 2006.
- [101] H. Vandeparre, M. Piñeirua, F. Brau, B. Roman, J. Bico, C. Gay, W. Bao, C. N. Lau, P. M. Reis, and P. Damman, “Wrinkling hierarchy in constrained thin sheets from suspended graphene to curtains,” *Phys. Rev. Lett.*, vol. 106, p. 224301, Jun 2011.
- [102] E. S. Matsuo and T. Tanaka, “Patterns in shrinking gels,” *Nature*, vol. 358, no. 6386, pp. 482–485, 1992.
- [103] E. P. Chan, K. A. Page, S. H. Im, D. L. Patton, R. Huang, and C. M. Stafford, “Viscoelastic properties of confined polymer films measured via thermal wrinkling,” *Soft Matter*, vol. 5, no. 23, pp. 4638–4641, 2009.

- [104] J. Kim and H. H. Lee, “Wave formation by heating in thin metal film on an elastomer,” *Journal of Polymer Science Part B: Polymer Physics*, vol. 39, no. 11, pp. 1122–1128, 2001.
- [105] T. Okayasu, H.-L. Zhang, D. G. Bucknall, and G. A. D. Briggs, “Spontaneous formation of ordered lateral patterns in polymer thin-film structures,” *Advanced Functional Materials*, vol. 14, no. 11, pp. 1081–1088, 2004.
- [106] C. Stafford and C. Harrison, “Elastic moduli of polymer thin films: A high-throughput metrology,” *Encyclopedia of Materials: Science and Technology*, 2006.
- [107] P.-C. Lin and S. Yang, “Spontaneous formation of one-dimensional ripples in transit to highly ordered two-dimensional herringbone structures through sequential and unequal biaxial mechanical stretching,” *Applied physics letters*, vol. 90, no. 24, p. 241903, 2007.
- [108] S. Cai, D. Breid, A. J. Crosby, Z. Suo, and J. W. Hutchinson, “Periodic patterns and energy states of buckled films on compliant substrates,” *Journal of the Mechanics and Physics of Solids*, vol. 59, no. 5, pp. 1094–1114, 2011.
- [109] C. S. Davis and A. J. Crosby, “Wrinkle morphologies with two distinct wavelengths,” *Journal of Polymer Science Part B: Polymer Physics*, vol. 50, no. 17, pp. 1225–1232, 2012.
- [110] X. Chen and J. W. Hutchinson, “Herringbone Buckling Patterns of Compressed Thin Films on Compliant Substrates,” *Journal of Applied Mechanics*, vol. 71, no. 5, p. 597, 2004.
- [111] L. Pellegrino, S. Khodaparast, and J. T. Cabral, “Orthogonal wave superposition of wrinkled, plasma-oxidised, polydimethylsiloxane surfaces,” *Soft Matter*, vol. 16, no. 3, pp. 595–603, 2020.
- [112] M. Watanabe, “Wrinkles with a well-ordered checkerboard pattern, created using dip-coating of poly(methyl methacrylate) on a UV–ozone-treated poly(dimethylsiloxane) substrate,” *Soft Matter*, vol. 8, no. 5, pp. 1563–1569, 2012.

- [113] L. Pellegrino, A. Tan, and J. T. Cabral, “Ripple patterns spontaneously emerge through sequential wrinkling interference in polymer bilayers,” *Physical Review Letters*, vol. 128, no. 5, p. 058001, 2022.
- [114] R. C. Fletcher, “Three-dimensional folding of an embedded viscous layer in pure shear,” *Journal of Structural Geology*, vol. 13, no. 1, pp. 87–96, 1991.
- [115] A. Volynskii, S. Bazhenov, O. Lebedeva, and N. Bakeev, “Mechanical buckling instability of thin coatings deposited on soft polymer substrates,” *Journal of materials science*, vol. 35, no. 3, pp. 547–554, 2000.
- [116] G. Gough, C. Elam, G. Tipper, and N. De Bruyne, “The stabilisation of a thin sheet by a continuous supporting medium,” *The Aeronautical Journal*, vol. 44, no. 349, pp. 12–43, 1940.
- [117] Z. Wang, A. A. Volinsky, and N. D. Gallant, “Crosslinking effect on polydimethylsiloxane elastic modulus measured by custom-built compression instrument,” *Journal of Applied Polymer Science*, vol. 131, no. 22, 2014.
- [118] A. S. Cruz-Félix, A. Santiago-Alvarado, J. Márquez-García, and J. González-García, “Pdms samples characterization with variations of synthesis parameters for tunable optics applications,” *Heliyon*, vol. 5, no. 12, p. e03064, 2019.
- [119] Y. Staudt, C. Odenbreit, and J. Schneider, “Failure behaviour of silicone adhesive in bonded connections with simple geometry,” *International Journal of Adhesion and Adhesives*, vol. 82, pp. 126–138, 2018.
- [120] A. Tan, L. Pellegrino, and J. T. Cabral, “Tunable phase gratings by wrinkling of plasma-oxidized pdms: Gradient skins and multiaxial patterns,” *ACS Applied Polymer Materials*, vol. 3, no. 10, pp. 5162–5170, 2021.
- [121] C. Yu, K. O’Brien, Y.-H. Zhang, H. Yu, and H. Jiang, “Tunable optical gratings based on buckled nanoscale thin films on transparent elastomeric substrates,” *Applied Physics Letters*, vol. 96, no. 4, p. 041111, 2010.

- [122] Y. Meng, X. Gong, Y. Huang, and L. Li, “Mechanically tunable opacity effect in transparent bilayer film: Accurate interpretation and rational applications,” *Applied Materials Today*, vol. 16, pp. 474–481, 2019.
- [123] E. Stoykova, J. Harizanova, and V. Sainov, “Pattern projection with a sinusoidal phase grating,” *EURASIP Journal on Advances in Signal Processing*, vol. 2009, pp. 1–10, 2008.
- [124] A. Groisman, S. Zamek, K. Campbell, L. Pang, U. Levy, and Y. Fainman, “Optofluidic  $1 \times 4$  switch,” *Optics Express*, vol. 16, no. 18, pp. 13499–13508, 2008.
- [125] T. Kavc, G. Langer, W. Kern, G. Kranzelbinder, E. Toussaere, G. A. Turnbull, I. D. Samuel, K. F. Iskra, T. Neger, and A. Pogantsch, “Index and relief gratings in polymer films for organic distributed feedback lasers,” *Chemistry of materials*, vol. 14, no. 10, pp. 4178–4185, 2002.
- [126] D. Breid and A. J. Crosby, “Surface wrinkling behavior of finite circular plates,” *Soft Matter*, vol. 5, no. 2, pp. 425–431, 2009.
- [127] Y.-C. Chen and A. J. Crosby, “High aspect ratio wrinkles via substrate prestretch,” *Advanced Materials*, vol. 26, no. 32, pp. 5626–5631, 2014.
- [128] D. B. H. Chua, H. T. Ng, and S. Li, “Spontaneous formation of complex and ordered structures on oxygen-plasma-treated elastomeric polydimethylsiloxane,” *Appl. Phys. Lett.*, vol. 76, pp. 721–723, 2000.
- [129] S. Befahy, P. Lipnik, T. Pardoen, C. Nascimento, B. Patris, P. Bertrand, and S. Yunus, “Thickness and elastic modulus of plasma treated pdms silica-like surface layer,” *Langmuir*, vol. 26, no. 5, pp. 3372–3375, 2010.
- [130] K. Efimenko, M. Rackaitis, E. Manias, A. Vaziri, L. Mahadevan, and J. Genzer, “Nested self-similar wrinkling patterns in skins,” *Nat. Mater.*, vol. 4, pp. 293–297, 04 2005.
- [131] K. Efimenko, W. E. Wallace, and J. Genzer, “Surface modification of sylgard-184 poly(dimethyl siloxane) networks by ultraviolet and ultraviolet/ozone treatment,” *J. Colloid Interface Sci.*, vol. 254, no. 2, pp. 306 – 315, 2002.

- [132] H. Hillborg, J. Ankner, U. Gedde, G. Smith, H. Yasuda, and K. Wikström, “Crosslinked polydimethylsiloxane exposed to oxygen plasma studied by neutron reflectometry and other surface specific techniques,” *Polymer*, vol. 41, no. 18, pp. 6851 – 6863, 2000.
- [133] A. Tan, L. Pellegrino, Z. Ahmad, and J. T. Cabral, “Tunable structural color with gradient and multiaxial polydimethylsiloxane wrinkling,” *Adv. Opt. Mater.*, vol. 10, no. 17, p. 2200964, 2022.
- [134] M. Srinivasarao, “Nano-optics in the biological world: beetles, butterflies, birds, and moths,” *Chemical reviews*, vol. 99, no. 7, pp. 1935–1962, 1999.
- [135] P. Vukusic and J. R. Sambles, “Photonic structures in biology,” *Nature*, vol. 424, pp. 852 EP –, 08 2003.
- [136] S. Kinoshita, S. Yoshioka, and J. Miyazaki, “Physics of structural colors,” *Reports on Progress in Physics*, vol. 71, no. 7, p. 076401, 2008.
- [137] B.-K. Hsiung, R. H. Siddique, D. G. Stavenga, J. C. Otto, M. C. Allen, Y. Liu, Y.-F. Lu, D. D. Deheyn, M. D. Shawkey, and T. A. Blackledge, “Rainbow peacock spiders inspire miniature super-iridescent optics,” *Nature communications*, vol. 8, no. 1, pp. 1–8, 2017.
- [138] D. Gur, B. A. Palmer, S. Weiner, and L. Addadi, “Light manipulation by guanine crystals in organisms: biogenic scatterers, mirrors, multilayer reflectors and photonic crystals,” *Advanced Functional Materials*, vol. 27, no. 6, p. 1603514, 2017.
- [139] A. SAITO, K. Yamashita, T. Hattori, and Y. Kuwahara, “Novel optical applications inspired by the morpho butterfly’s coloration: technology transfer from reflection to transmission,” *Japanese Journal of Applied Physics*, 2022.
- [140] Z. Dong, H. Zhao, L. Nie, S. Tang, C. Li, and X. Wang, “Effects of measurement configurations on the sensitivity of morpho butterfly scales based chemical biosensor,” *Frontiers in Physics*, p. 792, 2022.
- [141] H. Wang and K.-Q. Zhang, “Photonic crystal structures with tunable structure color as colorimetric sensors,” *Sensors*, vol. 13, no. 4, pp. 4192–4213, 2013.

- [142] H. S. Lee, T. S. Shim, H. Hwang, S.-M. Yang, and S.-H. Kim, “Colloidal photonic crystals toward structural color palettes for security materials,” *Chemistry of Materials*, vol. 25, no. 13, pp. 2684–2690, 2013.
- [143] W. Yang, S. Xiao, Q. Song, Y. Liu, Y. Wu, S. Wang, J. Yu, J. Han, and D.-P. Tsai, “All-dielectric metasurface for high-performance structural color,” *Nature communications*, vol. 11, no. 1, pp. 1–8, 2020.
- [144] F. Cheng, J. Gao, T. S. Luk, and X. Yang, “Structural color printing based on plasmonic metasurfaces of perfect light absorption,” *Scientific reports*, vol. 5, no. 1, pp. 1–10, 2015.
- [145] K. Yamashita, K. Kunitsu, T. Hattori, Y. Kuwahara, and A. Saito, “Demonstration of a diffraction-based optical diffuser inspired by the morpho butterfly,” *Optics Express*, vol. 29, no. 19, pp. 30927–30936, 2021.
- [146] Z. Xuan, J. Li, Q. Liu, F. Yi, S. Wang, and W. Lu, “Artificial structural colors and applications,” *The Innovation*, vol. 2, no. 1, p. 100081, 2021.
- [147] G. Chen and W. Hong, “Mechanochromism of structural-colored materials,” *Advanced Optical Materials*, vol. 8, no. 19, p. 2000984, 2020.
- [148] Q. Zhou, J. G. Park, J. Bae, D. Ha, J. Park, K. Song, and T. Kim, “Multimodal and covert–overt convertible structural coloration transformed by mechanical stress,” *Advanced Materials*, vol. 32, no. 25, p. 2001467, 2020.
- [149] L. Zhou, L. Yang, Y. Liu, Z. Xu, J. Yin, D. Ge, and X. Jiang, “Dynamic structural color from wrinkled thin films,” *Adv. Opt. Mater.*, vol. 8, no. 12, p. 2000234, 2020.
- [150] Z. Mao, S. Zeng, K. Shen, A. P. Chooi, A. T. Smith, M. D. Jones, Y. Zhou, X. Liu, and L. Sun, “Dynamic mechanochromic optics with tunable strain sensitivity for strain-responsive digit display,” *Advanced Optical Materials*, vol. 8, no. 24, p. 2001472, 2020.
- [151] B. Voisiat, W. Wang, M. Holzhey, and A. F. Lasagni, “Improving the homogeneity of diffraction based colours by fabricating periodic patterns with gradient spatial period using direct laser interference patterning,” *Scientific reports*, vol. 9, no. 1, pp. 1–9, 2019.

- [152] J. S. Lee, H. Hong, S. J. Park, S. J. Lee, and D. S. Kim, "A simple fabrication process for stepwise gradient wrinkle pattern with spatially-controlled wavelength based on sequential oxygen plasma treatment," *Microelectronic Engineering*, vol. 176, pp. 101–105, 2017.
- [153] S. Hiltl, J. Oltmanns, and A. Böker, "A one-step screening process for optimal alignment of (soft) colloidal particles," *Nanoscale*, vol. 4, no. 23, pp. 7338–7345, 2012.
- [154] S. Raayai-Ardakani, J. Luis Yagüe, K. K. Gleason, and M. C. Boyce, "Mechanics of graded wrinkling," *Journal of Applied Mechanics*, vol. 83, no. 12, p. 121011, 2016.
- [155] A. Tan, Z. Ahmad, P. Vukusic, and J. T. Cabral, "Multifaceted structurally coloured materials: Diffraction and total internal reflection (tir) from nanoscale surface wrinkling," *Molecules*, vol. 28, no. 4, p. 1710, 2023.
- [156] S. L. Burg and A. J. Parnell, "Self-assembling structural colour in nature," *Journal of Physics: Condensed Matter*, vol. 30, no. 41, p. 413001, 2018.
- [157] J. N. Lee, C. Park, and G. M. Whitesides, "Solvent compatibility of poly (dimethylsiloxane)-based microfluidic devices," *Anal. Chem.*, vol. 75, no. 23, pp. 6544–6554, 2003.
- [158] M. W. Toepke and D. J. Beebe, "Pdms absorption of small molecules and consequences in microfluidic applications," *Lab on a Chip*, vol. 6, no. 12, pp. 1484–1486, 2006.
- [159] R. Dangla, F. Gallaire, and C. N. Baroud, "Microchannel deformations due to solvent-induced pdms swelling," *Lab on a Chip*, vol. 10, no. 21, pp. 2972–2978, 2010.
- [160] C. Rumens, M. Ziai, K. Belsey, J. Batchelor, and S. Holder, "Swelling of pdms networks in solvent vapours; applications for passive rfid wireless sensors," *J. Mater. Chem. C*, vol. 3, no. 39, pp. 10091–10098, 2015.
- [161] J. G. Ramsay, "The geometry and mechanics of formation of " similar " type folds," *The Journal of Geology*, vol. 70, no. 3, pp. 309–327, 1962.



- [162] H. Ramberg, "Selective buckling of composite layers with contrasted rheological properties, a theory for simultaneous formation of several orders of folds," *Tectonophysics*, vol. 1, no. 4, pp. 307–341, 1964.
- [163] S. Sengupta, S. K. Ghosh, S. K. Deb, and D. Khan, "Opening and closing of folds in superposed deformations," *Journal of Structural Geology*, vol. 27, no. 7, pp. 1282–1299, 2005.
- [164] J. Carreras, E. Druguet, and A. Griera, "Shear zone-related folds," *Journal of Structural Geology*, vol. 27, no. 7, pp. 1229–1251, 2005.
- [165] G. Lin, P. Chandrasekaran, C. Lv, Q. Zhang, Y. Tang, L. Han, and J. Yin, "Self-similar hierarchical wrinkles as a potential multifunctional smart window with simultaneously tunable transparency, structural color, and droplet transport," *ACS Applied Materials & Interfaces*, vol. 9, no. 31, pp. 26510–26517, 2017.
- [166] J. Yin and C. Lu, "Hierarchical surface wrinkles directed by wrinkled templates," *Soft Matter*, vol. 8, no. 24, pp. 6528–6534, 2012.
- [167] D. Rhee, W.-K. Lee, and T. W. Odom, "Crack-free, soft wrinkles enable switchable anisotropic wetting," *Angewandte Chemie*, vol. 129, no. 23, pp. 6623–6627, 2017.
- [168] S.-I. Lim, E. Jang, D. Yu, J. Koo, D.-G. Kang, K. M. Lee, N. P. Godman, M. E. McConney, D.-Y. Kim, and K.-U. Jeong, "When chirophotonic film meets wrinkles: Viewing angle independent corrugated photonic crystal paper," *Advanced Materials*, vol. 35, no. 1, p. 2206764, 2023.

## Appendices

The following appendices are the published articles as a result of the work reported in this thesis. These works are appended in the following order:

1. Tan, Annabelle, Zain Ahmad, Pete Vukusic, and João T. Cabral. 2023. "Multifaceted Structurally Coloured Materials: Diffraction and Total Internal Reflection (TIR) from Nanoscale Surface Wrinkling" *Molecules* 28, no. 4 (2023): 1710.
2. Tan, Annabelle, Luca Pellegrino, Zain Ahmad, and João T. Cabral. "Tunable Structural Color with Gradient and Multiaxial Polydimethylsiloxane Wrinkling." *Advanced Optical Materials* (2022): 2200964.
3. Tan, Annabelle, Luca Pellegrino, and João T. Cabral. "Tunable Phase Gratings by Wrinkling of Plasma-Oxidized PDMS: Gradient Skins and Multiaxial Patterns." *ACS Applied Polymer Materials* 3, no. 10 (2021): 5162-5170.

## Tunable Phase Gratings by Wrinkling of Plasma-Oxidized PDMS: Gradient Skins and Multiaxial Patterns

Annabelle Tan, Luca Pellegrino, and João T. Cabral\*

Cite This: *ACS Appl. Polym. Mater.* 2021, 3, 5162–5170

Read Online

ACCESS |

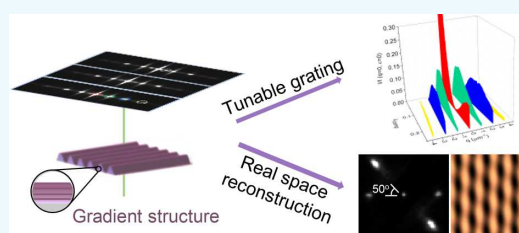
Metrics &amp; More

Article Recommendations

Supporting Information

**ABSTRACT:** Wrinkling instabilities in polymeric bilayers have been exploited as optical phase gratings with tunable performance. Here, we report strain modulated 1D and 2D phase gratings fabricated by the ubiquitous process of plasma-oxidation of polydimethylsiloxane (PDMS). While surface oxidation provides a remarkably facile glassy skin formation approach, minimizing delamination and debonding, it inherently results in a gradient conversion profile emanating from the top film interface. We examine and quantitatively model the consequences of this gradient layer on the optical properties of the resulting strain-tunable phase gratings. Diffraction efficiencies up to 48% are demonstrated. We then develop and validate a surface reconstruction methodology based on the diffraction pattern of our sinusoidal gratings and our model, which we extend to the high deformation regimes and to 2D gratings, obtained by superposition of two wrinkling generations, where both amplitudes and wavelengths can be independently tuned. Overall, this approach provides a rapid, robust and predictive framework for the design and fabrication of tunable, single, and multiaxial surface gratings.

**KEYWORDS:** PDMS, wrinkling, plasma oxidation, phase grating, diffraction, optics



## INTRODUCTION

Patterned micro- and nanostructured topographies abound in natural and synthetic surfaces and can impart or modulate various functionalities, including surface wetting and spreading, adhesion, mechanical, and optical properties.<sup>1–3</sup> Complementary to established patterning methods, such as photolithography, nanoimprint lithography, and ion-beam lithography,<sup>4,5</sup> spontaneous and mask-less processes, such as surface wrinkling offer attractive routes for large-scale and versatile patterning.<sup>6</sup> While wrinkling can be detrimental for material performance, for example, degrading electronic thin film properties,<sup>7</sup> it can also impart or augment device functionality such as in solar panels,<sup>8</sup> organic lasers,<sup>9</sup> and phase gratings.<sup>10</sup> Surface wrinkling can yield highly ordered mono and multidimensional periodical patterns, depending on the nature of the mechanical instability involved and the applied strain field. Among the plethora of achievable patterns are 1-dimensional sinusoidal patterns and 2-dimensional herringbones, hexagonal and checkerboard structures of varying wavelength and amplitude, and hierarchical (or nested) and multifrequency patterns.<sup>11–14</sup>

Spontaneous wrinkling can occur via a well-understood mechanical instability, specifically in sandwiched structures or bilayers often fabricated through film sputtering, deposition and lamination, or chemical modification of an elastomeric substrate.<sup>15–18</sup> When a thin sheet of relatively stiffer material is adhered strongly to a thick elastomeric substrate, a mismatch in the mechanical properties in the bilayer is produced. By

subjecting a bilayer to an uniaxial, compressive strain, a buckling instability can be excited, producing sinusoidal surface undulations arising from the minimization of energy of bulk deformation and skin bending. At low deformations (strain  $\epsilon \lesssim 10\%$ ), the wavelength and amplitude of the sinusoidal surface profile are well described by<sup>19</sup>

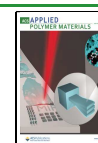
$$\lambda = 2\pi h \left( \frac{\bar{E}_f}{3\bar{E}_s} \right)^{1/3} \quad (1)$$

$$A = h \left( \frac{\epsilon}{\epsilon_c} - 1 \right)^{1/2} \quad (2)$$

where  $h$  is the film thickness,  $\bar{E}_f$  and  $\bar{E}_s$  are the in-plane strain moduli of the film and substrate, respectively, given by  $\bar{E} = E/(1 - \nu^2)$ , where  $E$  is the Young's modulus and  $\nu$  is the Poisson ratio ( $\approx 0.5$  for PDMS). A critical strain must be exceeded to trigger the buckling instability:

Received: July 23, 2021

Published: September 15, 2021



$$\epsilon_c = \frac{1}{4} \left( \frac{3\bar{E}_s}{\bar{E}_f} \right)^{2/3} \quad (3)$$

In this limit, the amplitude alone depends on strain, thus allowing for  $\lambda$  and  $A$  to be decoupled in surface patterning. Generally, at “high-deformation” (HD),<sup>20</sup> the wrinkling wavelength too becomes strain dependent and

$$\lambda_{\text{HD}} = \frac{\lambda}{(1 + \epsilon)(1 + \xi)^{1/3}} \quad (4)$$

$$A_{\text{HD}} = \frac{A}{(1 + \epsilon)^{1/2}(1 + \xi)^{1/3}} \quad (5)$$

where  $\xi = 5\epsilon(1 + \epsilon)/32$ , accounting for the nonlinearity of the stress–strain relationship of the substrate in the finite deformation regime (i.e., non-Hookean response), with  $\lambda$  and  $A$  given by eq 1,2). Under high deformation conditions, uniaxial strain leads to a transition from the low deformation sinusoidal patterns into further modes, such as the formation of folds, period-doubling, and ridges.<sup>21</sup>

### ■ PHASE GRATINGS GENERATED BY WRINKLING OF PLASMA-OXIDIZED PDMS SURFACES

The use of wrinkling bilayers in the fabrication of tunable phase grating has been previously demonstrated with thin polymer films (deposited or laminated) supported onto an elastomer, such as polydimethylsiloxane (PDMS).<sup>22–24</sup> Grating efficiencies can be tuned by employing sinusoidal phase gratings, where the distribution of energy in the diffraction orders can be varied.<sup>25,26</sup> This property has applications in optics, such as projection systems,<sup>27</sup> optical switches,<sup>28</sup> and lasers.<sup>29</sup> Transmission phase gratings are thin transparent optical elements that can consist of periodic refractive index variations or of a periodic surface relieves, and these can be fabricated exciting sinusoidal wrinkles on a surface. The diffraction pattern of the resulting phase grating can be modeled for all diffraction orders  $p$  according to<sup>22,30</sup>

$$I \approx \sum_{p=-\infty}^{\infty} J_p^2 \left( \frac{m}{2} \right) \text{sinc}^2 \left[ \frac{W}{\pi} \left( q - \frac{2p\pi}{d} \right) \right] \quad (6)$$

where  $J_p$  is a Bessel function of the first kind,  $W$  is the half-width of the aperture,  $d$  is the wrinkling wavelength (referred to as  $\lambda$  in the experimental data),  $m/2$  is the maximum phase shift impart to the light, and  $p$  is an index accounting for the  $p$ th diffraction order. Often  $W \approx 0.5$  mm, determined by the typical profile of laser beam (in the Fraunhofer limit conditions). The maximum intensity of the  $p$ th order can be approximated to be proportional to the Bessel function  $J_p^2(m/2)$  as the *sinc* function is narrowly distributed in  $q$  about each order without significant overlap between adjacent orders. The phase contrast,  $m(\Delta)$ , can be rationalized in terms of the wrinkling bilayer model of amplitude,  $A(\Delta)$ , by

$$\frac{m(\Delta)}{2} = 2\pi \frac{A(\Delta)}{\lambda} [n - 1] \quad (7)$$

where  $A(\Delta)$  is taken from the high deformation model as described in eq 5, with  $n$  is the refractive index, and here,  $\lambda$  is the laser wavelength (532 nm in our work).

While this approach can be implemented via polymer<sup>22</sup> and metal<sup>24</sup> thin film deposition, surface oxidation of PDMS provides an attractive, facile route to PDMS patterning that has

recently been explored to control opacity of otherwise transparent films.<sup>23</sup> Significantly, the surface oxidation of PDMS using an oxygen (or air) plasma source, generates a gradient glassy skin,<sup>11,31–34</sup> whose density and, thus, refractive index varies in the direction normal to the surface. To explore the fabrication of tunable phase gratings by wrinkling of oxidized PDMS, we consider quantitatively the impact of such gradients, intrinsic to this ubiquitous approach in soft matter patterning.

Plasma-oxidation of PDMS results in a thin glassy skin layer to form upon conversion from the bulk material, therefore inducing a mismatch in elastic moduli between the thin skin and the soft substrate. This methodology is suited for fabrication of patterns ranging from nanometer scales to several hundreds microns by several by tuning the oxidation and strain conditions. The wrinkling instability can be mechanically induced through a predetermined extensional or compressive strain, with approximately micrometer resolution, allowing for a precise pattern control, as compared to drying and thermal alternatives to skin deposition and strain. The skin formation via oxidation proceeds via a frontal process,<sup>32,33</sup> where an increase in skin thickness is accompanied by surface densification by cleaving of Si–CH<sub>3</sub> groups. The rate of conversion fraction of the glassy skin thin film follows a sigmoidal profile with respect to depth from the surface, leading to a gradient bilayer system in a three-step process: “induction”, where no evidence of wrinkling is found, “formation”, where the buildup of the glassy layer develops, and “film propagation”, during which the fully propagated glassy layer propagates normal to the surface, increasing the skin thickness. This fabrication method allows for the production of ON or OFF samples, where a strain is applied before or after plasma-treatment of the sample, respectively.<sup>35</sup> ON samples lead to a wrinkling pattern at rest, while OFF samples, only when strain is applied.

In this work, we explore the fabrication and use of single and multifrequency sinusoidal phase gratings generated by plasma-oxidized PDMS, where additional generations can be obtained by superposition of sinusoidal waves at variable angles between them.<sup>11,14</sup> Specifically, we explore the effect of compressive strain and the overall mechanical response of ON samples, on its grating efficiency by means of tracking intensity modulation of the diffraction patterns using static light scattering (SLS). Novel aspects of our work include quantitatively examining and modeling the role of the gradient oxide layer in the light diffraction response, and evaluating the diffraction from multifrequency and multiangle wrinkled surfaces. Further, we investigate the reconstruction of real-space patterns from the combination of a simple optical model and diffraction images obtained by SLS.

### ■ RESULTS AND DISCUSSION

**Wrinkled Bilayer Characterization.** When an uniaxial strain ( $\epsilon_{\text{prestrain}}$ ) is applied to a flat PDMS coupon from  $L_0$  (initial length) to  $L_1$  (final length), which undergoes plasma-oxidation, a stiff skin gradient bilayer is created. The gradient interface is generated, conversely to lamination and floating methodologies,<sup>17,36,37</sup> through a temporal conversion of the bulk material into a mixed silicon oxide layer, where thickness and modulus increase with applied plasma exposure time.<sup>11,19,38</sup> Wrinkles are generated in the glassy skin upon compression of the bilayer because of a strain release, creating a buckled surface when a strain exceeding the critical strain  $\epsilon_c$

is applied. When a range of PDMS samples are treated with oxygen plasma conditions of 70 W for 7 min at different applied prestrains, a set of different wavelengths and amplitudes are obtained. The characterization of the PDMS surfaces was performed on the samples by means of AFM ( $\lambda$  and  $A$ ) and SLS ( $\lambda$  only) (Figure 1), showing good agreement

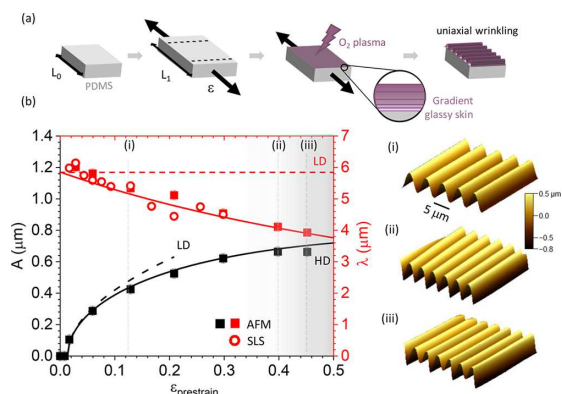


**Figure 1.** (a) Schematic of the formation of a 1D wrinkled surface on PDMS by prestraining ( $\epsilon_{\text{prestrain}}$ ) an elastomer coupon, followed by plasma oxidation and relaxation of strain; the resulting glassy skin layer exhibits a conversion gradient normal to the surface. (b) Wrinkling wavelength ( $\lambda$ , red) and amplitude ( $A$ , black) measured by AFM (■) and SLS (○) as a function of prestrain  $\epsilon_{\text{prestrain}}$  for plasma-treated (40 kHz) PDMS coupons at power  $P = 70$  W for a duration  $t = 7$  min. The dashed and solid lines correspond to the low and high-deformation models, respectively (see text). The vertical dashed lines correspond the AFM scans on the right, representative of (i) low-deformation, (ii) high-deformation, and (iii) period-doubling.

between the two techniques. The experimental data are initially described by the red and black dashed lines until  $\epsilon_{\text{prestrain}} = 0.1$ , corresponding to the low deformation model for wavelength  $\lambda$  and amplitude  $A$  as expressed by eq 1 and 2. Assuming the bilayer model, we can estimate that the elastic modulus increases from 1.02 MPa (for neat PDMS) to 40 GPa for the glassy skin (obtained from the wrinkling aspect ratio, as shown in Figure S1), and a film thickness of  $\approx 30$  nm (corroborated by X-ray reflectivity measurements<sup>32</sup>). While this skin thickness is in line with previous literature,<sup>32–34,39</sup> the modulus is higher than those estimated by nanoindentation for UVO<sup>40</sup> or MHz plasma exposure<sup>39</sup> (up to  $\sim 7$  GPa), which we associate with the more aggressive and faster 40 kHz process conditions.<sup>33</sup> The amplitude model predicts a square root dependency directly proportional to the thickness of the glassy layer and the critical strain  $\epsilon_c$  while  $\lambda$  is described by a straight line with dependence on  $h$  and the mismatch in the elastic modulus of the bilayer, expressed as a constant elastic moduli ratio  $\bar{E}_t/\bar{E}_s$ . However, this representation is not sufficient to describe the experimental data in this PDMS/SiO<sub>x</sub> system because of the progressive build up in the glassy skin thickness and ultimately elastic modulus in “induction” and “formation” stages.<sup>32</sup> In order to take into account the evolution of  $\lambda$  and  $A$  beyond prestrain of 0.1 two solid lines are represented solid, corresponding to a implemented “high deformation model” for wrinkling instabilities developed employing prestrains above 0.2, described by eqs 4 and 5, respectively, where a bellow mechanics model is introduced to take into account deviations from linearity of the elastic modulus of PDMS with strain.<sup>20</sup>

The evolution of initially sinusoidal wrinkled bilayers with strain can be visualized in the 3D AFM micrographs reported in Figure 1b (i–iii), showing a 25 by 25  $\mu\text{m}$  region of the surface structures in samples having a prestrains  $\epsilon$  of 0.115 and in the higher deformation region where  $\epsilon = 0.4$  and 0.45, respectively. As prestrain increases, the surface deviates from the original sinusoidal regime toward more complex buckling instabilities, such as period-doubling, characterized by a splitting in the original periodicity, induced by lateral compression because of the increase in applied prestrain.

On the basis of these initial findings, we seek to elucidate the mechanisms behind the formation of gradient-interface phase gratings and the correlation between the observed diffraction patterns with the operative conditions employed in the plasma oxidation step. We, therefore, explore a set of fabrication conditions enabling the access of a range of pattern wavelengths and amplitudes characterized with the SLS setup depicted in Figure 2a to accommodate the observation, modulation, and evolution up to the third diffraction order (Figure 2b).

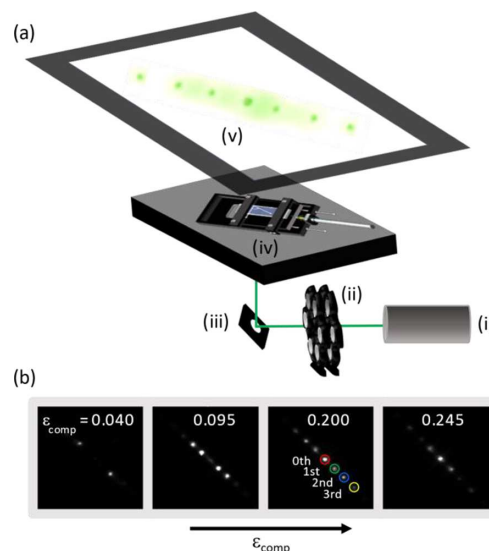


**Figure 2.** (a) SLS setup depicting the (i) 532 nm diode laser, (ii) ND filter wheel, (iii) 45° mirror, (iv) motorized linear strain stage, (v) diffraction pattern imaged on a screen, and recorded by a cooled CCD detector. (b) Series of diffraction patterns obtained at varying  $\epsilon_{\text{comp}}$  and constant ND attenuation, for a PDMS sample prestrained at  $\epsilon_{\text{prestrain}} = 0.3$  and plasma treated at  $P = 70$  W for 7 min. The intensity of diffraction orders 0th (red), 1st (green), 2nd (blue), and 3rd (yellow) is tunable with  $\epsilon_{\text{comp}}$ .

**Diffraction Intensity Modulation in Wrinkled Tunable Gratings.** To evaluate the diffraction properties of the wrinkled skins, a motorized strain release rate of 0.005 mm/s, in increments of 0.5% and a plasma-oxidized sample with initial prestrain  $\epsilon = 0.3$ , were employed while monitoring under SLS. Prior to release under extensional strain conditions ( $\epsilon_{\text{comp}} = 0$ ), the sample shows no diffraction pattern with only the direct beam observed. Despite the presence of the glassy skin, the buckling instability can only be excited, as expected from the model, above a specific critical strain. Indeed, laser light diffraction is only observed past the critical strain, reflecting the



development of sinusoidal undulations on the sample surface, into a phase grating. The use of neutral density (ND) filters allows for the control of the light intensity, avoiding the saturation of the CCD camera sensor, adjusted for each order as required. Diffraction patterns resembling phase gratings can be obtained through formation of wrinkles observed with the same set of ND filters (0.2 and 2.0), when a strained sample is slowly released and buckles because of the applied compressive strain. With a single set of ND filters, Figure 2b visually captures the modulation of intensities of the different orders as the sample undergoes compressive strain ( $\epsilon_{\text{comp}}$ ). The compressive strain ( $\epsilon_{\text{comp}}$ ) can be calculated by  $\epsilon_{\text{prestrain}} - \epsilon$ , where for example a sample starting at a prestrain of 0.30 released to 0.20 would give  $\epsilon_{\text{comp}}$  of 0.10. The intensities of the orders can be tuned by the amount of applied compressive strain. At  $\epsilon = 0.20$ , zeroth, first, second, and third orders (red, green, blue, yellow circles, respectively) are observable using the same set of ND filters, indicative that the intensities are of the same order of magnitude to one another. Varying the compressive strain, ND filters need to be adjusted to increase or decrease the attenuation factor for other orders to be observed, within the finite dynamic range and background of our setup.

The intensities of these individual orders are normalized with respect to the intensity of the zeroth order at  $\epsilon_{\text{comp}} = 0.0$  ( $I/I$  ( $q = 0, \epsilon = 0$ )) and mapped out as a function of compressive strain and wavenumber  $q$  ( $\mu\text{m}^{-1}$ ). Figure 3a demonstrates that a sample prestrained at  $\epsilon_{\text{prestrain}} = 0.3$  and

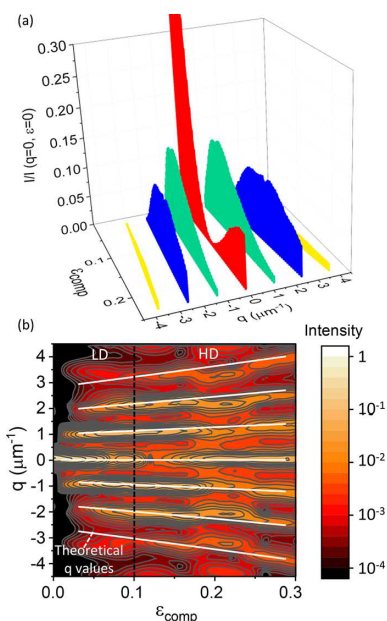


**Figure 3.** (a) Dependence of (normalized) diffraction intensities with  $\epsilon_{\text{comp}}$  and  $q$  for a PDMS sample at  $\epsilon_{\text{prestrain}} = 0.3$  and plasma treated at  $P = 70$  W for 7 min (shown in Figure 2b). Note the modulation of intensity and presence of well-defined maxima and minima with  $\epsilon_{\text{comp}}$  ( $\equiv \epsilon_{\text{prestrain}} - \epsilon$ , see text). (b) Contour plot of the diffraction data, showing the variation of wavenumber  $q_n$  with strain  $\epsilon_{\text{comp}}$ . The white lines represent the theoretical wavenumber calculated from  $\lambda_{\text{HD}}$ , and vertical black line indicates the approximate boundary for applicability of the LD model.

plasma treated at 70 W for 7 min is able, upon compression, to exhibit strain-dependent phase grating behavior, similar to previously reported by Harrison et al.<sup>22</sup> in wrinkled bilayers fabricated via polystyrene film floating onto PDMS. The light intensity of the four observable orders is quantitatively modulated with strain. Within the explored strain range, the zeroth order can be seen to modulate through a minimum and maximum while the other orders have intensities reaching a maximum before decreasing with strain. The transition from low to high deformation regime for the wavelength, is reflected in the  $q$  range in Figure 3b. By definition, wavenumber  $q$  shows an inverse relationship with wavelength  $\lambda$ . In the LD regime, the positioning of the orders is independent of strain and hence, the  $q$  range of the contour plots shows its independence from strain below  $\epsilon = 0.1$ , accounted as LD limit. Past this threshold, however, the  $q$  dependence in the experimental data “fans out”, following the high deformation approximation, as the pattern wavelength depends on strain because of nonlinearities in the stress–strain response of the sample.<sup>20</sup> To compute this strain dependence, the high deformation wavelength eq 4 needs to be employed instead. Following this behavior, we are able to quantitatively characterize the angular variation of each diffraction order and corresponding intensity in these phase gratings.

#### Modeling of Plasma-Oxidized Tunable Grating: Effect of Gradient Interface on Diffraction.

In a sinusoidal phase grating with a single refractive index  $n$ , the model described by eqs 6 and 7 is expected to account for the diffraction pattern and the individual diffraction intensities of each order. In bilayers obtained by thin polymer film deposition (with thickness much smaller than the  $\lambda$  of light) onto PDMS, a sharp interface is formed to the bulk, and a single refractive index (that of bulk PDMS) suffices to model the diffraction pattern.<sup>22</sup> Following the diffraction model, in practice, the value of  $n$  shifts the positions of the minima and depth of the individual orders, describing the specific strain and intensity modulation for the diffraction pattern. An increase in  $n$  results in a “left” shift in a graph of intensity versus amplitude (or strain), as shown by the dashed lines of Figure 4a, calculated with the model. We find that in our case, however, a single refractive index phase grating mode does not suffice to quantitatively describe the experimental data. We hypothesize that this discrepancy can be due to the different nature of plasma oxidized bilayers, which are known to yield a gradient conversion layer toward bulk PDMS, in contrast to laminated bilayers. Therefore, the heterogeneous, frontal, conversion induced by plasma oxidation, is expected to introduce a distribution of refractive indices  $n$  within the skin, effectively yielding a “gradient skin” phase grating.

Evidence for gradient bilayer (illustrated in Figure 4) formation in plasma oxidized PDMS abounds, as previously reported by X-ray reflectivity (XRR)<sup>32</sup> (data reproduced in Figure 4c) and transmission electron microscopy (TEM)<sup>39</sup> (data reproduced in Figure 4d). XRR can be employed to determine the scattering length density profile for surface-oxidized PDMS, and in Figure 4c, such profile indicates that the densification of the top layer increases with plasma exposure time at a given power, with a gradual surface to bulk interface with thickness showing the plasma conversion in the PDMS. A frontal model has been used to describe the skin growth of the glassy layer, where the hydrogen and methyl groups are substituted with hydroxyl groups and oxide links, creating a thin, silica-like skin layer.<sup>42</sup> This conversion is

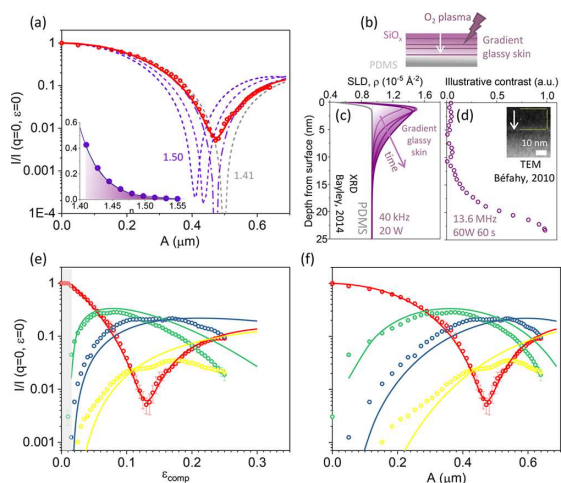


**Figure 4.** (a) Zeroth diffraction order intensity as a function of pattern amplitude (red data points), modeled by eq 8 by assuming an exponential distribution of refractive index (from  $n = 1.41$ , pure PDMS to 1.55, silica; shown in inset and described in the text), shown by the solid red line. The dashed lines correspond to model predictions from single  $n$  values. (b) Schematic of the conversion in a gradient bilayer toward silicon oxide when PDMS is exposed to oxygen plasma. (c) X-ray reflectivity data<sup>32</sup> supports the refractive index distribution in graded bilayers fabricated by means of oxygen plasma through an increase in the scattering length density in the formation of thicker glassy skin layer, reported by several authors (e.g., ref 41). Data reproduced with permission from ref 32. Copyright 2014 Royal Society of Chemistry. (d) Representative TEM data<sup>39</sup> illustrating the skin conversion with thickness, progressing from a darker region, corresponding to the denser silicon oxide gradient to a lighter background value, corresponding to untreated PDMS. Inset image reproduced with permission from ref 39. Copyright 2010 American Chemical Society. (e) The distribution described in panels a and b is, then, applied in modeling the modulation of experimental diffraction patterns from zeroth to third order (red, green, blue, and yellow solid lines respectively) ( $^{\circ}$ ), as a function of (e) strain,  $\epsilon_{\text{comp}}$  and (f) amplitude,  $A$ .

dependent on the plasma dose applied and creates a logarithmic dependence conversion profile with thickness,

where the surface of the layer is fully reacted into a denser silica-like layer with decreasing conversion in the subsequent intermediate layers.<sup>32</sup> A representative TEM data by Befahy et al. also supports the gradient nature through width contrast. The chemical modification and surface densification because of plasma treatment is responsible for the contrast observed in a TEM image.<sup>39</sup> By tracing a line through the image, spanning from a plasma-oxidized PDMS surface to the bulk, a qualitative profile can be estimated, showing contrast variation from fully converted plasma surface, with illustrative contrast = 0, to pure PDMS, approaching 1. The width, reflecting the gradient skin thickness, can be approximated to 20 nm.

Because of the nature of the wavefront kinetics of film growth in the plasma oxidation of PDMS, this system is unlike to behave as a perfect bilayer phase grating, where a single, sharp interface is usually defined. Therefore, to account for the graded silicon-oxide interface, instead of using a single refractive index for the skin as in eq 7, we define a refractive index distribution, which is able to better represent the densification from the bulk PDMS ( $n \approx 1.41$ ) to glass ( $n \approx 1.46$ – $1.55$ ) as suggested by XRR and TEM experiments. Hence, we consider the signal to arise from a distribution of  $n$  values with an exponential decay function, such that

$$\overline{I(x, y)} \approx \sum_{i=0}^8 A_0 e^{-kn_i} I_{n_i}(x, y) \quad (8)$$

where  $n_i$  ranges from 1.41 to 1.55. The choice of 9 (or more) terms to implement the normalized exponential curve is supported by the subsequent TEM and XRR data, where  $A_0 = 8.0 \times 10^{18}$  and  $k = 31.5$ . In Figure 4a, this resultant model using a distribution (red solid line) quantitatively captures the representation the data (red circles) for zeroth order intensities. We find that a Gaussian distribution (among others) can also adequately model the data (Figure S2). The application of the gradient distribution of refractive index implemented in the model for the zeroth and the other orders (first to third) is reported in Figure 4e, where the models (in solid lines) show an agreeable representation of the experimental data. Because of the correlation of strain and amplitude established in the bilayer model eq 2, we are able to obtain a relationship between the intensity of orders with amplitude in Figure 4f. The intensity modulation of the orders

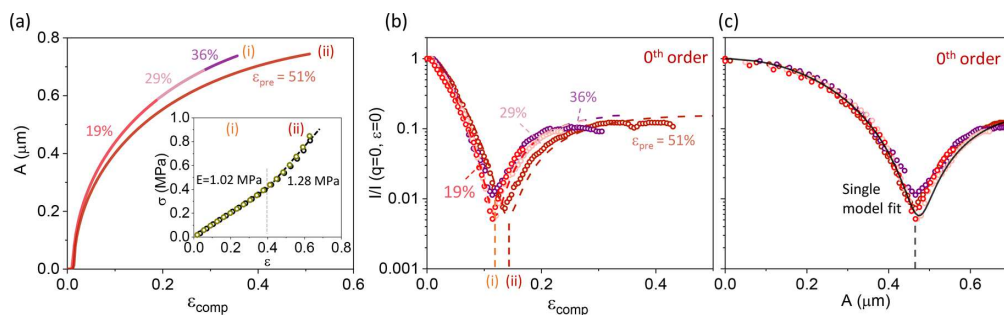


**Figure 5.** (a) Dependence of pattern amplitude on compressive strain  $\epsilon_{\text{comp}}$  employing different prestrains. The disparity between the two lines (from  $\epsilon_{\text{prestrain}} = 19$ – $36\%$  and  $51\%$ ) is ascribed to the onset of non-Hookean behavior in PDMS in high-deformation conditions, and nonlinearity in the stress–strain relationship shown in inset. (b) Normalized zeroth order intensities comparing experimental data ( $^{\circ}$ ) and modeled profile (---) at different prestrains. The slight variation in the minimum position, at the highest prestrain (0.51), is due to the non-Hookean behavior of  $E$ , resulting in a higher critical strain. (c) Near collapse of all zeroth order normalized intensity data when plotted as a function of pattern amplitude (demonstrating that apparent offsets in panel b arise from the mechanical history of the material).

describes the diffraction efficiency dependence on the profile of the grating as a function of strain or amplitude. Specifically, the maximum efficiency for the grating can be estimated when the zeroth order goes through the main minimum around  $\epsilon_{\text{comp}} \approx 0.11$  or  $A \approx 0.45$ . (Figure S3) Here, the other three orders modulate toward a maximum, progressively increasing the amount of diffracted light. This can be calculated as a percentage with respect to the total diffracted intensity (zeroth order at 0 strain or amplitude), reaching  $\approx 30\%$  of the total light for the first and second order, and 5% for the third order. The residual loss might be ascribed to adsorption/diffusion phenomena because of the PDMS thickness and additional light coming from the zeroth order.

**Effect of PDMS Mechanical Properties on Diffraction of Tunable Gratings.** When samples with different initial prestrains undergo an identical plasma treatment (i.e., same power and exposure time), we observe that the modulation of intensities is dependent on the amplitude versus strain evolution of the wrinkles. When the intensity of the zeroth order is compared in samples having prestrains of 19%, 29%, 36%, and 51%, initial discrepancies in intensity against  $\epsilon_{\text{comp}}$  were observed. When the intensities are plotted with  $\epsilon_{\text{comp}}$  it appears that the position of the minimum for the highest  $\epsilon_{\text{prestrain}}$  differs from the lower three, in Figure 5b. This can be ascribed to the non-Hookean behavior of the PDMS mechanical properties with strain. When a PDMS coupon is stretched beyond  $\epsilon = 0.4$ , the linearity of the stress–strain relationship deviates leading to two different values for the elastic modulus, curves i and ii as shown in the inset in Figure 5a. Since the elastic modulus of PDMS directly affects  $\epsilon_c$  and hence  $A$ , we are able to remodel the  $A$  versus  $\epsilon_{\text{comp}}$  curve accounting for the different mechanical response at a given prestrain. When the intensity versus  $\epsilon$  graphs are converted to intensity versus  $A$  (using the relationship between  $\epsilon$  and  $A$ ), the results for the different prestrains collapse onto one curve, implying that the intensities are solely dependent on the amplitude evolution of the samples for a given condition (demonstrated also for the first diffraction order in Figure S4).

**Additional Diffraction Orders at High Deformations: Period Doubling Instability.** We next seek to investigate the effect of high deformations, specifically for prestrain above 50% on the sample. An initial  $\epsilon_{\text{prestrain}}$  of 0.6 was applied to the PDMS coupon undergoing plasma treatment, and the observation of the buckling development as the sample relaxes was assessed using a photopolymer. As the sample is partially released, a drop of Norland Optical Adhesive (NOA) is placed on the surface and covered with a glass slide. The NOA is UV cured, and the glass slide is removed to produce a replica at a specific intermediate strain. This is repeated to produce a series at varying compressive strains and the wavelengths of the replicas are characterized via AFM and SLS. As expected, the primary wavelength  $\lambda_1$  decreases with increasing strain, as per eq 4. However, as  $\epsilon_{\text{comp}}$  increases, the initially sinusoidal-like buckling (Figure 6c(iii)) deviates into a period doubling regime (Figure 6c(i)), resulting in the arise of a secondary wavelength,  $\lambda_2$  when  $\epsilon_{\text{comp}} \geq 0.36$ .

This transition to frequency doubling can be observed and quantified with SLS. The occurrence of an additional order can be clearly seen between the zeroth and first order, giving rise to wavelengths corresponding to  $\lambda_2$ . The order has a smaller wavenumber because of the formation of a larger wavelength in a period doubling. By monitoring the intensity of the new order as the sample is continually released, we are able to

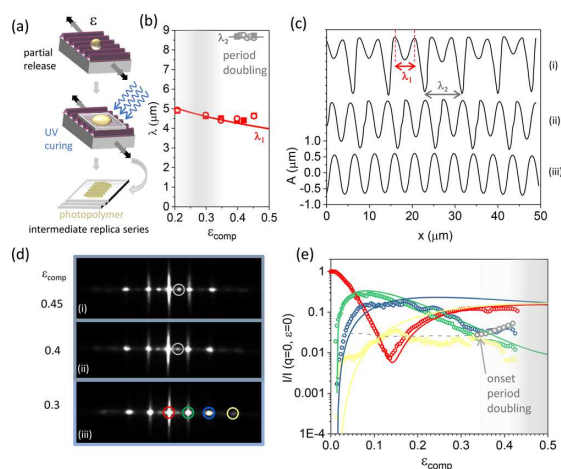


**Figure 6.** (a) Schematic describing the process of characterization of wrinkled samples in partial release, using a photopolymer (NOA) replica. (b) Pattern wavelength  $\lambda$  and secondary period-doubling  $\lambda_2$  obtained by AFM (■) and SLS (°) measurements of the replicas. (c) AFM cross-sectional line profiles of conditions in the (iii) sinusoidal-like regime, (ii) transition, and (i) period doubling regime. (d) SLS images showing the onset of period doubling as an additional observable order (light gray) between the original zeroth and first orders, whose intensity becomes increasingly pronounced with  $\epsilon_{\text{comp}}$ . (e) Dependence of the normalized diffraction intensities of the 0th–3rd order with strain into high deformation regime, depicting the emergence of period doubling at  $\epsilon_{\text{comp}} \gtrsim 0.3$ .

observe more accurately the point of transition from sinusoidal to period doubling. In Figure 6e, the gray circles indicate the formation of a new order, where its intensity increases as the period doubling formation becomes more prominent. For the other orders, the experimental data (°) and model (—) were plotted accordingly with strain, showing good agreement for the zeroth and first order. The discrepancies for the second and third order, where the experimental data show lower intensities compared to the model curves could be attributed to the light being redirected toward the formation of the new additional order, causing therefore a different phase shift in the phase grating.

**Real-Space Reconstruction from Diffraction Pattern (1D).** With the relationships between wavenumber  $q$  and  $\lambda$ , as well as the intensity and  $A$  established for the graded wrinkled gratings, we devise a way to reconstruct a pattern real space structure from a SLS image. For a given SLS image, such as one in Figure 7a, we can observe three diffraction orders. Wrinkling wavelengths can be readily obtained for spatially calibrated SLS data, as shown in Figure S5. We, further, develop the model reported in Figure 4 to compare intensity ratios between adjacent orders. This eliminates the need for a reference intensity (at zero strain for zeroth order), leaving the dependency to the intensities of the orders solely within the image. Only 2 sets of adjacent orders are required ( $I_0/I_1$ ,  $I_1/I_2$ ) to extrapolate the corresponding amplitude of the sample. The first three orders (0th to 2nd) are chosen because of the smallest standard error between the experimental results and the model. For a given SLS image, we can calculate the ratio of intensities for the two set of orders, intersecting the corresponding amplitude of the wrinkles. With both the wavelength and amplitude, we are able to create the real space



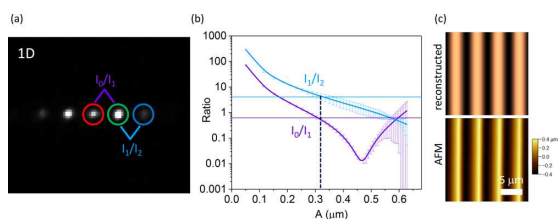


**Figure 7.** Reconstruction of a real-space image using a SLS diffraction patterns. (a) A standard 1D SLS image with its zeroth, first, and second order intensities identified. (b) The purple and blue line represent model  $I_0/I_1$  and  $I_1/I_2$  with amplitude of the pattern, reported in Figure 4. Intersecting the equivalent intensity ratios from the experimental SLS image with the model curve ratios, the surface amplitude can be extrapolated. (c) Reconstructed AFM image obtained plotting a sinusoidal profile with amplitude and wavelength extracted using the previous analysis, compared with the relative experimental AFM profile.

image by inputting  $A$  and  $\lambda$  in a sine wave equation describing the wrinkled surface where  $f(x) = A \sin(2\pi x/\lambda)$ , producing Figure 7c, which agrees well with the experimentally measured AFM profile.

**Real-Space Reconstruction from Diffraction Pattern (2D).** The diffraction of buckled samples is of course not only limited to one-dimensional profiles. Two-dimensional wrinkles can also exhibit varying diffraction patterns, possessing two different sets of orders depending on the fabrication conditions. 2D wrinkling patterns can be fabricated through an intermediary replication step, to minimize crack-formation.<sup>14</sup> A 2D wrinkling pattern was fabricated through the replication of an initial 1D sample where the sample has an initial  $\epsilon_{\text{prestrain}} = 0.10$ , undergoing plasma treatment of 20 W for 2 min. The replica was subsequently rotated through an angle  $\theta$ , before undergoing the same conditions of exposure under strain. When released, this results in a 2D wave superposition creating “sand ripple”-like patterns, which can be tuned with angle with a final pattern morphology described as a superposition of sine waves. Therefore, 2 sets of first order intensities can be observed, each set corresponding to either the first or second generation. An intensity– $A$  model (Figure 8b) can be established given wavelength and amplitude data (Figure 8) with strain for the given conditions. In a similar manner to the 1D, by taking the ratio of intensities between the generations, the amplitudes of both the generations can be deduced from a model. For a 1D sample, the  $A$  for the maximum  $\epsilon$  of 0.10 is  $0.115 \mu\text{m}$ . When 2D samples with angles ranging from  $20^\circ$  to  $90^\circ$  are measured under light scattering, it is observed that there is a boundary between  $35^\circ$  and  $45^\circ$ , where the intensity of the first generation exceeds that of the second below this range, while the converse happens beyond (Figure S6). As a result, it can be observed that at  $20^\circ$ , the first generation is brighter than the second, while at  $50^\circ$  the second generation is more prominent. At lower angles where  $\theta < 35^\circ$ , the development of amplitude of the first generation takes precedence over the second, while when  $\theta > 45^\circ$ , the second generation formation dominates the first. This is due to the relation of formation of the surface topography with respect to its principal coordinates  $x$  and  $y$ . When the second generation has a larger strain component in the  $y$  direction than  $x$ , it suppresses the amplitude in the first generation. As a result, when  $\theta = 20^\circ$ , we can take the maximum amplitude to belong to the first generation, while for  $\theta = 50^\circ$ , we can take it to

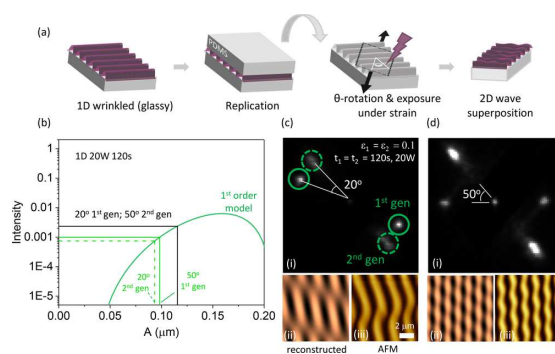


**Figure 8.** (a) Schematic of 2D wrinkling pattern formation: An initial 1D wrinkled sample ( $P = 20 \text{ W}$ ,  $t = 120 \text{ s}$ ,  $\epsilon = 0.1$ ) is replicated with fresh PDMS. The replica is, then, stretched uniaxially, rotated at an angle  $\theta$ , and exposed to a second plasma oxidation. Upon release of the secondary strain, a secondary pattern is formed as result of a 2D Fourier wave superposition. (b) Green solid line shows the first-order intensity model at  $P = 20 \text{ W}$  and  $t = 120 \text{ s}$ . Black solid line shows the amplitude and intensity at  $\epsilon = 0.1$  (experimental prestrain), with  $A = 0.11$  (maximum amplitude). At smaller angles, below the range of  $35\text{--}45^\circ$ , the first generation component in the maximum amplitude is predominant, while at larger angles, the second generation component takes over. (c) Construction of a real space image of a 2D pattern. The SLS image of a 2D pattern with  $\theta = 20^\circ$  shows two sets of first-order diffraction, belonging to the first and second generation, at an angle  $\theta$ . Wavelengths and amplitudes can be extracted and used to build a real-space image from the 2D SLS, shown in curve ii. (d) For  $\theta = 50^\circ$ , the SLS image shows 2 sets of first-order intensities separated by  $50^\circ$ , with intensity of the second generation brighter than the first. The amplitude and wavelengths from the SLS allows for the reconstruction of real space image in curve ii, agreeing with the experimental in curve iii.

belong to the second generation. Subsequently, by taking the ratio of intensities of the two generations, the other generation can be deduced using the model. The wavelengths of the individual generations can be gathered as in the 1D case (Figure S7). With both information on amplitude and wavelengths of the two cosine waves, a real space image can be reconstructed, in good agreement with the experimental AFM images.

## CONCLUSIONS

We have explored the fabrication of 1D and 2D strain-tunable phase gratings by means of the mechanical wrinkling of plasma oxidized PDMS employing, respectively, uni- and biaxial strain fields. While 1D phase gratings have been previously demonstrated by the wrinkling of bilayers comprising a polymer thin-film supported onto PDMS,<sup>15,22</sup> the fabrication method employed, here, is considerably simpler, removing the need to float and deposit the glassy film, as well as more robust, by ensuring covalent bonding of the skin layer and preventing delamination or crumpling. We resolve and quantify up to 4 diffraction orders resulting from plasma-oxidized PDMS samples, which are strain-controlled and thus tunable, or fixed (or static) by the release of a selected prestrain condition. The intensity of the various diffraction orders is modulated by strain, as the sample undergoes relaxation ( $\epsilon_{\text{comp}}$ ), providing a maximum total diffraction efficiency of 48%.

We find that phase gratings fabricated via this method cannot, however, be described by conventional sinusoidal phase grating equations. We attribute this fact to the gradient nature of the glassy skin layer, originating from the directional conversion process that emanates from the top surface during plasma oxidation. By incorporating a distribution of refractive index in the skin formed, we succeed in quantitatively modeling the diffraction data. Further, the precise data modeling of the strain dependence of the diffraction data requires the consideration of non-Hookean properties of PDMS because of the change in elastic modulus at sufficiently high strain affecting primarily the buckling amplitude.

We, then, also examine the optical behavior of these phase grating at higher deformation, when buckling deviates from the sinusoidal regime toward period doubling. This leads to the emergence of an additional diffraction order, as a result of a secondary wavelength formed upon “doubling” events. The precise strain of period doubling formation can be monitored through light scattering, where the increase in intensity of the new order is an indication of its development.

Significantly, we find that diffraction patterns can be used to fully resolve the surface structure in simple manner. The real-space image of a wrinkled sample can be effectively reconstructed by obtaining the wavelength and amplitude through a diffraction image, and this can be extended beyond the one-dimensional to two-dimensional samples showing double sets of diffraction series corresponding to the respective generations. Light scattering is thus demonstrated as an rapid and effective tool to resolve the surface topology of these systems.

We believe that our findings are relevant to a range of applications, including the development of flexible responsive optics benefiting for a facile manufacturing route. The structural color exhibited from such gratings could also give rise to mechanochromic functionalities with potential applications in displays and smart windows.

## EXPERIMENTAL SECTION

**Sample Preparation.** Sylgard 184 (Dow Corning) was employed by mixing the prepolymer and cross-linker at a 10:1 ratio by mass; the mixture was vigorously stirred with a spatula, degassed under vacuum, deposited on a glass slab, and cured at 75 °C in a convection oven for 1 h to cross-link into an elastomer that, despite containing several additives, we term polydimethylsiloxane (PDMS) for simplicity. The PDMS slab obtained, with a thickness of 2.5 mm, was cut into coupons of 2.5 cm × 3 cm. Samples were clamped onto a strain stage attached by a motor actuator and strained to the required  $\epsilon_{\text{prestrain}}$  at a speed of 0.02 mm<sup>2</sup> with a precision of ±0.001 mm. The applied prestrain is calculated with respect to the initial and final distance between the clamps before and after stretching,  $L_0$  and  $L_1$ , respectively:  $\epsilon_{\text{prestrain}} = (L_1 - L_0)/L_0$ .

**Surface Oxidation.** Surface plasma oxidation was performed using a 40 kHz Diener Plasma (Femto), fitted with a pressure sensor (TM 101, Thermovac) and an oxygen gas cylinder (BOC, 99.5% purity). The chambers were evacuated to a pressure of 0.2 mbar, before flowing the gas for 5 min until the desired pressure was reached and stabilized. The plasma was then ignited, at the required power, and exposure, controlled with a timer. Power setting of  $p = 70$  W and oxygen pressure of  $P = 1$  mbar was used, with exposure time  $t = 420$  s.

**Pattern Characterization.** Wrinkling morphology of samples were evaluated by means of atomic force microscopy (AFM) employing a Bruker Innova microscope in tapping mode, equipped with Si tips (MPP-11100-W, Bruker), at 0.2 Hz, and analyzed with the in-built Nanoscope software. Wavelengths and amplitudes were

averaged over a series of three measurements recorded over areas of 50  $\mu\text{m} \times 50 \mu\text{m}$  scanning windows.

**Static Light Scattering.** Static light scattering setup consisting of a diode-pumped CrystaLaser (532 nm, 500 mW) (Figure 2a (i)) and neutral density filter wheel consisting of 2 sets of filters –0.2–0.6 and 1.0–4.0 (Thor Laboratories) (ii). The laser light is reflected by a mirror (iii) at 45° and passes perpendicular through the sample. The distance from the sample to the screen is 10 cm. The diffraction patterns (v) formed on the screen are monitored when the sample undergo light scattering as it undergoes motorized compression through an automated strain stage (iv) to form sinusoidal wrinkles. SLS images are collected by means of a 16-bit CCD cooled camera (Hamamatsu Orca), controlled by the in-built software Wasabi. The use of a photodiode attached to a digital console (Thor Laboratories) was also supplemented to monitor single point diffraction orders (Figure S8). The range of ND filters utilized were varied throughout the experiment to maximize the intensities observed without saturating the CCD camera.

## ASSOCIATED CONTENT

### Supporting Information

The Supporting Information is available free of charge at <https://pubs.acs.org/doi/10.1021/acsapm.1c00906>.

Estimation of glassy thin film elastic modulus from the aspect ratio of wrinkles; alternative gradient distributions implemented into phase grating model; diffraction efficiency of tunable phase grating; non-Hookean behavior and impact in the first diffraction order; pixel/wavelength calibration of SLS; amplitude and wavelength data implemented into 2D SLS reconstruction; angle boundary in 2D wrinkling reconstruction; and extraction of SLS diffraction image intensity using background correction and confirmation intensity reading using photodiode detector (PDF)

## AUTHOR INFORMATION

### Corresponding Author

João T. Cabral – Department of Chemical Engineering, Imperial College London, London SW7 2AZ, U.K.; Centre for Processable Electronics, Imperial College London, London SW7 2AZ, U.K.; [orcid.org/0000-0002-2590-225X](https://orcid.org/0000-0002-2590-225X); Email: [j.cabral@imperial.ac.uk](mailto:j.cabral@imperial.ac.uk)

### Authors

Annabelle Tan – Department of Chemical Engineering, Imperial College London, London SW7 2AZ, U.K.; Centre for Processable Electronics, Imperial College London, London SW7 2AZ, U.K.

Luca Pellegrino – Department of Chemical Engineering, Imperial College London, London SW7 2AZ, U.K.

Complete contact information is available at: <https://pubs.acs.org/doi/10.1021/acsapm.1c00906>

### Author Contributions

A.T. and L.P. performed all experiments: sample preparation, light diffraction, optical and atomic force microscopy, and mechanical measurements. J.T.C. conceived and directed the project. All authors analyzed the data, wrote, and revised the manuscript.

### Notes

The authors declare no competing financial interest.

## ACKNOWLEDGMENTS

The authors thank Procter & Gamble and the EPSRC-funded Plastic Electronics CDT for a PhD scholarship (Grant Number EP/L016702/1) and the Royal Academy of Engineering (RAEng, UK) for funding and a research chair.

## REFERENCES

- (1) Dou, X.-Q.; Zhang, D.; Feng, C.; Jiang, L. Bioinspired hierarchical surface structures with tunable wettability for regulating bacteria adhesion. *ACS Nano* **2015**, *9*, 10664–10672.
- (2) Tripathy, A.; Sen, P.; Su, B.; Briscoe, W. H. Natural and bioinspired nanostructured bactericidal surfaces. *Adv. Colloid Interface Sci.* **2017**, *248*, 85–104.
- (3) Kim, J. B.; Kim, P.; Pegard, N. C.; Oh, S. J.; Kagan, C. R.; Fleischer, J. W.; Stone, H. A.; Loo, Y.-L. Wrinkles and deep folds as photonic structures in photovoltaics. *Nat. Photonics* **2012**, *6*, 327–332.
- (4) Guo, L. Nanoimprint Lithography: Methods and Material Requirements. *Adv. Mater.* **2007**, *19*, 495–513.
- (5) Nie, Z.; Kumacheva, E. Patterning surfaces with functional polymers. *Nat. Mater.* **2008**, *7*, 277.
- (6) Bowden, N.; Brittain, S.; Evans, A. G.; Hutchinson, J. W.; Whitesides, G. M. Spontaneous formation of ordered structures in thin. *Nature* **1998**, *393*, 146–149.
- (7) Tardani, F.; Neri, W.; Zakri, C.; Kellay, H.; Colin, A.; Poulin, P. Shear rheology control of wrinkles and patterns in graphene oxide films. *Langmuir* **2018**, *34*, 2996–3002.
- (8) Parker, A. R.; Hegedus, Z.; Watts, R. A. Solar-absorber antireflector on the eye of an Eocene fly (45 Ma). *Proc. R. Soc. London, Ser. B* **1998**, *265*, 811–815.
- (9) Li, R.; Yi, H.; Hu, X.; Chen, L.; Shi, G.; Wang, W.; Yang, T. Generation of diffraction-free optical beams using wrinkled membranes. *Sci. Rep.* **2013**, *3*, 2775.
- (10) Schauer, S.; Schmager, R.; Hüinig, R.; Ding, K.; Paetzold, U. W.; Lemmer, U.; Worgull, M.; Hölscher, H.; Gomard, G. Disordered diffraction gratings tailored by shape-memory based wrinkling and their application to photovoltaics. *Opt. Mater. Express* **2018**, *8*, 184–198.
- (11) Chiche, A.; Stafford, C. M.; Cabral, J. T. Complex micropatterning of periodic structures on elastomeric surfaces. *Soft Matter* **2008**, *4*, 2360.
- (12) Chen, X.; Hutchinson, J. W. Herringbone Buckling Patterns of Compressed Thin Films on Compliant Substrates. *J. Appl. Mech.* **2004**, *71*, 597.
- (13) Davis, C. S.; Crosby, A. J. Wrinkle morphologies with two distinct wavelengths. *J. Polym. Sci., Part B: Polym. Phys.* **2012**, *50*, 1225–1232.
- (14) Pellegrino, L.; Khodaparast, S.; Cabral, J. T. Orthogonal wave superposition of wrinkled, plasma-oxidised, polydimethylsiloxane surfaces. *Soft Matter* **2020**, *16*, 595–603.
- (15) Stafford, C. M.; Harrison, C.; Beers, K. L.; Karim, A.; Amis, E. J.; VanLandingham, M. R.; Kim, H.-C.; Volksen, W.; Miller, R. D.; Simonyi, E. E. A buckling-based metrology for measuring the elastic moduli of polymeric thin films. *Nat. Mater.* **2004**, *3*, 545–550.
- (16) Bowden, N.; Huck, W. T.; Paul, K. E.; Whitesides, G. M. The controlled formation of ordered, sinusoidal structures by plasma oxidation of an elastomeric polymer. *Appl. Phys. Lett.* **1999**, *75*, 2557–2559.
- (17) Chan, E. P.; Smith, E. J.; Hayward, R. C.; Crosby, A. J. Surface Wrinkles for Smart Adhesion. *Adv. Mater.* **2008**, *20*, 711–716.
- (18) Bowden, N.; Brittain, S.; Evans, A. G.; Hutchinson, J. W.; Whitesides, G. M. Spontaneous formation of ordered structures in thin. *Nature* **1998**, *393*, 146–149.
- (19) Allen, H. *Analysis and Design of Structural Sandwich Panels*; The Commonwealth and International Library: Structures and Solid Body Mechanics Division; Pergamon, 1969.
- (20) Jiang, H.; Khang, D.-Y.; Song, J.; Sun, Y.; Huang, Y.; Rogers, J. A. Finite deformation mechanics in buckled thin films on compliant supports. *Proc. Natl. Acad. Sci. U. S. A.* **2007**, *104*, 15607–15612.
- (21) Wang, Q.; Zhao, X. A three-dimensional phase diagram of growth-induced surface instabilities. *Sci. Rep.* **2015**, *5*, 8887.
- (22) Harrison, C.; Stafford, C.; Zhang, W.; Karim, A. Sinusoidal phase grating created by a tunably buckled surface. *Appl. Phys. Lett.* **2004**, *85*, 4016–4018.
- (23) Meng, Y.; Gong, X.; Huang, Y.; Li, L. Mechanically tunable opacity effect in transparent bilayer film: Accurate interpretation and rational applications. *Applied Materials Today* **2019**, *16*, 474–481.
- (24) Yu, C.; O'Brien, K.; Zhang, Y.-H.; Yu, H.; Jiang, H. Tunable optical gratings based on buckled nanoscale thin films on transparent elastomeric substrates. *Appl. Phys. Lett.* **2010**, *96*, 041111.
- (25) Meshalkin, A. Y.; Podlipnov, V.; Ustinov, A.; Achimova, E. Analysis of diffraction efficiency of phase gratings in dependence of duty cycle and depth. *J. Phys.: Conf. Ser.* **2019**, *1368*, 022047.
- (26) Stürmer, M.; Wapler, M. C.; Schmitt, J.; Völklein, F.; Wallrabe, U. Phase gratings with tunable diffraction efficiency. *Opt. Express* **2016**, *24*, 23765–23776.
- (27) Stoykova, E.; Harizanova, J.; Sainov, V. Pattern projection with a sinusoidal phase grating. *EURASIP Journal on Advances in Signal Processing* **2009**, 351626.
- (28) Groisman, A.; Zamek, S.; Campbell, K.; Pang, L.; Levy, U.; Fainman, Y. Optofluidic 1×4 switch. *Opt. Express* **2008**, *16*, 13499–13508.
- (29) Kavc, T.; Langer, G.; Kern, W.; Kranzelbinder, G.; Toussaere, E.; Turnbull, G. A.; Samuel, I. D.; Iskra, K. F.; Neger, T.; Pogantsch, A. Index and relief gratings in polymer films for organic distributed feedback lasers. *Chem. Mater.* **2002**, *14*, 4178–4185.
- (30) Goodman, J. W. *Introduction to Fourier Optics*; Roberts and Company Publishers, 2005.
- (31) Owen, M. J.; Smith, P. J. Plasma treatment of polydimethylsiloxane. *J. Adhes. Sci. Technol.* **1994**, *8*, 1063–1075.
- (32) Bayley, F. A.; Liao, J. L.; Stavrinou, P. N.; Chiche, A.; Cabral, J. T. Wavefront kinetics of plasma oxidation of polydimethylsiloxane: limits for sub-[small mu ]m wrinkling. *Soft Matter* **2014**, *10*, 1155–1166.
- (33) Nania, M.; Matar, O. K.; Cabral, J. T. Frontal vitrification of PDMS using air plasma and consequences for surface wrinkling. *Soft Matter* **2015**, *11*, 3067–3075.
- (34) Nania, M.; Foglia, F.; Matar, O. K.; Cabral, J. T. Sub-100 nm wrinkling of polydimethylsiloxane by double frontal oxidation. *Nanoscale* **2017**, *9*, 2030–2037.
- (35) Li, Z.; Liu, Y.; Marin, M.; Yin, Y. Thickness-dependent wrinkling of PDMS films for programmable mechanochromic responses. *Nano Res.* **2020**, *13* (7), 1882.
- (36) Breid, D.; Crosby, A. J. Surface wrinkling behavior of finite circular plates. *Soft Matter* **2009**, *5*, 425–431.
- (37) Chen, Y.-C.; Crosby, A. J. High aspect ratio wrinkles via substrate prestretch. *Adv. Mater.* **2014**, *26*, 5626–5631.
- (38) Chua, D. B. H.; Ng, H. T.; Li, S. Spontaneous formation of complex and ordered structures on oxygen-plasma-treated elastomeric polydimethylsiloxane. *Appl. Phys. Lett.* **2000**, *76*, 721–723.
- (39) Befahy, S.; Lipnik, P.; Pardoen, T.; Nascimento, C.; Patris, B.; Bertrand, P.; Yunus, S. Thickness and elastic modulus of plasma treated PDMS silica-like surface layer. *Langmuir* **2010**, *26*, 3372–3375.
- (40) Efimenko, K.; Rackaitis, M.; Manias, E.; Vaziri, A.; Mahadevan, L.; Genzer, J. Nested self-similar wrinkling patterns in skins. *Nat. Mater.* **2005**, *4*, 293–297.
- (41) Efimenko, K.; Wallace, W. E.; Genzer, J. Surface Modification of Sylgard-184 Poly(dimethyl siloxane) Networks by Ultraviolet and Ultraviolet/Ozone Treatment. *J. Colloid Interface Sci.* **2002**, *254*, 306–315.
- (42) Hillborg, H.; Ankner, J.; Gedde, U.; Smith, G.; Yasuda, H.; Wikström, K. Crosslinked polydimethylsiloxane exposed to oxygen plasma studied by neutron reflectometry and other surface specific techniques. *Polymer* **2000**, *41*, 6851–6863.



### Tunable Phase Gratings by Wrinkling of Plasma-Oxidized PDMS: Gradient Skins and Multiaxial Patterns

Author: Annabelle Tan, Luca Pellegrino, João T. Cabral

Publication: ACS Applied Polymer Materials

Publisher: American Chemical Society

Date: Oct 1, 2021

Copyright © 2021, American Chemical Society

#### PERMISSION/LICENSE IS GRANTED FOR YOUR ORDER AT NO CHARGE

This type of permission/license, instead of the standard Terms and Conditions, is sent to you because no fee is being charged for your order. Please note the following:

- Permission is granted for your request in both print and electronic formats, and translations.
- If figures and/or tables were requested, they may be adapted or used in part.
- Please print this page for your records and send a copy of it to your publisher/graduate school.
- Appropriate credit for the requested material should be given as follows: "Reprinted (adapted) with permission from {COMPLETE REFERENCE CITATION}. Copyright {YEAR} American Chemical Society." Insert appropriate information in place of the capitalized words.
- One-time permission is granted only for the use specified in your RightsLink request. No additional uses are granted (such as derivative works or other editions). For any uses, please submit a new request.

If credit is given to another source for the material you requested from RightsLink, permission must be obtained from that source.

[BACK](#)

[CLOSE WINDOW](#)



# Tunable Structural Color with Gradient and Multiaxial Polydimethylsiloxane Wrinkling

Annabelle Tan, Luca Pellegrino, Zain Ahmad, and João T. Cabral\*

The generation of structural color from wrinkled polydimethylsiloxane (PDMS) surfaces, fabricated by plasma exposure, subjected to uni- and multi-axial, and sequential strain fields is examined. The approach is based on the well-known, mechanically-induced, buckling instability of a supported bilayer, whereby the top glassy “skin” is formed by plasma oxidation. Surface periodicities  $200 \text{ nm} \lesssim d \lesssim 3 \text{ }\mu\text{m}$ , encompassing the visible spectrum, are investigated in terms of the observed color, intensity spectrum, and color mixing from different diffraction orders, exhibiting good agreement with model predictions. By contrast with complex fabrication methods, color tunability and mechanochromic response are readily achieved by adjusting plasma and strain parameters, and by dynamically varying strain ( $\epsilon \lesssim 50\%$ ). Prescribed strain directionality, employing uniaxial, isotropic, gradient strain, and wave-sum wrinkling superposition, as well as skin thickness (and thus  $d$ ) and amplitude gradients, using facile and scalable fabrication approaches, yield striking spatial color variation, homogeneity, and directionality.

in dragonflies *Rhyothemis resplendens*.<sup>[20]</sup> Randomly oriented wrinkles were demonstrated to produce uniform bright structural colors with broad viewable angles, which can further be tunable using light sensitive polymers skins.<sup>[23]</sup>

Mechanochromic response, that is, the change of color under stress, of wrinkled structures has been recently reported, employing various bilayer film structures.<sup>[22,24,25]</sup> The use of soft matter substrates, including elastomers, is advantageous as it readily allows optical properties to be tuned by the applied strain, by adjusting surface periodicity and amplitude, in addition to film thickness and mechanical modulus. Further, a wide range of surface patterns, including uni- and multiaxial and hierarchical wrinkles, can be readily fabricated. Bilayers are generally fabricated by deposition or lamination

of a thin and stiff film, typically a few 10–100 nm and GPa modulus, atop a thicker (mm) and softer ( $\approx$ MPa), for instance an evaporated metal of a spun-coated glassy polymer supported by a polydimethylsiloxane (PDMS) elastomer. The mismatch in mechanical properties between films, provided that there is strong adhesion between them (to minimize delamination, crack formation, etc.), leads to surface buckling under strain. Strain can be induced thermally, by film evaporation/shrinkage, and commonly, by mechanical strain.

Plasma oxidation provides a facile route to generating a thin, glass-like film onto PDMS,<sup>[26]</sup> enabling precise control of film thickness growth kinetics.<sup>[27–29]</sup> We have previously demonstrated the design of tunable optical gratings<sup>[30]</sup> using this method (building on the previous demonstrations with polymer bilayer laminates<sup>[31]</sup>). The impact of the PDMS substrate thickness on the mechanochromic response of 1D plasma oxidized PDMS films has been recently reported,<sup>[32,33]</sup> and color tunability according to illumination and viewing angle examined. Recently, the incorporation of polystyrene nanoparticles and the use of wire-bar coating (yielding regular arrays) was demonstrated to produce both angle-independent and -dependent structural colors, upon plasma exposure and wrinkling.<sup>[34]</sup>


In this study, we build upon the structural color and mechanochromic response exhibited by 1D plasma oxidized wrinkled PDMS topographies ranging from nano to the micronscale, and quantitatively examines the emergence of color mixing, by superposition of diffraction orders of distinct colors at similar observation angles. We then quantify the joint roles of amplitude and periodicity in color brightness, and finally consider

## 1. Introduction

Inspired by the abundance of structural color in nature,<sup>[1–7]</sup> a range of material synthesis and processing approaches have been developed to design nano- and microstructures, including multilayer films,<sup>[8,9]</sup> photonic crystals,<sup>[10,11]</sup> and metasurfaces,<sup>[12,13]</sup> exhibiting static and variable structural colors, tailored to various practical applications.<sup>[14–17]</sup> Wrinkled surface structures, found in flowers and insects<sup>[18–20]</sup> have been shown to act as surface diffraction gratings, imparting structural color to flower petals such as in the queen of the night tulip<sup>[21]</sup> and the *Hibiscus trionum*,<sup>[22]</sup> as well as enhancing the diffuse reflection

A. Tan, L. Pellegrino, Z. Ahmad, J. T. Cabral  
Department of Chemical Engineering  
Imperial College London  
London SW7 2AZ, UK  
E-mail: j.cabral@imperial.ac.uk

A. Tan, J. T. Cabral  
Centre for Processable Electronics  
Imperial College London  
London SW7 2AZ, UK

 The ORCID identification number(s) for the author(s) of this article can be found under <https://doi.org/10.1002/adom.202200964>.

© 2022 The Authors. Advanced Optical Materials published by Wiley-VCH GmbH. This is an open access article under the terms of the Creative Commons Attribution License, which permits use, distribution and reproduction in any medium, provided the original work is properly cited.

DOI: 10.1002/adom.202200964

color modulation and directionality with gradient wrinkles (i.e., surfaces with spatially varying periodicity) and multi-axial (bi-directional and isotropic) patterns that can be readily fabricated. We demonstrate both uniform and spatially varying colors with observation angle, and further expand the palette of pattern complexity by leveraging wrinkling wave superposition in both simultaneous and sequential steps,<sup>[35,36]</sup> to yield directional color resulting from the interference and relative orientation of wrinkling generations.

## 2. Results and Discussion

### 2.1. Plasma Oxidation of PDMS and Surface Wrinkling

Plasma oxidation of PDMS provides an effective means of generating glassy skin films onto bulk PDMS (and thus a bilayer) with precisely tunable thickness, which therefore yield a library of surfaces of varying wrinkling periodicity ( $d$ ) and amplitude ( $A$ ). By varying the strain field, a range of 1D, 2D, and isotropic structures can be formed. In short, if the plasma exposure is carried out under (pre-)strain conditions, wrinkled surfaces form upon strain relaxation, termed “on” samples; conversely, if plasma exposure is carried out when PDMS is in its relaxed state, then the sample is termed “off”, and thus surface wrinkling is induced upon the (active) application of strain. Specifically, in this work we fabricate 1D structures by uniaxial mechanical strain, and isotropic structures by a thermal cycling treatment, expanding and contracting the bilayer as illustrated in **Figure 1a**. Furthermore, we take advantage of simultaneous and sequential wrinkling wave superposition to access different 2D topographies. By diffracting a narrow light beam (e.g., a

laser), periodic 1D surfaces respond as planar (tunable) 1D phase gratings,<sup>[30,31]</sup> displaying a series of diffraction spots symmetric with respect to the direct beam (center), whose spacing in reciprocal space reflects the pattern periodicity in real space. Isotropic wrinkles yield single-frequency centro-symmetric diffraction patterns, with a circular annulus reflecting the average pattern periodicity, as shown in **Figure 1b**.

The mechanisms and kinetics of the frontal growth and propagation of the glassy skin layer on PDMS by oxygen plasma has been previously reported,<sup>[28,37]</sup> and can be effectively tuned by plasma power, oxygen pressure, and exposure time. Upon strain, the bilayer yields a sinusoidal profile with periodicity  $d$  and amplitude  $A$  which can be generally expressed as<sup>[38]</sup>

$$d = \frac{2\pi h(\bar{E}_f/(3\bar{E}_s))^{1/3}}{(1+\varepsilon)(1+\xi)^{1/3}} \quad (1)$$

$$A = \frac{h(\varepsilon/\varepsilon_c - 1)^{1/2}}{(1+\varepsilon)^{1/2}(1+\xi)^{1/3}} \quad (2)$$

where  $h$  is the glassy film thickness,  $\bar{E}_f$  and  $\bar{E}_s$  are, respectively, the in-plane strain moduli of the film and substrate, given by  $\bar{E} = E/(1-\nu^2)$ , where  $E$  is the Young's modulus and  $\nu$  the Poisson ratio ( $\approx 0.5$  for PDMS);  $\xi = 5\varepsilon(1 + \varepsilon)/32$ , accounting for the non-linearity of the stress–strain relationship of the substrate in the finite deformation regime (i.e., non-Hookean response). Note that we refer to  $d$ , instead of the customary surface wavelength  $\lambda$ , as the surface periodicity to avoid confusion with the wavelength of light. A critical strain must be exceeded to trigger the mechanical instability,  $\varepsilon_c$

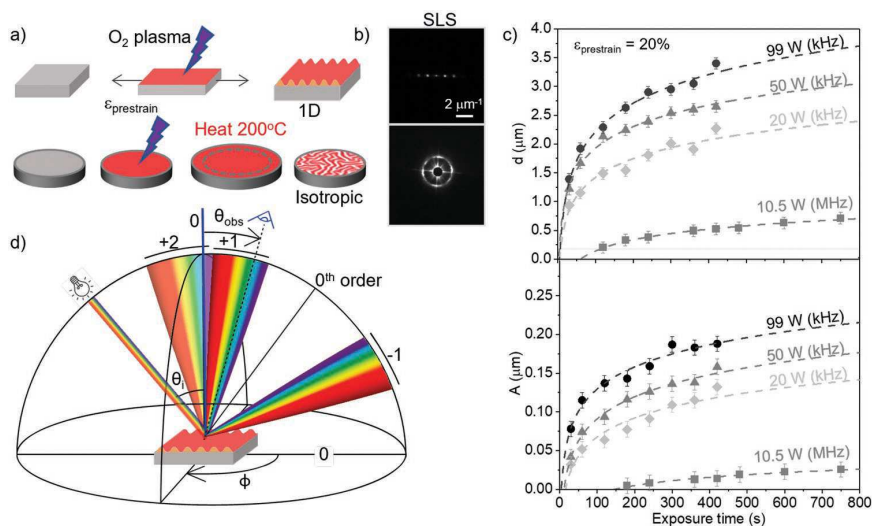


**Figure 1.** a) Schematic of the formation of 1D and isotropic wrinkling samples. 1D wrinkles: plasma oxidation on a prestrained PDMS elastomer coupon and relaxation of strain. Isotropic wrinkles: plasma oxidation on a flat, round PDMS elastomer coupon, heated to 200 °C for 30 min to induce strain through thermal expansion, and cooled to induce the wrinkles. b) Diffraction pattern for the 1D (99 W, 120 s) shows orders zero to second and a ring diffraction of first order for the isotropic (20 W, 120 s). c) Wrinkling periodicity ( $d$ ) and amplitude ( $A$ ) measured as a function of plasma exposure time (s) for treated PDMS coupons with different power and plasma frequency (13.6 MHz: 10.5 W; 40 kHz: 20, 50, and 99 W). d) Schematic of light diffraction of wrinkled samples showing up to three orders (–1, +1, +2): a white LED light at  $\theta_i$ , observer/camera at  $\theta_{obs}$ .

$$\varepsilon_c = \frac{1}{4} \left( \frac{3\bar{E}_s}{\bar{E}_f} \right)^2 \quad (3)$$

In the low deformation limit ( $\varepsilon \lesssim 0.1$ ), the amplitude alone depends on strain, thus allowing for  $d$  and  $A$  to be decoupled in surface patterning. At high strains ( $\varepsilon \gtrsim 0.5$ ) sinusoidal patterns give rise to further modes, including the formation of folds, period-doubling, and ridges.<sup>[39]</sup> The experimentally measured logarithmic dependence of  $d$  and  $A$  on plasma exposure time,<sup>[28,37]</sup> for both a 13.6 MHz and 40 kHz plasma chambers employed in this work, is shown in Figure 1c. More complex wrinkling geometries, beyond 1D and isotropic gratings, were readily generated with different strain field or exposure arrangements. Gradient wrinkled surfaces, varying both periodicity and amplitude, can be fabricated using tapered PDMS coupons (which spatially vary  $\varepsilon$ ),<sup>[40,41]</sup> or a stepped, or gradient, plasma oxidation process (with spatially varying  $h$ ).<sup>[42–45]</sup> Multi-axial strain fields can induce a plethora of patterns; for instance 2D wrinkles can be fabricated, either through the simultaneous or sequential application of strain in two directions, yielding hexagonal, checkerboard, and herringbone wrinkled structures.<sup>[46–48]</sup> Sequential wrinkling approaches,<sup>[35,36]</sup> use surface wave superposition at varying angles (from  $0^\circ$  to  $90^\circ$ ) to tune wrinkled surfaces from 1D to checkerboard, creating a variety of “s and ripple” structures, with additional in-plane ( $xy$ ) periodicities. Representative topographies were designed and fabricated to yield desired optical effects detailed below.

## 2.2. Wrinkled Surfaces as Phase Gratings

Wrinkled bilayers have been used in the fabrication of diffraction gratings exhibiting mechanochromic properties,<sup>[49]</sup> whose diffraction pattern can be readily computed from Bragg’s Law. For an incident light at an angle  $\theta_i$ , the pathway difference between the incident light on the adjacent wrinkle crest is  $d \times \sin\theta_i$ , where  $d$  represents the wrinkling spacing. Similarly, the pathway difference between the reflected light on the adjacent wrinkle crest is  $-d \times \sin\theta_r$ , where  $\theta_r$  is the angle of detection, yielding

$$n\lambda = d(\sin\theta_i + \sin\theta_r) \quad (4)$$

where integer  $n$  is the diffraction order of light wavelength  $\lambda$ . Tunable phase gratings have been previously demonstrated in case of thin polymer films deposition or lamination onto an elastomeric foundation,<sup>[31,50,51]</sup> giving access to a variable distribution of energy in the diffraction orders. In a phase grating, the resulting diffraction pattern can be modeled for all diffraction orders  $p$  according to<sup>[31,52]</sup>

$$I \approx \sum_{p=-\infty}^{\infty} J_p^2\left(\frac{m}{2}\right) \text{sinc}^2\left[\frac{W}{\pi}\left(q - \frac{2p\pi}{d}\right)\right] \quad (5)$$

where  $J_p$  is a Bessel function of the first kind,  $W$  is the half-width of the aperture,  $d$  is the wrinkling periodicity,  $m/2$  is the maximum phase shift impart to the light, and  $p$  is an index accounting for the  $p$ th diffraction order. Often  $W \approx 0.5$  mm,

determined by the typical profile of laser beam (in the Fraunhofer limit conditions). The maximum intensity of the  $p$ th order can be approximated to be proportional to the Bessel function  $J_p^2(m/2)$  as the sinc function is narrowly distributed in  $q$  about each order without significant overlap between adjacent orders. The phase contrast,  $m(\Delta)$  can be rationalized in terms of the wrinkling bilayer model of amplitude,  $A(\varepsilon)$  by

$$\frac{m(\varepsilon)}{2} = 2\pi \frac{A(\varepsilon)}{\lambda} [n - 1] \quad (6)$$

where  $A(\varepsilon)$  is extracted from the wrinkling high deformation model (Equation (2)),  $n$  is the refractive index, and  $\lambda$  the light wavelength. In a simple bilayer with a sufficiently thin skin, the refractive index  $n$  can be approximated by that of the bulk material.<sup>[31]</sup>

In a 1D wrinkled sample, light diffraction is perpendicular to the direction of the wrinkles (Figure 1d). For sufficiently large wrinkling periodicity, multiple orders of diffracted light can be observed, where positive orders are denoted as those in between the incident light and the reflected 0th order, and conversely for negative orders. The observation angle  $\theta_{\text{obs}}$  represents the position of the observer or camera. The variation in  $\theta_{\text{obs}}$  allows for different structural colors to be viewed.

## 2.3. Structural Color from Nano- to Microscale Wrinkles

Diffraction of white light from wrinkled surfaces, acting as phase gratings, can yield brilliant structural colors which depend on pattern periodicity  $d$  as well as observation angle  $\theta_{\text{obs}}$ . Such colors are optimally observed by minimizing light reflection and scattering from the substrate. This can be achieved through doping the PDMS elastomer, for instance with carbon-black, resulting in uniform light absorbance in the visible range (Figures S1 and S2, Supporting Information). Depending on the plasma oxidation conditions and strain, the wrinkling periodicity and amplitude can be precisely tuned to select the color observed from the surface. The relation between pattern topography and observation diffraction angle, given by Equation (4) enables the prediction of the color wavelength  $\lambda$  at all angles,  $0^\circ \geq \theta_{\text{obs}} \geq 90^\circ$ , for instance when the incident white light is normal to the sample surface ( $\theta_i = 0^\circ$ ). Practically, beyond  $\theta_{\text{obs}} = 70^\circ$ , the observer’s field of the surface becomes restricted. Figure 2a shows the first diffraction order for wrinkled surfaces with periodicities up to  $d = 800$  nm. When wrinkles display periodicities shorter than the wavelength of visible light, no color will be seen to be diffracted from the surface. In these regions, UV and X-ray diffraction could be accessed. MHz plasma oxidation allows for the fabrication of sub-micron structures, yielding single structural color diffraction at accessible observation angles. By varying the plasma exposure time,  $d$  ranging from 490–710 nm were achieved as shown in atomic force microscopy (AFM) micrographs in Figure 2b. The resulting diffracted colors were captured at different  $\theta_{\text{obs}}$ . For  $d = 490$  nm, diffracted wavelengths are limited to larger  $\theta_{\text{obs}}$ , where color is only accessible beyond  $60^\circ$  (Figure 2c(i)). As plasma exposure time increases, resulting in larger  $d$ , a red-shift is observed with  $\theta_{\text{obs}}$  with colors detected

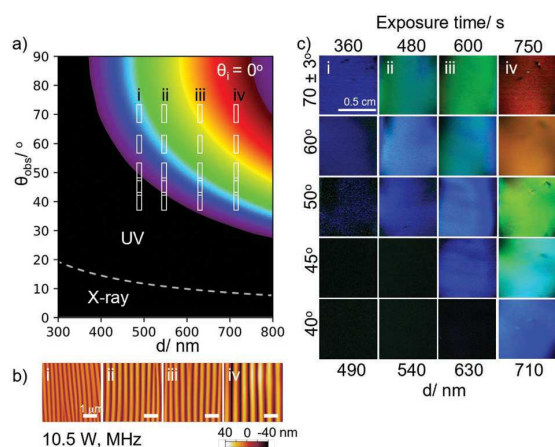


**Figure 2.** a) Nano-wrinkled samples formed using 10.5 W, MHz plasma displaying discrete angular dependency of colors when white light is shone normal to the sample,  $\theta_i = 0^\circ$ . Color observed in the first order with observation angle  $\theta_{\text{obs}}$  and wrinkling periodicity,  $d$  up to 800 nm. White boxes indicates the region of colors accessible ( $\pm 3^\circ$ ) for each sample (i–iv), at different  $\theta_{\text{obs}}$ , corresponding to Figure 2c. Below the threshold light wavelength of 380 nm, diffraction limits of UV and X-ray are reached. b) AFM scans corresponding to the samples (i–iv). c) Single color diffraction observed in plasma-treated samples at exposure times of 360, 480, 600, and 750 s yielding periodicities of 490, 540, 630, and 710 nm respectively.

at lower observation angles. When  $d = 710$  nm, a red color can be observed for  $\theta_{\text{obs}} = 70^\circ$  (Figure 2c(iv)).

In the case of micron-scale surface wrinkles, additional diffraction orders can be observed. The diffraction orders, initially discrete and well separated at low surface periodicities, start to overlap resulting in color mixing when  $d \gtrsim 1.1 \mu\text{m}$ . The color

mixing arises from the contribution of different diffraction orders at the same  $\theta_{\text{obs}}$  at fixed periodicity. Figure 3a shows the expected resulting colors by taking into consideration diffraction order mixing (computed by expressing and combined each diffracted color in RGB format). Plasma oxidation at KHz, performed at 99 W at different exposure times, allows the development of  $d$  ranging from 1.3–3.4  $\mu\text{m}$  (Figure 3b). The observed colors at varying  $\theta_{\text{obs}}$  are shown in Figure 3c, with the contributing orders labeled within each image. When  $d = 1.3 \mu\text{m}$ , single color diffraction is observed until  $\theta_{\text{obs}} \geq 60^\circ$  where the resulting “magenta” color is a contribution from the second and third order. As the wrinkle wavelengths increase, the overlap of two or more orders results in non-discrete colors. Illumination with a red light instead ( $\lambda \approx 650$  nm), induces diffracted red colors at different intensities as the contribution in red increases with the wrinkling periodicity  $d$  (Figure S3, Supporting Information).

Theoretically, diffraction intensities for colored wrinkled structures can be quantified for each order modifying Equation (5) to account for the gradient glassy skin<sup>[30]</sup>

$$I(\bar{x}, \gamma) \approx \sum_{i=0}^8 A_0 e^{-kx_i} I_{ni}(x, \gamma) \quad (7)$$

where  $n_i$  ranges from 1.41–1.55,  $A_0 = 8.0 \times 10^{18}$ , and  $k = 31.5$ . From this, we use the relationship between exposure time with  $d$  and  $A$  to compute an intensity plot, which is also dependent on the wavelength of light  $\lambda$ . We would expect that for a given condition and diffraction order, the intensity of a longer wavelength of light like red light (760 nm) would have a lower intensity than a violet light (380 nm). In Figure S4a, Supporting Information, the theoretical dependence of diffraction intensities with exposure time for different wavelengths of light—from violet of 380 nm to red of 760 nm are plotted for the first

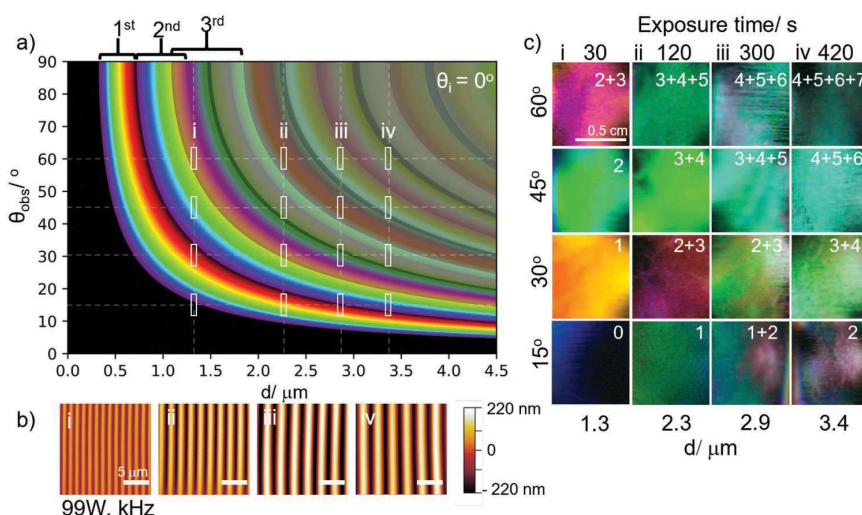


**Figure 3.** a) Micro-wrinkled samples formed using 99 W, kHz plasma exhibiting colors contributed from up to seven diffraction orders. From the second diffraction order, overlap of different orders becomes prominent, resulting in mixed colors with increasing angles. b) AFM scans corresponding to the samples (i–iv). c) Color diffraction for plasma-treated samples at  $p = 99$  W and exposure time of 30, 120, 300, and 420 s yielding wavelengths of 1.3, 2.3, 2.9, and 3.4  $\mu\text{m}$ , respectively. The diffraction orders contributing to the final color are reported at the top right corners of each condition.



order. The intensity for larger wavelength of light are lower and the intensities can be seen to modulate with exposure time, as a result of the evolution of wrinkling periodicity and amplitudes. With increasing order, it is expected that the intensities of light decrease for a single wavelength. In Figure S4b, Supporting Information, the plot of intensities for 533 nm wavelength of light is shown from the first to sixth order. Due to the spread of intensities from shorter to longer wavelength, intensity of different colors from adjacent orders can occur. Indeed, the intensities for longer wavelengths of the fifth order would overlap with those of the shorter wavelengths from the sixth.

#### 2.4. Mechanochromic Response: Tuning Colors with Strain

The mechanochromic response of wrinkled surfaces can be tuned modulating the compressive strain release after the plasma oxidation step. The sensitivity in color variation can be adjusted by considering the relationship between pattern periodicity  $d$  and strain, ensuring that only the first diffraction order ( $n = 1$ ) contributes at the accessible  $\theta_{\text{obs}}$ , to avoid color mixing. The bilayer film parameters can be designed to achieve the appropriate periodicity range. For a system with a smaller periodicity change under strain, (single) color sensing would be optimal with surfaces of smaller wrinkling periodicity at higher  $\theta_{\text{obs}}$ ; conversely with larger periodicity changes, sensing would

be optimal with surfaces of larger  $d$  at lower  $\theta_{\text{obs}}$ , as detailed in Figure S5, Supporting Information. The observed color at a given  $\theta_{\text{obs}}$  can be readily calculated as a function of strain  $\varepsilon$ , by combining Equations (1)–(4) to yield

$$\lambda = \frac{2\pi h(\bar{E}_f/(3\bar{E}_s))^{1/3}}{(1+\varepsilon)(1+\xi)^3} \sin \theta_{\text{obs}} \quad (8)$$

Specifically, **Figure 4a** reports the color shifting from red (buckling onset) to blue (full release) as a function of compressive strain  $\varepsilon$  for a sample treated at  $p = 50$  W and  $t = \sim 30$  s and prestrained to 0.5. At a fixed  $\theta_{\text{obs}}$ , the diffracted color observed can be manipulated by a change in the wrinkling periodicity,  $d$ . When  $\theta_{\text{obs}} = 31^\circ$ , the spectrum of the rainbow can be observed when  $d$  is tuned between 0.9 and 1.5  $\mu\text{m}$  as described in Figure 4b. Due to the intrinsic nature of the buckling relaxation process and as described by Equation (1), we are able to exploit this relationship to create tunable colors with strain. Indeed, the decrease of the wrinkling periodicity with strain fulfills the required range to tune the sample to the color of the spectrum. As the sample experiences compressive strain, the wrinkling amplitude increases with strain, therefore it is possible to determine the theoretical relationship with diffraction intensity through the previously established diffraction model in Equation (7). Following the ability to tune the wrinkling

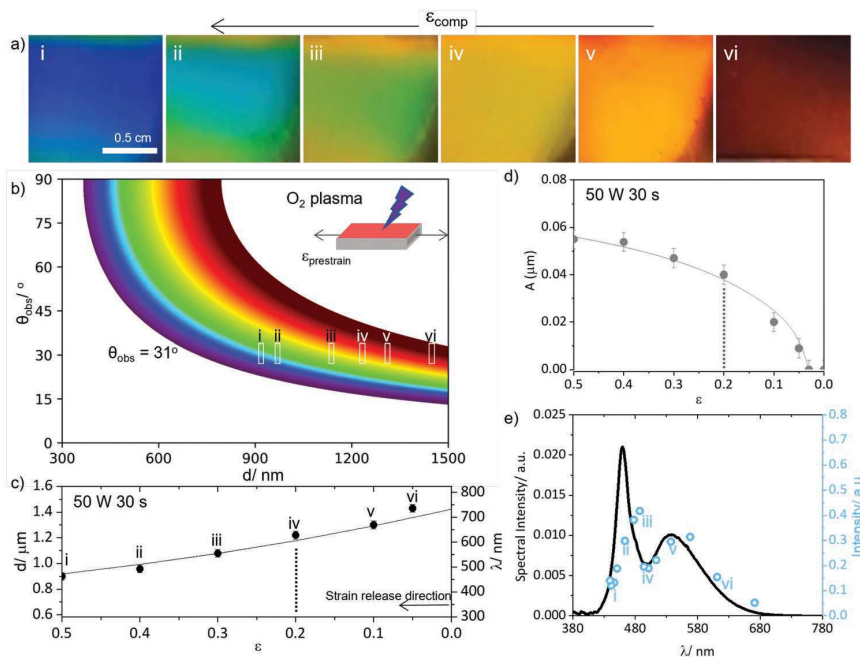


**Figure 4.** a) Mechanochromic variation in CB-PDMS samples oxidized at 50 W, 30 s undergoing compressive strains from (i)  $\varepsilon = 0.5$  to (vi)  $\varepsilon = 0.05$ , at  $\theta_{\text{obs}} = 31^\circ$ . b) First order colors observed at wrinkling periodicity from 300–1500 nm. Series of colors in the first order observed from  $\lambda \approx 700$  nm (red), when  $d \approx 1.4$   $\mu\text{m}$ , to  $\lambda \approx 450$  nm (blue), when  $d \approx 900$  nm. White boxes (i–vi) correspond to the color areal region reported in (a). c) Wrinkling periodicity,  $d$ , as a function of strain for samples (i–vi). The solid line corresponds to Equation (1). Each  $d$  corresponds to an observed diffracted wavelength,  $\lambda$  on the right y-axis. d) Amplitude of wrinkles as a function of strain with the solid line corresponding to Equation (2). e) Calculated diffracted intensity (black line) as function of  $\lambda$ , parametrized by the white light and CB-PDMS absorbance across the spectrum. Measured intensities (blue points) were extracted via RGB decomposition (RGB/3) of (i–vi).

periodicity and amplitude with strain, we would expect the sample to experience a continuous increase in intensity from red to blue (Figure S4, Supporting Information). However, this model alone assumes an equal intensity of the white light at all wavelengths, and it is thus insufficient to explain the intensity exhibited by the samples at their respective colors. Unsurprisingly, there is an effect on the intensity of the light source with the resultant intensity of the color observed. Therefore, modeled color intensity was parametrized by the light spectrum and the absorbance of the CB-PDMS in the required range (Figure S6, Supporting Information). The light spectrum and absorbance were normalized, and combined with the previous description to attain the final model. The intensity of the samples were taken by normalizing the RGB values to one through ImageJ. From Figure 4e, we find that the experimental results agree well with the model, taking into account the spectrum of the light source.

## 2.5. Effect of Relative Illumination and Viewing Angles on Color Perception

The variation in incident angle of light with respect to the sample extends the range of colors observed for structures with smaller wrinkling periodicities instead of incident light normal to the sample. When the angle between the incident light and the camera is fixed at  $50^\circ$  with the sample being rotated along its axis, this allows for the simultaneous change in  $\theta_i$  and  $\theta_{obs}$  as reported in the schematic in Figure 5a(i–iii). By using Equation (4), we can predict the color wavelength while rotating the sample. Conventionally, when  $\theta_{obs}$  and  $\theta_i$  are on opposite sides with respect to the normal,  $\theta_{obs}$  would be denoted as a negative angle. When a plasma treated sample with wrinkling periodicity of 490 nm is observed at  $\theta_{obs}$  with a simultaneous change in  $\theta_i$ , color wavelengths up to  $\approx 650$  nm in the first order can be viewed between  $50^\circ \leq \theta_i \leq 70^\circ$ , while no color can be seen at other angles (Figure 5a). By changing the incident light angle, the sample can exhibit up to a yellow hue when  $\theta_i = 70^\circ$  (Figure 5b), compared to the limited accessibility in color when  $\theta_i$  is fixed at the normal, where only blue can be accessed at higher viewing angles (Figure 2c(i)). For  $d$  of 630 nm, three distinct orders ( $-1$ ,  $+1$ ,  $+2$ ) can be observed while rotating the sample such that  $0^\circ \leq \theta_i \leq 70^\circ$ . Between  $8^\circ < \theta_i \leq 44^\circ$ , no color can be observed. At  $0^\circ \leq \theta_i \leq 8^\circ$ , the  $-1$  order can be seen, the  $+1$  order at  $44^\circ \leq \theta_i \leq 70^\circ$ , and  $+2$  order at  $68^\circ \leq \theta_i \leq 70^\circ$  (Figure 5c). As a result, up to a red hue at  $\lambda = 760$  nm is observable when  $\theta_i = 70^\circ$  and  $\theta_{obs} = 20^\circ$ , as compared to a green visible when  $\theta_i$  is fixed at  $0^\circ$  (Figure 2c(iii)).

## 2.6. Azimuthal Viewing Angle and Color of 1D and Isotropic Wrinkles

1D surfaces have structural colors limited to the direction of diffraction. When a 1D sample (kHz, 99 W, 60 s) is rotated about  $\phi$  ( $\theta_i = 0^\circ$ ,  $\theta_{obs} = 40^\circ$ ), the intensity of the colored sample can be monitored and observed as function of the angle as showed in Figure 6a. When  $\phi = 0$ , the intensity of the sample, measured by  $(R + G + B)/3$  can be seen at a maximum. As  $\phi$  increases, the

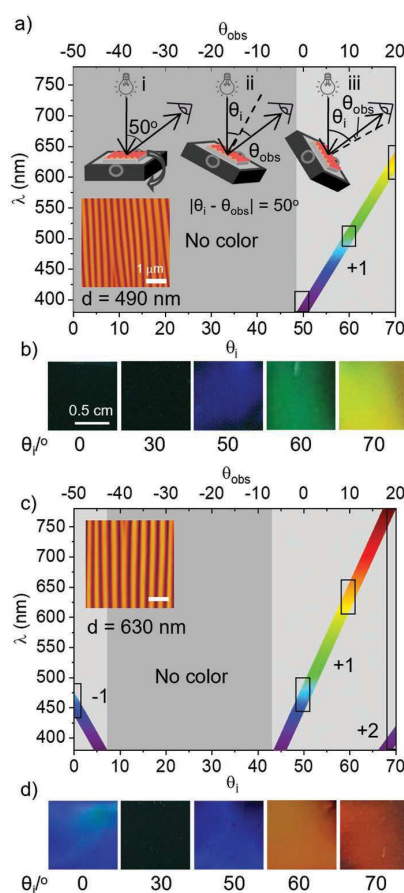


**Figure 5.** a) Color variation observed changing simultaneously  $\theta_i$  and  $\theta_{obs}$ , for a MHz plasma-treated sample at 10.5 W, 360 s yielding  $d$  of 490 nm. b) Images of sample showing increase range of accessible wavelength diffracted compared to in Figure 2c(i) with blue color observed at  $50^\circ$  while yellow at  $70^\circ$ . c) Color variation observed on a sample for MHz plasma-treated sample at 10.5 W, 600 s yielding  $d$  of 630 nm. Light can be observed to be diffracted in  $-1$  order from  $0^\circ$  to  $6^\circ$ ,  $+1$  order from  $45^\circ$  to  $68^\circ$ , and  $+2$  order from  $68^\circ$  to  $70^\circ$ . d) Images of sample showing corresponding diffracted colors.

intensity can be seen to decrease until it reaches a minimum at  $\phi \approx \pi/6$  (Figure 6b). This occurs when the direction of diffraction becomes out of line with the observer. As the diffraction of sinusoidal wrinkles are perpendicular to the wrinkle direction, this only allows observation of the color in one axis with respect to the sample (Figure 6c). The inset shows the first diffraction order pattern of a 1D structure.

In order to increase the viewing angle of structural colors, isotropic wrinkles can be employed. When an isotropic sample is fabricated under the same plasma conditions, it exhibits structural color as the sample rotates  $2\pi$  about  $\phi$ . The intensity (a.u.) of the color was measured to be comparatively lower between  $40^\circ$ – $60^\circ$  while undergoing rotation, displaying color at every  $\phi$  ( $\theta_i = 0^\circ$ ,  $\theta_{obs} = 40^\circ$ ) as reported in Figure 6d. These isotropic structures have a ring diffraction pattern, diffracting light in all directions. Due to the light being diffracted in all

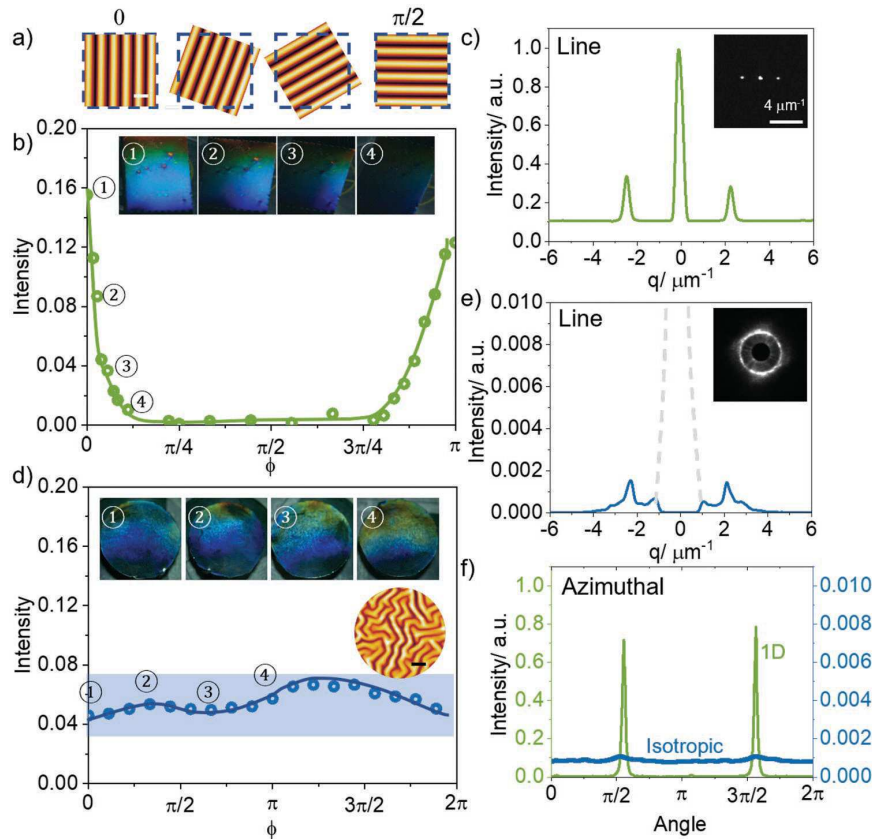


**Figure 6.** a) Schematic of the rotation of wrinkled sample along  $\phi$ . b) Plot of normalized intensity for a 1D sample (kHz plasma, 99 W, 60 s) with  $\phi$  shows a decreasing intensity from 0 to  $\pi/6$ . c) The 1D diffraction pattern intensity where zeroth and first diffraction orders are shown, with the light scattering image shown in the inset. d) Plot of normalized intensity for an isotropic sample (kHz plasma, 99 W, 60 s) when rotated along  $\phi$ . e) The diffraction intensity of isotropic diffraction along a line. The gray dotted line reflects the middle beam where a beam stopped was used. f) Azimuthal averages for 1D and isotropic diffraction patterns. In the 1D diffraction, two intensity peaks are seen which reflects the positions of observed structural color. In the isotropic, the azimuthal average stays relatively in a constant range of 0.001, reflecting structural color  $2\pi$  about  $\phi$ .

directions, the line diffraction pattern is of a much lower intensity than the peaks in the 1D. An azimuthal average measurement can be used to clearly show the comparison between the two structures. In the 1D diffraction, two distinct intensity peaks are seen, reflecting the position of structural color observation. In the isotropic sample, the azimuthal average stays relatively constant, with structural color reflected about  $2\pi$  of  $\phi$ .

## 2.7. Homogeneity and Directional Color

An implication arising from the fabrication of regular 1D wrinkling structures with homogenous wrinkling periodicity is a characteristic “rainbow” color perceived especially for large areas, which is enhanced at a close observation distance. As the colors viewed are sensitive to  $\theta_{\text{obs}}$ , a small change can lead to different colors being seen at a single wrinkle periodicity. The spread of color occurs as the light reaching the observer has different viewing angles from the top and bottom of the sample ( $\theta_{\text{obs1}}$  and  $\theta_{\text{obs2}}$ , respectively), thus yielding different

wavelengths ( $\lambda_1, \lambda_2$ ) (Figure 7a). The respective  $\theta_{\text{obs}}$  can be calculated with respect to the position of the observer

$$\theta_{\text{obs1}} = 90 - \arctan \frac{L}{h} \quad (9)$$

$$\theta_{\text{obs2}} = 90 - \arctan \frac{(L-W)}{h} \quad (10)$$

where  $h$  and  $L$  describes the vertical and horizontal position of the observer, and  $W$  the distance between the observed reflected light. Conversely, it is possible to create a variable structure to create local spatial periods required to only see a specific color, depending on the position of the observer (Figure S7, Supporting Information). Previously, Voisiat et al., have demonstrated that the homogeneity of large samples can be improved through creating varying periodic spacing using direct laser interference patterning.<sup>[53]</sup> Gradient wrinkling topographies can be induced either tuning the thickness of the exposed glassy skin generated by plasma oxidation or by applying a gradient strain field, changing the geometry of the sample and therefore

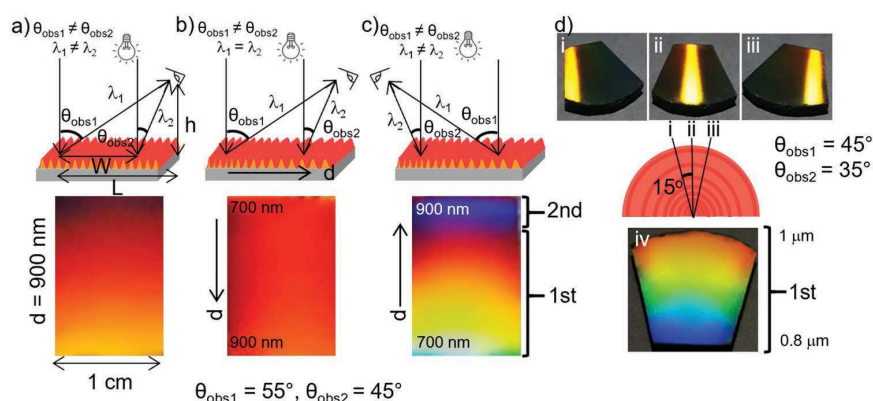


**Figure 7.** Structural color behavior at various observation angles for a) a 1D wrinkle surface, displaying a heterogeneous colored surface; b) step-wise gradient 1D wrinkles, observed from the longest periodicity ( $d = 900$  nm), showing a homogeneous red color. c) The same sample as in (b), observed from the shortest periodicity ( $d = 700$  nm), exhibiting an accentuated "rainbow" effect. d) Samples prepared employing geometric graded coupons, exhibiting curved wrinkles and directional color when rotated about  $\phi$ . (i–iii) show homogeneous strips of yellow while (iv) showing a "rainbow" effect.

altering the strain components. The resulting periodicity gradient can produce a distinct diffracted wavelength of light at a given angular range. In both methods, no significant variation of the wrinkling amplitude was observed, thus with a negligible impact on the color intensity. For the first approach, here referred to as step-wise plasma oxidation, different sections of the same area treated at different exposure times, yielding varying periodicities and amplitudes. As the exposure time for an area increases, this gives rise to larger periodicity and amplitudes. When a stepwise sample (Figure S8, Supporting Information) is viewed from a position with  $L = 10$  cm,  $W = 3$  cm, and  $h = 7$  cm, this gives rise to  $\theta_{obs1} = 55^\circ$  and  $\theta_{obs2} = 45^\circ$ . The resulting wrinkling periodicities, ranging 700–900 nm, when viewed from the end of the sample with largest periodicity, exhibit a homogeneous red color spanning the entirety of the sample, as  $\lambda_1 = \lambda_2$ . Conversely, when the same gradient structured sample is viewed from the other end of the sample, the "rainbow" effect of colors is accentuated, where the periodic change leads to an even greater variation in color observed (Figure 7b,c).

The second approach allows for the fabrication of varying periodic structure by altering the geometry of the stretched sample, by using a trapezoidal shape for example (Figure S9, Supporting Information). When a non-rectangular shape undergoes an extensional or compressive uni-axial strain, the magnitude of the strain will scale with the sample surface area. In the case of a trapezoidal shape, this induces a torsional strain field that is reflected in a curvature of the wrinkling pattern. The sample experiences a higher strain at the narrow side, and lower strain on the wider side. The overall patterns can be rationalized as a damped sine wave evolving from the narrow side, or higher strain region. The curve graded wrinkles display directional structural color, as the 1D wrinkles can only diffract perpendicular to the wrinkling direction (Figure 7d). When the wrinkles are convex with respect to the viewer, the sides of the sample are such that it diffracts color out of plane with respect to the center of the sample. Strips of homogeneous color can be manipulated and seen dependent on the viewing angle  $\phi$ . When  $\phi = 0^\circ$ , a strip in the center can be seen (Figure 7d(i)). Upon

rotation of  $\pm 15^\circ$ , the strip of color can be seen to move toward the edge of the sample (Figure 7d(ii, iii)). When the sample is positioned such that the wrinkles concave with respect to the viewer, the diffraction of the wrinkles converge onto the viewer and a "rainbow" effect can be seen to be exhibited by the entire sample (Figure 7d(iv)). Similarly, we have also demonstrated that these varying periodic structures can be extended beyond the 1D to isotropic samples. Such radial-gradient isotropic samples exhibit "rainbow" colors in a crescent formation, attributed to the change in periodicity across the sample as well as  $\theta_{obs}$ , as detailed in Figure S10, Supporting Information.

The idea of directionality of wrinkle surfaces can be extended to that of 2D structures, where we can further manipulate the colors exhibited depending on the observer's perspective. As previously mentioned, 2D structures can be fabricated through either a simultaneous or sequential step,<sup>[35,36,46]</sup> where the sequential step can be performed at different angles. A symmetrical checkerboard was achieved through a sequential step performed at  $90^\circ$  with the conditions stated in the Experimental Section, achieving  $d = 680$  nm. When observed at  $\theta_{obs} = 40^\circ$ , a blue structural color can be observed at intervals of  $90^\circ$  along  $\phi$ , with no color exhibited at other angles, reflecting the orthogonal superimposed first and second generation wrinkling waves, respectively at  $\phi = 0^\circ$  and  $\phi = 90^\circ$ . Therefore, the overall structural color is exhibited only alongside the specific generation orientation and not visible at other angles. On the other hand in a herringbone structure, arising from the simultaneous relaxation of a two-directional strain field, structural color can be observed for different  $\phi$ , however with varying intensities. Specifically, at  $\phi = 0^\circ$ , a lower intensity is observed progressively increasing at  $\phi = 45^\circ$  and  $\phi = 90^\circ$ . This can be ascribed to the more complex intrinsic morphology exhibited by the herringbone pattern, where the color observed at  $\phi = 45^\circ$  is given by the overlap of two different periodicity, namely a "long"  $d$  ( $xy$  plane) along  $\phi = 90^\circ$ , giving a stronger blue reflectance, a "short"  $d$  ( $xz$  plane) showing a dimmer blue color. For "sand ripple" patterns, generated by sequential wrinkling superposition, and in this case a  $20^\circ$  pattern (Figure 8c), is able to exhibit color up to  $\phi$  rotation of  $45^\circ$ . Initially when  $\phi$  is at  $0^\circ$ , the contribution of



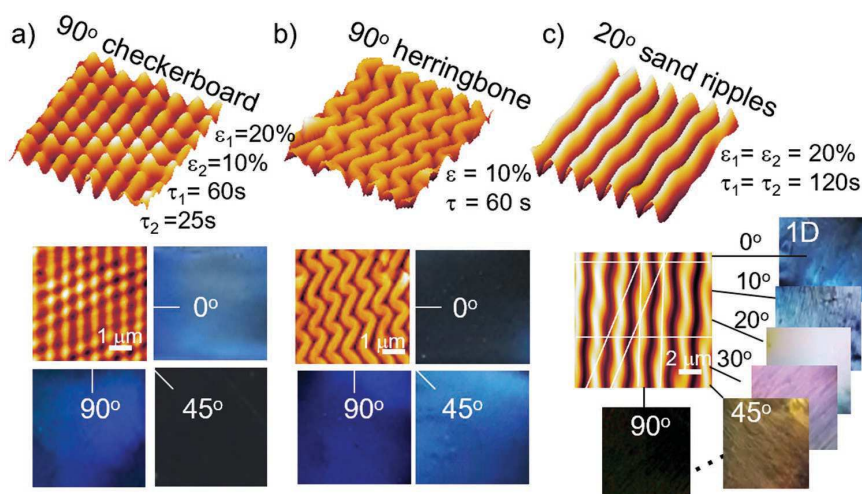


**Figure 8.** Structural color in 2D wrinkled surfaces. a) Symmetrical checkerboard exhibiting colors in phases of 90°. At  $\theta_{\text{obs}}$  of 40°, a blue can be seen at  $\phi = 0^\circ$  and  $\phi = 90^\circ$  which “switches off” at  $\phi = 45^\circ$ . b) In a herringbone structure, a rotation through  $\phi = 0^\circ - 90^\circ$  shows a blue hue that varies in intensity. c) A 2D 20° “sand ripple” structure exhibiting a blue color as a result of the second generation 1D structure at  $\phi = 0^\circ$ . As  $\phi$  increases, it transitions to a yellow hue until beyond 45° where it goes beyond the direction of diffracted light.

color is primarily due to the second generation of wrinkles. As  $\phi$  increases, color mixing arises reaching  $\phi = 20^\circ$ , orientation of the first generation pattern, transitioning from a blue to a yellow and opalescent shade. From  $\phi = 45^\circ$ , the overall structural color decreases in intensity and ultimately at  $\phi = 90^\circ$  the only contribution to the overall structural color is given by  $\lambda_{\text{xy}}$  arising from the superposition of the two wrinkling waves.

### 3. Conclusions

In this paper, we demonstrate the generation of both simple and intricate tunable structural color response in 1D and 2D (biaxial and sequential) and isotropic wrinkling patterns, fabricated by plasma oxidation of PDMS and mechanical or thermally-induced buckling. From the inspection of the mechanochromic response in both micron and nanoscale 1D wrinkling structures we benchmark and quantify the impact of surface periodicity in the accessible colors. From these consolidated foundations, we evaluate the effect of color mixing induced by overlap of multiple diffraction orders. We establish quantitative relations between color intensity, the interplay between illumination and viewing angles, accounting for the wrinkling mechanics and diffraction phenomena. Our model incorporates the gradient nature of the glassy skin, alongside the established phase grating optics system, to quantitatively model the intensity of the various diffraction orders. We inspect the effect of complex topographies on the structural color response, inducing a gradient in pattern periodicity and amplitude by either tuning the glassy skin thickness (via stepwise exposure) or by inducing gradient strain field (via a non-rectangular sample geometry, e.g., trapezoidal). We demonstrate how these surface patterns exhibit either spatially uniform color or enhanced “rainbow” color depending on the observation angle. Furthermore, we report isotropic wrinkled surfaces exhibiting

color at all  $\phi$  angles, that is, “around” the patterned surface. We explore the concept of optical and color directionality by creating multi-frequency patterns, achieved by superposing two independent wrinkling waves onto the *same* surface (by analogy to birefringent media), fabricated either by the application of a simultaneous bi-axial strain (in which the two wrinkling generations are strongly coupled) or a sequential wrinkling process with greater flexibility in  $d$  and  $A$  of each generation, as well as their relative angle, and thus of the corresponding optical axes. Overall, we expect our findings to be relevant to a range of applications such as packaging, smart displays, wearable electronic devices, and sensors.

### 4. Experimental Section

A carbon-black PDMS (CB-PDMS) (Sylgard 184, Dow Corning) substrate was prepared by casting a mixture of prepolymer, curing, and carbon black acetylene powder (50% compressed, 99.9%, VWR) at a 10:1:0.03 mass ratio for 1D and 2D samples, and a mass ratio of 20:1:0.03 for isotropic samples. The mixture was stirred vigorously, degassed under vacuum, deposited onto a glass plate and cured at 75 °C in a convection oven for 1 h to crosslink into an elastomer with the resultant CB-PDMS with a thickness of 2.5 mm.

Surface plasma oxidation of the samples were performed using two different plasma chambers: a 13.6 MHz Harrick Plasma PDC-002 at  $P = 10.5$  W for sub-micron wrinkle periodicity samples, and a 40 kHz Diener plasma (Femto), fitted with a pressure sensor (TM 101, Thermovac) at  $P = 20, 50,$  and  $99$  W and variable exposure times for samples with a larger wrinkle periodicity. Oxygen (BOC, 99.5%) supplied both plasma chambers. The chambers were evacuated to a pressure of 0.2 mbar, before flowing the gas for 5 min until the desired pressure was reached and stabilized. The plasma was then ignited, at the required power and exposure time.

1D, regular periodic sinusoidal patterns were fabricated through uniaxial strain of a PDMS coupon (2.5 cm  $\times$  2.5 cm) using a strain stage. The applied prestrain was calculated with respect to the initial ( $L_0$ ) and final distance ( $L_1$ ) between the clamps,  $\epsilon_{\text{prestrain}} = \frac{L_1 - L_0}{L_0}$ .

The sample was stretched with a prestrain of 0.2, before it undergo plasma oxidation and subsequently released to form sinusoidal wrinkles. Samples with a varying periodic structure were fabricated either by a step-wise plasma oxidation or by changing the geometry of the sample to a trapezoidal shape.

2D samples were fabricated through either a simultaneous or sequential step. The simultaneous 90° sample was created through a biaxial strain of 10% of a PDMS coupon which undergo plasma treatment ( $P = 20$  W,  $\varepsilon = 0.1$ ) before the simultaneous release of strain to form a herringbone structure. 2D wrinkles through a sequential step were created through the replication of a 1D sample on fresh PDMS, followed by a second generation strain and plasma at an angle before the release. For a 90° symmetrical checkerboard, the first generation was performed at  $P = 20$  W,  $\tau = 60$  s,  $\varepsilon = 0.2$ , and the second generation at  $P = 20$  W,  $\tau = 25$  s,  $\varepsilon = 0.1$ . The 20° sand ripples were fabricated with the same conditions in both the generations,  $P = 20$  W,  $\tau = 120$  s,  $\varepsilon = 0.2$ . Isotropic samples were fabricated through the plasma treatment of an unstretched circular CB-PDMS coupon (2.5 cm radius) which then undergo thermal heating to 200 °C for 30 min and cooled to room temperature to form the isotropic wrinkles.

Surface topographies were characterized by AFM using a Bruker Innova microscope, in tapping mode at 0.2 Hz, equipped with Al-coated Si tips (MPP-11100-W, Bruker) and analyzed with the in-built Nanoscope software. The mechanochromic phenomena were observed and recorded on a Basler acA2040-90uc camera with a white light source (Advanced Illumination) in a dark environment, which were then analyzed with ImageJ software.

## Supporting Information

Supporting Information is available from the Wiley Online Library or from the author.

## Acknowledgements

The authors thank Procter & Gamble and the EPSRC-funded Plastic Electronics CDT for a Ph.D. scholarship (Grant No. EP/L016702/1) and the Royal Academy of Engineering (RAEng, UK) for funding and a research chair.

## Conflict of Interest

The authors declare no conflict of interest.

## Data Availability Statement

The data that support the findings of this study are available from the corresponding author upon reasonable request.

## Keywords

mechanochromic, polydimethylsiloxane, plasma-oxidation, structural color, tunable, wrinkling superposition, diffraction grating

Received: April 25, 2022

Published online:

- [1] M. Srinivasarao, *Chem. Rev.* **1999**, *99*, 1935.  
 [2] P. Vukusic, J. R. Sambles, *Nature* **2003**, *424*, 852.  
 [3] S. Kinoshita, S. Yoshioka, J. Miyazaki, *Rep. Prog. Phys.* **2008**, *71*, 076401.

- [4] B.-K. Hsiung, R. H. Siddique, D. G. Stavenga, J. C. Otto, M. C. Allen, Y. Liu, Y.-F. Lu, D. D. Deheyn, M. D. Shawkey, T. A. Blackledge, *Nat. Commun.* **2017**, *8*, 2278.  
 [5] P. Vukusic, J. Sambles, C. Lawrence, R. Wootton, *Proc. R. Soc. London, Ser. B* **1999**, *266*, 1403.  
 [6] D. Gur, B. A. Palmer, S. Weiner, L. Addadi, *Adv. Funct. Mater.* **2017**, *27*, 1603514.  
 [7] J. Teyssier, S. V. Saenko, D. Van Der Marel, M. C. Milinkovitch, *Nat. Commun.* **2015**, *6*, 6368.  
 [8] A. Saito, K. Yamashita, T. Hattori, Y. Kuwahara, *Jpn J. Appl. Phys.* **2022**, *61*, SD0801  
 [9] Z. Dong, H. Zhao, L. Nie, S. Tang, C. Li, X. Wang, *Front. Phys.* **2022**, *792*, 806904.  
 [10] H. Wang, K.-Q. Zhang, *Sensors* **2013**, *13*, 4192.  
 [11] H. S. Lee, T. S. Shim, H. Hwang, S.-M. Yang, S.-H. Kim, *Chem. Mater.* **2013**, *25*, 2684.  
 [12] W. Yang, S. Xiao, Q. Song, Y. Liu, Y. Wu, S. Wang, J. Yu, J. Han, D.-P. Tsai, *Nat. Commun.* **2020**, *11*, 1864.  
 [13] F. Cheng, J. Gao, T. S. Luk, X. Yang, *Sci. Rep.* **2015**, *5*, 11045.  
 [14] K. Yamashita, K. Kunitsu, T. Hattori, Y. Kuwahara, A. Saito, *Opt. Express* **2021**, *29*, 30927.  
 [15] Z. Xuan, J. Li, Q. Liu, F. Yi, S. Wang, W. Lu, *Innovation* **2021**, *2*, 100081.  
 [16] G. Chen, W. Hong, *Adv. Opt. Mater.* **2020**, *8*, 2000984.  
 [17] Q. Zhou, J. G. Park, J. Bae, D. Ha, J. Park, K. Song, T. Kim, *Adv. Mater.* **2020**, *32*, 2001467.  
 [18] X. Huang, Y. Hai, W.-H. Xie, *Theor. Appl. Mech. Lett.* **2017**, *7*, 169.  
 [19] C. Chen, C. A. Airoidi, C. A. Lugo, R. K. Bay, B. J. Glover, A. J. Crosby, *Adv. Funct. Mater.* **2021**, *31*, 2006256.  
 [20] M. Nixon, A. Orr, P. Vukusic, *J. R. Soc., Interface* **2015**, *12*, 20140749.  
 [21] J. H. Oh, J. Y. Woo, S. Jo, C.-S. Han, *ACS Appl. Mater. Interfaces* **2019**, *11*, 26442.  
 [22] C. A. Airoidi, C. A. Lugo, R. Wightman, B. J. Glover, S. Robinson, *Cell Rep.* **2021**, *36*, 109715.  
 [23] L. Zhou, L. Yang, Y. Liu, Z. Xu, J. Yin, D. Ge, X. Jiang, *Adv. Opt. Mater.* **2020**, *8*, 2000234.  
 [24] Z. Mao, S. Zeng, K. Shen, A. P. Chooi, A. T. Smith, M. D. Jones, Y. Zhou, X. Liu, L. Sun, *Adv. Opt. Mater.* **2020**, *8*, 2001472.  
 [25] J. Li, X. Lu, Y. Zhang, X. Ke, X. Wen, F. Cheng, C. Wei, Y. Li, K. Yao, S. Yang, *Adv. Funct. Mater.* **2021**, *31*, 2102350.  
 [26] N. Bowden, W. T. Huck, K. E. Paul, G. M. Whitesides, *Appl. Phys. Lett.* **1999**, *75*, 2557.  
 [27] A. Chiche, C. M. Stafford, J. T. Cabral, *Soft Matter* **2008**, *4*, 2360.  
 [28] F. A. Bayley, J. L. Liao, P. N. Stavrinou, A. Chiche, J. T. Cabral, *Soft Matter* **2014**, *10*, 1155.  
 [29] G. Ferretti, M. Nania, O. Matar, J. T. Cabral, *Langmuir* **2016**, *32*, 2199.  
 [30] A. Tan, L. Pellegrino, J. T. Cabral, *ACS Appl. Polym. Mater.* **2021**, *3*, 5162.  
 [31] C. Harrison, C. Stafford, W. Zhang, A. Karim, *Appl. Phys. Lett.* **2004**, *85*, 4016.  
 [32] Z. Li, Y. Liu, M. Marin, Y. Yin, *Nano Res.* **2020**, *13*, 1882.  
 [33] K. Wu, T. Zhu, L. Zhu, Y. Sun, K. Chen, J. Chen, H. Yuan, Y. Wang, J. Zhang, G. Liu, X. Chen, J. Sun, *Nano Lett.* **2022**, *22*, 2261.  
 [34] Y. Qi, C. Zhou, S. Zhang, Z. Zhang, W. Niu, S. Wu, W. Ma, B. Tang, *Dyes Pigm.* **2021**, *189*, 109264.  
 [35] L. Pellegrino, S. Khodaparast, J. T. Cabral, *Soft Matter* **2020**, *16*, 595.  
 [36] L. Pellegrino, A. Tan, J. T. Cabral, *Phys. Rev. Lett.* **2022**, *128*, 058001.  
 [37] M. Nania, O. K. Matar, J. T. Cabral, *Soft Matter* **2015**, *11*, 3067.  
 [38] H. Jiang, D.-Y. Khang, J. Song, Y. Sun, Y. Huang, J. A. Rogers, *Proc. Natl. Acad. Sci. USA* **2007**, *104*, 15607.  
 [39] Q. Wang, X. Zhao, *Sci. Rep.* **2015**, *5*, 8887.  
 [40] S. Raayai-Ardakani, J. Luis Yagüe, K. K. Gleason, M. C. Boyce, *J. Appl. Mech.* **2016**, *83*, 121011.  
 [41] C. Gao, Y. Li, *Int. J. Solids Struct.* **2017**, *104*, 92.

- [42] J. S. Lee, H. Hong, S. J. Park, S. J. Lee, D. S. Kim, *Microelectron. Eng.* **2017**, *176*, 101.
- [43] B. A. Glatz, A. Fery, *Soft Matter* **2019**, *15*, 65.
- [44] L. Ma, L. He, Y. Ni, *J. Appl. Phys.* **2020**, *127*, 111101.
- [45] S. Hiltl, J. Oltmanns, A. Böker, *Nanoscale* **2012**, *4*, 7338.
- [46] X. Chen, J. W. Hutchinson, *J. Appl. Mech.* **2004**, *71*, 597.
- [47] X. Chen, J. W. Hutchinson, *Scr. Mater.* **2004**, *50*, 797.
- [48] C. S. Davis, A. J. Crosby, *J. Polym. Sci., Part B: Polym. Phys.* **2012**, *50*, 1225.
- [49] S. Chen, T. Ma, J. Bai, X. Ma, J. Yin, X. Jiang, *Adv. Sci.* **2020**, *7*, 2002372.
- [50] Y. Meng, X. Gong, Y. Huang, L. Li, *Appl. Mater. Today* **2019**, *16*, 474.
- [51] C. Yu, K. O'Brien, Y.-H. Zhang, H. Yu, H. Jiang, *Appl. Phys. Lett.* **2010**, *96*, 041111.
- [52] J. W. Goodman, *Introduction to Fourier Optics*, Roberts and Company Publishers, Greenwood Village, CO **2005**.
- [53] B. Voisiat, W. Wang, M. Holzhey, A. F. Lasagni, *Sci. Rep.* **2019**, *9*, 7801.

Article

# Multifaceted Structurally Coloured Materials: Diffraction and Total Internal Reflection (TIR) from Nanoscale Surface Wrinkling

Annabelle Tan <sup>1,2</sup> , Zain Ahmad <sup>1</sup> , Pete Vukusic <sup>3</sup> and João T. Cabral <sup>1,2,\*</sup> <sup>1</sup> Department of Chemical Engineering, Imperial College London, London SW7 2AZ, UK<sup>2</sup> Centre for Processable Electronics, Imperial College London, London SW7 2AZ, UK<sup>3</sup> School of Physics, University of Exeter, Stocker Road, Exeter EX4 4QL, UK

\* Correspondence: j.cabral@imperial.ac.uk

**Abstract:** We investigate the combined effects of surface diffraction and total internal reflection (TIR) in the design of 3-dimensional materials exhibiting distinct structural colour on various facets. We employ mechanical wrinkling to introduce surface diffraction gratings (from the nano to the micron scales) on one face of an elastomeric rectangular parallelepiped-shaped slab and explore the roles, in the perceived colours, of wrinkling pattern, wavelength, the directionality of incident light and observation angles. We propose a simple model that satisfactorily accounts for all experimental observations. Employing polydimethylsiloxane (PDMS), which readily swells in the presence of various liquids and gases, we demonstrate that such multifaceted colours can respond to their environment. By coupling a right angle triangular prism with a surface grating, we demonstrate the straightforward fabrication of a so-called GRISM (GRating + prISM). Finally, using a range of examples, we outline possibilities for a predictive material design using multi-axial wrinkling patterns and more complex polyhedra.

**Keywords:** structural colour; multifaceted; diffraction; total internal reflection (TIR); polydimethylsiloxane (PDMS); wrinkling; plasma oxidation; multiaxial; polyhedra; GRISM



**Citation:** Tan, A.; Ahmad, Z.; Vukusic, P.; Cabral, J.T. Multifaceted Structurally Coloured Materials: Diffraction and Total Internal Reflection (TIR) from Nanoscale Surface Wrinkling. *Molecules* **2023**, *28*, 1710. <https://doi.org/10.3390/molecules28041710>

Academic Editor: Chris E. Finlayson

Received: 18 January 2023

Revised: 3 February 2023

Accepted: 7 February 2023

Published: 10 February 2023



**Copyright:** © 2023 by the authors. Licensee MDPI, Basel, Switzerland. This article is an open access article distributed under the terms and conditions of the Creative Commons Attribution (CC BY) license (<https://creativecommons.org/licenses/by/4.0/>).

## 1. Introduction

Structural colour abounds in nature, in both the animal and plant kingdoms, emerging from microscopically structured surfaces and bulk materials, able to cause visible light interference [1–7], with or without the presence of chemical pigments. During the past two decades or so, a range of bioinspired synthetic and processing strategies have been proposed to engineer structural colour on surfaces and bulk materials. These include multilayer film lamination [8,9], the assembly of photonic crystals [10,11] and metasurfaces [12,13], whose colour can be static or respond to external stimuli [14–17]. Recently, novel structural coloured films and microscale concave interfaces based on total internal reflection (TIR) interference have also been reported, combining the effects of thin-film interference and TIR [18–20]. A number of practical applications of such materials have been reported, where structural colour sensors and devices based on responsive soft materials have been fabricated [21–24].

Surface topography and, specifically, undulations caused by buckling or wrinkling, are found in a range of flowers and insects [25–29], where these wrinkled surfaces, effectively acting as diffraction gratings, can yield brilliant structural colours which depend on pattern periodicity  $d$  and sufficiently large pattern amplitudes, and observation angle. Pattern orientation, from uni-directional to isotropic (or random), can further restrict or modulate the viewable angles of the perceived structural colour [30,31]. When white light impinges onto a wrinkled surface, it can diffract in transmission or reflection, or both, and propagate



further. While the combination of TIR and light diffraction has been reported in the characterisation of fluids in microfluidic cells [32] and in the measurement of the refractive index of liquids [33], to the best of our knowledge, their combination has not been exploited in the design and fabrication of multi-faceted materials exhibiting structural colour. Naturally occurring materials exhibiting structural colour generally often exhibit colour and colour modulations across multiple viewing angles. By contrast, colour generated from surface diffraction is directional, even in isotropic or multiaxial diffractive surfaces [30,31], contrasting with the appearance of bulk photonic and anisotropic structures. We therefore explore the feasibility of designing multi-faceted and modulated structural colour through the combination of wrinkling and diffraction and TIR selection and propagation. We expect that such multi-faceted structurally coloured materials can approximate more closely 'bulk' structural colours found in nature [34].

Visible light diffraction through reflection can lead to the emergence of structural colour from patterned surfaces, of appropriate periodicity and amplitude, which varies with observation angle, as illustrated in Figure 1. Evidently, the surface can also act as a transmission grating where the light diffracts *into* the sample. If the material properties support TIR, we envisage that structural colour can be indirectly observed at the facet (or facets) of the material, which we term here "facet TIR colour" (Figure 1a). However, light diffraction will generate a distribution of wavelengths at different angles, and several diffractions of varying intensities; therefore, such colour may differ from the original diffraction spectrum owing to TIR propagation rules. With structural colour observable from two (or more) different viewing perspectives for such a material, we introduce the different nomenclatures for the observation angles with respect to the surface normal, one associated with the surface,  $\theta_{DG}$ , and the other with the facet,  $\theta_{edge}$ . The offset angle when viewing the surface with respect to  $\theta_{DG}$  is termed  $\theta_{DG'}$ , which depends on the length of unwrinkled material  $L_{edge}$  (Figure 1b). Figure 1c depicts the cross-sectional profile of light diffracting into the medium, and propagating through the medium, by total internal reflection, toward a facet (Figure 1c). Ray tracing for two wavelengths, 450 and 730 nm, is shown, to illustrate the colour and diffraction order selection, indicating that different colours to those diffracted by the surface pattern may be expected at the material facets. Figure 1d demonstrates the TIR of monochromatic light ( $\lambda = 533$  nm laser) within a slab of PDMS.

Soft materials, such as elastomers, are advantageous in the fabrication of stiff-soft bilayers and wrinkled surfaces, and mechanical strain can readily tune the surface periodicity and amplitude. Typically, bilayers are fabricated through the deposition or lamination of a thin and stiff film on a soft substrate such as polydimethylsiloxane (PDMS). Mismatches between the mechanical properties of two films, provided they adhere strongly together (to minimize delamination, cracking, etc.), result in surface buckling under strain, which can be induced commonly through mechanical deformation, through thermal expansion/contraction, volume changes, etc. Plasma oxidation of PDMS provides a convenient route to generating a glassy (SiOx) thin film atop the PDMS surface [35], inducing a mismatch in elastic moduli between the thin skin and the bulk. Further, it enables the precise control of film thickness growth [36–40], and the fabrication of wrinkled surfaces with varying periodicity ( $d$ ) and amplitude ( $A$ ), that can range from the nm scale to several 100s  $\mu\text{m}$ . Permanent wrinkles can be formed when the plasma exposure is carried out with the PDMS coupon under pre-strained conditions, while transient wrinkles can be excited on otherwise planar surfaces upon the application of strain on a bilayer fabricated at rest. Transparent elastomers, such as PDMS, are well suited for optical devices, and the design and fabrication of PDMS sinusoidal phase gratings, with tunable periodicity and amplitude, via plasma-oxidation, has been previously demonstrated, resulting in structural colour and mechanochromic response [17,31,41–44] for a judicious choice of system parameters (skin thickness, mechanical moduli, strain, etc.).

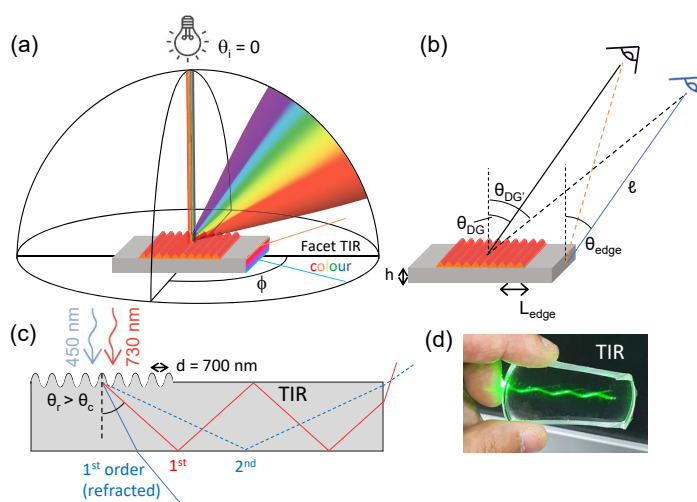


**Figure 1.** (a) Schematic of light diffraction from a 1D wrinkled surface, with normal incident light, and total internal reflection (TIR) leading to light propagation onto the sample facet. (b) Experimental geometry, defining different observation angles  $\theta_{DG}$ , defined from the normal of the diffraction grating;  $\theta_{edge}$ , defined from the normal of the sample edge, or facet;  $\theta_{DG'}$ , defined for the “edge observer” from the normal of the diffraction grating when  $\theta_{edge} = \theta_{DG}$ . The lines from the facet (orange and blue) correspond to a (fixed) sample-observer distance of  $\ell$ . (c) Cross-sectional schematic of TIR propagation, illustrated for two incident wavelengths ( $\lambda = 450$  and  $730$  nm) and surface periodicity  $d = 700$  nm: for the shorter  $\lambda$ , the 1st diffraction order is below the critical angle on the sample’s bottom surface and is thus refracted out of the sample, while the 2nd order propagates by TIR and exits at the sample edge; the 1st diffraction order of the longer  $\lambda$  undergoes TIR thus also contributes to the edge colour. (d) Visualisation of TIR within a 5 mm thick PDMS coupon, with a monochromatic beam (laser  $\lambda = 533$  nm) at a high incident angle.

Building upon previous work on reflective diffraction gratings fabricated by surface wrinkling, we consider the possible roles of light transmission/refraction, in the design of materials exhibiting structural colour on various facets. Specifically, we seek to establish and model the conditions and limits for total internal reflection (TIR), wavelength and diffraction order selection, the roles played by the geometry of the surface grating, as well as overall polyhedral shape and environmental conditions, on the resulting colour.

## 2. Results and Discussion

### 2.1. Structural Colour of Wrinkled Surfaces through Surface Diffraction

We have fabricated a range of one-dimensional (1D) wrinkled structures by applying uni-axial mechanical strain ( $\epsilon = 0.5$ ) on PDMS coupons, subsequently exposed to oxygen plasma at varying power (20–60 W). Upon relaxation of strain, the bilayer yields a sinusoidal profile, at sufficiently low deformations (Figure 2a). Wrinkles of different periodicities are readily obtained from the variation in plasma power (at constant exposure time), as shown by the atomic force microscopy (AFM) profiles in Figure 2b. The associated periodicity  $d$  and amplitude  $A$  can be expressed as [45,46],

$$d = \frac{2\pi h \left( \bar{E}_f / (3\bar{E}_s) \right)^{\frac{1}{3}}}{(1 + \epsilon)(1 + \zeta)^{\frac{1}{3}}} \quad (1)$$

$$A = \frac{h(\epsilon/\epsilon_c - 1)^{\frac{1}{2}}}{(1 + \epsilon)^{\frac{1}{2}}(1 + \zeta)^{\frac{1}{3}}} \quad (2)$$

where  $h$  is the converted film thickness,  $\bar{E}_f$  and  $\bar{E}_s$  are the in-plane strain moduli of the film and substrate, respectively, given by  $\bar{E} = E/(1 - \nu^2)$ , where  $E$  is Young's modulus and  $\nu$  the Poisson ratio ( $\approx 0.5$  for PDMS);  $\xi = 5\epsilon(1 + \epsilon)/32$ , accounting for the nonlinearity of the stress–strain relationship of the substrate in the finite deformation regime (i.e., non-Hookean response). Here, we refer to the surface periodicity as  $d$ , instead of the customary surface wavelength  $\lambda$ , to avoid confusion with the wavelength of light. In order to trigger the mechanical instability, a certain “critical” strain  $\epsilon_c$  must be exceeded:

$$\epsilon_c = \frac{1}{4} \left( \frac{3\bar{E}_s}{\bar{E}_f} \right)^{\frac{2}{3}} \quad (3)$$

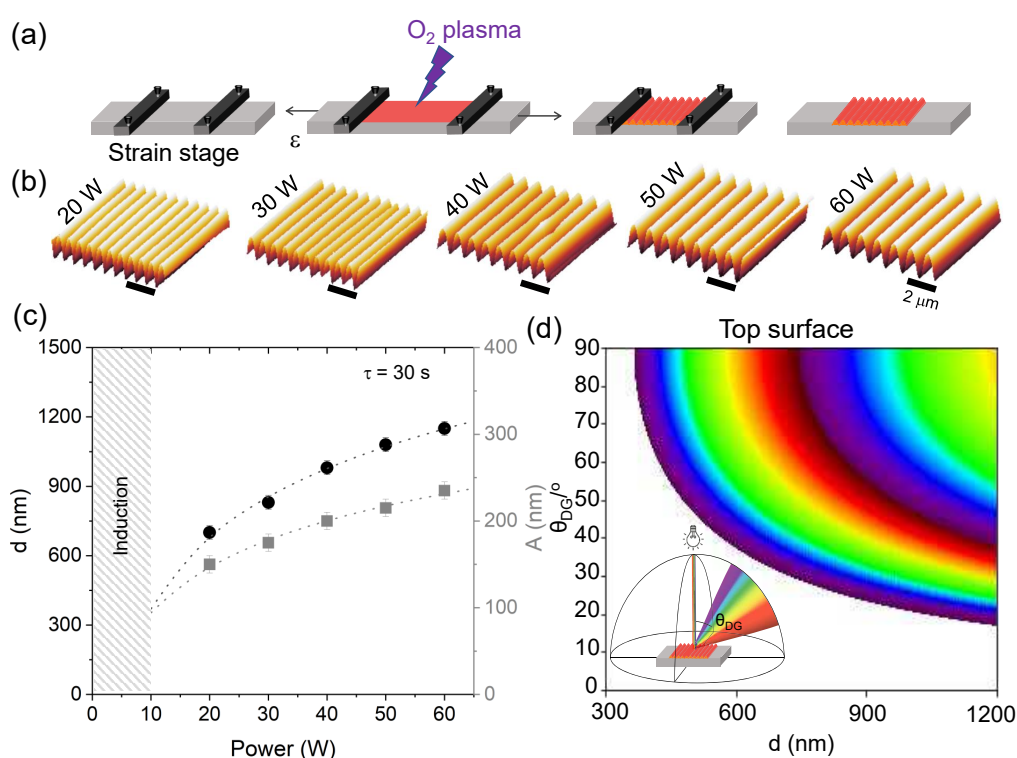


**Figure 2.** (a) Schematic of the fabrication of a 1D wrinkled sample: a PDMS elastomer coupon is mechanically strained and then exposed to oxygen plasma. Upon strain relaxation, a wrinkled surface remains (at rest conditions). (b) AFM scans of samples fabricated at different plasma powers ( $P = 20$  W to 60 W) and fixed exposure time  $\tau = 30$  s, and pre-strain  $\epsilon = 0.5$ ; the scale bar corresponds to  $2 \mu\text{m}$ . (c) Wrinkling periodicity ( $d$ ) and amplitude ( $A$ ) measured for the samples above; the shaded area corresponds to an induction stage for glassy skin and wrinkling onset. (d) Structural colour map computed for incident white light at  $\theta_i = 0$ , surface periodicity  $300 \leq d \leq 1200$  nm, and observation angle  $0 \leq \theta_{DG} \leq 90^\circ$ , considering the first two diffraction orders (adapted from Ref. [31]). At lower  $d$  ( $\lesssim 380$  nm), UV can take place.

The experimentally measured logarithmic dependence of periodicity and amplitude with plasma exposure power (20 to 60 W), at a fixed exposure time  $\tau = 30$  s, is shown in Figure 2c. This dependence is attributed to the mechanisms and kinetics of the frontal growth and propagation of the glassy skin layer [37,38]. With this range of conditions, wrinkle periodicities from 700 nm to 1150 nm can be readily obtained.

In previous literature, we [31] and others [42–44] have demonstrated that wrinkling by plasma oxidation of PDMS provides an effective means of fabricating surfaces with structural colour, via the light diffraction on the surface grating. Control of colour brightness, hue, and viewable-angle mechanochromism were demonstrated. The approach is attractive due to the versatility of the fabrication method, where the wrinkling profile ( $d$ ,  $A$ ) can be tuned via plasma exposure conditions (defining  $h$  and moduli) and/or applied strain. The behaviour of the diffraction gratings can be described by the general form of the diffraction equation,

$$m\lambda = d(\sin\theta_i + \sin\theta_{DG}) \quad (4)$$

where integer  $m$  is the diffraction order of light of wavelength  $\lambda$ . From Equation (4), we compute the wavelength of light diffracted by wrinkles of varying periodicities across a range of detection angles, from  $0^\circ$  to  $90^\circ$ . Figure 1d shows the expected light diffraction at each  $\theta_{DG}$  for wrinkled surfaces with periodicities up to  $d = 1200$  nm, when the incident light is normal to the surface ( $\theta_i = 0^\circ$ ). When the periodicity of the wrinkles is shorter than that of the wavelength of visible light, no colour will be observed at the surface. At this range of  $d$ , discrete structural colours can be observed since the grating diffracts with no colour mixing of different orders involved.

## 2.2. Total Internal Reflection (TIR) and Selection of Facet Colour

Similarly to surface structural colour derived from the diffraction of light in reflection from a wrinkled surface, the observation of facet TIR colour is also expected to be angle-dependent. Light diffracted in transmission can be further propagated via TIR, under specific conditions, resulting in structural colour (indirectly) appearing on the facets of transparent materials. Figure 3a shows a series of optical images, taken at varying observation angles, of a sample with surface grating periodicity  $d = 700$  nm (fabricated with plasma conditions  $P = 20$  W,  $\tau = 30$  s,  $\epsilon = 0.5$ ), that exhibits a range of structural colours. For clarity, the sample was placed on a mirror that acts as a reflective substrate and was observed at  $\theta_{edge}$  at  $10^\circ$  intervals of observation angle, from  $20$  to  $60^\circ$ . Concurrently, the surface structural colour can also be viewed, but with an offset angle of  $\theta_{DG}$  ranging from  $30$  to  $65^\circ$  when  $l = 10$  cm and  $L_{edge} = 2$  cm. The white line on the optical images indicates the boundaries between facet colour and the mirror reflection. Figure 3b shows a schematic of the sample set-up, including the role of the “TIR (mirror)” where refracted rays from the facet impinging onto the mirror result in an additional colour perceived (which can be different from the facet colour).

As  $\theta_{edge}$  increases, the facet colour transitions from purple/red to dark blue while the surface colour is red-shifted from blue to orange. Transmission measurements were taken with respect to both facet and surface. The associated spectroscopy measurements at the facet are shown in Figure 3, indicating that the reflectance peak shifts from the red region ( $\approx 730$  nm) to the blue region ( $\approx 450$ – $480$  nm). For surface structural colour, 2 different sets of spectroscopy measurements are represented: Figure 3d shows the spectra when the measurements are taken with respect to  $\theta_{DG}$ , where  $\theta_{DG} = \theta_{edge}$  while Figure 3e show measurements taken at  $\theta_{DG}$ , where the angle is offset with respect to  $\theta_{edge}$  (relationship shown in inset). The transmission spectra are recorded and then normalised for background and incident light intensities (Figure S1). Both spectra show that, as the observation angle increases, the measured spectra are red-shifted as the peak shifts from the blue region at  $\lambda \approx 450$  nm to  $\lambda \approx 650$  nm.

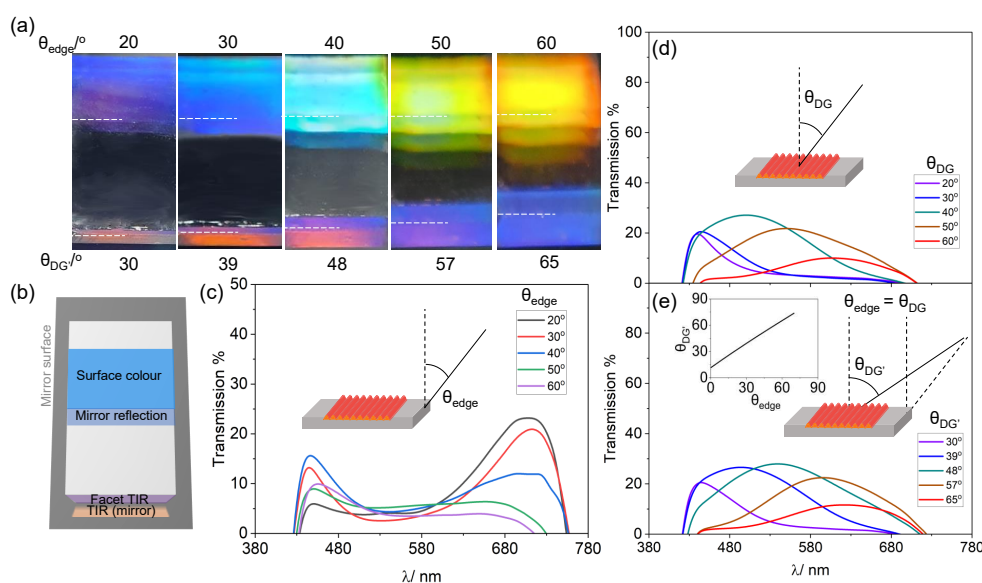


**Figure 3.** (a) Optical image of the structural colour of a 1D surface wrinkled sample with  $d = 700$  nm ( $P = 20$  W,  $\tau = 30$  s,  $\epsilon = 0.5$ ): reflective diffraction (top) and TIR (facet) lead to distinct colours at fixed observation angles. (b) Experimental setup depicting the sample support on a mirror (reflecting also the downward refracted light) the dashed line in (a) demarcates the lower sample edge. (c) Spectroscopic measurements of (TIR) structural colour at the facet at varying  $\theta_{edge}$ . (d) Spectra of reflected diffracted light, measured as a function of  $\theta_{DG}$ , and (e)  $\theta_{DG'}$ , the offset in observation angle when  $\theta_{edge} = \theta_{DG}$ , defined in Figure 1, and related to  $\theta_{edge}$ , are shown in the inset.

#### A Minimal Model for Facet Colour: TIR and Incident Light Dispersion

The resulting structural colour at the facet can be modelled using the principles of TIR within a medium. The angular dispersion of the incident white light from a flood-illuminating source is also included in the model, to reflect practically-relevant conditions. We first describe the behaviour of a sample with a surface diffraction grating of periodicity  $d = 700$  nm, depicted in Figure 3. Figure 4a is a schematic diagram showing three selected wavelengths,  $\lambda = 450$ , 480 and 730 nm, of light incident on the diffracting surface of the sample. These wavelengths were chosen due to their peak positions in the transmission measurements. We first consider that the rays are incident on the grating where  $\theta_i = 0^\circ$ . Within the medium, the general diffraction equation can be modified for a transmission diffraction grating to take into account the respective refractive index ( $n_0$  in air,  $n_1$  in PDMS):

$$m\lambda = d(n_0 \sin\theta_i + n_1 \sin\theta_r) \quad (5)$$

where  $\theta_r$  denotes the angle at which light is diffracted into the sample.  $\lambda = 450$  nm diffracts at  $27.1^\circ$  (1st order) and  $65.8^\circ$  (2nd order),  $\lambda = 480$  nm at  $29.1^\circ$  (1st order) and  $76.6^\circ$  (2nd order), and  $\lambda = 730$  nm at  $45.17^\circ$  (1st order). When the angle of light in the medium (with respect to the normal) exceeds the critical angle, the light undergoes total internal reflection. The critical angle within PDMS, taking into account the refractive index of air ( $n_0 = 1$ ) and of PDMS ( $n_1 \simeq 1.41$ ) is estimated to be

$$\theta_c = \arcsin\left(\frac{n_0}{n_1}\right) = 45.17^\circ \quad (6)$$

As the 1st order of 450 nm and 480 nm wavelengths does not exceed the critical angle, the ray of light refracts out of the sample without being reflected internally when reaching the boundary of the sample. On the other hand, as the angle of diffraction for the 2nd order of  $\lambda = 450$  nm and 480 nm and 1st order of 730 nm exceeds that of the critical angle

for the system, these undergo TIR and propagate through the sample before exiting at the edge we term the “facet” with an angle of  $\theta_{r'}$ , with respect to the (horizontal) facet normal, where  $\theta_{r'} = 90^\circ - \theta_r$ . From there, we can calculate  $\theta_{edge}$  from Equation (7), which is the complementary angle to that of the ray refracted at the facet:

$$\theta_{edge} = 90^\circ - \arcsin(n_1 \times \sin \theta_{r'}) \quad (7)$$

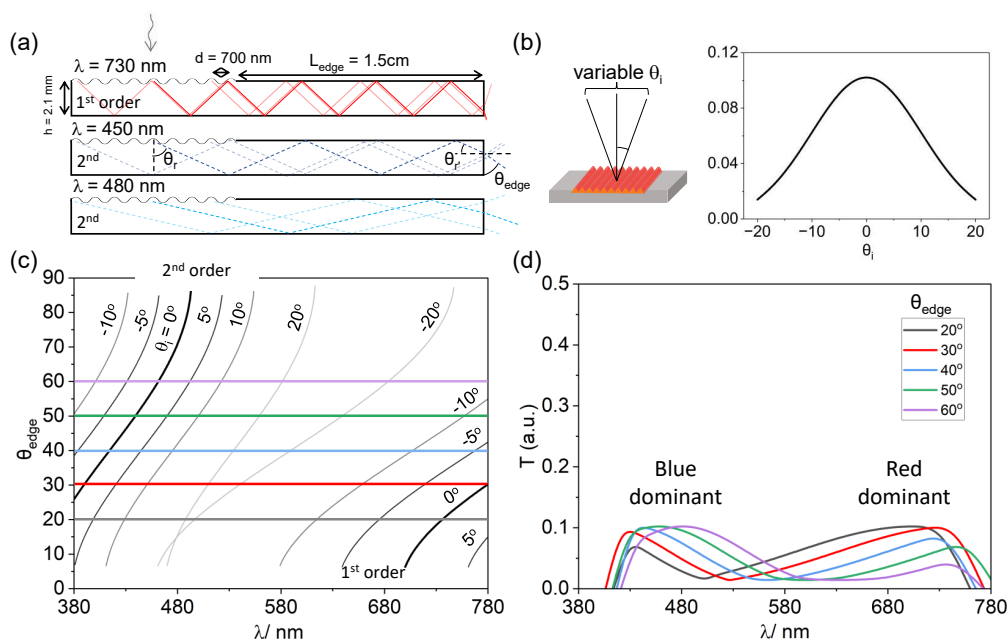


**Figure 4.** (a) Schematic diagram representing the modelling calculations, for a given coupon dimensions (height  $h$ , length  $L_{DG} + L_{edge}$ ) and periodicity  $d$ , each individual wavelength is ray-traced, diffraction orders that do not meet TIR conditions are excluded, and the refracted colours at the edge computed as a function of  $\theta_{edge}$ . (b) Schematic depicting the distribution of incident angles  $\theta_i$  onto a point in the sample and illustrative of angular dispersion, described by a Gaussian profile with a half-width at half-maximum (HWHM) of  $10^\circ$ . (c) Computed relation between ( $\theta_{edge}$ ) and  $\lambda$  at fixed  $\theta_i$  for the 1st and 2nd diffraction orders. Representative fixed  $\theta_{edge}$  angles are shown by the horizontal lines. (d) Predicted spectra for the edge colour, assuming the Gaussian distribution shown in (b), and accounting for the light source  $\lambda$  distribution (Figure S1). At this  $d$ , the edge colour is expected to change from red-dominant to blue-dominant upon increasing  $\theta_{edge}$ , in agreement with Figures 3a,c.

Refracted rays at the facet can either exit towards the mirror (below the sample) or the observer. Due to the size of the incident beam spot, light is incident across the entirety of the grating. As a result, it is insufficient to consider the pathway of only a singular ray incident on the grating, but it is also important to consider incidence at different points along the wrinkles (transparent lines). By considering this, it offers a better understanding of the colours emerging at the facet, thereby leaving the sample at an angle of  $\theta_{r'}$  with respect to the facet’s normal, and refracting towards the observer/ mirror with  $\theta_{edge}$ . This effect is also affected by the geometry of the sample, by changing the optical path of the rays travelling in the medium (Figure S2).

In order to describe the experimental observations, we also consider the intrinsic divergence of most incident light sources and account for the distribution of angles of incidence (variable  $\theta_i$ ) on the surface grating. We model our results using a Gaussian distribution of  $\theta_i$ , ranging from  $-20^\circ$  to  $20^\circ$  (Figure 4b). Combining Equations (5)–(7), we compute the wavelength of light  $\lambda$  observable at  $\theta_{edge}$  accounting for an incident angle  $\theta_i$



distribution (Figure 4c). When  $d = 700$  nm, light diffracts up to two diffraction orders within the medium, where the observation of higher wavelengths arises due to the contribution of the 1st order, while the lower wavelengths are due to the 2nd order. Graphically, for each fixed  $\theta_{edge}$ , the intersection with the  $\theta_i$  dispersion curves yields a series of  $\lambda$  values. In other words, imposing  $\theta_{edge}(\theta_i, \lambda) = \text{fixed value}$  (e.g.,  $20^\circ$  leads to a  $\lambda(\theta_i)$  series. The intensity  $T(\lambda)$  of each  $(\lambda, \theta_i)$  pair (sampled every  $2.5^\circ$ ) is then assigned the corresponding Gaussian pre-factor attributed in Figure 4b, namely  $g(\theta_i) = \exp(\theta_i^2 / (2\sigma^2)) / (\sqrt{2\pi}\sigma)$  (with  $\sigma \simeq 10$ , to match experimental observation). This results in the spectra shown in panel (d); the expression is discretised with 17 terms and normalised to 1. Taking  $\theta_{edge} = 20^\circ$  for example,  $\lambda = 730$  nm is expected to be observed when  $\theta_i = 0^\circ$  (Figure 4c). As our model assumes this incident angle experiences a maximum, Figure 4d indicates this was associated with maximum intensity at 730 nm. Similarly, there is a minimum at  $\lambda \approx 480$  nm due to the smallest weighting when  $\theta_i = \pm 20^\circ$ . Below 480 nm, the contributions of wavelengths are due to the diffraction of the 2nd order, while above this, it is contributed by the 1st order. From this model, we observe that when  $\theta_{edge}$  is  $20^\circ$  and  $30^\circ$ , the measured spectrum shows that the colour observed is red in appearance while for  $40\text{--}60^\circ$ , it is blue in appearance. This is in line with the experimental results, where we observe that there is a greater contribution in red at the facet at smaller  $\theta_{edge}$  while at  $40\text{--}60^\circ$  the facet has a more discernible blue hue to it. The profile of the modelled spectrum agrees with the experimental results in Figure 3c. The spectral signature of the incident white light source does not emit below 400 nm, and therefore, the model does not yield results below 400 nm. The measured intensities are also dependent on the geometry of the sample which affects the distance over which each ray travels; accordingly, longer ray paths lead to lower intensities recorded for their observed wavelengths (Figure S3).

From the modelling of the structural colour, we establish that the colour observed is only dependent on the periodicity of the wrinkles and the observation angle (which themselves are affected by the incidence angle on the grating surface). We can take advantage of the tunability of plasma oxidation of PDMS to fabricate a range of structural colour designs that would achieve multifaceted structural colours. By increasing plasma oxidation power from 20 to 60 W in 10 W increments, we design wrinkles with periodicities ranging from 700 to 1150 nm. Viewing each sample at different  $\theta_{edge}$  angles,  $20^\circ$ ,  $40^\circ$  and  $60^\circ$ , a gamut of colours is observed. The surface structural colour can be predicted based on previous work (Figure 2d) [31,47]. A similar colour map can also be used to design and predict the observed facet colour at  $\theta_{edge}$  with  $d$ . This map was constructed from  $d = 300$  to 1200 nm, which includes up to three diffraction orders, with the assumption that  $\theta_i = 0^\circ$  and only taking into account the dominant colour with no colour mixing from contributions of different orders, and is shown in Figure 5b. Beyond 1.2  $\mu\text{m}$ , we reach the limits in the observation of the facet colour, as the sample generates increasing numbers of diffraction orders mixing additively together (Figure S4). Overall, the model shows good agreement with the experimental results. Transmission spectra were also taken for each sample at the different angles, quantitatively showing that the structural colour is red-shifted, or shifted into higher orders, as the periodicity and  $\theta_{edge}$  increases.

### 2.3. Colour Changes Induced by Environmental Conditions

Structural colour can reflect environmental conditions that affect the surface grating nanostructure. Environmental factors can include the presence of solvents in a liquid or gas atmosphere, or a medium with different refractive indices. When PDMS is exposed to a range of solvents, it can swell and deform significantly. Wrinkled samples ( $P = 30$  W,  $\tau = 30$  s) were soaked in different solvents, ethyl acetate, toluene, and chloroform for 10 min each. These solvents were chosen for their different swelling ratios: 1.18, 1.31, and 1.39, respectively [48]. Prior to optical and AFM imaging, solvent-soaked PDMS coupons were carefully pad-dried with absorbent tissue paper to remove excess solvent, and allowed to air-dry for 2 min. Care was taken not to over-dry the sample and reverse swelling (as demonstrated with toluene and chloroform, for instance) [48–50]. The solvent-soaked

samples can be seen in the optical images in Figure 6a, viewed at increasing  $\theta_{edge}$  at 20, 40 and 60°. When the samples are exposed to solvents with increasing swelling ratios, the facet colours appear to be disproportionately affected, decreasing in intensity. From the AFM scans of the solvent-exposed samples in Figure 6b, we observe that the wrinkling amplitude decreases from its original to a greater extent with solvents of higher swelling ratios (from  $A \approx 175$  nm with no solvent to 12 nm with chloroform) while experiencing a marginal increase in periodicity ( $d = 830$  nm to  $\approx 900$  nm). The marginal increase in periodicity results in a negligible change in structural colour on the surface, however, the decrease in amplitude causes a decrease in measured transmission intensity, shown in Figure 6c. Due to the reversibility of the swelling process [51], such systems have potential uses in sensor technology.

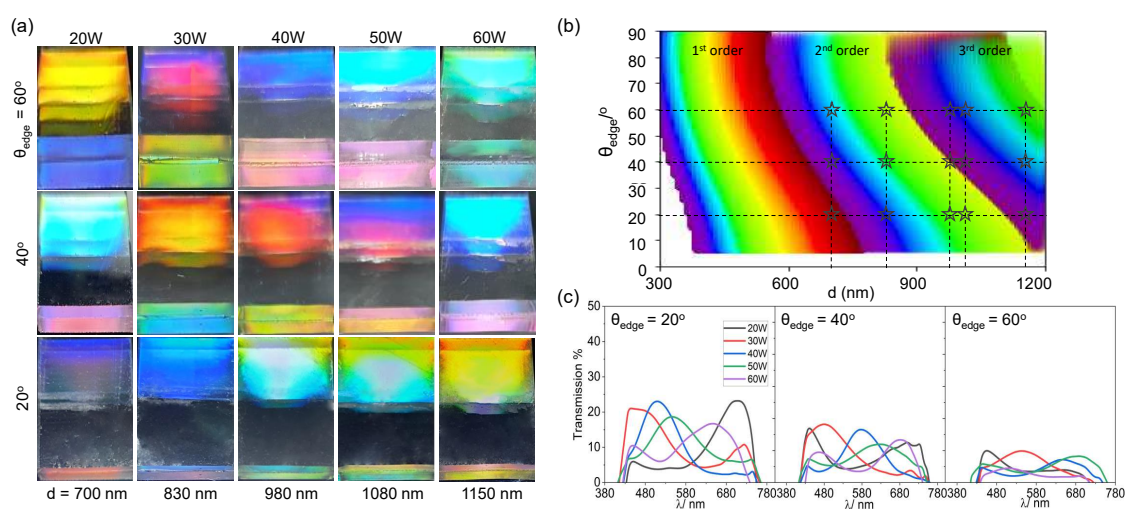


**Figure 5.** Effect of surface periodicity  $d$  on top (reflective diffraction) and facet (TIR) structural colour. (a) Optical images of illustrative samples of varying  $d$  (from 700 to 1150 nm) prepared through varying oxygen plasma power exposure ( $P = 20\text{--}60$  W,  $\tau = 30$  s,  $\epsilon = 0.5$ ), acquired at  $\theta_{edge} = 20, 40$  and  $60^\circ$ . (b) Computed colour map for TIR facet colour, as a function of  $d$  and  $\theta_{edge}$ , for the first three diffraction orders. The star markers indicate conditions investigated experimentally in (a), showing qualitative agreement (see text). (c) Measured spectra of TIR facet colour, corresponding to the samples shown in (a) at the reference  $\theta_{edge} = 20^\circ, 40^\circ$  and  $60^\circ$ . As  $P$  increases, the observed colour is red-shifted and/or transitions into a higher diffraction order at a lower wavelength.

Specimen geometry can be exploited to further expand the variation of multifaceted structural colours. To date, results for 1D samples prepared using a rectangular slab were presented, resulting in facet colour to be observed in the same direction as that from the wrinkled surface. From such samples, the edges can be subsequently cut at different angles, to examine the impact of geometry. Cutting is carried out only after the fabrication of wrinkles to prevent any inhomogeneities in strain application. A schematic of the side and top view shows the expected direction travel of light rays while exiting a sample as shown in Figure 7a. In a rectangular sample, we only need to consider the side view to determine the pathway of ray travel. As previously shown, we can determine the  $\theta_{edge}$  for observed wavelengths, and the facet colours are observed in the same direction as the surface. However, in a cut sample, we also have to consider another dimension for light refraction, where the direction of observation of facet colour is offset from that of the surface colour.



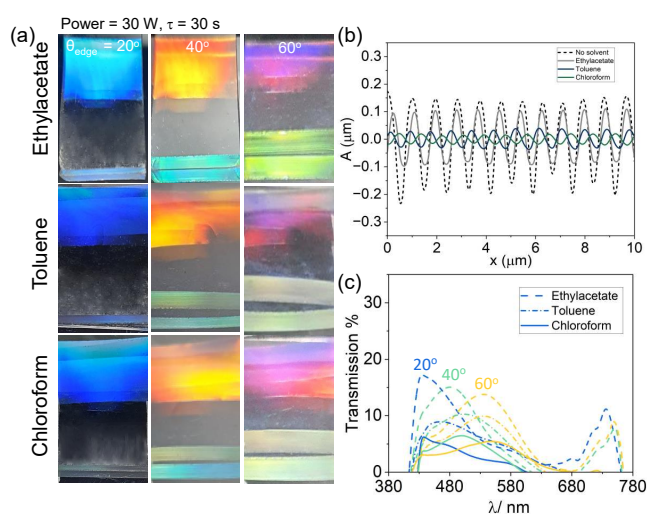


**Figure 6.** Top and facet structural colour change upon solvent-induced swelling. (a) Optical images of illuminated wrinkled samples with  $d = 830$  nm ( $P = 30$  W,  $\tau = 30$  s,  $\epsilon = 0.5$ ) after immersion in ethyl acetate, toluene and chloroform (in increasing order of swelling) for 10 min, at  $\theta_{edge} = 20$ ,  $40$  and  $60^\circ$ . (b) AFM line scans showing the decrease in amplitude  $A$ , and marginal increase in  $d$  upon immersion, and air drying by excess solvent removal (see text). (c) Measured spectra of the TIR facet colour after soaking in ethyl acetate (dash), toluene (dash-dot), chloroform (solid), at observation angles  $\theta_{edge} = 20^\circ$  (blue),  $40^\circ$  (green),  $60^\circ$  (yellow). The reference dry images and spectra are shown in Figure 5a (second column) and Figure 5c.

To demonstrate this effect, Figure 7a shows two samples with “diamond” cuts at the edges, the top row sample prepared at  $P = 20$  W,  $\tau = 30$  s,  $\epsilon = 0.7$  with periodicity  $d = 620$  nm, while the bottom at  $P = 20$  W,  $\tau = 30$  s,  $\epsilon = 0.5$  with  $d = 700$  nm. The sample with periodicity  $d = 620$  nm was observed with increasing  $\theta_{edge}$  at an angle  $\phi = 40^\circ$  offset, where  $\phi$  is defined as the angle about the sample’s horizontal axis (Figure 1a), causing the wrinkling direction to be non-perpendicular to the observer. Since uniaxial wrinkled surfaces act as 1D phase gratings [52], these diffract light solely in the direction perpendicular to that of the orientation of the wrinkles. As a result, structural colour is only observable along that direction, and within a narrow off-specular range (of approximately  $\Delta\phi \pm 5\text{--}10^\circ$ , associated with wrinkling disorder and finite illuminated spot size). Structural colour is otherwise not observable away from this diffraction plane, as illustrated in Figure 7a where only edge colour, due to facet TIR, is visible. As with the other samples, the colour of the facet can be seen to change with increasing  $\theta_{edge}$ , where it transitions from yellow to red. In the 2nd sample, where  $d = 700$  nm, the sample was observed at a fixed  $\theta_{edge} = 50^\circ$ , and rotated about  $\phi$ . We observe that the surface colour yellow can be effectively ‘switched on or off’ along with the facet colours. By exploiting different directions of cuts in the samples, we can manipulate different variations and combinations in the multi-faceted structural colours of these samples.

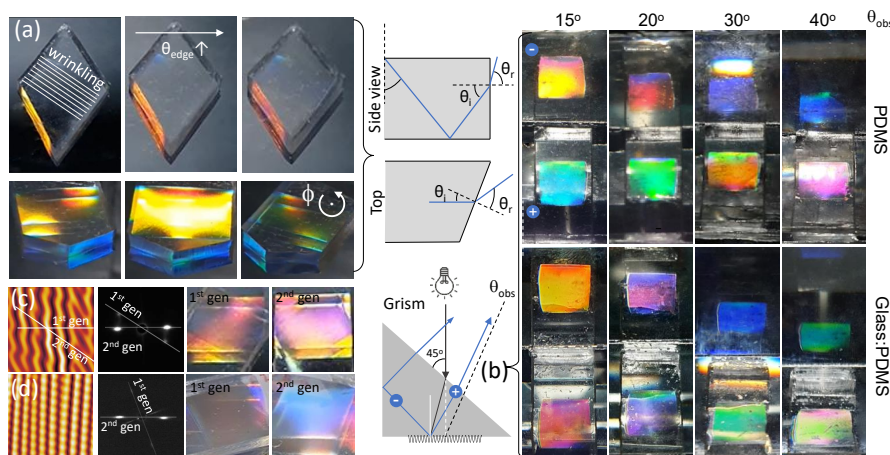


**Figure 7.** (a) Effect of polyhedron shape, illustrated with a diamond cut and relative orientation of the 1D wrinkled surface. The top row  $d = 620$  nm ( $P = 20$  W,  $\tau = 30$  s,  $\epsilon = 0.7$ ) depicts increasing  $\theta_{edge}$ , and the row below ( $d = 700$  nm,  $P = 20$  W,  $\tau = 30$  s,  $\epsilon = 0.5$ ) to varying rotation angle  $\phi$ ; the ray tracing diagrams schematically show the observations described and discussed in the text. (b) Experimental realisation of the coupling of a grating (on a facet) and a prism, termed “grism”, whose setup is illustrated in the sketch. Optical images obtained for PDMS (top) and glass (bottom) prisms, obtained with  $d = 980$  nm ( $P = 40$  W,  $\tau = 30$  s,  $\epsilon = 0.5$ ). Colour dispersion can be finely tuned by these two optical elements. (c) AFM scans of 2-dimensional (or biaxial) “sand ripple” wrinkled surfaces, fabricated by two equal mechanical wrinkling steps with  $\epsilon = 0.2$ ,  $P = 50$  W,  $\tau = 30$  s, at an angle of  $\phi = 30^\circ$  between the two generations; (d) 2D pattern generated with 1st generation  $\epsilon_1 = 0.5$ ,  $P = 50$  W,  $\tau = 30$  s, and 2nd generation  $\epsilon_2 = 0.2$ ,  $P = 20$  W,  $\tau = 30$  s, with  $\phi = 70^\circ$  between generations.

Incorporating surface grating with a prism, we demonstrated the fabrication of GRISMs (Figure S5). In this context, a GRISM is a compound optical element that significantly reduces the influence of light dispersion from the individual elements. A prism deflects violet light more than red, while a diffraction grating deflects red more than violet. By combining the two, light can be separated into its components while offsetting the beam deviations resulting from each element. In a simple realisation of a GRISM, we placed model prisms made of either PDMS ( $n = 1.41$ ) or glass ( $n = 1.52$ ) on top of a wrinkled PDMS sample ( $P = 40$  W,  $d = 980$  nm) to create GRISMs (PDMS, and Glass:PDMS) as shown in the schematic in Figure 7b. The samples were placed such that the wrinkled surface was in contact with the prism. Employing white light, the GRISMs were viewed at increasing  $\theta_{obs}$ , from  $15^\circ$  to  $40^\circ$ .  $\theta_{obs}$  is taken from the normal of the base of the GRISM, directly under the centre of the incident light.

GRISMs show a “dual” image of the wrinkled surface exhibiting different colours. When white light is shone vertically, it illuminates the prism surface at an angle of  $45^\circ$ , and then refracts into the medium, thus impinging on the grating at an angle, before diffracting back into the medium. The grating diffracts positive and negative diffraction orders, denoted in the schematic as + and -. The rays from the positive orders are then incident on the top face of the GRISM and are refracted out, while those from the negative orders will first hit the side face of the grism. If the angle of the rays incident on the side face exceeds the critical angle, it undergoes TIR before exiting from the top. The combination of the two diffraction orders produces dual-coloured appearances, shown in the optical images. From an observer’s perspective in an optical image, the top colour is produced by the negative diffraction order while the bottom is from the positive order. As  $\theta_{obs}$  increases, we observe a gamut of different colours, which can also be manipulated by changing the material composition of the prism. Figure 7b shows that by changing the refractive index of the medium (PDMS to glass), we are able to obtain distinct colours in the GRISMs.

Finally, building on our previous work, we explore the manipulation of structural colour in two-dimensional (2D) samples further [31,53,54]. 2D samples can either be fabricated in a sequential or simultaneous wrinkling step. Here, the 2D samples are fabricated through the superposition of wrinkles in a sequential step (details described in the Methods section). By manipulating the conditions in the first and second steps, we achieve different intensities and/or colours depending on the orientation of the sample. Figure 7c illustrates a specimen fabricated with two equal mechanical wrinkling steps with  $\epsilon = 0.2$ ,  $P = 50$  W,  $\tau = 30$  s, at an angle of  $\phi = 30^\circ$  between the 2 wrinkling generations. The resulting structure shows a ‘sand ripple’ pattern, producing a diffraction grating where two sets of diffraction orders can be observed. In the light scattering image, the 1st generation diffraction appears at  $\phi = 30^\circ$  from the horizontal with an associated wrinkle wavelength of  $d_1$ , while the 2nd generation diffraction pattern is along the horizontal ( $x$ ) axis with  $d_2$ . As the conditions of the two generations are equal,  $d_1 = d_2$  and the structural colour observed by the two generations at a given  $\theta_{edge}$  are similar. However, in the superposition of wrinkles, the 2nd generation suppresses the 1st generation’s amplitude, causing the intensity of the 2nd generation to be greater than that of the 1st generation.

As the angle between the generations,  $\phi$  increases, the 2nd generation dominates. This is the result of the relationship between the formation of the surface topography and its principal coordinates  $x$  and  $y$ . When the second generation has a larger strain component in the  $y$  direction compared to the  $x$  direction, it suppresses the amplitude in the first generation to a greater extent. Figure 7d shows a 2D sample fabricated under two different conditions: 1st generation  $\epsilon_1 = 0.5$ ,  $P = 50$  W,  $\tau = 30$  s, and 2nd generation  $\epsilon_2 = 0.2$ ,  $P = 20$  W,  $\tau = 30$  s, with  $\phi = 70^\circ$  between generations. In order to observe any structural colour in the 1st generation at high  $\phi$ , a large mismatch in strain and plasma conditions is required to compensate for the decrease in amplitude in the 1st generation. This mismatch in conditions results in different colours being observed in the generations, with a low-intensity red hue in the 1st generation, and a bright blue observed in the 2nd generation.

### 3. Materials and Methods

PDMS (Sylgard 184, Dow Corning, Midland, MI, USA) coupons were prepared by casting a mixture of prepolymer and curing agent with a mass ratio of 10:1. The liquid mixture was stirred vigorously, degassed under vacuum, deposited onto a glass plate and cured at  $75^\circ\text{C}$  in a convection oven for 1 h to crosslink into a PDMS elastomer slab with the required thickness (ranging from 2.0 to 3.0 mm). The coupons of 1.5 cm in width and varying lengths (4–8 cm) were then cut with a blade.

In order to create a bilayer with a glassy skin, surface plasma oxidation of the PDMS coupon samples was performed with a 40 kHz Diener Plasma (Femto, Diener Electronic, Ebhausen, Germany), fitted with a pressure sensor (TM 101, Thermovac, Leybold GmbH, Cologne, Germany) and connected to oxygen (BOC, 99.5%). Samples were treated under plasma at 10 W intervals from  $P = 20$  to 60 W, with exposure time kept constant at  $\tau = 30$  s. The chambers were evacuated to a pressure of 0.1 mbar, before introducing oxygen for 5 min until the pressure reached 0.2 mbar and stabilised. The plasma was then ignited, at the required power and exposure time.

One-dimensional (1D), regular, sinusoidal patterns were fabricated by imposing uni-axial strain on a PDMS coupon (typically 2.5 cm long  $\times$  1.5 cm wide) using a strain stage. The strain clamps were placed 1 cm apart onto the PDMS coupon, and the samples were stretched to a prestrain of 0.5, before undergoing plasma oxidation, and subsequently released from strain, yielding a sinusoidal diffraction grating (1 cm long) of prescribed wavelength and amplitude. The prestrain is calculated with respect to the initial ( $L_0$ ) and final distance ( $L_1$ ) between the clamps,  $\epsilon = \frac{L_1 - L_0}{L_0}$ .

Two dimensional (2D) surfaces were fabricated by a wave superposition method, reported previously [36,53,54]. In short, an initial 1D sample is fabricated and then replicated onto fresh PDMS. The “replica” is generated by first coating the “master” with octadecyl trichlorosilane (OTS) (Acros Organics, 95%) from the vapour phase, and then casting

liquid PDMS, which is then crosslinked at 75 °C for 1 h and peeled off from the master. This process offers excellent replication fidelity. The replica is then tilted so that the 1D pattern is oriented along the desired  $\phi$  angle and cropped in a rectangular shape, to avoid inhomogeneities during the secondary strain application ( $\epsilon_2$ ) and plasma oxidation step (with independently variable parameters of  $\epsilon$ ,  $P$  and  $\tau$ ). Once the strain is released a 2D secondary pattern is formed.

The surface topographies were characterised by atomic force microscopy (AFM) using a Bruker Innova microscope, in tapping mode at 0.2 Hz, equipped with Al-coated Si tips (MPP-11100-W, Bruker, Billerica, MA, USA) and analysed with the in-built Nanoscope software. Structural colour spectra were recorded using BLACK-Comet UV-VIS Spectrometer (StellarNet Inc, Tampa, FL, USA) with F600-VIS-NIR fiber optic cable with a white light source (Advanced Illumination, Rochester, VT, USA) in a dark environment. Optical photos were taken with a digital camera.

#### 4. Conclusions

In this paper, we demonstrate the design and fabrication of multi-faceted structural colour on a transparent elastomeric material (PDMS), by patterning surface diffraction grating via oxygen plasma oxidation and exploiting TIR. Tunable wrinkles on the surface yield striking structural color by acting as reflective diffraction gratings, whose response we model and validate experimentally. The main novelty of our paper is the exploration of TIR as a means to generate structural colour on the other facets of a 3D material, emulating a range of naturally-occurring materials. TIR selects a limited subset of diffracted colours which are propagated, while the rest are refracted. The “side” (facet) colour can thus differ from the surface-diffracted colour and can be controlled by well-defined design rules which we establish and describe in this work. The design and selection of sample geometry can pave the way for an extensive library of designs, with “gem cut-like” characteristics. Macroscopically shaped objects (such as cuboids, triangles, etc.) thus affect light propagation and colour appearance, and we generate a so-called GRISM for the illustration of an optical device. An elastomer colour sensor is also demonstrated since elastomeric materials are sensitive to some gaseous or liquid medium changes. The design parameter space for inducing “multifaceted” colour by coupling diffraction and TIR is very large and promising. Our findings are expected to be relevant to a wide range of applications, including displays, packaging, and sensors.

**Supplementary Materials:** The following supporting information can be downloaded at: <https://www.mdpi.com/article/10.3390/molecules28041710/s1>, Figure S1. Light source spectrum and PDMS optical attenuation; Figure S2. Effect of sample geometry (thickness); Figure S3. Effect of sample geometry (length); Figure S4. Limits of facet TIR; Figure S5. Fabrication of an illustrative GRISM.

**Author Contributions:** Conceptualization, A.T. and J.T.C.; methodology, A.T., Z.A. and P.V.; formal analysis, A.T.; validation, A.T., Z.A.; investigation, A.T.; writing—original draft preparation, A.T., Z.A., P.V., J.T.C.; writing—review and editing, A.T., Z.A., P.V., J.T.C.; supervision, J.T.C.; project administration, J.T.C.; funding acquisition, J.T.C. All authors have read and agreed to the published version of the manuscript.

**Funding:** This research was funded by Procter & Gamble and the EPSRC-funded Plastic Electronics CDT for a PhD scholarship (Grant Number EP/L016702/1).

**Data Availability Statement:** Data is contained within the article or supplementary material and available from the authors upon request.

**Acknowledgments:** The authors thank Procter & Gamble and the EPSRC-funded Plastic Electronics CDT for a PhD scholarship (Grant Number EP/L016702/1) and the Royal Academy of Engineering (RAEng, UK) for funding and a research chair. The authors also thank Imperial College Advanced Hackspace for the use of the laser cutter machine.

**Conflicts of Interest:** The authors declare no conflict of interest.

**Sample Availability:** Samples of the compounds are available from the authors upon request.

## References

1. Srinivasarao, M. Nano-optics in the biological world: Beetles, butterflies, birds, and moths. *Chem. Rev.* **1999**, *99*, 1935–1962.
2. Vukusic, P.; Sambles, J.R. Photonic structures in biology. *Nature* **2003**, *424*, 852–855.
3. Kinoshita, S.; Yoshioka, S.; Miyazaki, J. Physics of structural colors. *Rep. Prog. Phys.* **2008**, *71*, 076401.
4. Hsiung, B.K.; Siddique, R.H.; Stavenga, D.G.; Otto, J.C.; Allen, M.C.; Liu, Y.; Lu, Y.F.; Deheyn, D.D.; Shawkey, M.D.; Blackledge, T.A. Rainbow peacock spiders inspire miniature super-iridescent optics. *Nat. Commun.* **2017**, *8*, 1–8.
5. Vukusic, P.; Sambles, J.; Lawrence, C.; Wootton, R. Quantified interference and diffraction in single Morpho butterfly scales. *Proc. Royal Soc. B* **1999**, *266*, 1403–1411.
6. Gur, D.; Palmer, B.A.; Weiner, S.; Addadi, L. Light manipulation by guanine crystals in organisms: Biogenic scatterers, mirrors, multilayer reflectors and photonic crystals. *Adv. Funct. Mater.* **2017**, *27*, 1603514.
7. Teyssier, J.; Saenko, S.V.; Van Der Marel, D.; Milinkovitch, M.C. Photonic crystals cause active colour change in chameleons. *Nat. Commun.* **2015**, *6*, 1–7.
8. Saito, A.; Yamashita, K.; Hattori, T.; Kuwahara, Y. Novel optical applications inspired by the Morpho butterfly's coloration: Technology transfer from reflection to transmission. *JJAP* **2022**, *61*, SD0801.
9. Dong, Z.; Zhao, H.; Nie, L.; Tang, S.; Li, C.; Wang, X. Effects of Measurement Configurations on the Sensitivity of Morpho Butterfly Scales Based Chemical Biosensor. *Front. Phys.* **2022**, *9*, 792.
10. Wang, H.; Zhang, K.Q. Photonic crystal structures with tunable structure color as colorimetric sensors. *Sensors* **2013**, *13*, 4192–4213.
11. Lee, H.S.; Shim, T.S.; Hwang, H.; Yang, S.M.; Kim, S.H. Colloidal photonic crystals toward structural color palettes for security materials. *Chem. Mater.* **2013**, *25*, 2684–2690.
12. Yang, W.; Xiao, S.; Song, Q.; Liu, Y.; Wu, Y.; Wang, S.; Yu, J.; Han, J.; Tsai, D.P. All-dielectric metasurface for high-performance structural color. *Nat. Commun.* **2020**, *11*, 1–8.
13. Cheng, F.; Gao, J.; Luk, T.S.; Yang, X. Structural color printing based on plasmonic metasurfaces of perfect light absorption. *Sci. Rep.* **2015**, *5*, 1–10.
14. Yamashita, K.; Kunitsu, K.; Hattori, T.; Kuwahara, Y.; Saito, A. Demonstration of a diffraction-based optical diffuser inspired by the Morpho butterfly. *Optics Express* **2021**, *29*, 30927–30936.
15. Xuan, Z.; Li, J.; Liu, Q.; Yi, F.; Wang, S.; Lu, W. Artificial structural colors and applications. *Innovation* **2021**, *2*, 100081.
16. Chen, G.; Hong, W. Mechanochromism of Structural-Colored Materials. *Adv. Opt. Mater.* **2020**, *8*, 2000984.
17. Zhou, Q.; Park, J.G.; Bae, J.; Ha, D.; Park, J.; Song, K.; Kim, T. Multimodal and covert–overt convertible structural coloration transformed by mechanical stress. *Adv. Mater.* **2020**, *32*, 2001467.
18. Fan, W.; Zeng, J.; Gan, Q.; Ji, D.; Song, H.; Liu, W.; Shi, L.; Wu, L. Iridescence-controlled and flexibly tunable retroreflective structural color film for smart displays. *Sci. Adv.* **2019**, *5*, eaaw8755.
19. Zeng, J.; Fan, W.; Jia, K.; Tu, S.; Wu, L. Novel Retroreflective Structural Color Films Based on Total Internal Reflection Interference. *J. Colloid Interface Sci.* **2021**, *597*, 306–313.
20. Goodling, A.E.; Nagelberg, S.; Kaehr, B.; Meredith, C.H.; Cheon, S.I.; Saunders, A.P.; Kolle, M.; Zarzar, L.D. Colouration by total internal reflection and interference at microscale concave interfaces. *Nature* **2019**, *566*, 523–527.
21. Qin, M.; Sun, M.; Hua, M.; He, X. Bioinspired structural color sensors based on responsive soft materials. *Curr. Opin. Solid State Mater. Sci.* **2019**, *23*, 13–27.
22. Burgess, I.B.; Lončar, M.; Aizenberg, J. Structural colour in colourimetric sensors and indicators. *J. Mater. Chem. C* **2013**, *1*, 6075–6086.
23. Shiba, K.; Zhuang, C.; Minami, K.; Imamura, G.; Tamura, R.; Samitsu, S.; Idei, T.; Yoshikawa, G.; Sun, L.; Weitz, D.A. Visualization of Flow-Induced Strain Using Structural Color in Channel-Free Polydimethylsiloxane Devices. *Adv. Sci.* **2022**, *10*, 2204310.
24. Ma, T.; Chen, S.; Li, J.; Yin, J.; Jiang, X. Strain-ultrasensitive surface wrinkles for visual optical sensors. *Mater. Horiz.* **2022**, *9*, 2233–2242.
25. Huang, X.; Hai, Y.; Xie, W.H. Anisotropic cell growth-regulated surface micropatterns in flower petals. *Theor. App. Mech. Lett.* **2017**, *7*, 169–174.
26. Chen, C.; Airoidi, C.A.; Lugo, C.A.; Bay, R.K.; Glover, B.J.; Crosby, A.J. Flower Inspiration: Broad-Angle Structural Color through Tunable Hierarchical Wrinkles in Thin Film Multilayers. *Adv. Funct. Mater.* **2021**, *31*, 2006256.
27. Nixon, M.; Orr, A.; Vukusic, P. Wrinkles enhance the diffuse reflection from the dragonfly *Rhyothemis resplendens*. *J. R. Soc. Interface* **2015**, *12*, 20140749.
28. Oh, J.H.; Woo, J.Y.; Jo, S.; Han, C.S. Iridescent and Glossy Effect on Polymer Surface Using Micro-/Nanohierarchical Structure: Artificial Queen of the Night Tulip Petals. *ACS Appl. Mater. Interfaces* **2019**, *11*, 26442–26447.
29. Airoidi, C.A.; Lugo, C.A.; Wightman, R.; Glover, B.J.; Robinson, S. Mechanical buckling can pattern the light-diffracting cuticle of *Hibiscus trionum*. *Cell Rep.* **2021**, *36*, 109715.
30. Zhou, L.; Yang, L.; Liu, Y.; Xu, Z.; Yin, J.; Ge, D.; Jiang, X. Dynamic structural color from wrinkled thin films. *Adv. Opt. Mater.* **2020**, *8*, 2000234.
31. Tan, A.; Pellegrino, L.; Ahmad, Z.; Cabral, J.T. Tunable structural color with gradient and multiaxial polydimethylsiloxane wrinkling. *Adv. Opt. Mater.* **2022**, *10*, 2200964.
32. Sarov, Y.; Ivanov, T.; Ivanova, K.; Sarova, V.; Capek, I.; Rangelow, I. Diffraction under total internal reflection for micro-fluidic analysis. *Appl. Phys. A* **2006**, *84*, 191–196.

33. Tamulevičius, T.; Šeperys, R.; Andrulevičius, M.; Tamulevičius, S. Total internal reflection based sub-wavelength grating sensor for the determination of refractive index of liquids. *Photonics Nanostruct.-Fundam. Appl.* **2011**, *9*, 140–148.
34. Burg, S.L.; Parnell, A.J. Self-assembling structural colour in nature. *J. Phys. Condens. Matter* **2018**, *30*, 413001.
35. Bowden, N.; Huck, W.T.; Paul, K.E.; Whitesides, G.M. The controlled formation of ordered, sinusoidal structures by plasma oxidation of an elastomeric polymer. *Appl. Phys. Lett.* **1999**, *75*, 2557–2559.
36. Chiche, A.; Stafford, C.M.; Cabral, J.T. Complex micropatterning of periodic structures on elastomeric surfaces. *Soft Matter* **2008**, *4*, 2360–2364.
37. Bayley, F.A.; Liao, J.L.; Stavrinou, P.N.; Chiche, A.; Cabral, J.T. Wavefront kinetics of plasma oxidation of polydimethylsiloxane: limits for sub- $\mu\text{m}$  wrinkling. *Soft Matter* **2014**, *10*, 1155–1166.
38. Nania, M.; Matar, O.K.; Cabral, J.T. Frontal vitrification of PDMS using air plasma and consequences for surface wrinkling. *Soft Matter* **2015**, *11*, 3067–3075.
39. Ferretti, G.; Nania, M.; Matar, O.; Cabral, J.T. Wrinkling Measurement of the Mechanical Properties of Drying Salt Thin Films. *Langmuir* **2016**, *32*, 2199–2207.
40. Nania, M.; Foglia, F.; Matar, O.K.; Cabral, J.T. Sub-100 nm wrinkling of polydimethylsiloxane by double frontal oxidation. *Nanoscale* **2017**, *9*, 2030–2037.
41. Kim, G.H.; Woo, H.; Lim, G.; An, T. Development of Optical Strain Sensor with Nanostructures on a Poly-dimethylsiloxane (PDMS) Substrate. *J. Sens. Sci. Technol.* **2018**, *27*, 392–396.
42. Li, Z.; Liu, Y.; Marin, M.; Yin, Y. Thickness-dependent wrinkling of PDMS films for programmable mechanochromic responses. *Nano Res.* **2020**, *13*(7), 1–7.
43. Qi, Y.; Zhou, C.; Zhang, S.; Zhang, Z.; Niu, W.; Wu, S.; Ma, W.; Tang, B. Bar-coating programmable mechanochromic bilayer PDMS film with angle-dependent and angle-independent structural colors. *Dyes Pigm.* **2021**, *189*, 109264.
44. Wu, K.; Zhu, T.; Zhu, L.; Sun, Y.; Chen, K.; Chen, J.; Yuan, H.; Wang, Y.; Zhang, J.; Liu, G.; et al. Reversible Mechanochromisms via Manipulating Surface Wrinkling. *Nano Lett.* **2022**.
45. Owen, M.J.; Smith, P.J. Plasma treatment of polydimethylsiloxane. *J. Adhes. Sci. Technol.* **1994**, *8*, 1063–1075.
46. Jiang, H.; Khang, D.Y.; Song, J.; Sun, Y.; Huang, Y.; Rogers, J.A. Finite deformation mechanics in buckled thin films on compliant supports. *Proc. Natl. Acad. Sci. USA* **2007**, *104*, 15607–15612.
47. Tan, A.; Pellegrino, L.; Cabral, J.T. Tunable Phase Gratings by Wrinkling of Plasma-Oxidized PDMS: Gradient Skins and Multiaxial Patterns. *ACS Appl. Polym. Mater.* **2021**, *3*, 5162–5170.
48. Lee, J.N.; Park, C.; Whitesides, G.M. Solvent compatibility of poly (dimethylsiloxane)-based microfluidic devices. *Anal. Chem.* **2003**, *75*, 6544–6554.
49. Toepke, M.W.; Beebe, D.J. PDMS absorption of small molecules and consequences in microfluidic applications. *Lab Chip* **2006**, *6*, 1484–1486.
50. Dangla, R.; Gallaire, F.; Baroud, C.N. Microchannel deformations due to solvent-induced PDMS swelling. *Lab Chip* **2010**, *10*, 2972–2978.
51. Rumens, C.; Ziai, M.; Belsey, K.; Batchelor, J.; Holder, S. Swelling of PDMS networks in solvent vapours; applications for passive RFID wireless sensors. *J. Mater. Chem. C* **2015**, *3*, 10091–10098.
52. Harrison, C.; Stafford, C.; Zhang, W.; Karim, A. Sinusoidal phase grating created by a tunably buckled surface. *Appl. Phys. Lett.* **2004**, *85*, 4016–4018.
53. Pellegrino, L.; Khodaparast, S.; Cabral, J.T. Orthogonal wave superposition of wrinkled, plasma-oxidised, polydimethylsiloxane surfaces. *Soft Matter* **2020**, *16*, 595–603.
54. Pellegrino, L.; Tan, A.; Cabral, J.T. Ripple Patterns Spontaneously Emerge through Sequential Wrinkling Interference in Polymer Bilayers. *Phys. Rev. Lett.* **2022**, *128*, 058001.

**Disclaimer/Publisher's Note:** The statements, opinions and data contained in all publications are solely those of the individual author(s) and contributor(s) and not of MDPI and/or the editor(s). MDPI and/or the editor(s) disclaim responsibility for any injury to people or property resulting from any ideas, methods, instructions or products referred to in the content.